ÇUKUROVA UNIVERSITY
INSTITUTE OF SCIENCE

PhD THESIS

Susanne Marie JAMISON

SYNTHESIS AND CHARACTERIZATION OF NOVEL PRECURSORS FOR THE DEPOSITION OF NANOPARTICLE METALS ON MULTI-WALLED CARBON NANOTUBES IN SUPERCRITICAL CARBON DIOXIDE

DEPARTMENT OF CHEMISTRY

ADANA, 2013

ÇUKUROVA ÜNİVERSİTESİ
FEN BİLİMLERİ ENSTİTÜSÜ

DOKTORA TEZİ

Susanne Marie JAMISON

NOVEL PRECURSORS FOR THE DEPOSTITION OF METAL NANOPARTICLES ON CARBON NANOTUBES IN SUPERCRITICAL CARBON DIOXIDE

KİMYA ANABİLİM DALI

ADANA, 2014

ÇUKUROVA UNIVERSITY
INSTITUTE OF NATURAL AND APPLIED SCIENCES

NOVEL PRECURSORS FOR THE DEPOSITION OF METAL NANOPARTICLES ON CARBON NANOTUBES IN SUPERCRITICAL CARBON DIOXIDE

Susanne Marie JAMISON

PhD THESIS

DEPARTMENT OF CHEMISTRY

We certify that the thesis titled above was reviewed and approved for the award of degree of the Doctor of Philosophy by the board of jury on 15/07/2014.

…….	…….	……
Prof.Dr.Bilgehan GÜZEL	Prof.Dr.Selahattin SERİN	Prof.Dr.Ramazan ESEN
SUPERVISOR	MEMBER	MEMBER

…….....	…….....
Prof.Dr.Osman SERİNDAĞ	Asst.Prof.Dr.Göktürk AVŞAR
MEMBER	MEMBER

This PhD Thesis is written at the Chemistry Department of Institute of Natural And Applied Sciences of Çukurova University.
Registration Number:

Prof. Dr. Mustafa GÖK
Director
Institute of Natural and Applied Sciences

This study was supported by Management Unit of Scientific Research Projects of Ç.U.
Project No: FEF2012D22

ABSTRACT

PhD THESIS

SYNTHESIS AND CHARACTERIZATION OF NOVEL PRECURSORS FOR THE DEPOSITION OF NANOPARTICLE METALS ON MULTI-WALLED CARBON NANOTUBES IN SUPERCRITICAL CARBON DIOXIDE

Susanne Marie JAMISON

ÇUKUROVA UNIVERSITY
INSTITUTE OF SCIENCE
DEPARTMENT OF CHEMISTRY

Supervisor : Prof. Dr. Bilgehan GÜZEL
Year: 2014, Pages: 187
Jury : Prof. Dr. Bilgehan GÜZEL
: Prof. Dr. Ramazan ESEN
: Prof. Dr. Selahattin SERİN
: Prof. Dr. Osman SERİNDAĞ
: Asst. Prof. Dr. Göktürk AVŞAR

Pd(II), W(VI) and Ni(II) metal complexes with ligands derived from fluorous Schiff bases and oximes were synthesized in order to determine their use as precursors in the deposition of metal nanoparticles. Their structures were determined as well as their use in deposition onto multi-walled carbon nanotubes in $scCO_2$. The Schiff base ligands were made by reacting various aniline derivatives with aldehydes. The oxime derivatives were synthesized by reacting various diones with hydroxyl ammonium hydrochloride. In order to increase the solubility of the complexes in $scCO_2$, all of the ligands were synthesized with fluorine, some with long fluorous chains. All ligands were characterized by FT-IR and ^{1}H NMR. The complexes were also characterized via FT-IR and ^{1}H NMR. The metal complexes were qualitatively determined to be soluble in supercritical medium. The synthesized metal complexes were used as precursors for the deposition of the metals onto multiwalled carbon nanotubes, resulting in the synthesis of nano-sized metal catalysts. The synthesized nanocatalyst composites were analyzed by SEM and XRD. The Pd particles ranged from 3.8-13.8nm, the Ni nanoparticles ranged from 1.9-4.0nm, and the W nanoparticles were 0.9-3.0nm.

Key Words: Precursor, Schiff Base, Oxime, Supercritical Carbon Dioxide, deposition

ÖZ

DOKTORA TEZİ

ÇOK DUVARLI KARBON NANOTÜP DESTEKLİ METAL NANOPARTİKÜLLERİN SÜPER KRİTİK KARBON DİOKSİT ORTAMINDA DEPOZİSYONUNDA KULLANMAK AMACIYLA YENİ ÖNCÜLLERİN SENTEZİ VE KARAKTERİZASYONU

Susanne Marie JAMISON

ÇUKUROVA ÜNİVERSİTESİ
FEN BİLİMLERİ ENSTİTÜSÜ
KİMYA ANABİLİM DALI

Danışman : Prof. Dr. Bilgehan GÜZEL
Yıl: 2014, Sayfa: 187
Jüri : Prof. Dr. Bilgehan GÜZEL
: Prof. Dr. Ramazan ESEN
: Prof. Dr. Selahattin SERİN
: Prof. Dr. Osman SERİNDAĞ
: Yrd. Doç. Dr. Göktürk AVŞAR

Süper kritik CO_2 ortamında depozisyon işleminde öncül olarak kullanmak amacıyla florlu Schiff bazı ve oksim ligantları ve bu ligantların Pd(II), Ni(II) ve W(VI) metal kompleksleri sentezlendi. Sentezlenen ligand ve komplekslerin yapıları aydınlatıldı ve süper kritik karbon dioksit ortamında çok duvarlı karbon nanotüp üzerine depozisyon işleminde kullanılabilirlikleri incelendi. Schiff bazı ligantları, çeşitli anilin türevlerinin çeşitli aldehitler ile tepkimesi sonucu sentezlendi. Oksim ligantları ise farklı diketonlar ile hidroksilamin hidroklorürün tepkimesi sonucu sentezlendi. Süper kritik karbon dioksit ortamında komplekslerin çözünürlüğünü arttırmak için, sentezde flor atomu içeren reaktifler kullanıldı. Bazı ligantların sentezinde uzun flor zincirleri olan bileşikler kullanıldı. Bütün ligantlar ve kompleksler FT-IR ve ^{1}H NMR ile karakterize edildi. Metal komplekslerin süper kritik CO_2 ortamında nitel olarak çözündüğü belirlendi. Sentezlenen metal kompleksler, $scCO_2$ ortamında metallerin karbon nanotüp üzerine depozisyonu için öncül olarak kullanılarak nano boyutta metal katalizörler elde edildi. Sentezlenen nanokatalizörler SEM-EDX ve XRD ile analiz edildi. MWCNT destekli Pd nanopartiküllerin boyutunun 3.8-13.8 nm, Ni nanopartiküllerin boyutunun 1.9-4.0 nm ve W nanopartiküllerin boyutunun 0.9-3.0 nm arasında olduğu belirlendi.

Anahtar Kelimeler: Öncül, Schiff Bazı, Oksim, Süper kritik karbon dioksit, depozisyon

ACKNOWLEDGEMENTS

I would like to thank all of the people who have helped and supported me throughout the process of this whole doctorate program and research. This research would not have been possible without the support, help and guidance from many people.

First of all, I would like to thank my advisor, Professor Bilgehan Güzel, for helping me choose this topic, directing me in the research, helping me understand confusing results and finding a way to finish when it seemed impossible.

I would also like to thank the members of my committee, Professor Selahattin Serin, Professor Ramazan Esen, Professor Osman Serindağ and Assistant Professor Gokturk Avsar for their valuable insight and encouragement. I would like to say a special thanks to Professor Ramazan for his work with the XRD and to the head of the Chemistry department, Professor Giray Sultan, for her encouragement.

I could not have finished this research without the help of my lab mates, Fatma Ulusal, Burcu Darendeli and Asım Eğitmen. They worked tirelessly to help me complete my lab work to help me navigate the systems in Turkey and.

Thank you also to Çukurova University and the Chemistry department for providing me the finances needed to undertake and complete this research.

Finally, thanks to my husband who was a constant source of encouragement and help.

CONTENTS **PAGE**

LIST OF TABLES **PAGE**

LIST OF FIGURES **PAGE**

ABBREVIATIONS

°C	: Degrees Celsius
^{13}C NMR	: Carbon nuclear magnetic resonance
^{19}F NMR	: Fluorine nuclear magnetic resonance
^{1}H NMR	: Proton nuclear magnetic resonance
Å	: Angstrom
Ar	: Aromatic
ATR	: Attenuated total reflection
cm	: Centimeters
CNT	: Carbon nanotube
cps	: Counts per second
D	: Distance
d	: Dublet
deg	: Degree
DMSO	: Dimethyl sulfoxide
Ea	: Activation Energy
EDX	: Energy dispersive using x-ray
FT-IR	: Fourier transmission infrared spectroscopy
FWHM	: Full width at half maximum
g	: Gram
m	: Multiplet
m.p.	: Melting point
M/MWCNT	: Metal/mutli-walled carbon nanotube composite
mL	: Milliliter
mmol	: Millimole
mol	: Mole
MPa	: Megapascal
MW	: Molecular weight
MWCNT	: Multi-walled carbon nanotube

N : Normal

Ni-ox1 : Nickel (II) 1,1,1-trifluoro-2,4-pentanedione 2-oxime

Ni-ox2 : Nickel (II) 1,1,1-trifluoro-5,5-dimethylhexane-2,4-dione 2-oxime

Ni-SB1 : Nickel (II) Salicylidene-4-heptadecafluorooctyl aniline

Ni-SB2 : Nickel (II) 4-methoxy salicylidene-4-heptadecafluorooctyl aniline

Ni-SB3 : Nickel (II) 3-Hydroxy-2-naphthylidene-4-heptadecafluorooctyl aniline

Ni-SB4 : Nickel (II) 3-methoxy salicylidene-3-trifluoromethyl aniline

Ni-SB5 : Nickel (II) 5-methoxy salicylidene-3-trifluoromethyl aniline

Ni-SB6 : Nickel (II) 3-methoxy salicylidene-3,5-bistrifluoromethyl aniline

Ni-SB7 : Nickel (II) 5-methoxy salicylidene-3,5-bistrifluoromethyl aniline

nm : Nanometer

No. : Number

Ox1 : 1,1,1-trifluoro-2,4-pentanedione 2-oxime

Ox2 : 1,1,1-trifluoro-5,5-dimethylhexane-2,4-dione 2-oxime

P_c : Critical pressure

Pd-ox1 : Palladium (II) 1,1,1-trifluoro-2,4-pentanedione 2-oxime

Pd-ox2 : Palladium (II) 1,1,1-trifluoro-5,5-dimethylhexane-2,4-dione 2-oxime

Pd-SB1 : Palladium (II) salicylidene-4-heptadecafluorooctyl aniline

Pd-SB2 : Palladium (II) 4-methoxy salicylidene-4-heptadecafluorooctyl aniline

Pd-SB3 : Palladium (II) 3-Hydroxy-2-naphthylidene-4-heptadecafluorooctyl aniline

Pd-SB4 : Palladium (II) 3-methoxy salicylidene-3-trifluoromethyl aniline

Pd-SB5 : Palladium (II) 5-methoxy salicylidene-3-trifluoromethyl aniline

Pd-SB6 : Palladium (II) 3-methoxy salicylidene-3,5-bistrifluoromethyl aniline

Pd-SB7 : Palladium (II) 5-methoxy salicylidene-3,5-bistrifluoromethyl aniline

pH : Potential hydrogen

ppm : Parts per million

psi : Pounds per square inch

q : Quadruplet

R : Alkyl or aryl functional group

s : Singlet

SB1 : Salicylidene-4-heptadecafluorooctyl aniline

SB2 : 4-methoxy salicylidene-4-heptadecafluorooctyl aniline

SB3 : 3-Hydroxy-2-naphthylidene-4-heptadecafluorooctyl aniline

SB4 : 3-methoxy salicylidene-3-trifluoromethyl aniline

SB5 : 5-methoxy salicylidene-3-trifluoromethyl aniline

SB6 : 3-methoxy salicylidene-3,5-bistrifluoromethyl aniline

SB7 : 5-methoxy salicylidene-3,5-bistrifluoromethyl aniline

$scCO_2$: Supercritical carbon dioxide

SCF : Super critical fluid

SEM : Scanning electron microscope

t : Triplet

T_c : Critical temperature

THF : Tetrahydrofuran

UV : Ultraviolet

W-ox1 : Tungsten (VI) 1,1,1-trifluoro-2,4-pentanedione 2-oxime

W-SB1 : Tungsten (VI) Salicylidene-4-heptadecafluorooctyl aniline

X,Y : Starting reactants

XRD : X-ray powder diffraction

Z : Product

ΔG : Change in free energy

1. INTRODUCTION

In today's industrialized world, there is an ever-increasing demand for energy, both more renewable and reliable sources of it. Coupled with mounting environmental concerns, there is an escaladed demand for alternative energy options and research that could develop these ideas into viable commercial energy solutions for the future. Nanocatalysis is one of the main venues of current research because it has been shown to yield significant progress toward making alternative energy sources both more efficient and more environmentally friendly. Nanocatalysis is like catalysis, in much the same way that brewing a pot of coffee from ground beans is like brewing it from unground beans. It makes use of the same principals of catalysis, but in such a way that less catalyst (beans) produces more product (coffee).

It is well known that catalytic technologies are critical to present & future energy processes. For many years, there was a debate as to which type of catalysis was better, homogeneous or heterogeneous. Homogenous catalysts were argued by some to be better because they were more efficient, with as many active sites as molecules and an even distribution throughout the reaction medium. However, since they were soluble in the same solvents as the desired reactants, they are often difficult to recover or separate from the products. This resulted in expensive and tedious processes to extract the catalyst for a pure product and for reuse of the catalyst. Heterogeneous supporters argued that heterogeneous catalysts were more effective because they were very easily separated and reused- as easy as a filter. However, because only the molecules on the surface of the catalyst are available as active sites, the catalyst to reactant ratio is significantly higher than for homogenous catalysts. In nanocatalysis, many of the best properties of both types are met. Like a homogeneous catalyst, the nanocatalyst is distributed throughout the solution and there are many sites for reaction. Like a heterogeneous catalyst, the catalyst is easily separated from the reaction medium. Thus, much hope, thought and research has been put into furthering nanocatalysis technology and with much progress.

1.1. Nanotechnology

Nanotechnology is defined as the manipulation of matter on an atomic and molecular scale. The concepts that would lay the foundation for what eventually become the field of nanotechnology were first presented by the physicist Richard Feynman in 1959, although nanomaterials have been in use since the 17th century- nanoparticles of gold give off a red color, which was used then by Europeans to stain glass for use in cathedral windows and by Chinese artisans in crafting vases.

In 1959, when Feynman presented his ideas about atoms' ability to be directly manipulated, he was only proposing possibilities, mere conjectures at the time. That possibility has now become more and more a reality. The nanotechnology field really began to emerge in the 1980s, propelled forward by K. Eric Drexler. Also in the early eighties, new instrumentation was invented that allowed the field to grow by leaps and bounds. For example, the scanning tunneling microscope was introduced that allowed individual atoms and bonds to be viewed for the first time. Among the first successes in nanotechnology was the synthesis of fullerenes in 1985, even though they were not originally recognized as being in the nanotechnology field.

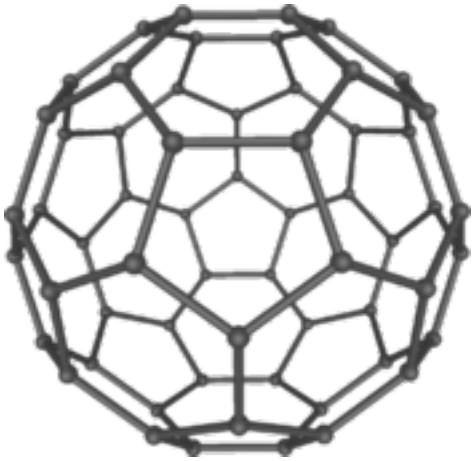

Figure 1.1. An example of a fullerene (Buckminsterfullerene C_{60}) (Ströck, 2006)

In the early 2000s, the field gained momentum and was not only a matter of conversation in the scientific realm, but was also being discussed in political and

commercial circles, because by this time, some nanotechnology was being commercialized. Nanoparticles were already being mass-produced and sold to the public at large as antibacterial agents, in transparent sunblock, and stain-resistant clothes. Since that time, the field of nanotechnology has experienced exponential growth, attention, and application.

A nanomaterial is defined as a particle that has at least one dimension between 1-100nm in size. A nanometer is one billionth of a meter, which makes the largest nanoparticle only twice the size of the smallest known cellular life form, a bacterium. A strand of human hair averages about 100,000 nanometers in width. Nanoparticles are defined as having one side less than 100nm because above that approximate length, the unique properties (discussed below) that make nanotechnology possible begin to wane (Allhoff et al, 2010)

Because nanomaterials have a massively increased relative surface area and different quantum effects from macromaterials, they can be effective catalysts (Zheng et al, 2005). As mentioned above, a nanoparticle is defined as a particle having at least one dimension smaller than 100nm. Among nanoparticles, usefulness in catalysis is dependent upon the extent of the nanoparticle's minuteness. A particle that is 30nm has 5% of its atoms on the surface, while a particle of 3nm has 50% (Chaturvedi et al, 2010). Since only surface atoms are able to act as catalysts, the smaller the particle, the more efficiently it can be used.

In recent years, nanocatalysis has been gaining interest because it has been seen to have potential in producing energy-efficient methods that are achieved within increasingly stringent environmental regulations. These low-cost catalysts are possible because of the reduction or replacement of precious metals through the effective use of the unique properties of nanocatalysts.

Many of these unique properties come from the high ratio of surface atoms, which are more active compared to bulk atoms because they usually have fewer adjacent coordinate atoms, unsaturated sites or more dangling bonds. This means there is a large amount of energy associated with the surface (Zhang et al, 2006).

Metal nanoparticles can be synthesized via two different approaches. In a "bottom-up" approach they are built up chemically from molecules. In the "top-down" approach, nanomaterials are built from larger units.

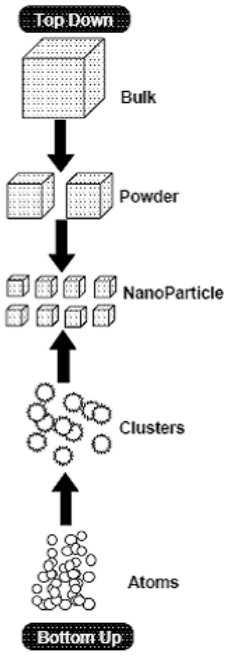

Figure 1.2. Schematic of the different approaches to building nanoparticles (Suneel, 2013)

In chemistry, metal nanoparticles are most commonly synthesized via a "bottom-up" approach, in which metal ions are attached to ligands, creating a precursor. Then, the precursor with the desired metal center is deposited on a solid substrate and reduced to its metallic form. This "bottom-up" approach is preferred because it is able to generate equivalent results to the other "top-down" approach, but more economically (Chaturvedi et al, 2010). There are, of course, limitations to this method, the most notable being the complexity of the assembly, which involves preparing a precursor, depositing it on a substrate while maintaining stability of the substrate and reducing to the desired metals.

Nanomaterials are used in an extremely large and varied range of fields and applications, so much so that they are categorized into different subfields. Some of these include: interface and colloid sciences, which produce materials such as nanotubes and nanorods; bulk applications, which are responsible for most of the

commercial applications of nanotechnology; nanomedicine, which includes drug delivery and anticancer applications; nanopillars, which can be used in solar cells; and semiconductor nanoparticles, which can increase fluorescence efficiency or increase the internal magnetic field strength in doped semiconductors.

Despite the complexity, the potential for application of nanoparticles synthesized via the "bottom-up" approach makes this a widely studied field that is already being applied in various ways (Daoushb et al, 2009; Park et al, 1998; Rather et al, 2007). The promise of the outcome outweighs the complexity associated with the process.

1.2. Catalysis

A catalyst is a substance that enters a chemical reaction without being consumed and which enables a chemical reaction to happen at a quicker rate or under less harsh conditions than would otherwise occur. A catalyst alters the transition state of a chemical reaction so that it requires less free energy to proceed; however the difference in free energy from the initial state to the final state does not change. The catalyst works by stabilizing the transition state. The kinetic barrier is decreased because the difference in the energy of the reactant and the transition state is smaller with the catalytic stabilization. The exact mechanism of catalysis is complex and there are many types of catalysts, such as acid catalysts, base catalysts, as well as catalysts that interact with the environment of the reaction. The general concept of catalysis is that it provides a different reaction pathway through which the reaction can proceed. This alternative pathway has a lower activation energy, which in turn increases the rate of the reaction.

A classic example of a catalyzed reaction is the dissociation of hydrogen peroxide to water and oxygen in the presence of manganese dioxide.

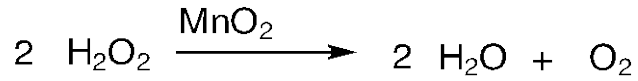

Figure 1.3. Dissociation of hydrogen peroxide to water and oxygen

Although the end products of this reaction (water and oxygen) are more stable than the reactant (hydrogen peroxide), the reaction proceeds slowly. This slow reaction rate is the reason that hydrogen peroxide is a commercially available product. However, when even just a small amount of manganese dioxide is added to the peroxide, the reaction toward water and oxygen proceeds very quickly. The manganese dioxide is not used up in the reaction and can be used indefinitely to continue enabling this reaction to proceed quickly. In other words, manganese dioxide catalyzes this reaction.

The way that catalysis generally works is that the catalyst forms an intermediate with the reactant. The intermediate proceeds to the final product, which then releases the catalyst back in its original form. Since a catalyst is not consumed in a reaction and is released back in its original form as soon as it catalyzes the formation of the product, it is immediately available to catalyze another reaction. Therefore, small amounts of catalyst are needed to effectively increase the rate of a reaction.

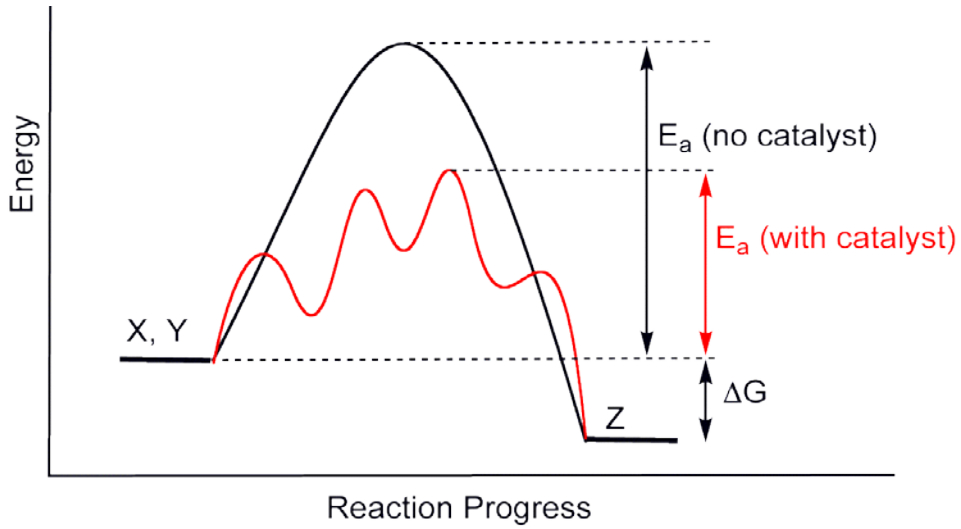

Figure 1.4. Diagram of potential energy for a theoretical reaction with and without a catalyst (Smokefoot, 2008)

As can be seen in the above diagram, a catalyst enables a pathway with a lower activation energy through which the reaction can proceed. This lower threshold allows a reaction to proceed more quickly because there are a greater number of collisions between molecules with enough energy to reach the lowered transition state. The addition of a catalyst may, as described previously, speed up a chemical reaction, but it may also increase the selectivity of the reaction (as in the case of enzymes) or allow reactions to proceed under less harsh conditions, such as lower temperatures or pressures.

Another interesting characteristic about catalysts is they cannot change the extent of the reaction. In other words, the chemical equilibrium is unaffected by the presence or absence of a catalyst. As in the previously mentioned example of hydrogen peroxide, the presence of the catalyst may seem to shift the reaction toward the product side, but it truly only increases the reaction rate. If peroxide were left until the system was at chemical equilibrium (which would take a very long time), the end ratio of reactant to product would be the same in the catalyzed and not catalyzed reactions. Catalysts cannot have an effect on the extent of the reaction because the rate of both the forward and the backward reactions are increased. The same transition state that increases the forward reaction also increases the reverse reaction.

Catalysts also affect the kinetics of chemical reactions. The rate of a reaction will depend on the rate-determining step, the slowest step in the overall mechanism of a chemical reaction. Typically, a catalyst speeds up a reaction by participating in this step. Thereby the amount (or concentration) of catalyst will have a large impact on the overall rate of the reaction.

A catalyst, by definition, is not consumed in a reaction. This does not mean, however, that the catalyst can be used effectively for an infinite number of catalytic cycles. Catalysts can be rendered ineffective by inhibition, deactivation or used up in side reactions. This can happen after only a few catalytic cycles or after many. As a result of this, the number of times a catalyst can be used effectively is an important measure in the overall usefulness of a catalyst.

The uses of catalysts are both varied and extremely widespread; they are used in the production of most industrially important chemicals. Catalysis is important in many fields of science, including: applied science, biochemistry, biology, environmental science, green chemistry, organometallic chemistry and materials science. It has been estimated that around 90% of all commercially produced chemicals include the use of catalysts in the production. (R&D magazine, 2005)

Many types of chemicals can be used as catalysts. Acids that can donate a proton are the most common type, but some solids like zeolites, alumia, graphitic carbon, nanoparticles and high-order oxides can also be used as catalysts. Transition metals also act as catalysts, especially in redox reactions. Organic chemistry makes wide use of heavier transition metals like palladium, platinum, gold and rhodium.

There are two main categories of catalysts: heterogeneous and homogeneous. A catalyst that exists in the same phase as the substrate is defined as homogeneous while one that is not in the same phase is considered heterogeneous. A third type of catalyst, biocatalysts, does not fit neatly in either of the primary groups and is therefore often considered a third type. The rate-limiting step for heterogeneous catalysis is the diffusion of the chemicals to the surface (this is also true for nanocatalysis). In homogeneous catalysis, the analogous rate-determining factor is related to substrate binding and the dissociation of the product.

1.2.1. Heterogeneous catalysis

Heterogeneous catalysts exist in a different phase than the substrates. Commonly, they are solids, and the reaction media are liquid or gaseous. In these reactions there are many limiting factors that constrain the effectiveness of the catalyst. Since the substrate needs to adsorb onto the catalyst and only molecules on the surface of the catalyst are accessible to the substrate, the total surface area has a large effect on the overall reaction rate. The smaller a particle's size, the higher ratio of surface area it will have and the more available sites for catalytic activity.

A heterogeneous catalyst is generally attached onto a second material called a support. A catalyst is spread over the support in order to maximize the surface area.

This is done to either enhance the effectiveness of the catalyst or decrease the cost associated with it. A good support will be a porous material because porous materials have more relative surface area. A few common supports are alumina and activated carbon.

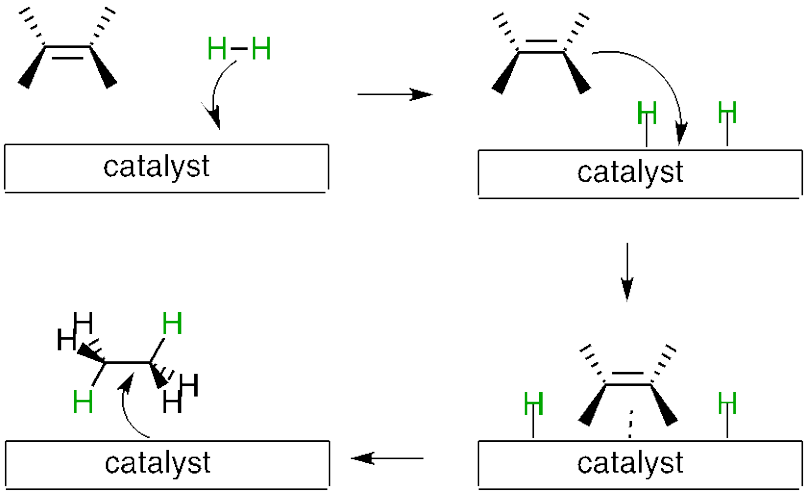

Figure 1.5. Schematic of a heterogeneous catalyst mechanism

1.2.2. Homogeneous Catalysis

Homogeneous catalysts exist in the same phase as the substrates and are generally dissolved in the same solution with the reactants. The general mechanistic principles are the same as in heterogeneous catalysis. Homogeneous catalysis is used extensively in organometallic catalysis. It can be considered more advantageous than heterogeneous catalysis because it is more selective and every molecule is available for catalytic activity allowing homogeneous catalysts to be effective at low concentrations. The main drawback is that is difficult to remove from the solution when the reaction is complete. This means that arduous separation techniques must sometimes be used to recover the catalyst and procure the pure, desired product.

1.2.3. Nanocatalysis

A subfield of catalysis that has gained increasing interest is nanocatalysis. This field has been increasingly researched and applied because it is able to capitalize on the strengths of both hetero- and homogeneous catalysis and minimize their disadvantages. Solid substrate supported nanocatalysts are classified as heterogeneous catalysts and like their group; they can be easily removed from a solution after the reaction. However, because of their very small mass, they possess characteristics special to nanomaterials. They have very high surface area to mass ratios, which allows for many active sites. This mean that less catalyst is needed and they can be used efficiently, like homogeneous catalysts. They are also chemically and thermally stable. The main disadvantage of solid supported nanocatalysts is that they can be difficult to synthesize.

1.3. Schiff Bases

A Schiff base, also called an azomethine, is a compound containing a C=N-R functional group, where the R represents an alkyl or aryl group. They are named after Hugo Schiff, who discovered them and other imines. Schiff bases are often used as ligands in metallo-organic chemistry because the nitrogen is basic and its orbitals act as π acceptors. Shiff bases with alkyl substituents tend to be relatively unstable, while ones formed with aryl substituents tend to be significantly more stable and easily synthesized (Nejo, 2009). Because the aim of this study is to provide precursors that can be simply synthesized and effectively used, the Schiff bases synthesized all have aryl substituents.

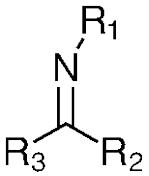

Figure 1.6. General structure of a Schiff base (R_2 and R_3 may be hydrogens)

A Schiff Base is most often formed by the condensation of a ketone or aldehyde with an amine; in this study, aldehydes were used. The mechanism follows a modified nucleophilic addition path. The amine acts as the nucleophile and in the first step forms an unstable carbinolamine, the compound then undergoes a dehydration step and loses a water molecule. This step can be catalyzed by an acid.

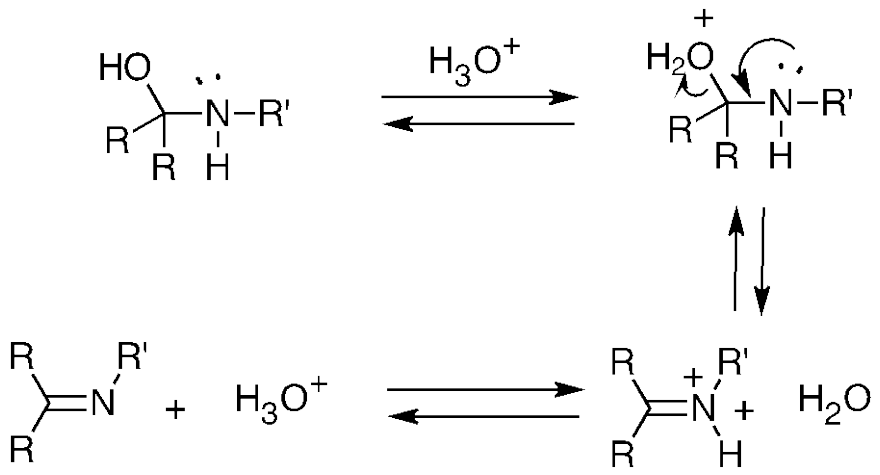

Figure 1.7. General mechanism of Schiff base formation

Schiff bases are used as catalysts in wide variety of reactions. They are used as catalysts in oxygenation, hydrolysis, electro-reduction and decomposition reactions (Kumar et al, 2009). They are also active in the oxygenation of alkenes and phenols (Nishinaga et al, 1988; Xi et al, 1986). Some of their metal complex derivatives have been shown to catalyze a reaction 10-50 times faster than simpler ligands on the same metal (Chakraborty et al, 1994). Some forms have been shown to catalyze the electro-reduction of oxygen (Zhao et al, 1988). There are also reports of Schiff bases being used in antimicrobial, antiviral and antifungal activities (Grumus et al, 1994; Meng et al, 2002; Dash et al, 1984). They have found use as plant growth regulators (Huneck et al, 1985), anti-tumor (Gaowen et al, 1995) and anti-cancer (Phatak et al, 2000) agents, and in dyes (Mennicke et al, 1986), Kaul, 1986).

A Schiff base ligand is a chelating agent because the free electron pair on the nitrogen can form a bond with a metal center. The hybrid orbitals for a generic aryl

Schiff base are shown below. The nitrogen has a sp^2 hybrid orbital that acts as a π acceptor. Schiff bases often contain a hydroxide group (an example is pictured below). The Schiff bases in this study all contained this hydroxide group, which allow the ligands to chelate from two sites, the nitrogen and the oxygen.

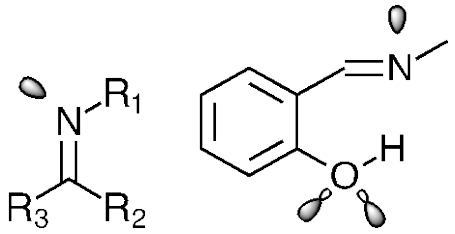

Figure 1.8. Example hybrid orbitals of Schiff base ligands

1.3.1. General spectroscopic trends for Schiff bases

The characteristic peaks that are expected to be seen in an infrared spectrum of Schiff bases arise from the stretching and vibration of the C=N, C-O, and O-H bonds. In a metal-coordinated Schiff base complex, the typical peaks arising from the O-H bond would not be expected to appear, as the metal center bonds in place of the hydrogen.

These three peaks generally are seen at around 3500-3200cm^{-1}, 1700-1600cm^{-1} and 1400-1300cm^{-1} for the O-H, C=N and C-O bonds, respectively.

The ^{1}H NMR reveals characteristic peaks from aryl and/or alkyl hydrogens, the α hydrogen (the hydrogen bonded to the carbon next to the nitrogen), and a hydroxyl hydrogen. Peaks for the hydroxyl hydrogen appear further up field in a Schiff base than is generally seen (El-Ansary et al, 2012) appearing around 16-10ppm. The α hydrogen appears around 8-10ppm. Aryl hydrogens appear between 6-8ppm and akyl hydrogens appear between 1-3ppm.

1.4. Oximes

An oxime is a compound containing a C=N-OH functional group. Its name comes from the combination of oxy and imine. The figure below shows the general structure of an oxime, one R group may be hydrogen, but at least one must be an organic side chain.

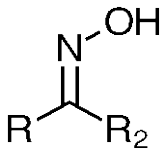

Figure 1.9. General structure of an oxime

Oximes are used in many different fields, including analytic chemistry, inorganic chemistry, industrial chemistry, agriculture, pharmaceutics, and biochemistry. Oximes can be used such a variety of areas because they possess some unique characteristics, including the abilities to chelate, carry oxygen, and spontaneously decompose. They also exhibit unusual effects in biological and photochemical reactions. Because oximes are so versatile and have unique tendencies, they are a well known compound and are found in many areas of research and developing technology, including use in the recovery of precious metals (Dempoulos, 1986), the softening of leather and fabrics (Marwan, 1970), bug extermination chemicals, some antibiotic medicines (Wermuth, Schwart, 1977), perfumes, and UV stabilization (Mathis et al, 1972). Because of some of the biological implications of some of their unique properties, their metal-coordinated compounds have seen a large increase in the realm of cancer and anti-tumor research (Soga et al, 2001).

Oximes are generally colorless. They also tend to decompose at room temperature due to their thermal instability. They are generally insoluble in water and soluble in organic solvents. Oximes are amphoteric, showing basic characteristics from the nitrogen atom and acidic characteristics from the hydroxyl group (Panzio et al, 1930). Because of their acidic characteristics, they can be

dissolved in sodium hydroxide. The addition of CO_2 produces their precipitation from solution. Because of their basic characteristics, they can be dissolved in concentrated acid solutions. Adding water to the solution will cause the precipitation of the oxime.

The most commonly used method for producing an oxime is reacting an aldehyde or ketone with hydroxylamine in a base-catalyzed medium. The reaction takes place under boiling temperatures and at an optimal pH (Abeywickrama et al, 2004). This is the method that was followed for the syntheses reported in this paper.

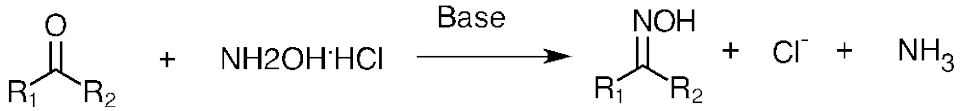

Figure 1.10. The base catalyzed synthesis of an oxime from a ketone (or aldehyde) and hydroxylamine

Oximes are often used as chelating ligands in metallo-organic compounds. The nitrogen atom has a free electron pair, giving it an sp^2 orbital which is free to create bonds. The oxygen, with two pairs of free electrons, uses its sp^3 hybrid orbital to bond. The oxime, using these free electron pairs, can create a variety of covalent bonds.

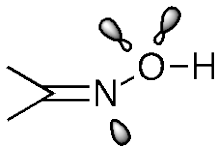

Figure 1.11. The hybrid orbitals of an oxime ligand

Especially with transition metals, oximes are able to bond in a number of different ways. However, they almost always bond to the nitrogen atom. Below are examples of the different ways they can bond.

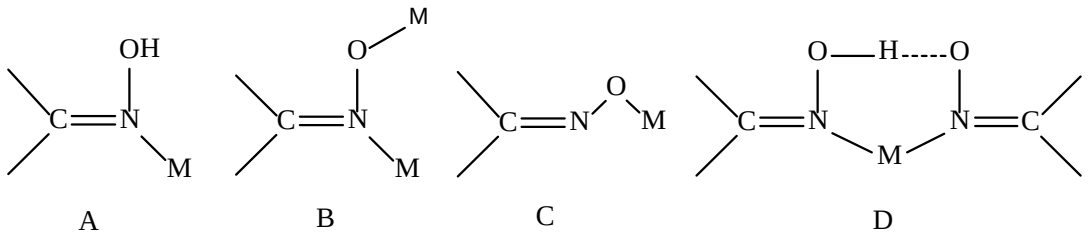

Figure 1.12. Various ways oximes can coordinate to metals

1.4.1. General spectroscopic trends for oximes

The peaks that are expected to be seen in an infrared spectrum of an oxime arise from the stretching and vibration of the C=N, C-O, and O-H bonds. In a metal-coordinated oxime compound, the peaks arising from the O-H bond would not be expected to be broad as observed in the free ligand, but a sharper peak arising due to hydrogen bonding.

These three peaks generally are seen at around 3500-3200cm^{-1}, 1700-1600cm^{-1} and 1400-1300cm^{-1} for the O-H, C=N and C-O bonds, respectively.

The ^{1}H NMR reveals characteristic peaks from aryl and/or alkyl hydrogens, and a hydroxyl hydrogen. Peaks for the hydroxyl hydrogen appear between 11-10ppm (Irez et al, 1983). Aryl hydrogens appear between 6-8ppm and akyl hydrogens appear between 1-3ppm.

1.5. Deposition medium (Supercritical fluids)

There are many ways to deposit nanoparticle metals on supports, but each is limited in its scope and has unique challenges in its synthesis. The use of supercritical fluids (SCFs) is a viable alterative to other deposition methods and has been shown to be a promising way to deposit metal nanoparticles on various substrates (Bozbag et al, 2011). This deposition process involves dissolving a metallic precursor in an SCF and then exposing it to a substrate. After this, the metallic precursor can be converted to its metal form via a variety of methods. One common method is chemical reduction with reducing agents such as H_2 and an alcohol while the precursor is still dissolved in the SCF.

An SCF is a useful medium for deposition procedures, because when its temperature and pressure are above its critical point, separate liquid and gas phases do not exist, giving rise to unique properties. Like a gas, it can effuse through solids and expand to fill its container; at the same time, it is able to dissolve materials and has density properties similar to a liquid.

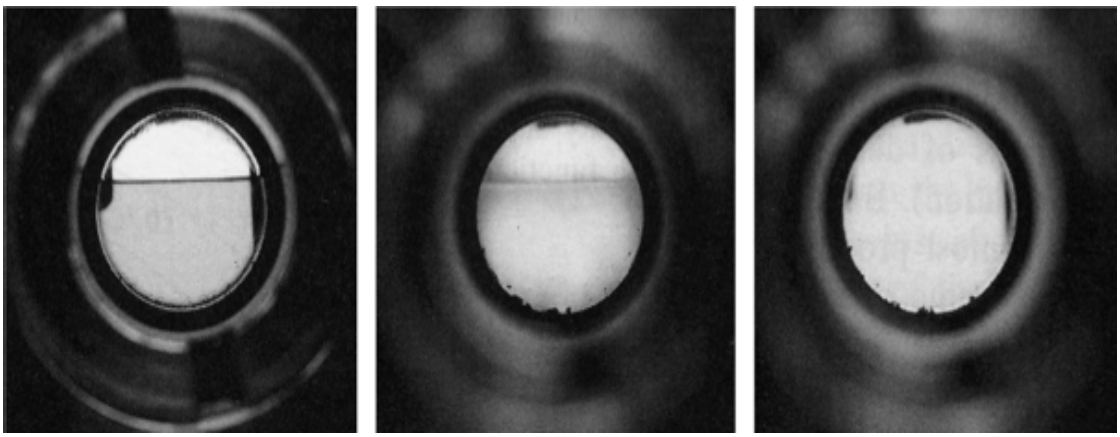

Figure 1.13. Separate liquid and gas phases of CO_2 merging into one supercritical phase (Anastas, 2010)

SCFs are advantageous due to these and other unique properties, including:

- Slight pressure and temperature changes allow for easy, specific control of density and viscosity
- High diffusivities and low viscosities result in enhanced mass-transfer characteristics
- Low surface tension permits better penetration of a substrate

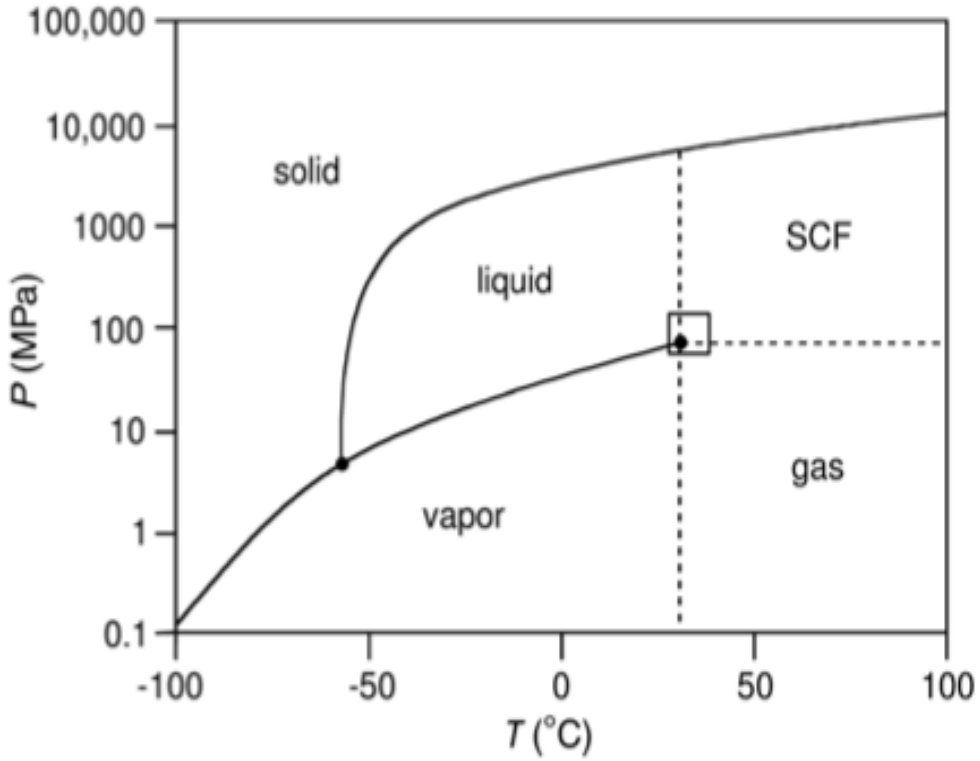

Figure 1.14. Temperature-pressure phase diagram (Anastas, 2010)

Using SCFs to deposit metal nanoparticles on the surface of porous solid supports has been shown to be a promising technique (Morley et al, 2002; Ye et al, 2003; Lin et al, 2005). Among the various commonly employed SCFs, the supercritical state of CO_2 is easily attainable with a T_c of 31 °C and a P_c of 7.38 MPa. It is also particularly appealing for such use because it is abundant, cheap and environmentally benign. CO_2 has a reputation as a molecule that depletes the ozone layer in Earth's atmosphere, but is considered a green solvent, because it can be taken from the atmosphere and after it is used, it simply is released back. There is no net gain or change to the amount in the environment. Using CO_2 as a solvent also allows for the many chemical processes to be completed without the use of harmful organic solvents.

Table 1.1. Critical properties of various solvents (Reid et al., 1987)

Solvent	**Critical temperature**	**Critical pressure**
	K	MPa
Carbon dioxide (CO_2)	304.1	7.38
Water (H_2O) (acc. IAPWS)	647.096	22.064
Methane (CH_4)	190.4	4.60
Ethane (C_2H_6)	305.3	4.87

1.6. Multi-walled Carbon Nanotubes as Supports

There are many types of supports on which the nanoparticle metals can be deposited including silica, alumina, and carbon nanotubes. Carbon nanotubes (CNTs) have been used since the 17th century (although much like the nano gold particles previously mentioned, they were not recognized as such until recently). They were discovered in Damascus steel, which was known for their incredible strength (Reibold et al, 2006). CNTs are tube-shaped structures made entirely of carbon. They are remarkable because they exhibit some unique thermal conductivity, mechanical and electrical properties. These properties make CNTs useful in a wide variety of fields, such as nanotechnology, electronics and optics.

CNTs are made of graphene sheets rolled up lengthwise into straw-like shapes. They are hollow and can be very long in proportion to their width. There are two categories of nanotubes, single-walled and multi-walled.

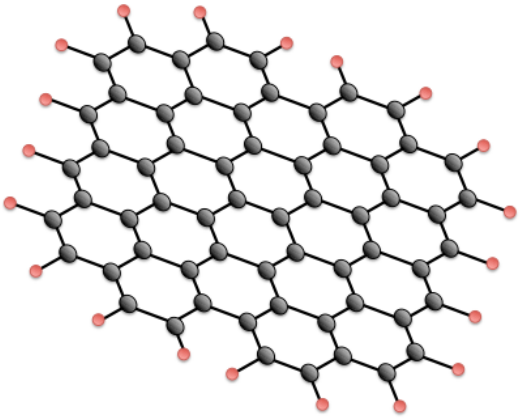

Figure 1.15. Diagram of graphene

Orbital hybridization is the reason for the strength of the nanotubes. All the bonds in the CNTs are sp^2 bonds. These bonds are stronger than sp^3 bonds (which are found in diamonds).

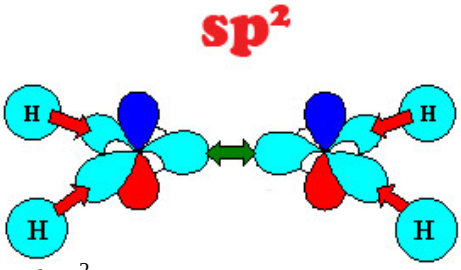

Figure 1.16. Diagram of sp^2 hybrid orbitals (Alexandrova, 2013)

From the diagram of graphene presented above, it can be seen that each carbon is bonded to 3 other carbons, as would be expected for sp^2 hybridized orbitals. The strength and flexibility that these bonds give the carbon nanotubes gives them the potential to be applied in many different ways, including their use as substrates for nanoparticle deposition. A lot of attention has been given to CNTs due to their potential applications in a wide variety of other fields (Zhang et al, 2006).

In addition to their strength, multi-walled carbon nanotubes are highly porous and stable. They were chosen for this study primarily due to their immense surface area and porous nature.

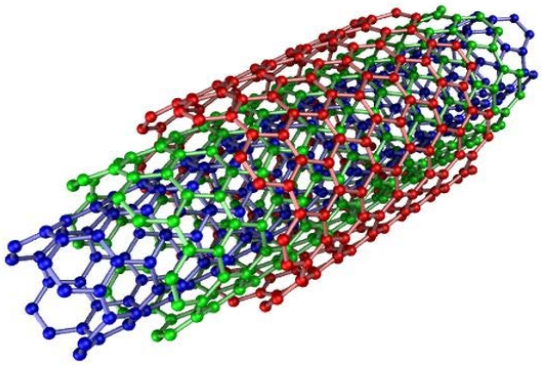

Figure 1.17. Sketch of a multi-walled carbon nanotube (Wieser, 2010)

1.7. Deposition of metals onto substrates

In this context, deposition refers to the positioning of metal on a solid surface. This can be accomplished via either a chemical process or a mechanical one. In metal deposition, transition metals like palladium, platinum, gold, silver, ruthenium, and copper are most commonly used because transition metals have an important place in catalytic chemistry. There are many different methods used for deposition. These can be categorized into three different types:

- Electrochemical deposition methods
- Chemical deposition via reduction methods
- Mechanical methods

This paper will focus on the chemical deposition method. This method uses H_2 gas to remove the ligands from the metal center after the metal has bonded to the solid substrate.

X-ray powder diffraction (XRD), an analytical technique that can characterize information about the crystal structure and unit cell dimensions, is a useful tool in the study of solid inorganic and crystalline materials made up of heavy elements and will be used in this study to characterize the metal composites. It is generally preferred for analysis of crystalline materials which is unknown by comparing that data of the sample with those of known materials.

The atomic structure of the crystal is determined by the intensity of the x-ray reflected through a sample. A crystal is made up of its unit cells structured in an organized and predictable way. A unit cell is the smallest repeating structural pattern in the lattice of a crystal. The frequency of the unit cell can be determined from the angle of the reflected x-ray.

1.8. Scope of this research

Carbon-supported nanoparticle metals are used widely as catalysts for a variety of reactions (Zhang et al, 2006). The metals used in this study are palladium, nickel and tungsten. Palladium catalysts deposited on multi-walled carbon nanotubes (MWCNTs) are often used in hydrogenation and oxidation reactions (Cerveny, 1989). Nickel is used as a catalyst in a wide variety of organic reactions. Among these, some of the more notable are the reversible hydration of CO_2 in the atmosphere to carbonic acid for CO_2's storage in mineral form (Bhaduri et al, 2013) and its use in the reduction of C=C double bonds in olefins (Alonso et al, 2009). Tungsten, although not most commonly used as a catalyst, has been shown to be useful in some catalytic procedures. Most notably, it has been used in olefin metathesis, an important step in the processing of petroleum (Schrock et al, 2003). Tungsten oxide has also been used in the selective catalytic reduction for coal-fired power plants (Spivey, 2002). Nanoparticles of tungsten have also been used in the manufacture of conducting and semi-conducting materials (Kanan et al, 2009).

Among the steps for preparing these deposited nanoparticle metals, the characteristics of the precursor have been shown to play a major role in overall success. The precursor's properties and concentration significantly affect the size and distribution of the metal nanoparticles on the substrate (Morley et al, 2002).

Currently, there are only a few known precursors that possess the necessary characteristics to help ensure a successful deposition of nanoparticle metals in supercritical carbon dioxide ($scCO_2$) (most notably, acetylacetone and cyclooctadiene; however, hexamethyl triethylene, hexamethylene glycol dimethyl ether and tetramethyl heptanedionate, along with some of their derivatives, have also

been reported) (Morley et al, 2002; Zhang et al, 2006). Unfortunately, for some metals, such as nickel, these precursors lead to a clustering and an uneven distribution of the nanoparticle metals (Peng et al, 2008). Tungsten is a metal that has not yet been researched in this capacity as far as the author is aware. It is hoped that by synthesizing new precursors, namely precursors with fluorous Shiff base and oxime ligands, better alternatives which allow for an adequately small size and uniform distribution of nickel, tungsten, and palladium nanoparticles on the substrate will be discovered. The use of palladium is primarily for comparison of these newly reported results to those of commonly used metals and precursors.

The scope of this research includes the synthesis of novel fluorous Schiff base and oxime ligands and their precursors, the testing of the precursors' solubility in $scCO_2$ and the deposition of their metals on MWCNTs.

To the author's knowledge, the synthesis of all reported ligands except one oxime ligand (1,1,1-trifluoro-2,4-pentanedione 2-oxime), the synthesis of all complexes and the use of all the reported complexes as precursors for deposition on MWCNTs in $scCO_2$ are reported for the first time.

2. PRELIMINARY WORK

2.1. Smart et al. (1997)

The solubility of 49 metal-containing compounds was tested in $scCO_2$. Solubilities were found to range over eight orders of magnitude. Metal complexes containing fluorine-substituted ligands were found to be the most soluble, and metal complexes containing phenyl-substituted ligands the least. Below a graph with the ln of the density of the fluid plotted versus the ln of the ligands' solubility is shown. The graph on the right has fluorine while the one on the left does not. It is clear from the order of magnitude that the solubility is significantly larger for the complex with fluorine.

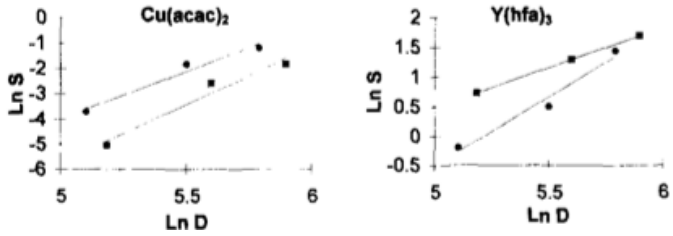

Figure 2.1. Comparison of solubility of ligands with and without fluorine in $scCO_2$

2.2. Belghoul et al. (2007)

Shiff base ligands were synthesized and reacted with metals to form polymeric films. They were prepared using multiple sequential adsorptions of metal ions and salen-based ligands. There was found to be two different growth mechanisms of the polymers, which led to the peaks seen below. One mechanism led to a homogeneous surface deposition, the other lead to a clustering resulting in the formation of 3-D aggregates. Deposition of the polymer based organo-metallic precursors on a carbon-based substrate was not in the scope of this research.

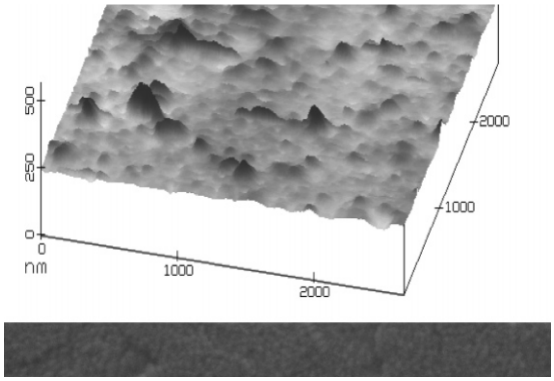

Figure 2.2. SFM picture of Cu-MBSA film

2.3. Ye et al. (2003)

A method of depositing nano-metal particles on MWCNTs was reported. Particles of rhenium, palladium, and ruthenium were successfully deposited through reduction of metal-β-diketone precursors via hydrogen in $scCO_2$. As shown below, the metal particles were uniform, small and evenly dispersed. The overall reaction was easy, environmentally friendly and quick.

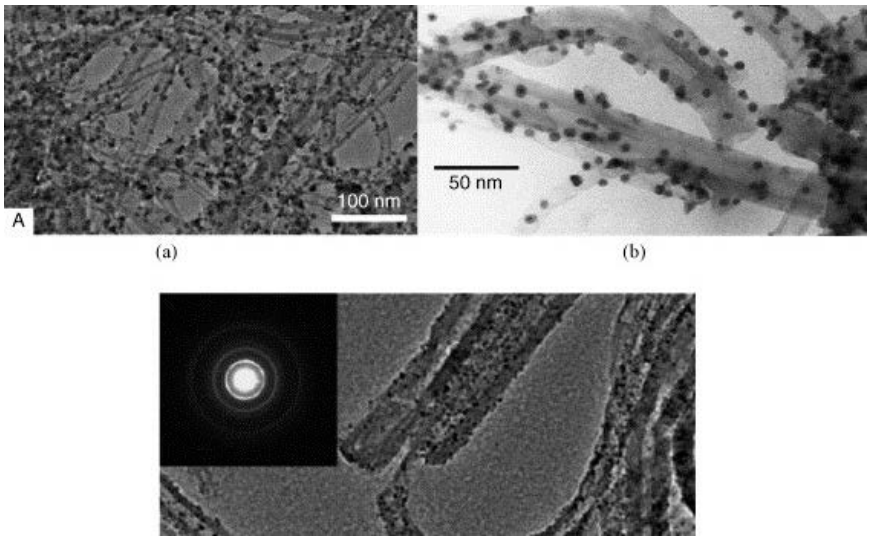

Figure 2.3. TEM of deposition of (a) Rh, (b) Pd and (c) Ru, on MWCNT in $scCO_2$

These highly dispersed nanoparticles, with a narrow range of size distribution, showed good adhesion on MWCNT surfaces.

2.4. Morley et al. (2002)

The synthesis of silver nanoparticles deposited on porous substrates, poly(styrene-divinylbenzene) beads and silica aerogels was reported.

The properties of the precursor were shown to control the size and distribution of the nanoparticles in the support material. The solubility of the precursor complexes in the supercritical solvent was also shown to be one of the key parameters in determining the size of the nanoparticles and the extent and homogeneity of their distribution within the support matrix.

The silver precursors were designed to be both CO_2 soluble and sufficiently reactive to ensure easy deposition to the metal.

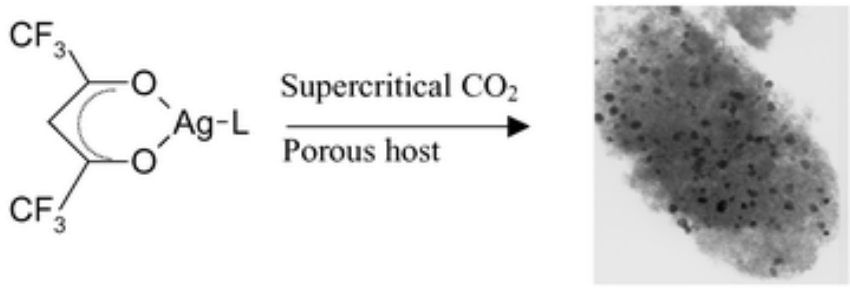

Figure 2.4. Deposition of silver nanoparticles on porous host

2.5. Lin et al. (2005)

In research similar to Le et al., platinum nanoparticles with sizes in the range of 5-10 nm depositied on CNTs was reported.

A high catalytic activity was also observed which is attributed to the large surface area of the CNTs and the smaller overpotenital for methanol oxidation and oxygen reduction reaction.

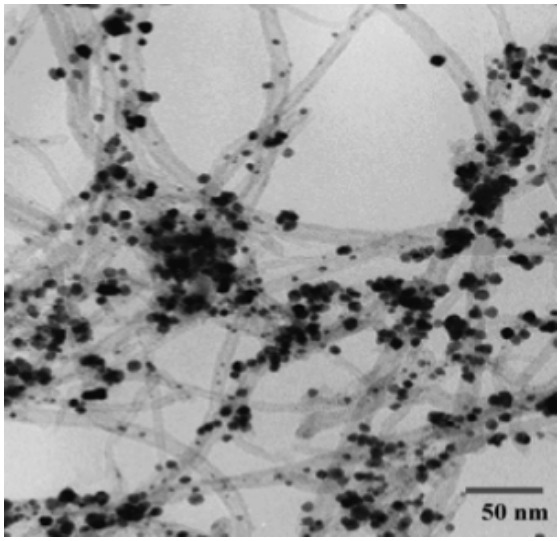

Figure 2.5. TEM of platinum nanoparticles on CNT

2.6. Peng et al. (2008)

The deposition of nickel onto CNTs was reported. As shown below, these depositions were less successful than with palladium and platinum. The nickel was deposited via the hydrogenolysis of nickelocene at low temperature (70°C) in $scCO_2$. Fairly uniformly dispersed nickel metal particles were produced, however the size of the nanoparticles was in the 50nm range.

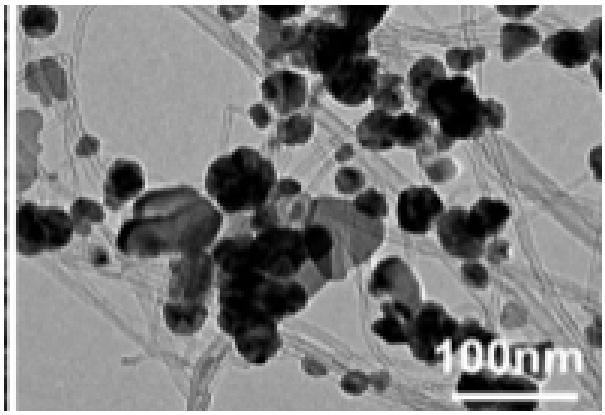

Figure 2.6. FESEM image of nickel nanoparticles on MWCNT

2.7. Erkey et al. (2012)

The deposition of nickel nanoparticles on carbon aerogels in $scCO_2$ with acetylacetone as ligands was reported. The nanoparticles were deposited in a fairly uniform distribution. This is a better result than previously seen, but the nickel particles were still about 25-50 nanometers in size.

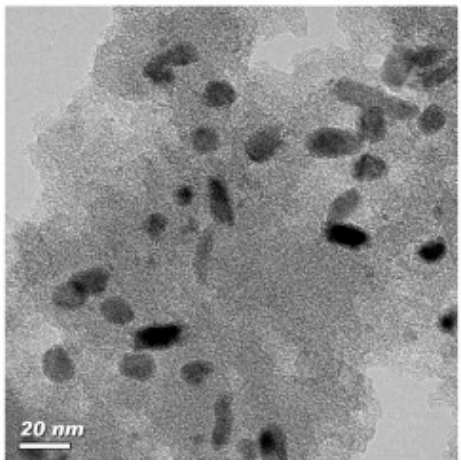

Figure 2.7. TEM image of nickel nanoparticles on carbon aerogels

2.8. Research in progress from lab at Çukurova University

There is research that is yet unpublished, but has seen good results of deposition of copper on CNTs in $scCO_2$ using dimethylglyoxime as a precursor.

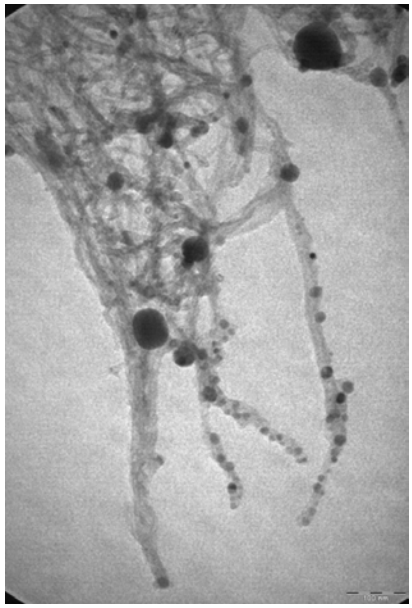

Figure 2.8. TEM of copper on MWCNT deposited using an oxime as precursor

3. Materials and Methods

3.1. Materials

3.1.1. Chemicals used

- Salicylaldehyde
- Hydrochloric acid (HCl)
- Ethanol (C_2H_5OH)
- 4-heptadecafluorooctylaniline
- Dichloromethane (CH_2Cl_2)
- n-hexane
- 4-methoxysalicyaldehyde
- Naphthaldehyde
- 3-trifluoromethylaniline
- 2-hydroxy-3-methoxybenzeldehyde
- 2-hydroxy-5-methoxybenzeldehyde
- 3,5-bistrifluoromethylaniline
- 1,1,1-trifluoro-2,4-pentanedione
- Hydroxylamine hydrochloride
- Distilled water
- Ethyl acetate
- Silica gel (SiO_2)
- 1,1,1-trifluoro-5,5-dimethyl-2,4-dione
- Acetic acid
- Nickel (II) acetate
- Methanol (CH_3OH)
- Palladium (II) chloride ($PdCl_2$)
- Nitrogen gas (N_2)
- Sodium tungstate dihydrate ($Na_2WO_4 \cdot H_2O$)

- Hydrogen peroxide (H_2O_2)
- Triethylamine
- Sodium acetate
- Carbon dioxide (CO_2)
- Multi-walled carbon nanotubes (MWCNTs)
- Hydrogen (H_2)
- Tetrahydrofuran (THF)
- Styrene

3.1.2. Instruments used

- Fourier transmission infrared spectroscopy (FT-IR)
- Elemental Analysis
- Proton nuclear magnetic resonance (^{1}H NMR)
- Carbon nuclear magnetic resonance (^{13}C NMR)
- Fluorine nuclear magnetic resonance (^{19}F NMR)
- Scanning electron microscope (SEM)
- X-ray powder diffraction (XRD)
- Magnetic stirrer and heater
- Drying oven
- High pressure reactor
- High pressure reactor with viewing window
- High pressure pump
- Schlenk line
- Silica column
- Electronic scale
- Vacuum desiccator
- Centrifuge machine
- X-ray crystallography

3.2. Methods

All chemicals were purchased from Sigma Aldrich and used as obtained without further purification. For the carbon support, multi-walled carbon nanotubes (MWCNTs) (average dimensions: O.D. xL (6-9nm x 5 μm), diameter (mode, 5.5nm; median 6.6nm)) were used. FT-IR, ^{1}H NMR, and Elemental Analysis were used to characterize the ligands. Select ligands were also characterized by ^{13}C NMR, ^{19}F NMR and x-ray crystallography. The compounds were characterized by FT-IR, ^{1}H NMR, elemental analysis and some by ^{19}F NMR. The M/MWCNT composites were characterized by XDR and SEM EDX.

FT-IR spectra were recorded on a Thermo FT-IR spectrophotometer, Smart ITR diamond attenuated total reflection (ATR). ^{1}H and ^{19}F NMR spectra were recorded on a Bruker AVANCE 500 (in CHCL3 and DMSO). Elemental analyses (C, H, N) were recorded on a Thermo Scientific Flash 2000, CHNS elemental analyses apparatus. Magnetic susceptibilities were determined on a Sherwood Scientific Magnetic Susceptibility Balance (Model MK1) at room temperature using $CuSO_4 \cdot 5H_2O$ as a calibrate; diamagnetic corrections were calculated from Pascal's constants. XRD spectra were recorded on Rigaku Miniflex CuKα, λ=0.154nm. Scanning Electron Microscopy (SEM) images were recorded on a Zeiss Supra 55. The resolution of the microscope is a working distance of 10nm at an acceleration voltage of 10kV. The M/MWCNTs composites were mounted on platinum pins with double-sided carbon tape and their corresponding SEM images were recorded. Elemental analysis was obtained from EDAX Genesis EDS system. Electronic spectra were obtained on a Perkin Elmer Lambda 25 UV spectrometer. The separation and washing of the MWCNTs by precipitation was preformed with a Serico 80-2 centrifuge machine.

In this study nine ligands derived from fluorous Schiff bases and floruous oximes were synthesized. Using these ligands, their respective Pd(II) and Ni(II) metal complexes, as well as two tungsten complexes were synthesized. Their solubility in an $scCO_2$ medium and their use as precursors in the deposition of metal nanoparticles onto multi-walled carbon nanotubes (MWCNTs) was determined. All

ligands were characterized by FT-IR and ^{1}H NMR. The complexes were also characterized by FT-IR and ^{1}H NMR. The solubility of the metal complexes in supercritical medium was also qualitatively determined. The synthesized metal complexes were used as precursors for the deposition of their metals on MWCNTs in an $scCO_2$ medium resulting in the synthesis of nano-sized metal catalysts. The size and distribution of the synthesized nanocatalysts was analyzed by SEM and XRD.

3.2.1. Synthesis of ligands

3.2.1.1. Salicylidene-4-heptadecafluorooctyl aniline [SB1]

This ligand was prepared via a modified method that was previously reported (Gilani and Mahmood, 2003). At room temperature, 3mmol (0.37g) of salicylaldehyde and 3 drops of 5pH HCl were added to 25mL of ethanol. 3mmol (1.53g) of heptadecafluorooctylaniline in 25mL of ethanol was slowly added to the stirred salicylaldehyde solution. The solution was refluxed at ≈70°C for an hour, then it was allowed to cool slowly. The bright yellow powder was filtered off and washed with water and dried in a vacuum desiccator. It was recrystallized with 3:1 CH_2Cl_2/n-hexane.

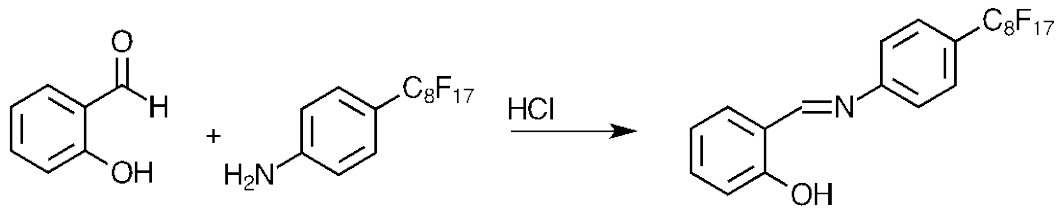

Figure 3.1. Synthesis of SB1

Yield: 71%

M.p.: 133-134°C

Color: yellow

Molecular formula: $C_{21}H_{10}F_{17}N_1O_1$

Molecular weight: 615.28g/mol

Elemental Analysis calculated: C, 40.99; H, 1.59; N, 2.28.

Elemental Analysis Found: C, 41.29; H, 1.64; N, 2.28.

IR: (cm^{-1}) C-H 3065, 3006; C=N 1621; C-0 1369; C-F 1242,1192, 1179 ^{1}HNMR: O-H (out of range) C-H (Ar) 6.9(t, 1H), 7.05(d, 1H), 7.42(m, 1H); N=CH 8.64 (s, 1H); C-H (Ar-CF) 7.65 (d, 2Hs), 7.38 (d, 2Hs);

^{19}FNMR: CF_3 -80.8; -CF_2- -110 to -123; CF_2-Ar -126

3.2.1.2. 4-methoxy salicylidene-4-heptadecafluorooctyl aniline [SB2]

2.25mmol (1.16g) of 4-heptadecafluorooctylaniline was dissolved in 4 mL of ethanol. 2.25mmol (0.35g) of 4-methoxysalicyaldehyde was mixed with 9mL of ethanol. 5 drops of pH 5 HCl was added to the aldehyde solution. The aniline solution was added slowly over the top. The solution turned bright yellow. The solution was refluxed in a water bath while stirring for 1 hour. The product was allowed to cool and then the bright yellow crystals were filtered off.

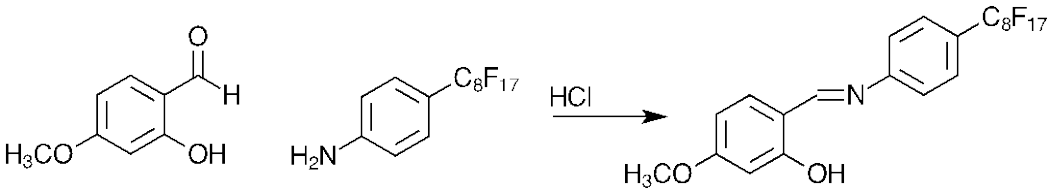

Figure 3.2. Synthesis of SB2

Yield: 93.3%

M.p.: 92-94°C

Color: yellow

Molecular formula: $C_{22}H_{12}F_{17}N_1O_2$

Molecular weight: 645.31g/mol

IR: (cm^{-1}) C-H (Ar) 3091, 3065; C-H (aliphatic) 2984-2843; C=N 1624; C-O 1369; C-F 1249, 1210, 1189

^{1}HNMR O-H 13.17 (s, 1H); C-H (Ar) 6.62(m, 1H) 6.55 (d, 1H) 4.06 (s ,1H); N=CH 8.95 (s 1H); C-H (Ar-CF) 7.77 (d, 2Hs), 7.61 (d, 2Hs); C-H(aliphatic) 3.35(s, 3Hs)

3.2.1.3. 3-Hydroxy-2-naphthylidene-4-heptadecafluorooctyl aniline [SB3]

5 mmol (1.12g) of 4-heptadecafluorooctylaniline was dissolved in 6 mL ethanol. 5 mmol (0.38g) of naphthaldehyde was dissolved separately in 15 mL of ethanol. 5 drops of pH 5 HCl was added to the aldehyde solution. The aniline solution was added slowly over the top. The solution was refluxed in a water bath while stirring for 1 hour. Product was allowed to cool and then the yellowish-orange crystals were filtered off.

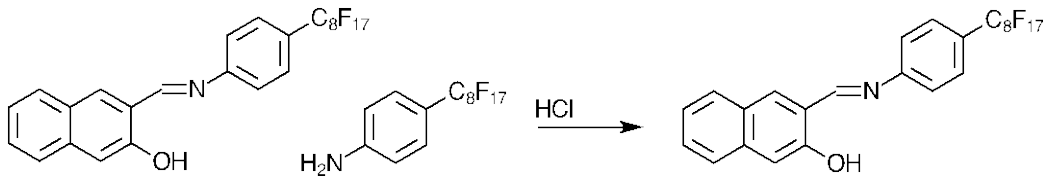

Figure 3.3. Synthesis of SB3

Yield: 79.2%

M.p.: 139-141°C

Color: yellowish-orange

Molecular formula: $C_{25}H_{12}F_{17}N_1O_1$

Molecular weight: 665.34g/mol

IR: (cm^{-1}) C-H (Ar) 3057-2920; C=N 1628; C-O 1369; C-F 1244, 1195

^{1}HNMR O-H 15.38 (s, 1H); N=CH 9.74 (d, 1H); C-H (Ar) 8.55 (d, 1H), 8.00 (d, 1H), 7.59 (t, 1H), 7.41 (t, 1H), 7.05 (d 1H), 4.06 (s, 1H); C-H (Ar-CF) 7.88-7.80 (m, 4Hs)

3.2.1.4. 3-methoxy salicylidene-3-trifluoromethyl aniline [SB4]

5 mmol (0.86g) of 3-trifluoromethylaniline was dissolved in 8 mL ethanol. 5 mmol (0.76g) of 2-hydroxy-3-methoxybenzeldehyde was dissolved separately in 8 mL of ethanol. 5 drops of pH 5 HCl were added to the aldehyde solution. The aniline solution was added slowly over the top. The solution was refluxed in a water

bath while stirring for 1.5 hours. Product was allowed to cool and then the peach colored crystals were filtered off.

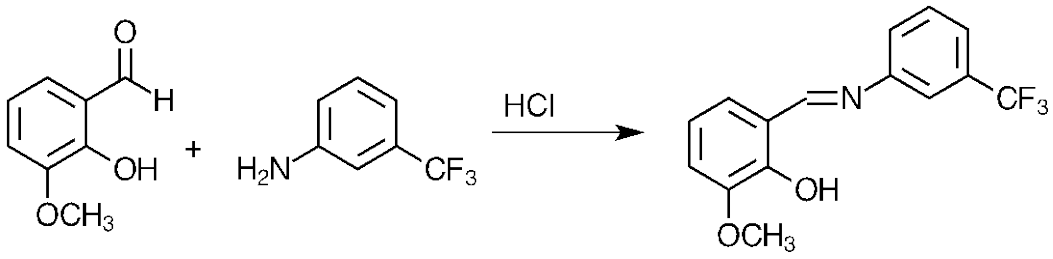

Figure 3.4. Synthesis of SB4

Yield: 92.0%

M.p.: 105-106°C

Color: peach

Molecular formula: $C_{15}H_{12}F_3N_1O_2$

Molecular weight: 295.26g/mol

IR: (cm^{-1}) C-H (Ar) 3070-2905; C-H (aliphatic) 2881-2784; C=N 1620; C-O 1325; C-F 1171, 1109, 1094

^{1}HNMR O-H 12.74 (s, 1H); N=CH 9.05 (d, 1H); C-H (Ar) 7.30 (m, 1H), 7.18 (m, 1H), 6.96 (t, 1H); C-H (Ar-CF) 7.81 (s, 1H), 7.73-7.68 (m, 3Hs), C-H (aliphatic) 3.85 (s, 3Hs)

3.2.1.5. 5-methoxy salicylidene-3-trifluoromethyl aniline [SB5]

15 mmol (2.49g) of 3-trifluoromethylaniline was dissolved in 15 mL ethanol. 15 mmol (2.30g) of 2-hydroxy-5-methoxybenzeldehyde was dissolved separately in 15 mL of ethanol. 5 drops of pH 5 HCl was added to the aldehyde solution. The aniline solution was added slowly over the top. The solution was refluxed in a water bath while stirring for 1.5 hours. Product was allowed to cool and then the yellowish-orange colored crystals were filtered off.

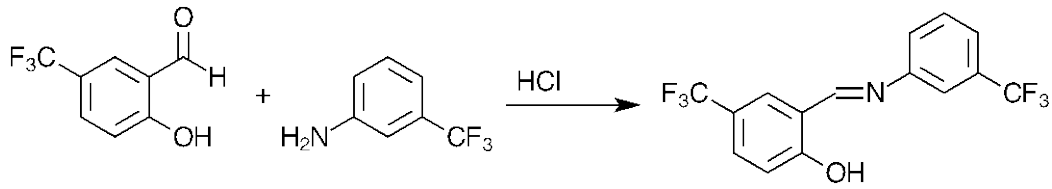

Figure 3.5. Synthesis of SB5

Yield: 100%

M.p.: 74-76°C

Color: yellowish-orange

Molecular formula: $C_{15}H_{12}F_3N_1O_2$

Molecular weight: 295.26g/mol

IR: (cm^{-1}) C-H (Ar) 3020, 2991; C-H (Aliphatic) 2962-2836; C=N 1619; C-O 1323; C-F 1167, 1152, 1137

^{1}HNMR O-H 12.00 (s, 1H); N=CH 9.01 (s, 1H); C-H (Ar) 7.31 (d, 1H), 7.09 (q, 1H), 6.95 (d, 1H); C-H (Ar-CF) 7.78 (s, 1H), 7.78-7.67 (m, 3Hs); C-H (aliphatic) 3.78 (s, 3Hs)

3.2.1.6. 3-methoxy salicylidene-3,5-bistrifluoromethyl aniline [SB6]

At room temperature, 5 mmol (1.19g) of 3,5-bistrifluoromethylaniline was dissolved in 12 mL ethanol. 5 mmol (0.78g) of 2-hydroxy-3-methoxybenzeldehyde was dissolved separately in 12 mL of ethanol. 5 drops of pH 5 HCl was added to the aldehyde solution. The aniline solution was added slowly over the top and refluxed in a water bath while stirring for 1.5 hours. The solution turned orange when mixed. Product was allowed to cool and then the peach colored crystals were filtered off.

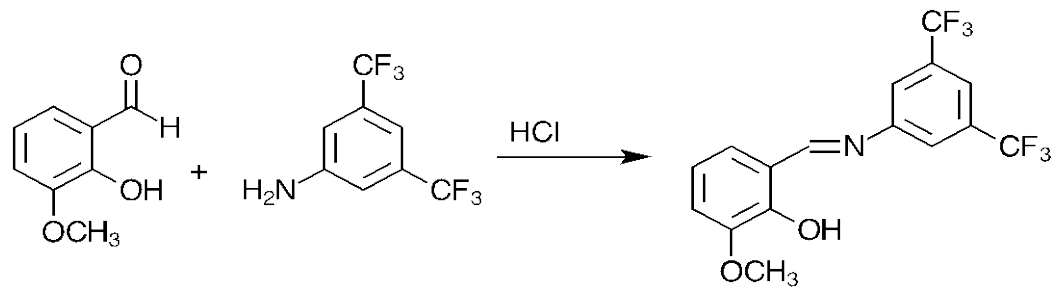

Figure 3.6. Synthesis of SB6

Yield: 66.0%

M.p.: 122-123°C

Color: peach

Molecular formula: $C_{16}H_{11}F_6N_1O_2$

Molecular weight: 363.25g/mol

IR: (cm^{-1}) C-H (Ar) 3094, 3032; C-H (aliphatic) 2970-2847; C=N 1614; C-O 1380; C-F 1172, 1108, 1092

^{1}HNMR O-H 12.29 (s, 1H); N=CH 9.11 (s, 1H); C-H (Ar) 7.34 (d, 1H), 7.32 (d, 1H), 6.97 (t, 1H); C-H (Ar-CF) 8.16 (s, 2Hs), 8.02 (s, 1H); C-H (aliphatic) 3.86 (s, 3Hs)

3.2.1.7. 5-methoxy salicylidene-3,5-bistrifluoromethyl aniline [SB7]

5 mmol (1.19g) of 3,5-bistrifluoromethylaniline was dissolved in 14 mL ethanol. 5 mmol (0.76g) of 2-hydroxy-5-methoxybenzeldehyde was dissolved separately in 14 mL of ethanol. 5 drops of pH 5 HCl was added to the aldehyde solution. The aniline solution was added slowly over the top and refluxed in a water bath while stirring for 1 hour. The solution turned bright orange when mixed. Product was allowed to cool and then the bright orange colored crystals were filtered off.

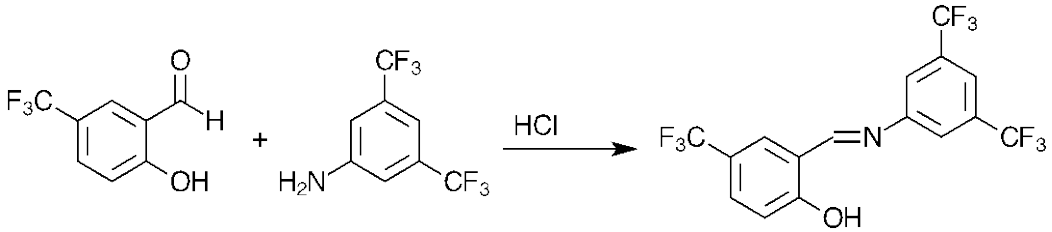

Figure 3.7. Synthesis of SB7

Yield: 54.2%

M.p.: 91-93°C

Color: orange

Molecular formula: $C_{16}H_{11}F_6N_1O_2$

Molecular weight: 363.25g/mol

IR: (cm^{-1}) C-H (Ar) 3059, 3020; C-H (aliphatic) 2964-2846; C=N 1619; C-O 1371; C-F 1158, 1121, 1109

^{1}HNMR O-H 11.65 (s, 1H); N=CH 9.06 (s, 1H); C-H (Ar) 7.32 (d, 1H), 7.12 (m, 1H), 6.96 (d, 1H); C-H (Ar-CF) 8.12 (s, 2Hs), 8.00 (s, 1H); C-H (Aliphatic) 3.78 (s, 3Hs)

3.2.1.8. 1,1,1-trifluoro-2,4-pentanedione 2-oxime [ox1]

This ligand was prepared via a modified method that was previously reported (Kim and Ryu, 1992).

25mL of 0.5N HCl was slowly added to 1.5436g (10mmol) of the trifluorodione in 24mL of ethanol. 1.422g (20mmol) $NH_2OH{\cdot}HCl$ in 5mL of water was added. The solution was stirred for 20 hours. The solvents were evaporated using a rotoevaporator. The product was extracted with 35mL of EtOAc (x2) and washed with 25mL of water (x2). The product was evaporated again and re-crystallized. A silica column (3:1 hexane/EtOAc) was used to separate the white perfluorooxime.

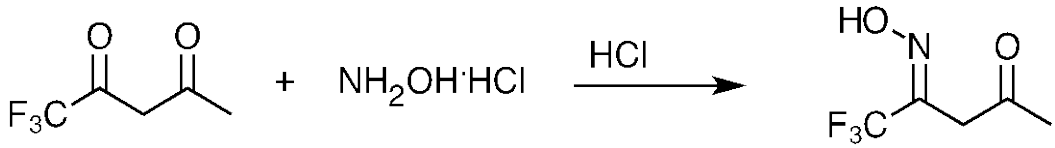

Figure 3.8. Synthesis of ox1

Yield: 22.3%

M.p.: 86-88°C (literature value 86-87°C),

Color: white

Molecular formula: $C_5H_6F_3N_1O_2$

Molecular weight: 169.10g/mol

IR: (cm^{-1}) C-H 2938, 2762; C=N 1643; N-O 1390; O-H 3132; C-F 1212, 1173, 1143

^{1}H NMR: CH_3 2.06(s, 3Hs); CH_2 3.33(d,1H), 3.07 (d,1H); O-H 4.45(b,1H)

^{13}C NMR: C=O 157, C=N 102, CH_2 77, CH_3 46, CF_3 121(q)

3.2.1.9. 1,1,1-trifluoro-5,5-dimethylhexane-2,4-dione 2-oxime [ox2]

10mmol (1.96g) of 1,1,1-trifluoro-5,5-dimethyl-2,4-dione was dissolved in 20mL of ethanol. 25mL of 0.5N HCl (10mL 37% HCl + 15mL water) was added over top. 20mmol (1.47g) of $NH_2OH{\cdot}HCl$ in 5mL of water was added slowly to the dione solution and stirred for 20 hours. The white crystals were filtered off and left in desiccator to dry.

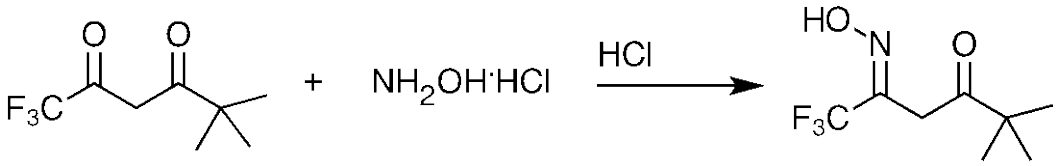

Figure 3.9. Synthesis of ox2

Yield: 60.7%

M.p.: 164-168°C

Color: white

Molecular formula: $C_8H_{12}F_3N_1O_2$

Molecular weight: 211.18g/mol

IR: (cm^{-1}) C-H 2981-2739; C=N 1624; N-O 1379; O-H 3348; C-F 1173, 1150, 1124

^{1}HNMR $C(CH_3)_3$ 1.17 (m, 9Hs); -CH2 3.43 (d, 1H), 3.15 (d, 1H); O-H 8.33 (b, 1H)

3.2.2. Synthesis of nickel complexes

3.2.2.1. Nickel (II) Salicylidene-4-heptadecafluorooctyl aniline [Ni-SB1]

0.2mmol (0.12g) of the perfluoro-Schiff base ligand was dissolved in 20mL ethanol. A few drops of acetic acid were added to the Schiff base solution. 0.1mmol (0.017g) of nickel acetate was dissolved in 15mL of ethanol and added slowly to the Schiff base. It was refluxed and stirred in a water bath for 1.5 hours. The solution was cooled and the green powder was filtered off and dried in a desiccator.

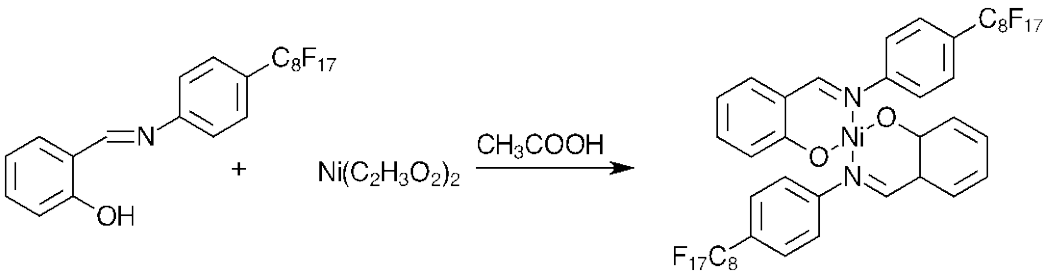

Figure 3.10. Synthesis of Ni-SB1

Yield: 51%

M.p.:155-157°C

Color: green

Molecular formula: $C_{42}H_{18}F_{34}Ni_1N_2O_2$

Molecular weight: 1287.24g/mol

IR: C-H 2987; C=N 1612; C-O 1369; C-F 1179; v(M-N) 528

^{1}HNMR: O-H (12.84 s, 1H); C-H (Ar) 6.9(t, 1H), 7.05(d, 1H), 7.42(m, 1H); N=CH 8.64 (s, 1H); C-H (Ar-CF) 7.65 (d, 2Hs), 7.38 (d, 2Hs)

3.2.2.2. Nickel (II) 4-methoxy salicylidene-4-heptadecafluorooctyl aniline [Ni-SB2]

0.75mmol (0.48g) of the perfluoro Schiff base ligand was dissolved in 3mL of ethanol. A few drops of acetic acid were added. 0.4mmol (0.07g) of nickel acetate was dissolved in 3mL of ethanol. The Ni solution was added slowly to the Schiff base solution and refluxed in a water bath for 1.5 hours. The solution was cooled and the bright green powder was filtered off and dried in a desiccator.

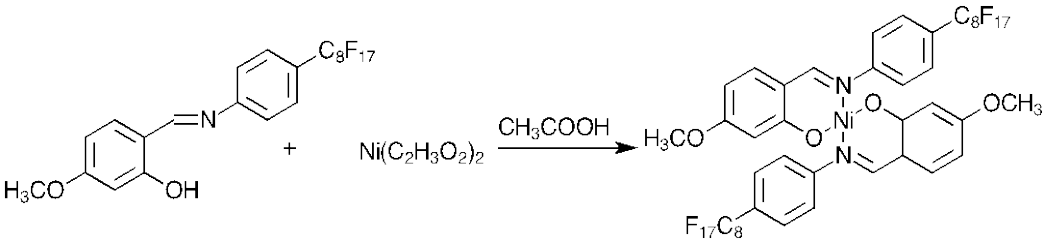

Figure 3.11. Synthesis of Ni-SB2

Yield: 90.9%

M.p.: 225-230°C

Color: green

Molecular formula: $C_{44}H_{22}F_{34}Ni_1N_2O_4$

Molecular weight: 1347.29g/mol

IR: C-H (Ar) 2987; C-H (Aliphatic) 2887; C=N 1611; C-O 1368; C-F 1213, 1196, 1180 v(M-N) 527

^{1}HNMR O-H 13.17 (s, 1H); C-H (Ar) 6.62(m, 1H) 6.55 (d, 1H) 4.06 (s ,1H); N=CH 8.95 (s, 1H); C-H (Ar-CF) 7.77 (d, 2Hs), 7.61 (d, 2Hs); C-H(aliphatic) 3.35(s, 3Hs)

3.2.2.3. Nickel (II) 3-Hydroxy-2-naphthylidene-4-heptadecafluorooctyl aniline [Ni-SB3]

0.55mmol (0.37g) of the perfluoro Schiff base ligand was dissolved in 5mL of ethanol. A few drops of acetic acid were added. 0.28mmol (0.05g) of nickel acetate was dissolved in 4mL of ethanol. The nickel solution was added slowly to the Schiff base solution and refluxed in a water bath for 1.5 hours. The solution was cooled and the greenish-yellow powder was filtered off and dried in a desiccator.

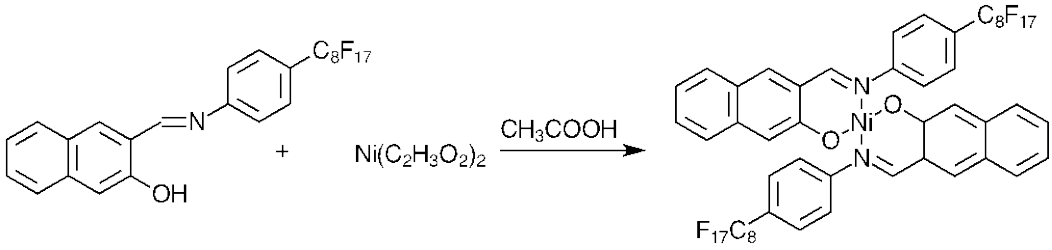

Figure 3.12. Synthesis of Ni-SB3

Yield: 78.2%

M.p.: 244-250°C

Color: greenish-yellow

Molecular formula: $C_{50}H_{22}F_{34}Ni_1N_2O_2$

Molecular weight: 1387.36g/mol

IR: C-H (Ar) 2987-2902; C=N 1615; C-O 1369; C-F 1247, 1191; v(M-N) 528

^{1}HNMR O-H 15.38 (s, 1H); N=CH 9.74 (d, 1H); C-H (Ar) 8.55 (d, 1H), 8.00 (d, 1H), 7.59 (t, 1H), 7.41 (t, 1H), 7.05 (d 1H), 4.06 (s, 1H); C-H (Ar-CF) 7.88-7.80 (m, 4Hs)

3.2.2.4. Nickel (II) 3-methoxy salicylidene-3-trifluoromethyl aniline [Ni-SB4]

1.27mmol (0.37g) of the trifluoro Schiff base ligand was dissolved in 5mL of ethanol. A few drops of acetic acid were added. 1.28mmol (0.23g) of nickel acetate was dissolved in 7mL of ethanol. The nickel solution was added slowly to the Schiff base solution and refluxed for 2 hours. The solution was cooled and the light brown powder was filtered off and dried in a desiccator.

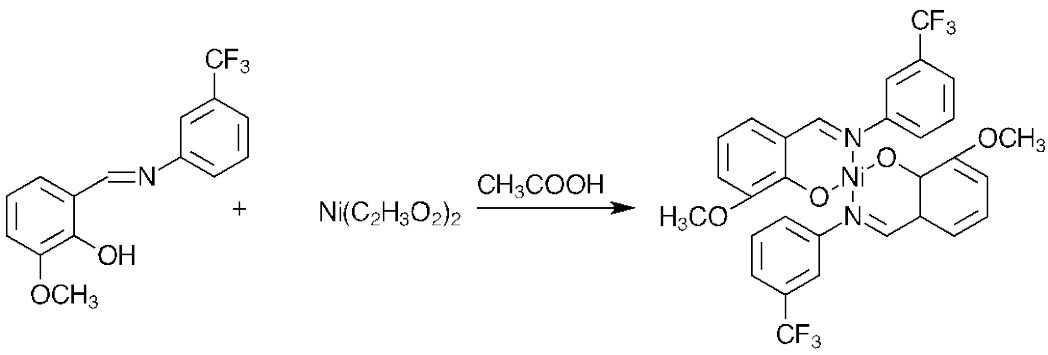

Figure 3.13. Synthesis of Ni-SB4

Yield: 83.3%
M.p.: 106 C
Color: yellow
Molecular formula: $C_{30}H_{22}F_6Ni_1N_2O_4$
Molecular weight: 647.19g/mol
IR: C-H (Ar) 3069, 3000; C-H (Aliphatic) 2964-2834; C=N 1620; C-O 1326; C-F 1194, 1157, 1111

3.2.2.5. Nickel (II) 5-methoxy salicylidene-3-trifluoromethyl aniline [Ni(SB)5$_2$]

3.75mmol (1.11g) of the trifluoro Schiff base ligand was dissolved in 5mL of ethanol. A few drops of acetic acid were added. 1.9mmol (0.34g) of nickel acetate

was dissolved in 17mL of ethanol. The nickel solution was added slowly to the Schiff base solution and refluxed for 2 hours. The solution was cooled and the bright yellow powder was filtered off and dried in a desiccator.

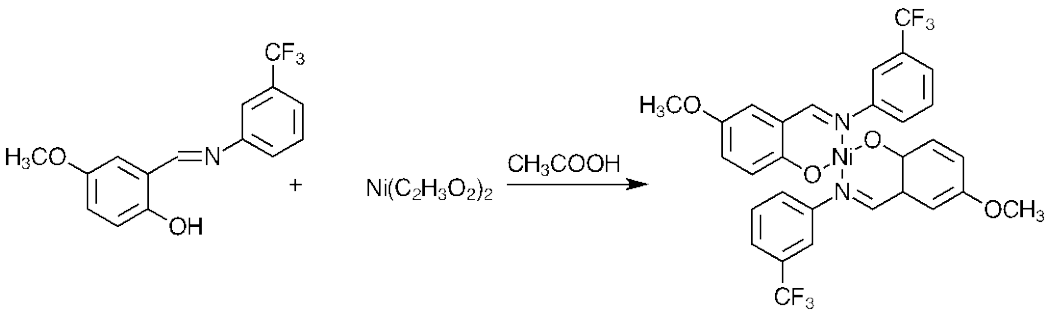

Figure 3.14. Synthesis of Ni-SB5

Yield: 51.1%

M.p.: 302-306°C

Color: yellow

Molecular formula: $C_{30}H_{22}F_6Ni_1N_2O_4$

Molecular weight: 647.19g/mol

IR: C-H (Ar) 2987; C-H (Aliphatic) 2902-2831; C-O 1325; C-F 1158, 1121; v(M-N) 528

^{1}HNMR O-H 12.00 (s, 1H); N=CH 9.01 (s, 1H); C-H (Ar) 7.31 (d, 1H), 7.09 (q, 1H), 6.95 (d, 1H); C-H (Ar-CF) 7.78 (s, 1H), 7.78-7.67 (m, 3Hs); C-H (aliphatic) 3.78 (s, 3Hs)

3.2.2.6. Nickel (II) 3-methoxy salicylidene-3,5-bistrifluoromethyl aniline [Ni-SB6]

1.25mmol (0.45g) of the Schiff base ligand was dissolved in 5mL of ethanol. A few drops of acetic acid were added. 0.0625mmol (0.11g) of nickel acetate was dissolved separately in 7mL of ethanol. The nickel solution was added slowly to the Schiff base solution and refluxed for 1.5 hours. The solution was cooled and the yellow powder was filtered off and dried in a desiccator.

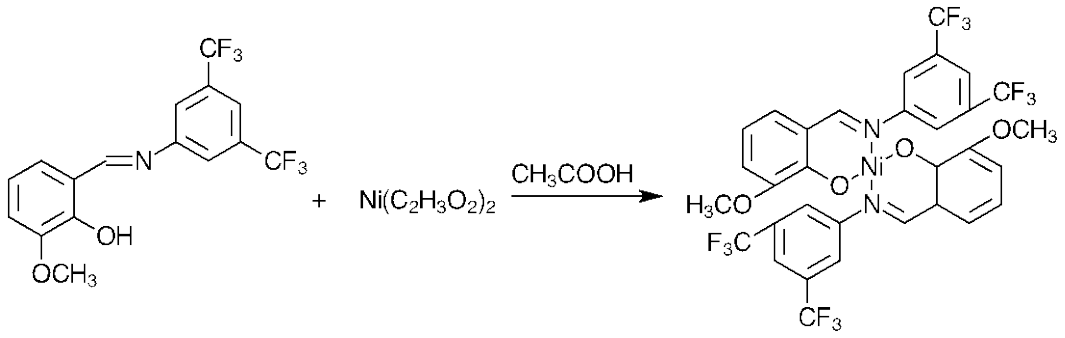

Figure 3.15. Synthesis of Ni-SB6

Yield: 78.9%

M.p.: 192-196°C

Color: yellow

Molecular formula: $C_{32}H_{20}F_{12}Ni_1N_2O_4$

Molecular weight: 783.19g/mol

IR: C-H (Ar) 3291-3178; C-H (Aliphatic) 2969-2769; C=N 1620; C-O 1384; C-F 1211, 1171, 1119

3.2.2.7. Nickel (II) 5-methoxy salicylidene-3,5-bistrifluoromethyl aniline [Ni-SB7]

1.15mmol (0.42g) of the Schiff base ligand was dissolved in 7.5mL of ethanol. A few drops of acetic acid were added. 0.0625mmol (0.11g) of nickel acetate was dissolved separately in 7mL of ethanol. The nickel solution was added slowly to the Schiff base solution and refluxed for 1 hour. The solution was cooled and the yellowish-orange powder was filtered off and dried in a desiccator.

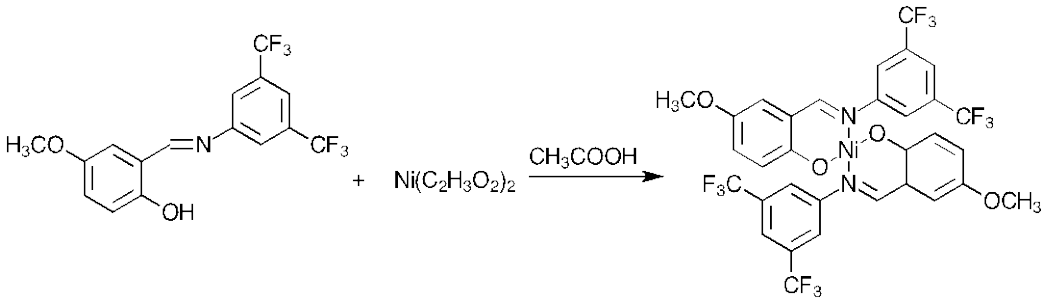

Figure 3.16. Synthesis of Ni-SB7

Yield: 54.0%

M.p.: 220-244°C

Color: yellowish-orange

Molecular formula: $C_{32}H_{20}F_{12}Ni_1N_2O_4$

Molecular weight: 783.19g/mol

IR: C-H (Ar) 3190-3120; C-H (Aliphatic) 2987-2843; C=N 1609; C-O 1370; C-F 1151, 1123, 1089; v(M-N) 528

^{1}HNMR O-H 12.00 (s, 1H); N=CH 9.01 (s, 1H); C-H (Ar) 7.31 (d, 1H), 7.09 (q, 1H), 6.95 (d, 1H); C-H (Ar-CF) 7.78 (s, 1H), 7.78-7.67 (m, 3Hs); C-H (aliphatic) 3.78 (s, 3Hs)

3.2.2.8. Nickel (II) 1,1,1-trifluoro-2,4-pentanedione 2-oxime [Ni-ox1]

1.2mmol (0.21g) of nickel acetate was dissolved in 5 mL of methanol. 2.3mmol (0.39g) of 1,1,1-trifluoro-2,4-pentanedione 2-oxime was added to the nickel mixture. The solution was refluxed for 3.5 hours in a water bath at 50°C. It was removed from heat and allowed to evaporate slowly. The green crystals were collected.

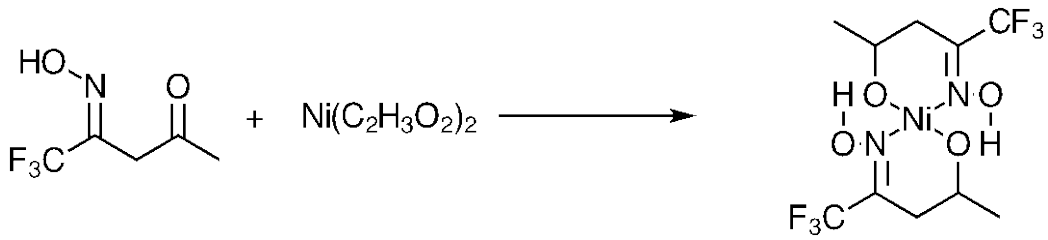

Figure 3.17. Synthesis of Ni-ox1

Yield: 58.8%

Color: green

Molecular formula: $C_{10}H_{12}F_6Ni_1N_2O_4$

Molecular weight: 396.90g/mol

IR: (cm^{-1}) C-H 2704; C=N 1618; C-O 1326; O-H 3386, 3175; C-F 1125

^{1}H NMR: CH_3 2.04 (s, 6Hs); -CH2 3.33 (d, 2Hs), 3.03 (d, 2Hs); O-H 4.78 (b, 2Hs)

3.2.2.9. Nickel (II) 1,1,1-trifluoro-5,5-dimethylhexane-2,4-dione 2-oxime [Ni-ox2]

5.2mmol (0.09g) of nickel acetate was dissolved in 5 mL of methanol. 9.7mmol (0.21g) of 1,1,1-trifluoro-5,5-dimethyl-2,4-hexadione was added to the nickel mixture. The solution was refluxed for 3.5 hours in a water bath and then allowed to evaporate slowly.

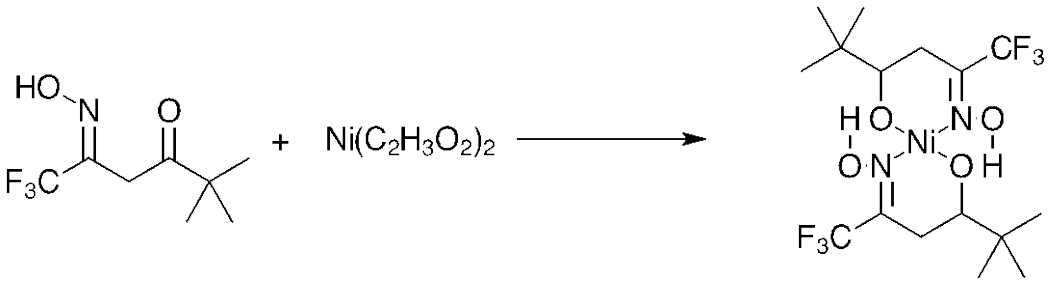

Figure 3.18. Synthesis of Ni-ox2

Yield: 99.1%
M.p.: 110-116°C
Color: green
Molecular formula: $C_{16}H_{24}F_6Ni_1N_2O_4$
Molecular weight: 481.06g/mol
IR: (cm^{-1}) O-H 3131; C-H 2979-2943; C=N 1559; C-O 1370; C-F 1206, 1176, 1152
^{1}HNMR $C(CH_3)_3$ 1.18 (m, 18Hs); -CH2 3.42 (d, 2Hs), 3.17 (d, 2Hs); O-H 8.56 (b, 2Hs)

3.2.3. Synthesis of palladium complexes

3.2.3.1. Palladium (II) salicylidene-4-heptadecafluorooctyl aniline [Pd-SB1]

0.5mmol (0.31g) of the perfluoro Schiff base ligand was dissolved in 30mL ethanol. 0.25mmol (0.04g) of $PdCl_2$ was placed in 45mL of ethanol and heated to

dissolve as well as possible. The palladium was added slowly to the Schiff base solution and a micro spatula of sodium bicarbonate was added as well to regulate the pH. The mixture was refluxed with stirring in a water bath for 1 hour. After allowing the solution to cool, the tan product was filtered off and dried in a desiccator.

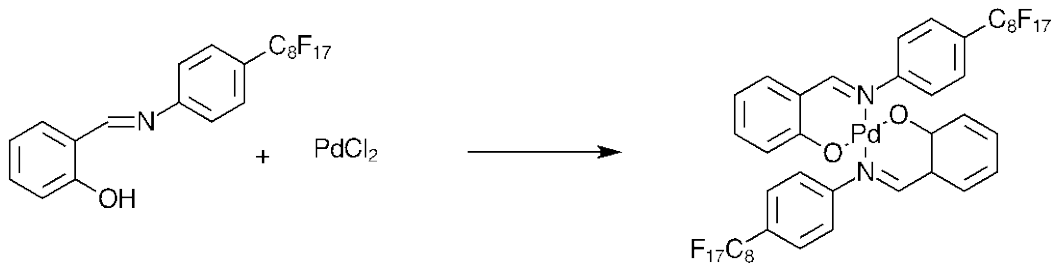

Figure 3.19. Synthesis of Pd-SB1

Yield: 66.8%

M.p.: 269-270°C

Color: tan

Molecular formula: $C_{42}H_{18}F_{34}N_2O_2Pd_1$

Molecular weight: 1334.97g/mol

IR: C-H (Ar) 2952, 2874; C=N 1613; C-O 1370; C-F 1197; Pd-N 554

^{1}HNMR: N=CH 7.64 (d, 1H); C-H(Ar:C-F) 7.47 (d, 1H), 6.68 (d, 2Hs); C-H(Ar) 7.24 (d, 3Hs), 5.88(b, 2Hs)

3.2.3.2. Palladium (II) 4-methoxy salicylidene-4-heptadecafluorooctyl aniline [Pd-SB2]

0.3mmol (0.20g) of the perfluoro-Schiff base ligand was dissolved in 3mL of ethanol. 0.3mmol (0.05g) of $PdCl_2$ was placed in 10mL of ethanol and heated to dissolve as well as possible. The palladium was added slowly to the Schiff base solution and a micro spatula of sodium bicarbonate was added as well to regulate the pH. The mixture was refluxed with stirring in a water bath for 4 hours. The solution was cooled and the gray powder was filtered off and dried in a desiccator.

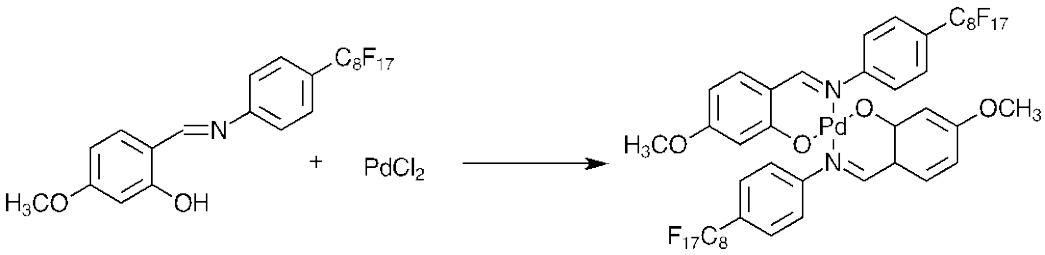

Figure 3.20. Synthesis of Pd-SB2

Yield: 45.9%

M.p.: 262-263°C

Color: gray

Molecular formula: $C_{44}H_{22}F_{34}N_2O_4Pd_1$

Molecular weight: 1395.02g/mol

IR: C-H (Ar) 3190-3171; C-H (Aliphatic) 3121; C=N 1613; C-O 1370; C-F 1225, 1198; Pd-N 553

^{1}HNMR: N=CH 7.64(s, 1H); C-H(Ar:C-F) 7.49(s, 1H), 7.25(s, 3Hs); C-H(Ar) 6.69(d, 3Hs)

3.2.3.3. Palladium (II) 3-Hydroxy-2-naphthylidene-4-heptadecafluorooctyl aniline [Pd-SB3]

0.55mmol (0.37g) of the perfluoro Schiff base ligand was dissolved in 3mL of ethanol. 0.28mmol (0.05g) $PdCl_2$ was placed in 15mL of ethanol and heated to dissolve as well as possible. The palladium was added slowly to the Schiff base solution and a micro spatula of sodium bicarbonate was added as well to regulate the pH. The mixture was refluxed with stirring in a water bath for 3.5 hours. The solution was cooled and the yellow-gray powder was filtered off and dried in a desiccator.

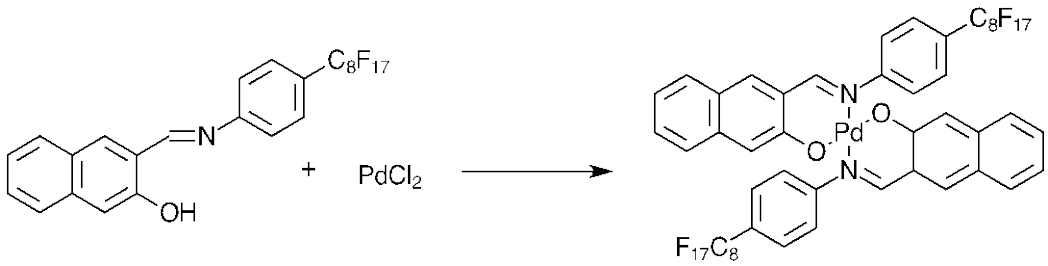

Figure 3.21. Synthesis of Pd-SB3

Yield: 57.8%

M.p.: 253-255°C

Color: yellow-gray

Molecular formula: $C_{50}H_{22}F_{34}N_2O_2Pd_1$

Molecular weight: 1435.09g/mol

IR: C-H (Ar) 298.7, 2893; C=N 1613; C-O 1370; C-F 1225, 1197 Pd-N 553

^{1}HNMR: N=CH 7.7(s, 1H), C-H(Ar:CF3) 7.28(d, 4Hs), C-H(Ar) 6.70(t, 3Hs), 5.94 (t, 3Hs)

3.2.3.4. Palladium (II) 3-methoxy salicylidene-3-trifluoromethyl aniline [Pd-SB4]

1.25mmol (0.081g) of the trifluoro Schiff base ligand was dissolved in 5mL of ethanol. 0.0625mmol (0.12g) of $PdCl_2$ was placed in 25mL of ethanol and heated to dissolve as well as possible. The palladium was added slowly to the Schiff base solution and a micro spatula of sodium bicarbonate was added as well to regulate the pH. The mixture was refluxed with stirring in a water bath for 2 hours. The solution was cooled and the sparkly gold powder was filtered off and dried in a desiccator.

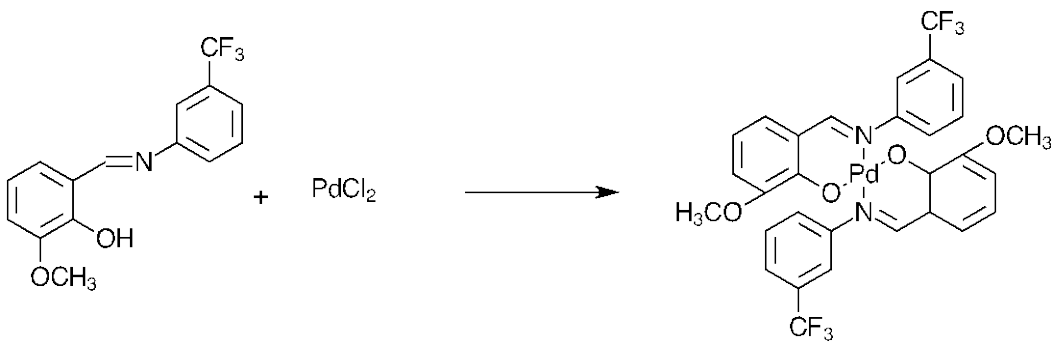

Figure 3.22. Synthesis of Pd-SB4

Yield: 46.4%

M.p.: 313°C

Color: gold

Molecular formula: $C_{30}H_{22}F_6N_2O_4Pd_1$

Molecular weight: 694.92g/mol

IR: C-H (Ar) 3124; C-H (Aliphatic) 2987, 2896; C=N 1601; C-O 1322; C-F 1168, 1126; Pd-N 546

^{1}HNMR: N=CH 7.58(s, 1H); C-H(Ar:C-F) 7.55(s, 2Hs), 7.23; C-H(Ar) 6.90(m, 3Hs); C-H(alkyl) 5.88

3.2.3.5. Palladium (II) 5-methoxy salicylidene-3-trifluoromethyl aniline [Pd-SB5]

3.75mmol (1.11g) of the trifluoro Schiff base ligand was dissolved in 5mL of ethanol. 1.9mmol (0.33g) of $PdCl_2$ was placed in 31mL of ethanol and heated to dissolve as well as possible. The palladium was added slowly to the Schiff base solution and a micro spatula of sodium bicarbonate was added as well to regulate the pH. The mixture was refluxed with stirring in a water bath for 3 hours. The solution was cooled and the shiny gold powder was filtered off and dried in a desiccator.

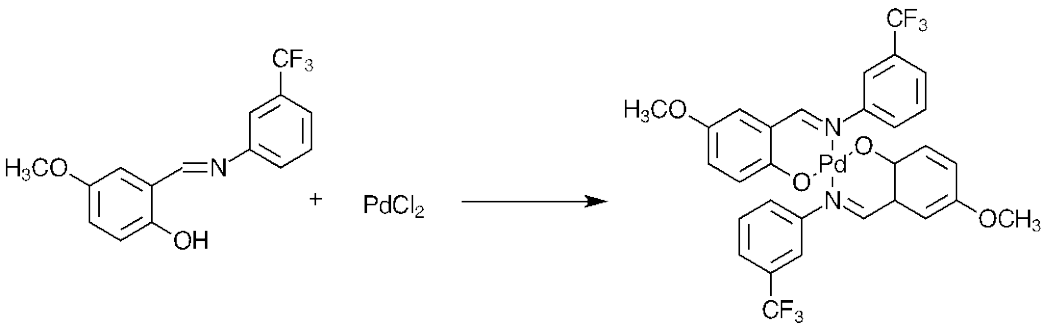

Figure 3.23. Synthesis of Pd-SB5

Yield: 40.7%

M.p.: 324°C

Color: gold

Molecular formula: $C_{30}H_{22}F_6N_2O_4Pd_1$

Molecular weight: 694.92g/mol

IR: C-H (Ar) 3124; C-H (Aliphatic) 2992, 2901; C=N 1601; C-O 1322; C-F 1169, 1127; Pd-N 546

^{1}HNMR: N=CH 7.55(s, 1H); C-H(Ar:C-F) 7.49(s, 1H), 7.22(t); C-H(Ar) 6.81(m, 3Hs); C-H(alkyl) 5.76(b)

3.2.3.6. Palladium (II) 3-methoxy salicylidene-3,5-bistrifluoromethyl aniline [Pd-SB6]

1.25mmol (0.45g) of the bistrifluoro Schiff base ligand was dissolved in 5mL of ethanol. 0.0625mmol (0.11g) of $PdCl_2$ was placed in 21mL of ethanol and heated to dissolve as well as possible. The palladium was added slowly to the Schiff base solution and a micro spatula of sodium bicarbonate was added to regulate the pH. The mixture was refluxed with stirring in a water bath for 4 hours. The solution was cooled and the orange powder was filtered off and dried in a desiccator.

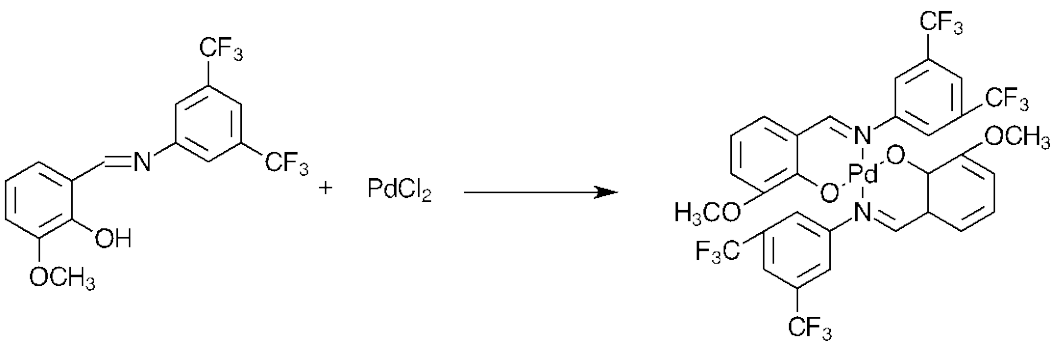

Figure 3.24. Synthesis of Pd-SB6

Yield: 24.7%

M.p.: 268-271°C

Color: orange

Molecular formula: $C_{32}H_{20}F_{12}N_2O_4Pd_1$

Molecular weight: 830.91g/mol

IR: C-H (Ar) 3127; C-H (Aliphatic) 2875, 2812; C=N 1594, C-O 1375; C-F 1170, 1127, 1106; v(M-N) 541

^{1}HNMR: N=CH 8.15(m, 1H); C-H(Ar) 7.12 (s, 3Hs); C-H (Ar-CF) 7.02 (s, 2Hs), 3.84(d, 1H); C-H (aliphatic) 6.13(b, 3Hs)

3.2.3.7. Palladium (II) 5-methoxy salicylidene-3,5-bistrifluoromethyl aniline [Pd-SB7]

1.15mmol (0.42g) of the bistrifluoro Schiff base ligand was dissolved in 7.5mL of ethanol. 0.0625mmol (0.11g) of $PdCl_2$ was placed in 19mL of ethanol and heated to dissolve as well as possible. The palladium was added slowly to the Schiff base solution and a micro spatula of sodium bicarbonate was added to regulate the pH. The mixture was refluxed with stirring in a water bath for 4 hours. The solution was cooled and the reddish brown powder was filtered off and dried in a desiccator.

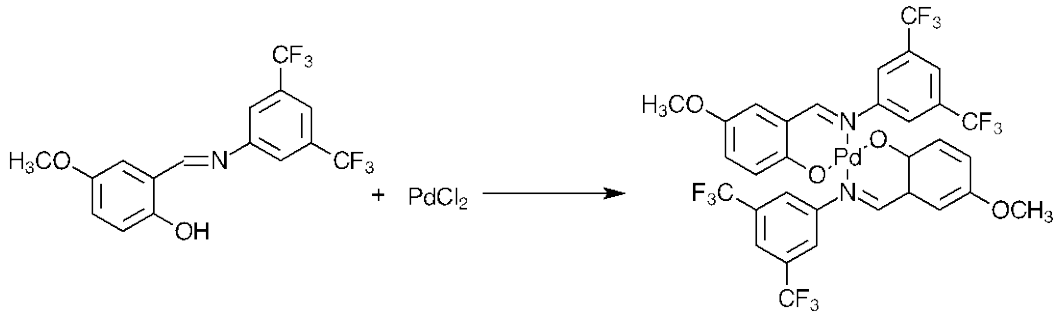

Figure 3.25. Synthesis of Pd-SB7

Yield: 78.7%

M.p.: 322-323°C

Color: reddish brown

Molecular formula: $C_{32}H_{20}F_{12}N_2O_4Pd_1$

Molecular weight: 830.91g/mol

IR: C-H (Ar) 2989, 2958; C-H (Aliphatic) 2896, 2840; C=N 1591 C-O 1365; C-F 1161, 1114; v(M-N) 543

^{1}HNMR: N=CH 8.25(s, 1H); C-H (Ar) 7.12 (m, 3Hs); C-H (Ar-CF) 8.12 (t, 1H), 6.93(d, 2Hs); C-H (aliphatic) 3.74 (q, 3Hs)

3.2.3.8. Palladium (II) 1,1,1-trifluoro-2,4-pentanedione 2-oxime [Pd-ox1]

1.2 mmol (0.21g) of $PdCl_2$ was dissolved in 25 mL of ethanol. 2.3mmol (0.39g) of 1,1,1-trifluoro-2,4-pentadione-2-oxime was added to the palladium mixture. After stirring for a few minutes, 2mL of 1% triethylamine was added to keep the solution from becoming too acidic. The solution was refluxed for 5 hours in a water bath and allowed to evaporate slowly. The brown powder was obtained by heating slightly while stirring and bubbling nitrogen gas through the solution until the solvent evaporated.

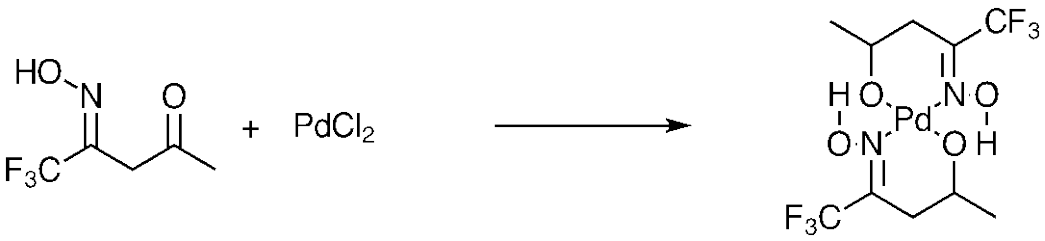

Figure 3.26. Synthesis of Pd-ox1

Yield: 65.6%

Color: brown

Molecular formula: $C_{10}H_{12}F_6N_2O_4Pd_1$

Molecular weight: 444.63g/mol

IR: (cm^{-1}) C-H 2987, 2901; C=N 1622; N-O 1392; C-F1176, 1128

NMR: CH_3 2.31(m, 6Hs); CH_2 3.35(d, 2Hs), 3.08 (m, 2Hs); O-H 4.91(b, 2Hs)

3.2.3.9. Palladium (II) 1,1,1-trifluoro-5,5-dimethylhexane-2,4-dione 2-oxime [Pd-ox2]

0.61mmol (0.09g) of $PdCl_2$ was dissolved in 25 mL of ethanol. 0.52mmol (0.22g) of 1,1,1-trifluoro-5,5-dimethyl-2,4-hexadione in 6 mL of ethanol was added to the palladium mixture. After stirring for a few minutes, 2mL of 1% triethylamine was added to keep the solution from becoming too acidic. The solution was refluxed for 5 hours in a water bath and allowed to evaporate slowly. The brown powder was obtained by heating slightly while stirring and bubbling nitrogen gas through the solution until the solvent evaporated.

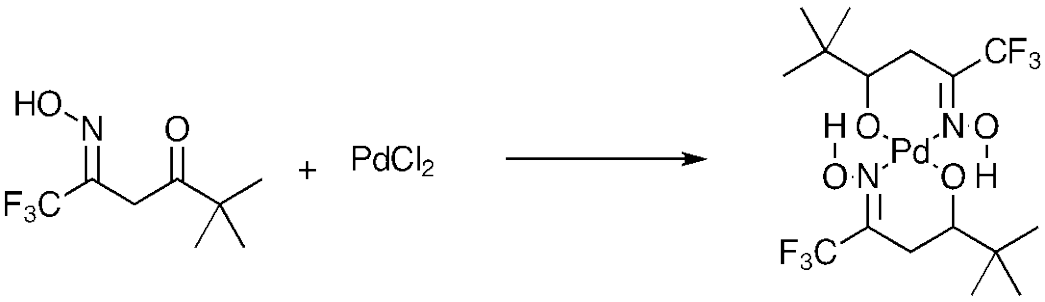

Figure 3.27. Synthesis of Pd-ox2

Yield: 74.9%

M.p.: 188°C

Color: brown

Molecular formula: $C_{16}H_{24}F_6N_2O_4Pd_1$

Molecular weight: 528.78g/mol

IR: (cm^{-1}) C-H 3174-2769; C=N 1616; N-O 1369; O-H 3458; C-F 1204, 1176, 1141

^{1}HNMR CH_3 1.17(m, 18Hs); CH_2 3.43(d, 2Hs), 3.13 (m, 2Hs); O-H 8.3(s, 2Hs)

3.2.4. Synthesis of Tungsten Complexes

3.2.4.1. Tungsten (VI) Salicylidene-4-heptadecafluorooctyl aniline [W-SB1]

Tungstic acid (H_2WO_4) was synthesized by dissolving 5mmol (1.65g) of Na_2WO_4 in 5 mL of water and adding 6M HCl until the precipitate stopped forming. The product was filtered, washed with water and dried in desiccator.

5mmol (1.25g) of tungstic acid was dissolved in 4 mL of H_2O_2. The perfluorous Schiff base was added over the top, it reacted slowly because the Schiff base is not soluble in hydrogen peroxide. The solution was refluxed in a water bath for 20 hours. The dark brown solid was filtered off and dried in a desiccator.

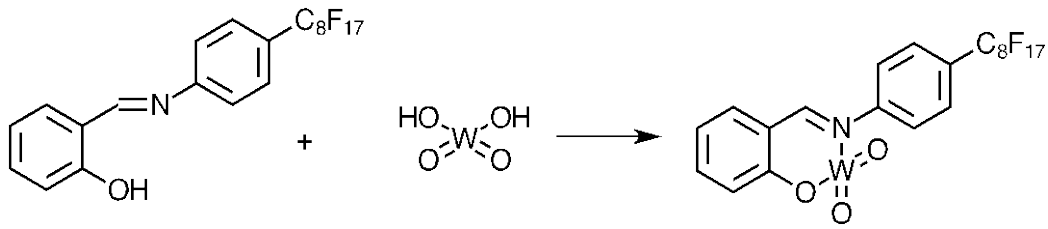

Figure 3.28. Synthesis of W-SB1

Yield: 56%

M.p.: 129-141°C

Color: dark brown

Molecular formula: $C_{21}H_9F_{17}N_1O_3W_1$

Molecular weight: 830.11g/mol

IR: O-H 3365; C-H hidden by OH peak; C=N 1618; C-O 1369; C-F 1195; M=O 683
^{1}HNMR: C-H (Ar) 7.25(s, 1H), 7.12(s, 1H), 7.00(a, 1H); N=CH 9.20(s, 1H); C-H (Ar-CF) 8.28(s, 3Hs), 5.86(d, 1H)

3.2.4.2. Tungsten (VI) 1,1,1-trifluoro-2,4-pentanedione 2-oxime [W-ox1]

5mmol (1.25g) of tungstic acid (H_2WO_4) was dissolved in 10ml H_2O_2. 5mmol (0.84g) of 1,1,1-trifluoro-2,4-pentadione-2-oxime was added to the tungstate acid solution, and refluxed in a water bath set at 35°C for 20 hours. The solvent was allowed to evaporate off leaving a yellow powder.

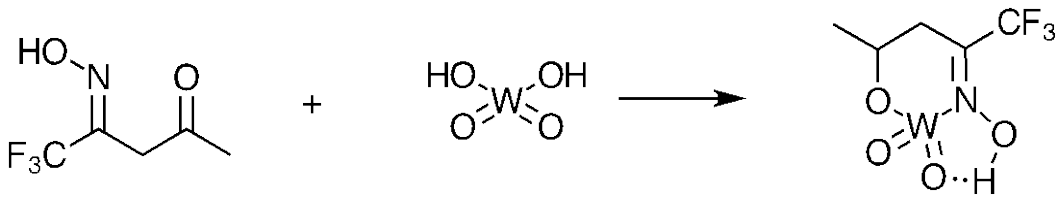

Figure 3.29. Synthesis of W-ox1

Yield: 23.0%
M.p.: <360°C
Color: yellow
Molecular formula: $C_5H_6F_3N_1O_4W_1$
Molecular weight: 384.94g/mol
IR: (cm^{-1}) C-H 2946, 22828; C=N 1625; C-O 1389; C-F1178, 1130
^{1}HNMR CH_3 2.32(m, 3Hs); CH_2 3.57(m, 1H), 3.22(m, 1H1); O-H 4.57(b, 1H)

3.2.5. Determination of solubility in $scCO_2$

Before the newly synthesized precursors were used in the deposition process to produce nanoparticle metals, their solubility in $scCO_2$ was tested. The tests were preformed in a stainless steel reactor with an inner volume of 54 mL. After the reactor was purged by adding CO_2 with a syringe pump until the pressure of 700 psi was reached. The reactor was sealed and brought to a pressure of 2200 psi and a

temperature of 90°C and held there for 1 hour. After the hour, the complexes' solubility in $scCO_2$ was assessed qualitatively.

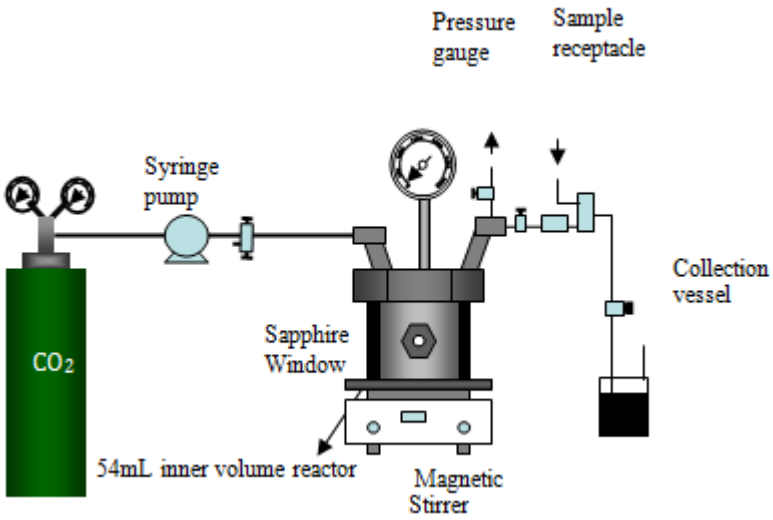

Figure 3.30. System used to test the solubility of precursors in $scCO_2$

3.2.6. Deposition of nanoparticle metals on MWCNTs

An Amar brand stainless steel reactor with an inner volume of 100ml was used to deposit the precursors onto MWCNTs and reduce them to their respective nanoparticle metals.

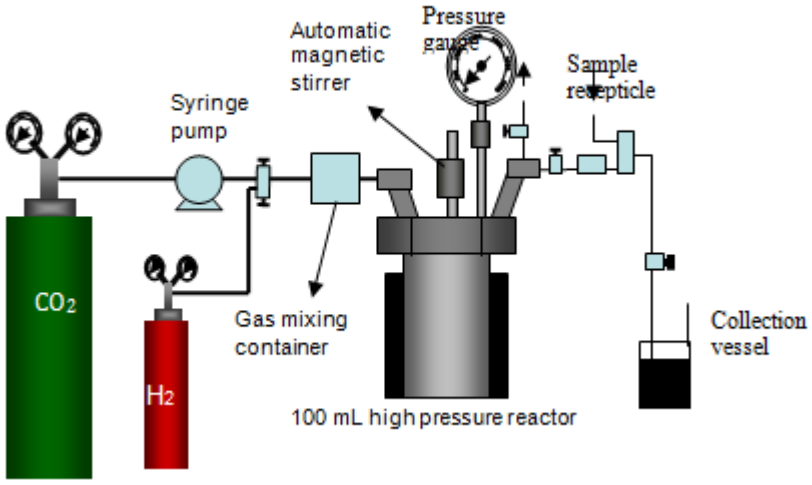

Figure 3.31. System used to deposit the nanoparticle metals on MWCNTs precursors

After the reactor was purged by adding CO_2 with a syringe pump until a pressure of 4.8 MPa was reached, the precursor and MWCNTs were added to the reactor in a precursor:MWCNT ratio of 1:1. A few drops of THF as a cosolvent were added and the reactor was closed. By adding H_2 gas, the pressure was increased to 150 psi and a temperature to 60^{o}C. Then CO_2 was added until the system reached a temperature and pressure of 90^{o}C and 4000psi. The system was stirred for 4 hours under these conditions, after which the reactor was allowed to cool to room temperature and the gas was carefully released. The solid that had formed was washed with THF and centrifuged. It was then placed in a drying oven set at 65^{o}C. XRD and SEM were used to confirm the presence of the metal, the size of its particles, and their distribution on the MWCNT.

4. RESULT AND DISCUSSION

The intent of this research, synthesis of novel precursors and their use in the deposition of nanoparticle metals onto MWCNTs, was accomplished. All synthesized ligands were characterized by FT-IR and ^{1}H NMR. Select ligands were also characterized by ^{13}C NMR, ^{19}F NMR, elemental analysis and x-ray crystallography. The complexes synthesized using these ligands were characterized by the same methods. These complexes (precursors) were tested in $scCO_2$ for solubility. The precursors were then deposited onto MWCNTs in $scCO_2$. The M/MWCNT composites were analyzed using SEM and XRD. The spectra for ligands and complexes are given in the appendix.

Table 4.1. Summary of the physical properties of the ligands and compounds synthesized

Compound	MW (g/mol)	Yield (%)	Color	M.p. (°C)
SB1	615.28	71.0	yellow	133-134
Ni	1287.24	51.0	green	155-157
Pd	1334.97	66.8	tan	269-270
W	830.11	56.0	dark brown	129-141
SB2	645.31	93.3	yellow	92-94
Ni	1347.29	90.9	green	225-230
Pd	1395.02	45.9	gray	262-263
SB3	665.34	79.2	orange-yellow	139-141
Ni	1387.36	78.2	yellow-green	244-250
Pd	1435.09	57.8	yellow-gray	252-255
SB4	295.26	92.0	peach	105-106
Ni	647.19	83.3	light brown	106
Pd	694.92	46.4	gold	313
SB5	295.26	100.0	orange-yellow	74-76
Ni	647.19	51.1	yellow	302-306
Pd	694.92	40.7	gold	324

Table 4.1.

SB6	363.25	66.0	peach	122-123
Ni	783.19	78.9	yellow	192-196
Pd	830.91	24.7	orange	268-271
SB7	363.25	54.2	orange	91-93
Ni	783.19	54.0	yellow-orange	220-244
Pd	830.91	78.7	red-brown	322-323
Ox1	169.10	22.3	white	86-88
Ni	369.90	84.0	blue green	95-100
Pd	444.63	15.8	brown	164-168
Ox2	211.18	60.7	white	164-168
Ni	481.06	99.1	green	110-116
Pd	528.78	74.9	brown	188
W	384.94	23.0	yellow	<360

4.1. Characterization of Schiff base ligands

The Schiff base ligands were synthesized without difficulty and generally in good yield. The spectral data collected matched what was expected based on data published for similar molecules (Feng et al., 2013). The synthesis of all Schiff base ligands is reported for the first time, as far as the author is aware. The proposed structural data is found in Figure 4.1. The IR and ^{1}H NMR data for the synthesized Schiff base ligands is summarized in Tables 4.1.1 and 4.1.2. All the Schiff base ligands were stable at room temperature and soluble in common organic solvents, such as ethanol, DMSO, and THF.

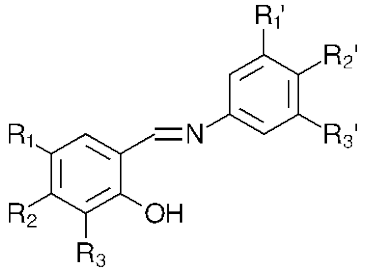

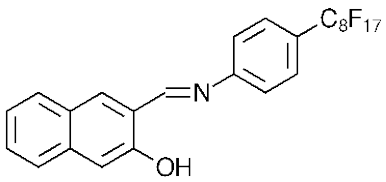

SB1: R_1, R_2, R_3, R_1', R_3'=H; R_2'=C_8F_{17} SB3

SB2: R_1, R_3, R_1', R_3'=H; R_2'=C_8F_{17}; R_2=OCH_3

SB4: R_1, R_2, R_2', R_3'=H; R_1'=CF_3; R_3=OCH_3

SB5: R_2, R_3, R_2', R_3'=H; R_1'=CF_3; R_1=OCH_3

SB6: R_1, R_2, R_2'=H; R_1', R_3'=CF_3; R_3=OCH_3

SB7: R_2, R_3, R_2'=H; R_1', R_3'=CF_3; R_1=OCH_3

Figure 4.1. Proposed structure of synthesized Schiff base ligands

Table 4.2. Summary of IR data for Schiff base ligands

	IR					
Ligand	C-H (Ar)	C-H (alkyl)	C=N	C-N	C-O	C-F
SB1	3065, 3006	-	1621	1369	1142, 1113	1242, 1192, 1179
SB2	3091, 3065	2984-2843	1624	1351	1137, 1109	1210, 1189, 1175
SB3	3057, 2920	-	1628	1369	1144, 1112	1244, 1195
SB4	3070, 3001	2970-2834	1620	1325	1094, 1070	1193, 1172, 1109
SB5	3020, 2991	2962-2836	1619	1323	1099, 1066	1167, 1152, 1137
SB6	3094, 3032	2970-2847	1614	1358	1108, 1092	1276, 1250
SB7	3059, 3020	2964-2846	1619	1371	1039	1158, 1121, 1109

Table 4.3. Summary of ^{1}H NMR data for Schiff base ligands

^{1}H NMR					
	O-H	C-H(ar)	C-H'(Ar)	C-H(Alkyl)	N=CH
SB1	out of range	6.9(t, 1H), 7.05 (d, 1H), 7.42 (m, 2Hs)	7.65(d, 2Hs), 7.38(d, 2Hs)	-	8.64(s, 1H)
SB2	13.17(s, 1H)	6.63(m, 1H), 6.55(d, 1H), 4.06(s, 1H)	7.77(d, 2Hs), 7.61(d, 2Hs)	3.35(s, 3Hs)	8.95(s, 1H)
SB3	15.38(s, 1H)	8.55(d, 1H) 8.00(d, 1H) 7.59(t, 1H) 7.41(t, 1H) 7.05(d, 1H) 4.06(s, 1H)	7.88-7.80(m, 4Hs)	-	9.74(d, 1H)
SB4	12.74(s, 1H))	7.30(m, 1H), 7.18(m, 1H), 6.96(t, 1H)	7.81(s, 1H), 7.73-7.86(m, 3H)	3.85(s, 3H)	9.05(d, 1H)
SB5	12.00 (s, 1H)	7.31(d, 1H), 7.09(q, 1H), 6.95(d, 1H)	7.78(s, 1H), 7.78-7.67(m, 3H)	3.78(s, 3H)	9.01(s, 1H)
SB6	12.29(s, 1H)	7.34(d, 1H), 7.32(d, 1H), 6.97(t, 1H)	8.16(s, 2H), 8.02(s, 1H)	3.86(s, 3H)	9.11(s, 1H)
SB7	11.65(s, 1H)	7.32(d, !H), 7.12(m,1H), 6.96(d, 1H)	8.12(s, 2H), 8.00(s,1)	3.78(s, 3H)	9.06(s, 1H)

4.1.1. Characterization of Salicylidene-4-heptadecafluorooctyl aniline [SB1]

SB1 was synthesized without difficulty in good yield. The elemental analysis was accurate to what was expected. Infrared peaks showing C-O bonds (1369cm^{-1}), C-F bonds (1242, 1192, 11791369cm^{-1}) and C=N bonds (1621cm^{-1}) were observed. An expected broad O-H peak was not observed. This is presumed to be because when the ligand is in its solid state, the hydrogen forms a strong hydrogen bond with the nearby nitrogen.

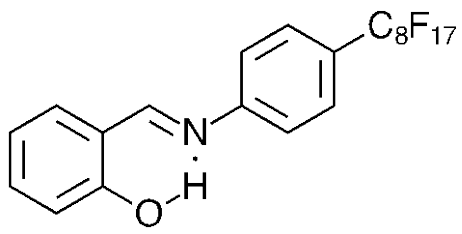

Figure 4.2. Proposed structure of solid state SB1

The proton and fluorine NMR spectra corroborated the evidence that the synthesized molecule was the desired structure with peaks observed in expected places: O-H 12.75(s, 1H); C-H (Ar) (6.9(t, 1H), 7.05(d, 1H), 7.42(m, 1H)); N=CH (8.64 (s, 1H); and C-H (Ar-CF) 7.65 (d, 2Hs), 7.38 (d, 2Hs)); **^{19}FNMR**: CF_3 (-80.8); CF_2 (-110 to -123); and CF_2-Ar (-126). These values agree with previously reported values for similar ligands (Gilani, 2003). The x-ray crystallography results further supported this structure proposal.

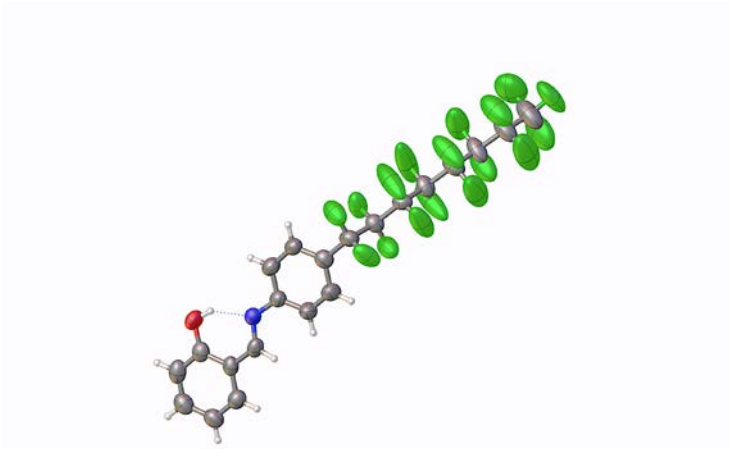

Figure 4.3. X-ray crystallography image of SB1

The FT-IR, ^{1}H NMR and ^{19}F NMR spectra can be found in the appendix.

4.1.2. 4-methoxy salicylidene-4-heptadecafluorooctyl aniline [SB2]

SB2 was synthesized without difficulty in good yield. Infrared peaks showing C-O bonds (1369cm^{-1}), C-F bonds (1249, 1210, 1189cm^{-1}) and C=N bonds (1624cm^{-1}) were observed. The expected broad O-H peak was not observed. This is presumed to be because when the ligand is in its solid state, the hydrogen forms a strong hydrogen bond with the nearby nitrogen.

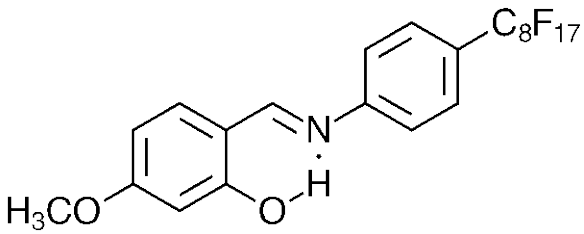

Figure 4.4. Proposed structure of solid state SB2.

The proton NMR spectra corroborated the evidence that the synthesized molecule was the desired structure with peaks observed in expected places: O-H (13.17(s, 1H)); C-H (Ar) (6.62(m, 1H), 6.55 (d, 1H), 4.06 (s ,1H)); N=CH (8.95 (s 1H)); C-H (Ar-CF) (7.77 (d, 2Hs), 7.61 (d, 2Hs)); and C-H (aliphatic) (3.35(s, 3Hs)). These values agree with other values reported for similar Schiff base ligands. The O-H peak in the ^{1}H NMR results shows that the molecule in a liquid state has the structure proposed in Figure 4.1, with the expected O-H bond. The FT-IR and ^{1}H NMR spectra can be found in the appendix.

4.1.3. 3-Hydroxy-2-naphthylidene-4-heptadecafluorooctyl aniline [SB3]

SB3 was synthesized without difficulty in good yield. Infrared peaks showing C-O bonds (1369cm^{-1}), C-F bonds (1244, 1195cm^{-1}) and C=N bonds (1628cm^{-1}) were observed. The expected broad O-H peak was not observed. This is presumed to be because when the ligand is in its solid state, the hydrogen forms a strong hydrogen bond with the nearby nitrogen.

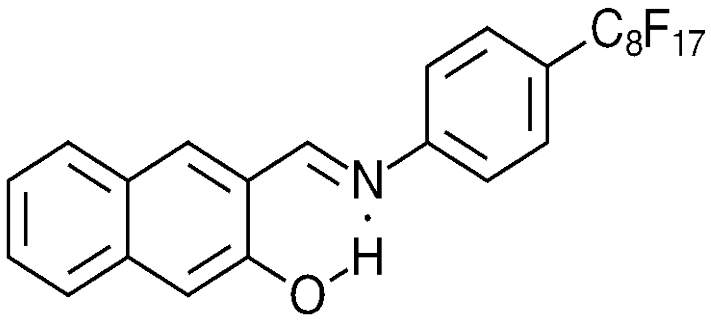

Figure 4.5. Proposed structure of solid state SB3

The proton NMR spectra corroborated the evidence that the synthesized molecule was the desired structure with peaks observed in expected places: O-H (15.38 (s, 1H)); N=CH (9.74 (d, 1H)); C-H (Ar) (8.55 (d, 1H), 8.00 (d, 1H), 7.59 (t, 1H), 7.41 (t, 1H), 7.05 (d 1H), 4.06 (s, 1H)); and C-H (Ar-CF) (7.88-7.80(m, 4Hs)). These values agree with other values reported for similar Schiff base ligands. The O-H peak in the ^{1}H NMR results shows that the molecule in a liquid state has the structure proposed in Figure 4.1 with the expected O-H bond. The FT-IR and ^{1}H NMR spectra can be found in the appendix.

4.1.4. 3-methoxy salicylidene-3-trifluoromethyl aniline [SB4]

SB4 was synthesized without difficulty in great yield. Infrared peaks showing C-O bonds (1325cm^{-1}), C-F bonds (1171, 1109, 1094cm^{-1}) and C=N bonds (1620cm^{-1}) were observed. The expected broad O-H peak was not observed. This is presumed to be because when the ligand is in its solid state, the hydrogen forms a strong hydrogen bond with the nearby nitrogen.

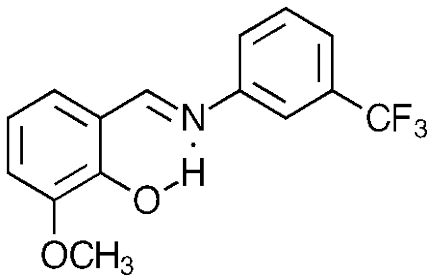

Figure 4.6. Proposed structure of solid state SB4

The proton NMR spectra corroborated the evidence that the synthesized molecule was the desired structure with peaks observed in expected places: O-H (12.74ppm); N=CH (9.05ppm); C-H (Ar) (7.30-6.96ppm); C-H (Ar-CF) (7.81-7.68ppm); and C-H (aliphatic) (3.85ppm). These values agree with other values reported for similar Schiff base ligands. The O-H peak in the ^{1}H NMR results shows that the molecule in a liquid state has the structure proposed in Figure 4.1 with the expected O-H bond. The FT-IR and ^{1}H NMR spectra can be found in the appendix.

4.1.5. 5-methoxy salicylidene-3-trifluoromethyl aniline [SB5]

SB5 was synthesized without difficulty in excellent yield. Infrared peaks showing C-O bonds (1323cm^{-1}), C-F bonds (1167, 1152, 1137cm^{-1}) and C=N bonds (1619cm^{-1}) were observed. The expected broad O-H peak was not observed. This is presumed to be because when the ligand is in its solid state, the hydrogen forms a strong hydrogen bond with the nearby nitrogen.

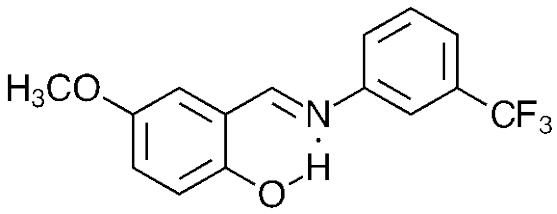

Figure 4.7. Proposed structure of solid state SB5

The proton NMR spectra corroborated the evidence that the synthesized molecule was the desired structure with peaks observed in expected places: O-H (12.00ppm); N=CH (9.01ppm); C-H (Ar) (7.31-6.95ppm); C-H (Ar-CF) (7.78-7.67ppm); and C-H (aliphatic) (3.78ppm). These values agree with other values reported for similar Schiff base ligands. The O-H peak in the ^{1}H NMR results shows that the molecule in a liquid state has the structure proposed in Figure 4.1 with the expected O-H bond. The FT-IR and ^{1}H NMR spectra can be found in the appendix.

4.1.6. 3-methoxy salicylidene-3,5-bistrifluoromethyl aniline [SB6]

SB6 was synthesized without difficulty in good yield. Infrared peaks showing C-O bonds (1380cm^{-1}), C-F bonds (1172, 1108, 1092cm^{-1}) and C=N bonds (1614cm^{-1}) were observed. The expected broad O-H peak was not observed. This is presumed to be because when the ligand is in its solid state, the hydrogen forms a strong hydrogen bond with the nearby nitrogen.

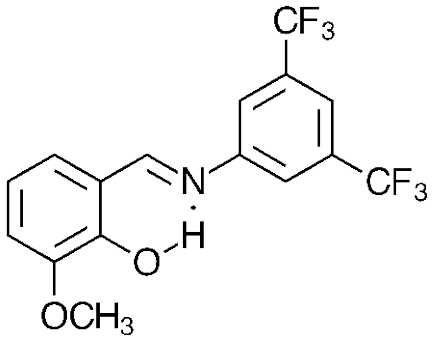

Figure 4.8. Proposed structure of solid state SB6.

The proton NMR spectra corroborated the evidence that the synthesized molecule was the desired structure with peaks observed in expected places: O-H (12.29ppm); N=CH (9.11ppm); C-H (Ar) (7.34-6.97ppm); C-H (Ar-CF) (8.16-8.02ppm); and C-H (aliphatic) (3.86ppm). These values agree with other values reported for similar Schiff base ligands. The O-H peak in the ^{1}H NMR results shows that the molecule in a liquid state has the structure proposed in Figure 4.1 with the expected O-H bond. The FT-IR and ^{1}H NMR spectra can be found in the appendix.

4.1.7. 5-methoxy salicylidene-3,5-bistrifluoromethyl aniline [SB7]

SB7 was synthesized without difficulty in acceptable yield. Infrared peaks showing C-O bonds (1371cm^{-1}), C-F bonds (1158, 1121, 1109cm^{-1}) and C=N bonds (1614cm^{-1}) were observed. The expected broad O-H peak was not observed. This is presumed to be because when the ligand is in its solid state, the hydrogen forms a strong hydrogen bond with the nearby nitrogen.

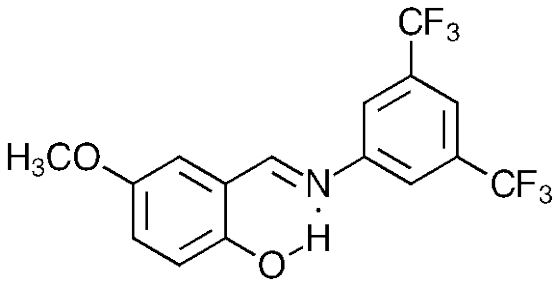

Figure 4.9. Proposed structure of solid state SB7

The proton NMR spectra corroborated the evidence that the synthesized molecule was the desired structure with peaks observed in expected places: O-H (11.65ppm); N=CH (9.06ppm); C-H (Ar) (7.32-6.96ppm); C-H (Ar-CF) (8.12-8.00ppm); and C-H (aliphatic) (3.78ppm). These values agree with other values reported for similar Schiff base ligands. The O-H peak in the ^{1}H NMR results shows that the molecule in a liquid state has the structure proposed in Figure 4.1 with the expected O-H bond. The FT-IR and ^{1}H NMR spectra can be found in the appendix.

4.2. Characterization of nickel Schiff base complexes.

Most of the nickel Schiff base complexes were synthesized without difficulty and generally in good yield. Two of them, SB4 and SB6, were unable to be successfully synthesized. The spectral data for the successfully synthesized complexes matched what was expected based on data published for similar molecules (Khalil, 2012). All synthesized nickel Schiff base complexes are reported for the first time as far as the author is aware. The proposed structural data is found in Figure 4.2. The FT-IR and ^{1}H NMR data for the synthesized complexes is summarized in Tables 4.2.1 and 4.2.2. All the complexes were stable at room temperature and soluble in common organic solvents, such as ethanol, DMSO and THF.

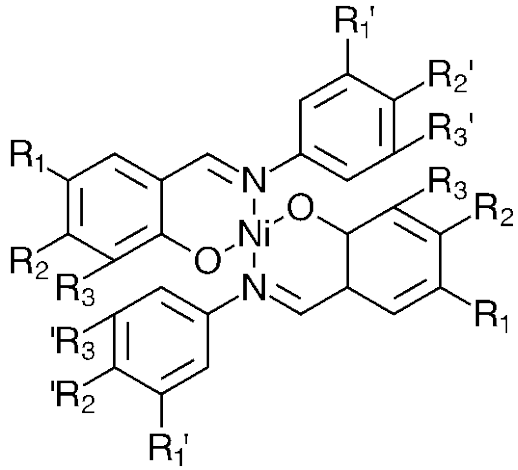

Ni-SB1: R_1, R_2, R_3, R_1', R_3'=H; R_2'=C_8F_{17}
Ni-SB2: R_1, R_3, R_1', R_3'=H; R_2'=C_8F_{17}; R_2=OCH_3

Ni-SB4: R_1, R_2, R_2', R_3'=H; R_1'=CF_3; R_3=OCH_3

Ni-SB5: R_2, R_3, R_2', R_3'=H; R_1'=CF_3; R_1=OCH_3

Ni-SB6: R_1, R_2, R_2'=H; R_1', R_3'=CF_3; R_3=OCH_3

Ni-SB7: R_2, R_3, R_2'=H; R_1', R_3'=CF_3; R_1=OCH_3

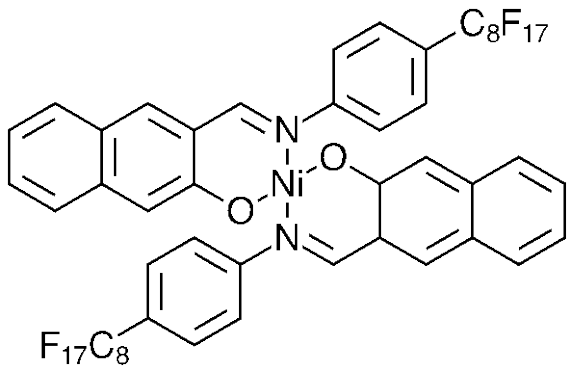

Ni-SB3
Figure 4.10. Proposed structure of nickel Schiff base complexes.

Table 4.4. Comparison of IR data for Schiff base ligands and their nickel complexes

	IR					
	C-H (Ar)	C-H (alkyl)	C=N	C-O	C-F	Ni-N
SB1	3065, 3006	-	1621	1369	1242, 1192, 1179	-
Ni-SB1	**2987**	**-**	**1612**	**1369**	**1197**	**528**
SB2	3091, 3065	2984-2843	1624	1369	1210, 1189, 1175	-
Ni-SB2	**2987**	**2887**	**1611**	**1368**	**1213, 1196, 1180**	**527**
SB3	3057, 2920	-	1628	1369	1244, 1195	-
Ni-SB3	**2987-2902**	**-**	**1615**	**1369**	**1247, 1191**	**528**
SB4	3070, 3001	2970-2834	1620	1325	1193, 1172, 1109	-
Ni-SB4	**3069, 3000**	**2964-2834**	**1620**	**1326**	**1194, 1157, 1111**	**-**
SB5	3020, 2991	2962-2836	1619	1323	1167, 1152, 1137	-
Ni-SB5	**2987**	**2831**	**-**	**1325**	**1158, 1121**	**528**
SB6	3094, 3032	2970-2847	1614	1358	1172, 1109	-
Ni-SB6	**3291-3178**	**2969-2769**	**1620**	**1384**	**1211, 1171, 1119**	**-**
SB7	3059, 3020	2964-2846	1619	1371	1158, 1121, 1109	-
Ni-SB7	**3190-3120**	**2987-2843**	**1609**	**1370**	**1151, 1123, 1089**	**528**

Table 4.5. Comparison of ^{1}H NMR data for Schiff base ligands and their nickel complexes

H NMR					
molecule	O-H	C-H(ar)	C-H'(Ar)	C-H(Alkyl)	N=CH
SB1	out of range	6.9(t, 1H), 7.05 (d, 1H), 7.42 (m, 2Hs)	7.65(d, 2Hs), 7.38(d, 2Hs)	-	8.64(s, 1H)
Ni-SB1	**12.84(s, 1H)**	**6.9 (t, 2Hs) 7.05(d, 2Hs) 7.42(m, 2Hs)**	**7.65(t, 1H) 7.38(d, 2Hs)**	**-**	**8.64(s, 1H)**
SB2	13.17(s, 1H)	6.63(m, 1H), 6.55(d, 1H), 4.06(s, 1H)	7.77(d, 2Hs), 7.61(d, 2Hs)	3.35(s, 3Hs)	8.95(s, 1H)
Ni-SB2	**13.17(s, 1H)**	**6.62(m, 1H) 6.55(d, 1H) 4.06(s, 1H)**	**7.77(d, 2Hs) 7.61(d, 2Hs)**	**3.35(s, 3Hs)**	**8.95(s, 1H)**
SB3	15.38(s, 1H)	8.55(d, 1H) 8.00(d, 1H) 7.59(t, 1H) 7.41(t, 1H) 7.05(d, 1H) 4.06(s, 1H)	7.88-7.80(m, 4Hs)	-	9.74(d, 1H)
Ni-SB3	**15.38(s, 1H)**	**8.55(d, 1H) 8.00(d, 1H) 7.59(t, 1H) 7.41(t, 1H) 7.05(d, 1H) 4.06(s, 1H)**	**7.88-7.80(m, 4H)**	**-**	**9.74(d, 1H)**
SB5	12.00 (s, 1H)	7.31(d, 1H), 7.09(q, 1H), 6.95(d, 1H)	7.78(s, 1H), 7.78-7.67(m, 3H)	3.78(s, 3H)	9.01(s, 1H)
Ni-SB5	**12.00 (s, 1H)**	**7.31(d, 1H), 7.09(q, 1H), 6.95(d, 1H)**	**7.78(s, 1H), 7.78-7.67(m, 3H)**	**3.78(s, 3H)**	**9.01(s, 1H)**
SB7	11.65(s, 1H)	7.32(d, 1H), 7.12(m,1H), 6.96(d, 1H)	8.12(s, 2H), 8.00(s,1)	3.78(s, 3H)	9.06(s, 1H)
Ni-SB7	**11.64(s, 1H)**	**7.32(d, 1H) 7.11(m, 1H) 6.96(d, 1H)**	**8.12(s, 2H), 8.00(s,1)**	**3.77(s, 3Hs)**	**9.06(s, 1H)**

4.2.1. Nickel (II) Salicylidene-4-heptadecafluorooctyl aniline [Ni-SB1]

Ni-SB1 was synthesized without difficulty in acceptable yield. Infrared peaks showing C-O bonds (1369cm^{-1}), C-F bonds (1179cm^{-1}) and C=N bonds (1612cm^{-1}) were observed. Also, a new peak from the Ni-N bond appeared at 528cm^{-1}, where Ni-N bonds are reported to appear in similar complexes (Khalil, 2012). A broad O-H peak was not observed, as would be expected in the complex form. As a result of back bonding from the metal, a noticeable shift in the C=N bond (from 1621 to 1612cm^{-1}) shows that the nickel bonded to the ligand. This shift shows the weakening of the C=N bond as the carbon π^* orbitals accept electrons from the metal center.

The proton and fluorine NMR spectra corroborated the evidence that the synthesized molecule was the desired structure with peaks observed in expected places: N=CH (8.64ppm); C-H (Ar) (7.42-6.90ppm); C-H (Ar-CF) (7.64-7.38ppm). These values agree with other values reported for similar nickel Schiff base complexes (Khalil, 2012). The number of hydrogen atoms and the lack of characteristic acetate peaks in the spectra also corroborated that two ligands replaced the acetate ligands that were on the nickel. The FT-IR, ^{1}H NMR, and ^{19}F NMR spectra can be found in the appendix.

4.2.2. Nickel (II) 4-methoxy salicylidene-4-heptadecafluorooctyl aniline [Ni-SB2]

Ni-SB2 was synthesized without difficulty in great yield. Infrared peaks showing C-O bonds (1368cm^{-1}), C-F bonds (1213, 1196, 1180cm^{-1}) and C=N bonds (1611cm^{-1}) were observed. Also, a new peak from the Ni-N bond appeared at 527cm^{-1}, where Ni-N bonds are reported to appear in similar complexes (Khalil, 2012). A broad O-H peak was not observed, as would be expected in the complex form. As a result of back bonding from the metal, a noticeable shift in the C=N bond (from 1624 to 1611cm^{-1}) shows that the nickel bonded to the ligand. This shift shows the weakening of the C=N bond as the carbon π^* orbitals accept electrons from the metal center.

The proton NMR spectrum corroborated the evidence that the synthesized molecule was the desired structure with peaks observed in expected places: N=CH (8.95ppm); C-H (Ar) (6.62-4.02ppm); C-H (Ar-CF) (7.77-7.61ppm); and C-H (aliphatic) (2.25ppm). These values agree with other values reported for similar nickel Schiff base complexes (Khalil, 2012). The number of hydrogen atoms and the lack of characteristic acetate peaks in the spectra corroborated that two ligands replaced the acetate ligands that were on the nickel. The FT-IR and ^{1}H NMR spectra can be found in the appendix.

4.2.3. Nickel (II) 3-Hydroxy-2-naphthylidene-4-heptadecafluorooctyl aniline [Ni-SB3]

Ni-SB3 was synthesized without difficulty in great yield. Infrared peaks showing C-O bonds (1369cm^{-1}), C-F bonds (1247, 1191cm^{-1}) and C=N bonds (1615cm^{-1}) were observed. Also, a new peak from the Ni-N bond appeared at 528cm^{-1}, where Ni-N bonds are reported to appear in similar complexes (Khalil, 2012). A broad O-H peak was not observed, as would be expected in the complex form. As a result of back bonding from the metal, a noticeable shift in the C=N bond (from 1628 to 1615cm^{-1}) shows that the nickel bonded to the ligand. This shift shows the weakening of the C=N bonds as the carbon π^* orbitals accept electrons from the metal center.

The proton NMR spectrum corroborated the evidence that the synthesized molecule was the desired structure with peaks observed in expected places: N=CH (9.74ppm); C-H (Ar) (8.55-4.06ppm); C-H (Ar-CF) (7.88-7.80ppm). These values agree with other values reported for similar nickel Schiff base complexes (Khalil, 2012). The number of hydrogen atoms and the lack of characteristic acetate peaks in the spectra also corroborated that two ligands replaced the acetate ligands that were on the nickel. The FT-IR and ^{1}H NMR spectra can be found in the appendix.

4.2.4. Nickel (II) 3-methoxy salicylidene-3-trifluoromethyl aniline [Ni-SB4]

The spectral data for Ni-SB4 showed that the desired complex had not been synthesized. The infrared peaks were very similar to those observed in the ligand. The C=N band had not shifted and the band corresponding to the Ni-N bond did not appear.

The proton NMR spectrum was not taken, as it was clear from the IR data that the desired complex had not been synthesized. The FT-IR spectrum can be found in the appendix.

4.2.5. Nickel (II) 5-methoxy salicylidene-3-trifluoromethyl aniline [Ni-SB5]

Ni-SB5 was synthesized without difficulty in acceptable yield. Infrared peaks showing C-O bonds (1325cm^{-1}) and C-F bonds (1158, 1121cm^{-1}) were observed. The C=N seems to have disappeared altogether. Most likely, the peak does not actually disappear, but rather shifts enough that it overlaps with the large, nearby peak (1548cm^{-1}). Also, a new peak from the Ni-N bond appeared at 528cm^{-1}, where Ni-N bonds are reported to appear in similar complexes (Khalil, 2012). A broad O-H peak was not observed, as would be expected in the complex form.

The proton NMR spectrum corroborated the evidence that the synthesized molecule was the desired structure with peaks observed in expected places: N=CH (9.01ppm); C-H (Ar) (7.31-6.95ppm); C-H (Ar-CF) (7.78-7.67ppm); and C-H (aliphatic) (3.78ppm). These values agree with other values reported for similar nickel Schiff base complexes (Khalil, 2012). The number of hydrogen atoms and the lack of characteristic acetate peaks in the spectra also corroborated that two ligands replaced the acetate ligands that were on the nickel. The FT-IR and ^{1}H NMR spectra can be found in the appendix.

4.2.6. Nickel (II) 3-methoxy salicylidene-3,5-bistrifluoromethyl aniline [Ni-SB6]

The spectral data for Ni-SB6 showed that the desired complex had not been synthesized. The infrared peaks were very similar to those observed in the ligand. The C=N band actually shifted slightly upfield and the band corresponding to the Ni-N bond did not appear.

The proton NMR spectrum was not taken as it was clear from the IR data that the desired complex had not been synthesized. The FT-IR spectrum can be found in the appendix.

4.2.7. Nickel (II) 5-methoxy salicylidene-3,5-bistrifluoromethyl aniline [Ni-SB7]

Ni-SB7 was synthesized without difficulty in acceptable yield. Infrared peaks showing C-O bonds (1370cm^{-1}), C-F bonds (1151, 1123, 1089cm^{-1}) and C=N bonds (1609cm^{-1}) were observed. Also, a new peak from the Ni-N bond appeared at 528cm^{-1}, where Ni-N bonds are reported to appear in similar complexes (Khalil, 2012). A broad O-H peak was not observed, as would be expected in the complex form. As a result of back bonding from the metal, a noticeable shift in the C=N bond (from 1619 to 1609cm^{-1}) shows that the nickel bonded to the ligand. This shift shows the weakening of the C=N bond as the carbon π^* orbitals accept electrons from the metal center.

The proton NMR spectrum corroborated the evidence that the synthesized molecule was the desired structure with peaks observed in expected places: N=CH (9.01ppm); C-H (Ar) (7.31-6.95ppm); C-H (Ar-CF) (7.78-7.67ppm); and C-H (aliphatic) (3.78ppm). These values agree with other values reported for similar nickel Schiff base complexes (Khalil, 2012). The number of hydrogen atoms and the lack of characteristic acetate peaks in the spectra also corroborated that two ligands replaced the acetate ligands that were on the nickel. The FT-IR and ^{1}H NMR spectra can be found in the appendix.

4.3. Characterization for palladium Schiff base complexes

The palladium Schiff base complexes were synthesized without difficulty and generally in good yield. The spectral data that was collected matched what was expected based on data published for similar molecules (Coombs et al, 2004; Uh et al, 2004). All synthesized palladium Schiff base complexes are reported for the first time, as far as the author is aware. The proposed structural data is found in Figure 4.3. The IR and ^{1}H NMR data for the synthesized complexes is summarized in Tables 4.3.1 and 4.3.2. It should be noted that the ^{1}HNMR spectra do not look as would be generally expected. The peak observed in these spectra have also been observed and published in other research (Uh, et al, 2004, Coombs et al, 2005). In the palladium complex, we see a significant downshift of the peak corresponding to the N=CH proton. It is thought that this is due to the deshielding effect caused by the metal complexation (Gharah et al, 2009). All the complexes were stable at room temperature and soluble in common organic solvents, such as ethanol, DMSO, and THF.

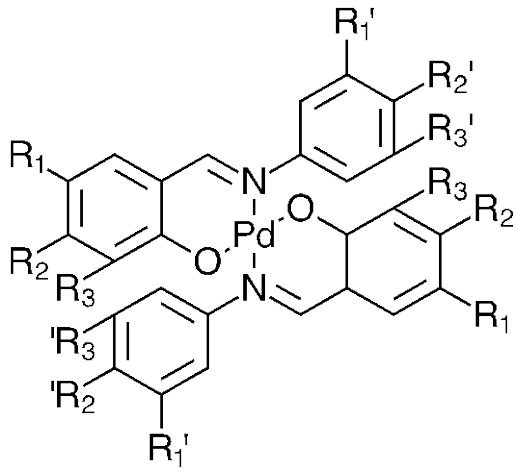

Pd-SB1: R_1, R_2, R_3, R_1', R_3'=H; R_2'=C_8F_{17}

Pd-SB2: R_1, R_3, R_1', R_3'=H; R_2'=C_8F_{17}; R_2=OCH_3

Pd-SB4: R_1, R_2, R_2', R_3'=H; R_1'=CF_3; R_3=OCH_3

Pd-SB5: R_2, R_3, R_2', R_3'=H; R_1'=CF_3; R_1=OCH_3

Pd-SB6: R_1, R_2, R_2'=H; R_1', R_3'=CF_3; R_3=OCH_3

Pd-SB7: R_2, R_3, R_2'=H; R_1', R_3'=CF_3; R_1=OCH_3

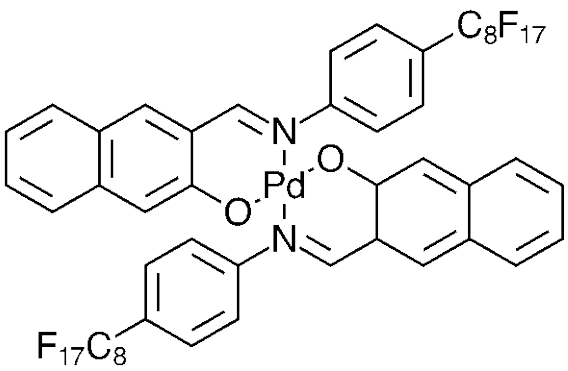

Pd-SB3

Figure 4.11. Proposed structure of palladium Schiff base complexes

Table 4.6. Comparison of IR data for Schiff base ligands and their palladium complexes

	IR						
molecule	C-H (Ar)	C-H (alkyl)	C=N	C-O	C-F	O=C-H	Pd-N
SB1	3065, 3006	-	1621	1369	1242, 1192, 1179		
Pd-SB1	**2952, 2874**	**-**	**1613**	**1370**	**1197**	**3290-3120**	**554**
SB2	3091, 3065	2984-2843	1624	1369	1210, 1189, 1175		
Pd-SB2	**3190-3171**	**3121**	**1613**	**1370**	**1225, 1198**	**3290-3294**	**553**
SB3	3057-2920	-	1628	1369	1244, 1195		
Pd-SB3	**2987, 2893**	**-**	**1613**	**1370**	**1225, 1197**	**3290-3120**	**554**
	IR						
SB4	3070, 3001	2970-2834	1620	1325	1193, 1172, 1109		
Pd-SB4	**3124**	**2987, 2896**	**1601**	**1322**	**1168, 1126**	**3235-3192**	**546**
SB5	3020, 2991	2962-2836	1619	1323	1167, 1152, 1137		
Pd-SB5	**3124**	**2992, 2901**	**1601**	**1322**	**1169, 1127**	**3235-3192**	**546**
SB6	3094, 3032	2970-2847	1614	1380	1172, 1109		
Pd-SB6	**3127**	**2875, 2812**	**1594**	**1375**	**1170, 1127, 1106**	**3236-3201**	**541**
SB7	3059, 3020	2964-2846	1619	1371	1158, 1121, 1109		
Pd-SB7	**2989, 2958**	**2896, 2840**		**1365**	**1161, 1114**	**-**	**543**

Table 4.7. Comparison of ^{1}H NMR data for Schiff base ligands and their palladium complexes

H NMR					
molecule	O-H	C-H(Ar)	C-H'(Ar)	C-H(Alkyl)	N=CH
SB1	out of range	6.9(t, 1H), 7.05 (d, 1H), 7.42 (m, 2Hs)	7.65(d, 2Hs), 7.38(d, 2Hs)	-	8.64(s, 1H)
Pd-SB1	**-**	**5.88 (b, 2Hs), 7.24 (d, 3Hs)**	**7.47(d, 1H), 6.68 (d, 2Hs)**	**-**	**7.64(d, 1H)**
SB2	13.17(s, 1H)	6.63(m, 1H), 6.55(d, 1H), 4.06(s, 1H)	7.77(d, 2Hs), 7.61(d, 2Hs)	3.35(s, 3Hs)	8.95(s, 1H)
Pd-SB2	**-**	**6.69(d, 3Hs)**	**7.49(s, 1H), 7.25(s, 3Hs)**	**5.90 (b, 3Hs)**	**7.64(s, 1H)**
SB3	15.38(s, 1H)	8.55(d, 1H) 8.00(d, 1H) 7.59(t, 1H) 7.41(t, 1H) 7.05(d, 1H) 4.06(s, 1H)	7.88-7.80(m, 4Hs)	-	9.74(d, 1H)
Pd-SB3	**-**	**6.70(t, 3Hs) 5.94(t, 3Hs)**	**7.28(d, 4Hs)**		**7.7(s, 1H)**
SB4	12.74(s, 1H))	7.30(m, 1H), 7.18(m, 1H), 6.96(t, 1H)	7.81(s, 1H), 7.73-7.86(m, 3H)	3.85(s, 3H)	9.05(d, 1H)
Pd-SB4		**6.90(m, 3Hs)**	**7.55(s, 2Hs), 7.23**	**5.88**	**7.58(s, 1H)**
SB5	12.00 (s, 1H)	7.31(d, 1H), 7.09(q, 1H), 6.95(d, 1H)	7.78(s, 1H), 7.78-7.67(m, 3H)	3.78(s, 3H)	9.01(s, 1H)
Pd-SB5		**6.81(m, 3Hs)**	**7.49(s, 2Hs), 7.22(t)**	**5.76(b)**	7.55(s, 1H)
SB6	12.29(s, 1H)	7.34(d, 1H), 7.32(d, 1H), 6.97(t, 1H)	8.16(s, 2H), 8.02(s, 1H)	3.86(s, 3H)	9.11(s, 1H)
Pd-SB6		**7.12(s, 3Hs)**	**7.02(s, 2Hs), 3.84(d, 1H)**	**6.13(b, 3Hs)**	8.15(m, 1H)
SB7	11.65(s, 1H)	7.32(d, 1H), 7.12(m,1H), 6.96(d, 1H)	8.12(s, 2H), 8.00(s,1)	3.78(s, 3H)	9.06(s, 1H)
Pd-SB7		**7.12(m, 3Hs)**	**8.12(t, 1H), 6.93(d, 2Hs)**	**3.74(q, 3Hs)**	8.25(s, 1H)

4.3.1. Palladium (II) Salicylidene-4-heptadecafluorooctyl aniline [Pd-SB1]

Pd-SB1 was synthesized without difficulty in acceptable yield. The elemental analysis was accurate to what was expected. Infrared peaks showing C-O bonds (1370cm^{-1}), C-F bonds (1197cm^{-1}) and C=N bonds (1613cm^{-1}) were observed. Also, a new peak from the Pd-N bond appeared at 554cm^{-1}, where Pd-N bonds are reported

to appear in similar complexes (Hegazy, 2012). A broad O-H peak was not observed, as would be expected in the complex form.

As a result of back bonding from the metal, a noticeable shift in the C=N bond (from 1621 to 1613cm^{-1}) shows that the palladium bonded to the ligand. This shift shows the weakening of the C=N bond as the carbon π* orbitals accept electrons from the metal center.

Peaks characteristic to acetate also appeared in the IR spectrum. During synthesis, sodium acetate was added to create a buffer system to keep the pH levels from becoming too acidic. Based on the evidence in the IR spectrum that the characteristic bonds for Pd-N appeared as well as a shift in the C=N peak, it is postulated that the palladium coordinated one Schiff base ligand and one acetate as a ligand.

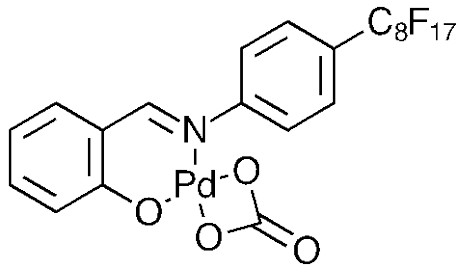

Figure 4.12. Proposed structure of Pd-SB1 based on spectral data

The proton NMR spectrum corroborated the evidence that the synthesized molecule was the structure pictured in the figure above in Figure 4.3.1 with peaks observed in expected places: N=C-H (7.64ppm); C-H(Ar) (7.24, 5.88ppm); C-H (Ar-CF) (7.47, 6.68ppm). These values agree with other values reported for similar palladium Schiff base complexes (Uh, et al, 2004; Coombs et al, 2005). The lack of O-H peak in the ^{1}H NMR results shows that the ligand did indeed coordinate to the metal. The FT-IR and ^{1}H NMR and spectra can be found in the appendix.

4.3.2. Palladium (II) 4-methoxy salicylidene-4-heptadecafluorooctyl aniline [Pd-SB2]

Pd-SB2 was synthesized without difficulty in acceptable yield. Infrared peaks showing C-O bonds (1370cm^{-1}), C-F bonds (1225, 1198 cm^{-1}) and C=N bonds (1613cm^{-1}) were observed. Also, a new peak from the Pd-N bond appeared at 553cm^{-1}, where Pd-N bonds are reported to appear in similar complexes (Hegazy and Gaafar, 2012). A broad O-H peak was not observed, as expected.

As a result of back bonding from the metal, a noticeable shift in the C=N bond (from 1624 to 1613cm^{-1}) shows that the palladium bonded to the ligand. This shift shows the weakening of the C=N bond as the carbon π^* orbitals accept electrons from the metal center.

Peaks characteristic to acetate also appeared in the IR spectrum. During synthesis, sodium acetate was added to create a buffer system to keep the pH levels from becoming too acidic. Based on the evidence in the IR spectrum that the characteristic bonds for Pd-N appeared as well as a shift in the C=N peak, it is postulated that the palladium coordinated one Schiff base ligand and one acetate as a ligand.

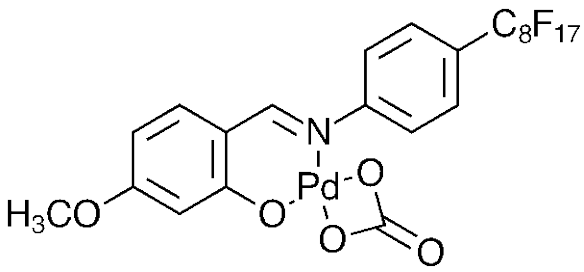

Figure 4.13. Proposed structure of Pd-SB2 based on spectral data

The proton NMR spectrum corroborated the evidence that the synthesized molecule was the above structure with peaks observed in expected places: N=C-H (7.64ppm); C-H(Ar) (6.69ppm); C-H(Ar-CF) (7.49, 7.25ppm). These values agree with other values reported for similar palladium Schiff base complexes (Uh, et al, 2004; Coombs et al, 2005). The lack of O-H peak in the ^{1}H NMR results shows that

the ligand did indeed coordinate to the metal. The FT-IR and ^{1}H NMR spectra can be found in the appendix.

4.3.3. Palladium (II) 3-Hydroxy-2-naphthylidene-4-heptadecafluorooctyl aniline [Pd-SB3]

Pd-SB3 was synthesized without difficulty in acceptable yield. Infrared peaks showing C-O bonds (1370cm^{-1}), C-F bonds (1225, 1197cm^{-1}) and C=N bonds (1613cm^{-1}) were observed. Also, a new peak from the Pd-N bond appeared at 553cm^{-1}, where Pd-N bonds are reported to appear in similar complexes (Hegazy, 2012). A broad O-H peak was not observed, as would be expected in the complex form.

As a result of back bonding from the metal, a noticeable shift in the C=N bond (from 1628 to 1613cm^{-1}) shows that the palladium bonded to the ligand. This shift shows the weakening of the C=N bond as the carbon π^* orbitals accept electrons from the metal center.

Peaks characteristic to acetate also appeared in the IR spectrum. During synthesis, sodium acetate was added to create a buffer system to keep the pH levels from becoming too acidic. Based on the evidence in the IR spectrum that the characteristic bonds for Pd-N appeared as well as a shift in the C=N peak, it is postulated that the palladium coordinated one Schiff base ligand and one acetate as a ligand.

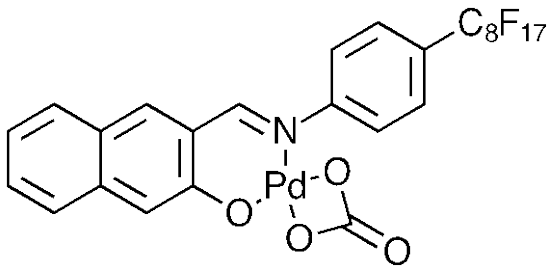

Figure 4.14. Proposed structure of Pd-SB3 based on spectral data

The proton NMR spectrum corroborated the evidence that the synthesized molecule was the above structure with peaks observed in expected places: N=C-H

(7.7ppm); C-H (Ar) (6.70, 5.94ppm); C-H (Ar-CF) (7.28ppm). These values agree with other values reported for similar palladium Schiff base complexes (Uh, et al, 2004; Coombs et al, 2005). The lack of O-H peak in the ^{1}H NMR results shows that the ligand did indeed coordinate to the metal. The FT-IR and ^{1}H NMR spectra can be found in the appendix.

4.3.4. Palladium (II) 3-methoxy salicylidene-3-trifluoromethyl aniline [Pd-SB4]

Pd-SB4 was synthesized without difficulty in acceptable yield. Infrared peaks showing C-O bonds (1322cm^{-1}), C-F bonds (1168, 1126 cm^{-1}) and C=N bonds (1601cm^{-1}) were observed. Also, a new peak from the Pd-N bond appeared at 546cm^{-1}, where Pd-N bonds are reported to appear in similar complexes (Hegazy, 2012). A broad O-H peak was not observed, as would be expected in the complex form.

As a result of back bonding from the metal, a noticeable shift in the C=N bond (from 1620 to 1601cm^{-1}) shows that the palladium bonded to the ligand. This shift shows the weakening of the C=N bond as the carbon π^* orbitals accept electrons from the metal center.

Peaks characteristic to acetate also appeared in the IR spectrum. During synthesis, sodium acetate was added to create a buffer system to keep the pH levels from becoming too acidic. Based on the evidence in the IR spectrum that the characteristic bonds for Pd-N appeared as well as a shift in the C=N peak, it is postulated that the palladium coordinated one Schiff base ligand and one acetate as a ligand.

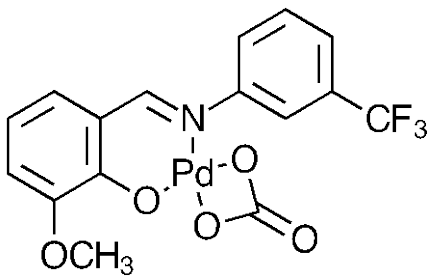

Figure 4.15. Proposed structure of Pd-SB4 based on spectral data

The proton NMR spectrum corroborated the evidence that the synthesized molecule was the above structure with peaks observed in expected places: N=C-H (7.58ppm); C-H(Ar) (6.90ppm); C-H(Ar-CF) (7.55, 7.23ppm); and C-H (aliphatic) (5.88ppm). These values agree with other values reported for similar palladium Schiff base complexes (Uh, et al, 2004; Coombs et al, 2005). The lack of O-H peak in the ^{1}H NMR results shows that the ligand did indeed coordinate to the metal. The FT-IR and ^{1}H NMR spectra can be found in the appendix.

4.3.5. Palladium (II) 5-methoxy salicylidene-3-trifluoromethyl aniline [Pd-SB5]

Pd-SB5 was synthesized without difficulty in acceptable yield. Infrared peaks showing C-O bonds (1322cm^{-1}), C-F bonds (1169, 1127cm^{-1}) and C=N bonds (1601cm^{-1}) were observed. Also, a new peak from the Pd-N bond appeared at 546cm^{-1}, where Pd-N bonds are reported to appear in similar complexes (Hegazy, 2012). A broad O-H peak was not observed, as would be expected in the complex form.

As a result of back bonding from the metal, a noticeable shift in the C=N bond (from 1619 to 1601cm^{-1}) shows that the palladium bonded to the ligand. This shift shows the weakening of the C=N bond as the carbon π^* orbitals accept electrons from the metal center.

Peaks characteristic to acetate also appeared in the IR spectrum. During synthesis, sodium acetate was added to create a buffer system to keep the pH levels from becoming too acidic. Based on the evidence in the IR spectrum that the characteristic bonds for Pd-N appeared as well as a shift in the C=N peak, it is postulated that the palladium coordinated one Schiff base ligand and one acetate as a ligand.

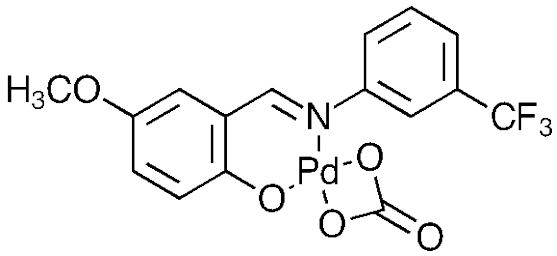

Figure 4.16. Proposed structure of Pd-SB5 based on spectral data

The proton NMR spectrum corroborated the evidence that the synthesized molecule was the above structure with peaks observed in expected places: N=C-H (7.55ppm); C-H(Ar) (6.81ppm); C-H(Ar-CF) (7.49, 7.22ppm); and C-H (aliphatic) (5.76ppm). These values agree with other values reported for similar palladium Schiff base complexes (Uh, et al, 2004; Coombs et al, 2009). The lack of O-H peak in the ^{1}H NMR results shows that the ligand did indeed coordinate to the metal. The FT-IR and ^{1}H NMR spectra can be found in the appendix.

4.3.6. Palladium (II) 3-methoxy salicylidene-3,5-bistrifluoromethyl aniline [Pd-SB6]

Pd-SB6 was synthesized without difficulty in acceptable yield. Infrared peaks showing C-O bonds (1375cm^{-1}), C-F bonds (1170, 1127,1106cm^{-1}) and C=N bonds (1594cm^{-1}) were observed. Also, a new peak from the Pd-N bond appeared at 541cm^{-1}, where Pd-N bonds are reported to appear in similar complexes (Hegazy, 2012). A broad O-H peak was not observed, as would be expected in the complex form.

As a result of back bonding from the metal, a noticeable shift in the C=N bond (from 1614 to 1594cm^{-1}) shows that the palladium bonded to the ligand. This shift shows the weakening of the C=N bond as the carbon π^* orbitals accept electrons from the metal center. The shift in this case is larger than in the other palladium complexes. It is hypothesized that the C=N peak is overlapped with another, larger peak causing it to appear to have shifted so dramatically.

Peaks characteristic to acetate also appeared in the IR spectrum. During synthesis, sodium acetate was added to create a buffer system to keep the pH levels

from becoming too acidic. Based on the evidence in the IR spectrum that the characteristic bonds for Pd-N appeared as well as a shift in the C=N peak, it is postulated that the palladium coordinated one Schiff base ligand and one acetate as a ligand.

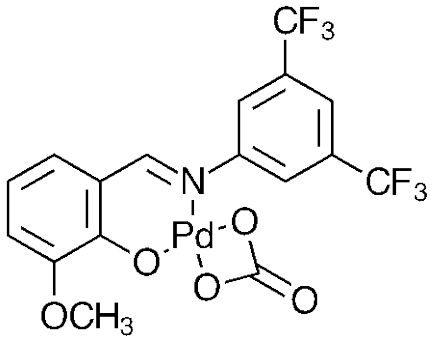

Figure 4.17. Proposed structure of Pd-SB6 based on spectral data

The proton NMR spectrum corroborated the evidence that the synthesized molecule was the above structure with peaks observed in expected places: N=C-H (8.15ppm); C-H(Ar) (7.12ppm); C-H(Ar-CF) (7.02, 3.84ppm); and C-H (aliphatic) (6.13ppm). These values agree with other values reported for similar palladium Schiff base complexes (Uh, et al, 2004; Coombs et al, 2005). The lack of O-H peak in the ^{1}H NMR results shows that the ligand did indeed coordinate to the metal. The FT-IR and ^{1}H NMR spectra can be found in the appendix.

4.3.7. Palladium (II) 5-methoxy salicylidene-3,5-bistrifluoromethyl aniline [Pd-SB7]

Pd-SB7 was synthesized without difficulty in acceptable yield. Infrared peaks showing C-O bonds (1365cm^{-1}), C-F bonds (1161, 1114cm^{-1}) and C=N bonds (1591cm^{-1}) were observed. Also, a new peak from the Pd-N bond appeared at 543cm^{-1}, where Pd-N bonds are reported to appear in similar complexes (Hegazy, 2012). A broad O-H peak was not observed, as would be expected in the complex form.

As a result of back bonding from the metal, a noticeable shift in the C=N bond (from 1619 to 1591cm^{-1}) shows that the palladium bonded to the ligand. This

shift shows the weakening of the C=N bond as the carbon π* orbitals accept electrons from the metal center. The shift, in this case, is larger than in the other palladium complexes. It is hypothesized that the C=N peak is overlapped with another, larger peak causing it to appear to have shifted so dramatically. Interestingly, in this complex, no peaks characteristic to acetate appeared in the IR spectrum. Therefore, the originally proposed structure is thought to have been synthesized.

The proton NMR spectrum corroborated the evidence that the synthesized molecule was the desired structure with peaks observed in expected places: N=CH (8.25ppm); C-H(Ar) (7.12ppm); C-H(Ar-CF) (8.12, 6.93ppm); and C-H (aliphatic) (3.74ppm). These values agree with other values reported for similar palladium Schiff base complexes (Uh, et al, 2004; Coombs et al, 2005). The FT-IR and ^{1}H NMR spectra can be found in the appendix.

4.4. Characterization of tungsten Schiff base complex

The tungsten Schiff base complex was synthesized without difficulty, but with poor yield. The spectral data collected matched what was expected based on data published for similar molecules (Zhou, 2004). This tungsten Schiff base complex is reported for the first time, as far as the author is aware. The IR and ^{1}H NMR data for the synthesized complex is summarized in Tables 4.8.1 and 4.8.2. The complex was stable at room temperature.

Table 4.8. Comparison of IR data from Schiff base ligand and its tungsten complex

	C-H (Ar)	C=N	C-O	C-F	O-H	M=O
SB1	3065, 3006	1621	1369	1242, 1192, 1179		-
W-SB1	hidden	1618	1369	1195	3365	683

Table 4.9. Comparison of ^{1}H NMR data from Schiff base ligand and its tungsten complex

	O-H	C-H(ar)	C-H'(Ar)	N=CH
SB1	12.84	6.9(t), 7.05 (d), 7.42 (m)	7.65(d), 7.38(d)	8.64(s)
W-SB1	-	7.25(s, 1H), 7.12(s, 1H), 7.00(s, 1H)	8.28(s, 3Hs), 5.86(d, 1H)	9.20(s, 1H)

4.4.1. Tungsten (VI) Salicylidene-4-heptadecafluorooctyl aniline [W-SB1]

W-SB1 was synthesized in acceptable yield. Infrared peaks showing C-O bonds (1369cm^{-1}), C-F bonds (1195 cm^{-1}) and C=N bonds (1618cm^{-1}) were observed.

As a result of back bonding from the metal, a noticeable shift in the C=N bond (from 1621 to 1618cm^{-1}) shows that the tungsten bonded to the ligand. This shift shows the weakening of the C=N bond as the carbon π^* orbitals are donated electrons by the metal center. A broad O-H peak was observed, which would not be expected in the complex form. Because the C=N peak shifted downfield, suggesting the ligand coordinated to the metal center, it is postulated that some protons were bonded to the oxygen atoms due to the acidic nature of the reaction medium. A new bond at 683cm-1 also appeared in the IR spectra corresponding to the M=O bond, further substantiating that the metal had complexed with the ligand.

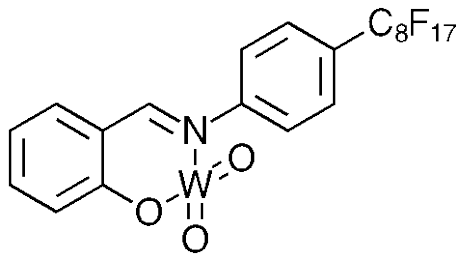

Figure 4.18. Proposed structure of tungsten Schiff base complex

The proton NMR spectrum corroborated the evidence that the synthesized molecule was the above structure with peaks observed in expected places; N=CH (9.20ppm); C-H (Ar) (7.25-7.00ppm); C-H (Ar-CF) (8.28-5.86ppm). These values agree with other values reported for similar tungsten Schiff base complexes (Zhou, 2004). The lack of O-H peak in the ^{1}H NMR results shows that the ligand did indeed

coordinate to the metal. The FT-IR, ^{1}H NMR, and spectra can be found in the appendix.

4.5. Characterization of oxime ligands

Two oxime ligands were synthesized, one with less difficulty than the other. The spectral data collected matched what was expected based on data published for similar molecules (Kim, 1992). Ox2 is reported for the first time, as far as the author is aware. The data for ox1 agrees with what was reported in its prior synthesis (Kim et al, 1992). The proposed structural data is found in Figure 4.5. The IR and ^{1}H NMR data for the synthesized oxime ligands is summarized in Tables 4.5.1 and 4.5.2. The oxime ligands decomposed slowly at room temperature; therefore, they were kept refrigerated. They were soluble in common organic solvents, such as ethanol, DMSO, and THF.

Table 4.10. Summary of IR data for oxime ligands

	IR				
	C-H	C=N	O-H	N-O	C-F
Ox1	2938-2762	1643	3132	1390	1212, 1173, 1143
Ox2	2981-2739	1624	3348	1379	1173, 1150, 1124

Table 4.11. Summary of ^{1}H NMR data for oxime ligands

	^{1}H NMR		
	O-H	CH2	CH3
ox1	4.45(b, 1H)	3.33(d, 1H), 3.07(d, 1H)	2.06(s, 3Hs)
ox2	8.33(b, 1H)	3.43(d, 1H), 3.15(d, 1H)	1.17(m, 9Hs)

4.5.1. 1,1,1-trifluoro-2,4-pentanedione 2-oxime [ox1]

Ox1 was synthesized. However, its synthesis was somewhat arduous and produced a low yield after purification processes. The elemental analysis was accurate to what was expected. Infrared peaks showing C=N bonds (1643cm^{-1}), C-F bonds (1212, 1173, 1143cm^{-1}), C-O bonds (1390cm^{-1}) and O-H bonds (3132cm^{-1}) were observed. A separate peak for the C=O and C=N peak would have been expected in the 1600-1700cm^{-1} range. This was not observed; therefore, a new structure is proposed for the solid state.

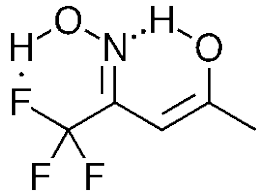

Figure 4.19. Proposed structure for ox1 in solid state

The proton NMR spectrum, in liquid phase, corroborated the evidence that the synthesized molecule was the originally proposed structure, with peaks observed in expected places: O-H (4.45ppm); C-H (aliphatic) (3.07, 2.06ppm). These values agree with values previously reported for this ligand (Kim et al, 1997). The ^{13}C NMR spectrum also supported the proposed structure with peaks corresponding to the five carbons (C=O 157, CF_3 121, C=N-O 102, CH_2 77, CH_3 46). The FT-IR, ^{1}H NMR and ^{13}C NMR spectra can be found in the appendix.

4.5.2. 1,1,1-trifluoro-5,5-dimethylhexane-2,4-dione 2-oxime [ox2]

Ox2 was synthesized without difficulty and in acceptable yield. Infrared peaks C=N bonds (1624cm^{-1}), C-F bonds (1173, 1150, 1124cm^{-1}), C-O bonds (1379cm^{-1}) and O-H bonds (3348cm^{-1}) were observed. A separate peak for the C=O and C=N peak would have been expected in the 1600-1700cm^{-1} range. This was not observed; therefore, a new structure is proposed for the solid state.

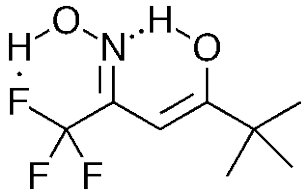

Figure 4.20. Proposed structure for ox2 in solid state

The proton NMR spectrum, in liquid phase, corroborated the evidence that the synthesized molecule was the originally proposed structure, with peaks observed in expected places; O-H (8.33ppm); and C-H (aliphatic) (3.43-1.17ppm). These values agree with values reported for similar oxime ligands. The FT-IR and ^{1}H NMR spectra can be found in the appendix.

4.6. Characterization of nickel oxime complexes

The nickel oxime complexes were synthesized without difficulty and generally in good yield. The spectral data collected matched what was expected based on data published for similar molecules (Martinez et al, 2013). All synthesized nickel oxime complexes are reported for the first time, as far as the author is aware. The proposed structural data is found in Figure 4.6. The IR and ^{1}H NMR data for the synthesized complexes is summarized in Tables 4.6.1 and 4.6.2. All the complexes were stable at room temperature and soluble in common organic solvents, such as ethanol, DMSO, and THF.

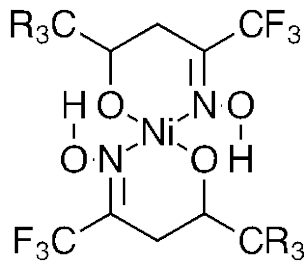

Ni-ox1: R=H
Ni-ox2: R=CH_3

Figure 4.21. Proposed general structure for nickel oxime complexes

Table 4.12. Comparison of IR data from oxime ligands and their nickel complexes

	IR					
molecule	C-H	C=N	O-H	C-O	C-F	Ni-N
ox1	2938-2762	1643	3132	1390	1212, 1173, 1143	-
Ni-ox1	2941-2801	1623	3147	1389	1217, 1147	528
ox2	2981-2739	1624	3348	1379	1173, 1150, 1124	-
Ni-ox2	2979-2872	1559	3131	1370	1176, 1152,1125	529

Table 4.13. Comparison of ^{1}H NMR data from oxime ligands and their nickel complexes

	H NMR		
molecule	O-H	CH2	CH3
ox1	4.45(b, 1H)	3.33(d, 1H), 3.07(d, 1H)	2.06(s, 3H)
Ni-ox1	4.78(b, 2Hs)	3.33(d, 2Hs), 3.03(d, 2Hs)	2.04(s, 6Hs)
ox2	8.33(b, 1H)	3.43(d, 1H), 3.15(d, 1H)	1.17(m, 9Hs)
Ni-ox2	8.56 (b, 2Hs)	3.42(d, 2Hs) 3.17(d, 2Hs)	1.18(m, 18Hs)

4.6.1. Nickel (II) 1,1,1-trifluoro-2,4-pentanedione 2-oxime [Ni-ox1]

Ni-ox1 was synthesized in good yield, but with significant difficulty. Infrared peaks showing C-O bonds (1389cm^{-1}), C-F bonds (1217, 11747cm^{-1}) and C=N bonds (1623cm^{-1}) were observed. Also, a new peak from the Ni-N bond appeared at 528cm^{-1}, where Ni-N bonds are reported to appear in similar complexes. A broad O-H peak was observed, as expected. As a result of back bonding from the metal, a noticeable shift in the C=N bond (from 1643 to 1623cm^{-1}) shows that the nickel bonded to the ligand. This shift shows the weakening of the C=N bond as the carbon π^* orbitals accepted electrons from the metal center.

The proton NMR spectra corroborated the evidence that the synthesized molecule was the desired structure with peaks observed in expected places: O-H (4.78ppm); and C-H (aliphatic) (3.33-2.04ppm). These values agree with other values reported for similar nickel oxime complexes. The number of hydrogen atoms

and the lack of characteristic acetate peaks in the spectra also corroborated that two ligands replaced the acetate ligands that were on the nickel.

4.6.2. Nickel (II) 1,1,1-trifluoro-5,5-dimethylhexane-2,4-dione 2-oxime [Ni-ox2]

Ni-ox2 was synthesized without difficulty in excellent yield. Infrared peaks showing C-O bonds (1370cm^{-1}), C-F bonds (1206, 1176, 1152cm^{-1}) and C=N bonds (1559cm^{-1}) were observed. Also, a new peak from the Ni-N bond appeared at 529cm^{-1}, where Ni-N bonds are reported to appear in similar complexes. A broad O-H peak was observed, as expected. As a result of back bonding from the metal, a noticeable shift in the C=N bond (from 1624 to 1559cm^{-1}) shows that the nickel bonded to the ligand. This shift shows the weakening of the C=N bond as the carbon π^* orbitals accepted electrons from the metal center. The shift is somewhat more than would be expected. It is hypothesized that the C=N peak is overlapped with another, larger peak causing it to appear to have shifted so dramatically.

The proton NMR spectra corroborated the evidence that the synthesized molecule was the desired structure with peaks observed in expected places: O-H (8.56ppm); and C-H (aliphatic) (3.42-1.18ppm). These values agree with other values reported for similar nickel oxime complexes. The number of hydrogen atoms and the lack of characteristic acetate peaks in the spectra also corroborated that two ligands replaced the acetate ligands that were on the nickel. The FT-IR and ^{1}H NMR spectra can be found in the appendix.

4.7. Characterization of palladium oxime complexes

The palladium oxime complexes were synthesized without difficulty and generally in good yield. The spectral data collected matched what was expected based on data published for similar molecules (Trendafilova et al, 1999). All synthesized palladium oxime complexes are reported for the first time, as far as the author is aware. The proposed structural data is found in Figure 4.7. The IR and ^{1}H NMR data for the synthesized complexes is summarized in Tables 4.7.1 and 4.7.2.

All the complexes were stable at room temperature and soluble in common organic solvents, such as ethanol, DMSO and THF.

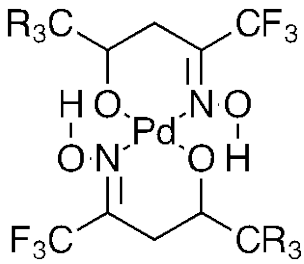

Pd-ox1: R=H
Pd-ox2: R=CH_3

Figure 4.22. Proposed general structure for palladium oxime complexes

Table 4.14. Comparison of IR data from oxime ligands and their palladium complexes

	IR					
molecule	C-H	C=N	O-H	C-O	C-F	Pd-N
ox1	2938-2762	1643	3132	1390	1212, 1173, 1143	-
Pd-ox1	2987-2901	1622	3300	1392	1176	581
ox2	2981-2739	1624	3348	1379	1173, 1150, 1124	-
Pd-ox2	2988-2872	1616	3458, 3174	1369	1176, 1152,1125	581

Table 4.15. Comparison of ^{1}H NMR data from oxime ligands and their palladium complexes

	H NMR		
molecule	O-H	CH2	CH3
ox1	4.45(b, 1H)	3.33(d, 1H), 3.07(d, 1H)	2.06(s, 3H)
Pd-ox1	4.91(b, 2Hs)	3.35(d, 2Hs), 3.08(d, 2Hs)	2.31(s, 6Hs)
ox2	8.33(b, 1H)	3.43(d, 1H), 3.15(d, 1H)	1.17(m, 9Hs)
Pd-ox2	8.56 (b, 2Hs)	3.45(d, 2Hs) 3.17(d, 2Hs)	1.18(m, 18Hs)

4.7.1. Palladium (II) 1,1,1-trifluoro-2,4-pentanedione 2-oxime [Pd-ox1]

Pd-ox1 was synthesized without difficulty, but in poor yield. Infrared peaks showing C-O bonds (1392cm^{-1}), C-F bonds (1176, 1128cm^{-1}) and C=N bonds (1622cm^{-1}) were observed. Also, a new peak from the Pd-N bond appeared at 581cm^{-1}, where Pd-N bonds are reported to appear in similar complexes (Trendafilova et al, 1999). A broad O-H peak was observed, as would be expected in the complex form. As a result of back bonding from the metal, a noticeable shift in the C=N bond (from 1643 to 1622cm^{-1}) shows that the palladium bonded to the ligand. This shift shows the weakening of the C=N bond as the carbon π^* orbitals accept electrons from the metal center.

The proton and fluorine NMR spectra corroborated the evidence that the synthesized molecule was the desired structure with peaks observed in expected places: O-H (4.91ppm); and C-H (aliphatic) (3.35-2.31ppm). These values agree with other values reported for similar palladium oxime complexes. The FT-IR spectrum can be found in the appendix.

4.7.2. Palladium (II) 1,1,1-trifluoro-5,5-dimethylhexane-2,4-dione 2-oxime [Pd-ox2]

Pd-ox2 was synthesized without difficulty and in good yield. Infrared peaks showing C-O bonds (1369cm^{-1}), C-F bonds (1204, 1176, 1141cm^{-1}) and C=N bonds (1616cm^{-1}) were observed. Also, a new peak from the Pd-N bond appeared at 581cm^{-1}, where Pd-N bonds are reported to appear in similar complexes. A broad O-H peak was observed, as would be expected in the complex form. As a result of back bonding from the metal, a noticeable shift in the C=N bond (from 1624 to 1616cm^{-1}) shows that the palladium bonded to the ligand. This shift shows the weakening of the C=N bond as the carbon π^* orbitals accept electrons from the metal center.

The proton and fluorine NMR spectra corroborated the evidence that the synthesized molecule was the desired structure with peaks observed in expected places: O-H (8.30ppm); and C-H (aliphatic) (3.43-1.17ppm). These values agree

with other values reported for similar palladium oxime complexes. The FT-IR and ^{1}H NMR spectra can be found in the appendix.

4.8. Characterization of tungsten oxime complex

The tungsten oxime complex was synthesized without difficulty but with poor yield. The spectral data collected matched what was expected based on data published for similar molecules (Gharah et al, 2009). This tungsten oxime complex is reported for the first time, as far as the author is aware. The IR and ^{1}H NMR data for the synthesized complex is summarized in Tables 4.8.1 and 4.8.2. The complex was stable at room temperature and soluble in common organic solvents, such as ethanol, DMSO, and THF.

Table 4.16. Comparison of IR data from oxime ligands and its tungsten complex

	IR					
Molecule	C-H	C=N	O-H	C-O	C-F	W-N
ox1	2938-2762	1643	3132	1390	1212, 1173, 1143	-
W-ox1	2946-2828	1625	3191	1389	1178, 1130	581

Table 4.17. Comparison of ^{1}H NMR data from oxime ligands and its tungsten complex

	^{1}H NMR		
Molecule	O-H	CH_2	CH_3
ox1	4.45(b, 1H)	3.33(d, 1H), 3.07(d, 1H)	2.06(s, 3Hs)
W-ox1	4.57(b, 1H)	3.57(m, 1H), 3.22(m, 1H)	2.32(s, 3Hs)

4.8.1. Tungsten (VI) 1,1,1-trifluoro-2,4-pentanedione 2-oxime [W-ox1]

W-ox1 was synthesized without difficulty, but in poor yield. Infrared peaks showing C-O bonds (1389cm^{-1}), C-F bonds (1178, 1130cm^{-1}) and C=N bonds (1625cm^{-1}) were observed. Also, a new peak from the W-N bond appeared at 581cm^{-}

[1], where W-N bonds are reported to appear in similar complexes (Gharah et al, 2009). A broad O-H peak was observed, as would be expected in the complex form. As a result of back bonding from the metal, a noticeable shift in the C=N bond (from 1643 to 1625cm^{-1}) shows that the tungsten bonded to the ligand. This shift shows the weakening of the C=N bond as the carbon π^* orbitals accepted electrons from the metal center.

The proton NMR spectra corroborated the evidence that the synthesized molecule was the desired structure with peaks observed in expected places: O-H (4.57ppm) and C-H (aliphatic) (3.57-2.32ppm). These values agree with other values reported for similar tungsten oxime complexes (Gharah et al, 2009). The FT-IR spectrum can be found in the appendix.

4.9. Solubility of compounds in $scCO_2$

In order for a precursor to be suitable for deposition in an $scCO_2$ medium, it needs be soluble in $scCO_2$. It has been shown that complexes with fluorine in them are more soluble than those without. (Erkey, 2012) However, if a complex is too soluble, that can also hinder the deposition. (Zhang and Erkey, 2006) Therefore, solubility within a specific range is desired. In this study, all of the metal complexes were qualitatively determined to be soluble in $scCO_2$. The ratio of fluorine atoms to molecular weight in each complex was varied to provide a spectrum of solubilities.

A representative molecule, Pd-SB1, was used to determine the approximate quantitative solubility of the molecules in $scCO_2$. It was determined to have a solubility of 0.000178 g/mL. This value is in agreement with previously reported values for solubility of fluorous molecules in $scCO_2$ (Smart, 1997). Other complexes with less fluorine atoms are expected to be less soluble in the medium, based on previously published research (Smart, 1997).

4.10. Deposition of nanoparticle metals on MWCNTs

The M/MWCNT composites were studied using scanning electron microscopy (SEM). The SEM images were taken to determine the distribution of the particles on the substrate as well as to determine the amount of the metal present on the nanotubes. The nanoparticle metals in this study showed an even distribution and with the exception of three composites (all Pd/MWCNT), no metal clusters were observed.

The XRD results showed that the mean size of the metal particles ranged from 1.9-4.0nm for nickel, 3.8-13.8nm for palladium and 0.9-3.0nm for tungsten.

4.10.1. Nickel precursors

The seven successfully synthesized nickel precursors were dissolved in $scCO_2$ and then attached to MWCNTs. After an hour had passed for the completion of this reaction, the precursors were reduced to their metallic forms in the presence of H_2 gas. Nickel is stable in its metallic form, so was able to be adsorbed on the solid substrate in its metallic form; this was verified by XRD. The XRD measurements were taken at 2θ angles be between 10 and 80°. The most common peaks were observed around 43° (2.0 Å) and 52° (1.75 Å), corresponding to Ni(111) and Ni(200) respectively. The X-ray pattern of the MWCNT displays the presence of two peaks around 25° (3.5 Å) and 43° (2.0 Å). These are assigned to diffractions resulting from the interlayer spacing of the nanotube (002) and reflection of the carbon atoms (100). These values are in good agreement with that of the previously reported values. The peak corresponding to nickel at 43° overlapped with the peak corresponding to the CNT at the same spot, making interpretation of that peak complex. Therefore, the peak corresponding to Ni(200) was used for analysis of the nickel nanoparticle metals. Previous studies have reported nickel nanoparticles as small as 25nm (Bozbağ et al, 2012), the average size of nickel nanoparticles reported in this study ranges from 1.9- 4.0nm.

4.10.1.1. Deposition of Ni-SB1 on MWCNTs

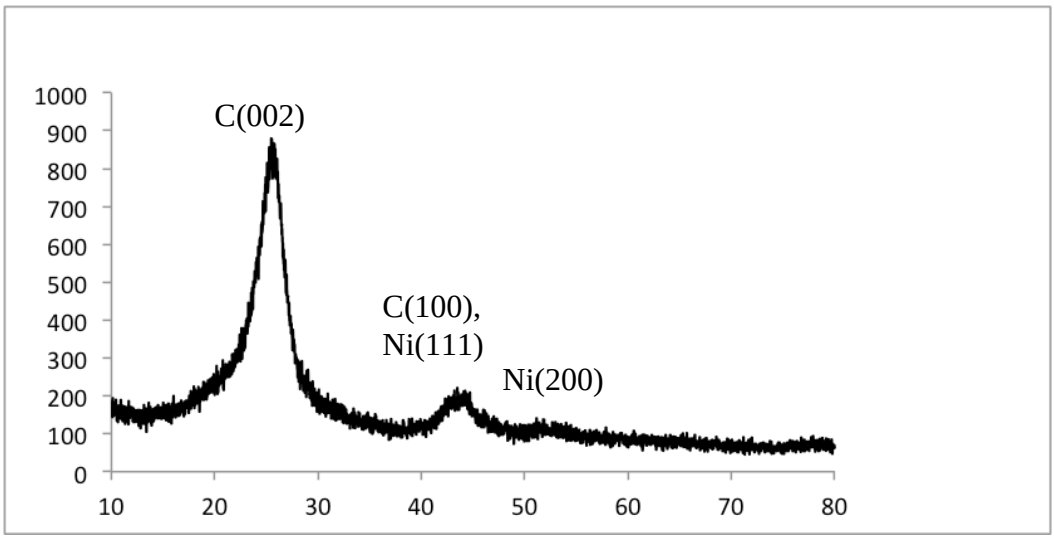

Figure 4.23. XRD image of Ni-SB1 deposited on MWCNTs

From the XRD, the size of the particles was determined according to the Scherrer equation. These values are given in the table below.

Table 4.18. XRD results for Ni-SB1

No.	2Theta(deg)	D (A)	Height(cps)	Int. I(cps deg)	FWHM(deg)	Size (A)
1	25.65(3)	3.471(4)	777(36)	3799(17)	3.09(4)	27.5(3)
2	43.99(10)	2.057(5)	89(12)	323(11)	3.00(10)	29.9(19)
3	**52.3(7)**	**1.75(2)**	**9(4)**	**23(9)**	**2.3(6)**	**40(10)**

Calculations were done based on the peak observed at 52.3°, belonging to Ni (200). The mode size of the nanoparticle metals was calculated to be 4.0 nm.

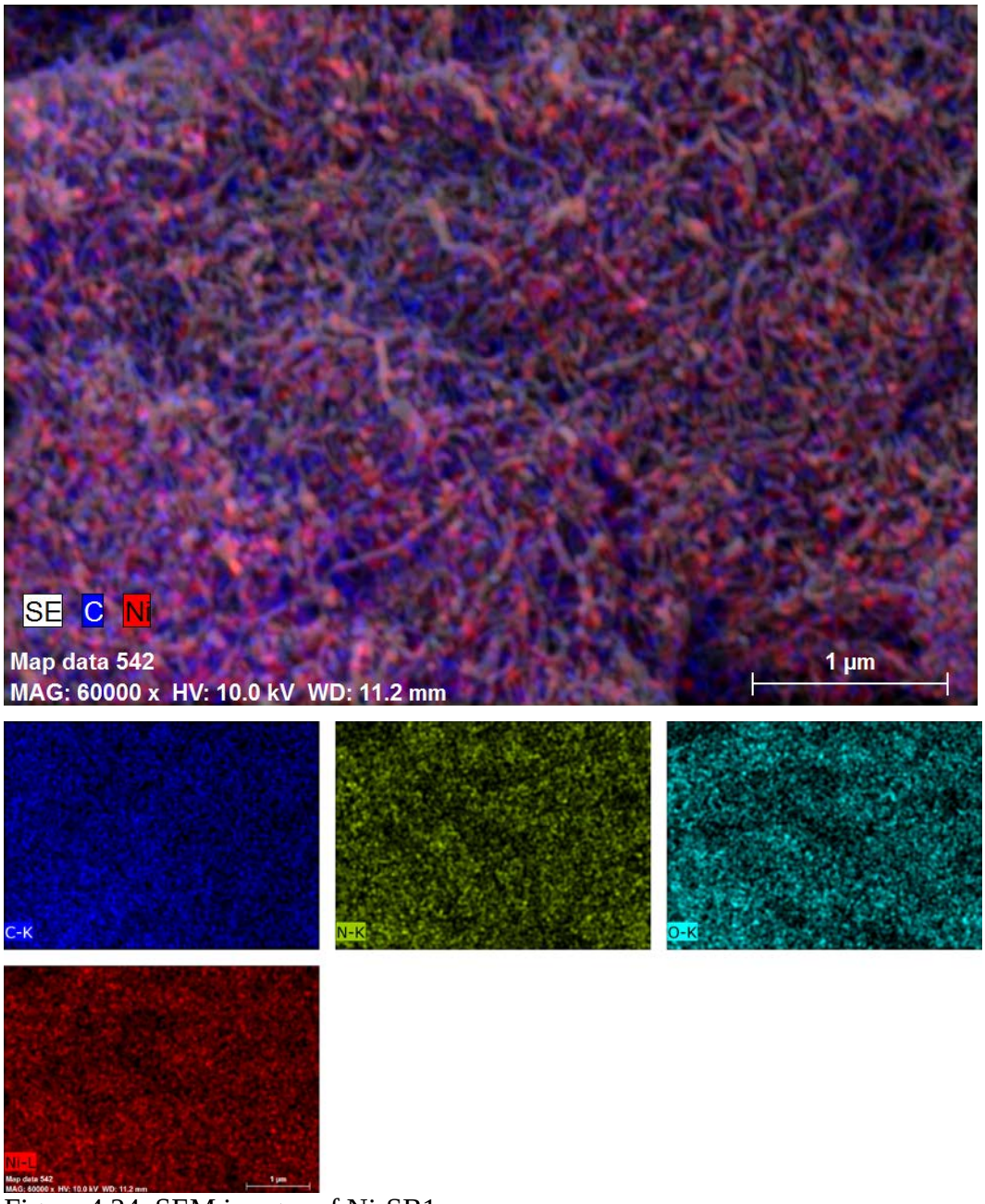

Figure 4.24. SEM images of Ni-SB1

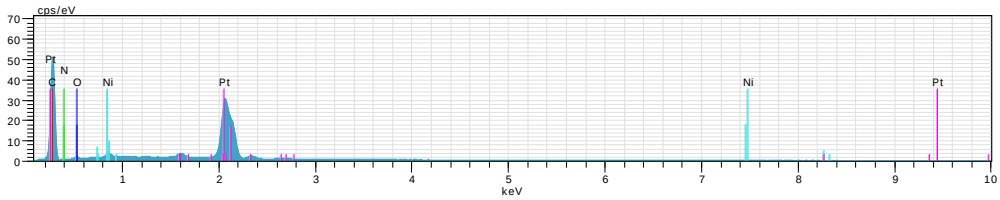

Figure 4.25. Point map of Ni-SB1 on MWCNT

Table 4.19. EDX point values for Ni-SB1

El AN	Series	Unn. C	norm. C	Atom. C	Error(1sigma)
Pt 78	M-series	43.95	47.37	5.47	1.69
C 6	K-series	43.83	47.24	88.59	4.77
Ni 28	L-series	1.80	1.94	0.75	0.27
O 8	K-series	1.65	1.78	2.50	0.27
N 7	K-series	1.55	1.67	2.69	0.29

Using the SEM EDX spectra, the percentage of metal adsorbed was calculated to be 3.69%. In Figure 4.10.1.2 the red is representative of the nickel metal and the blue is representative of the carbon from the nanotubes, turquoise and green represent impurities from oxygen and nitrogen, respectively, that were present in the precursor. From observing the images, it can be seen that the metal nanoparticles are distributed evenly with no visible metal clusters.

4.10.1.2. Deposition of Ni-SB2 on MWCNTs

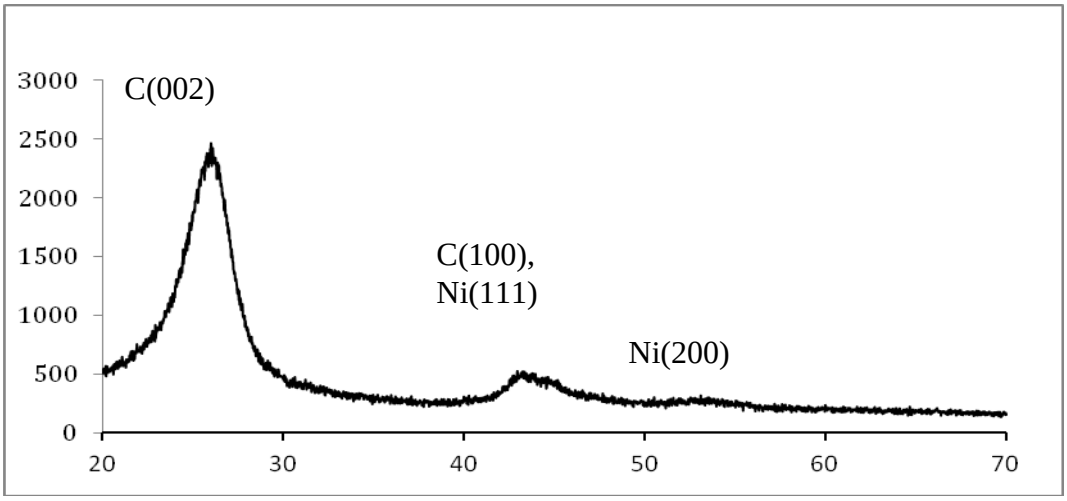

Figure 4.26. XRD image of Ni-SB2 deposited on MWCNTs

Table 4.20. XRD results for Ni-SB2

No.	2-theta(deg)	d (A)	Height(cps)	Int. I(cps deg)	FWHM(deg)	Size
1	26.22(2)	3.397(3)	1071(30)	4366(20)	3.092(19)	27.55(17)
2	43.43(7)	2.082(3)	117(10)	516(10)	3.46(8)	25.8(6)

The XRD did not recognize the peak corresponding to Ni(200). This is postulated to be because the size of the nanoparticle metals was small. From the SEM results shown below, it was determined that deposition did occur.

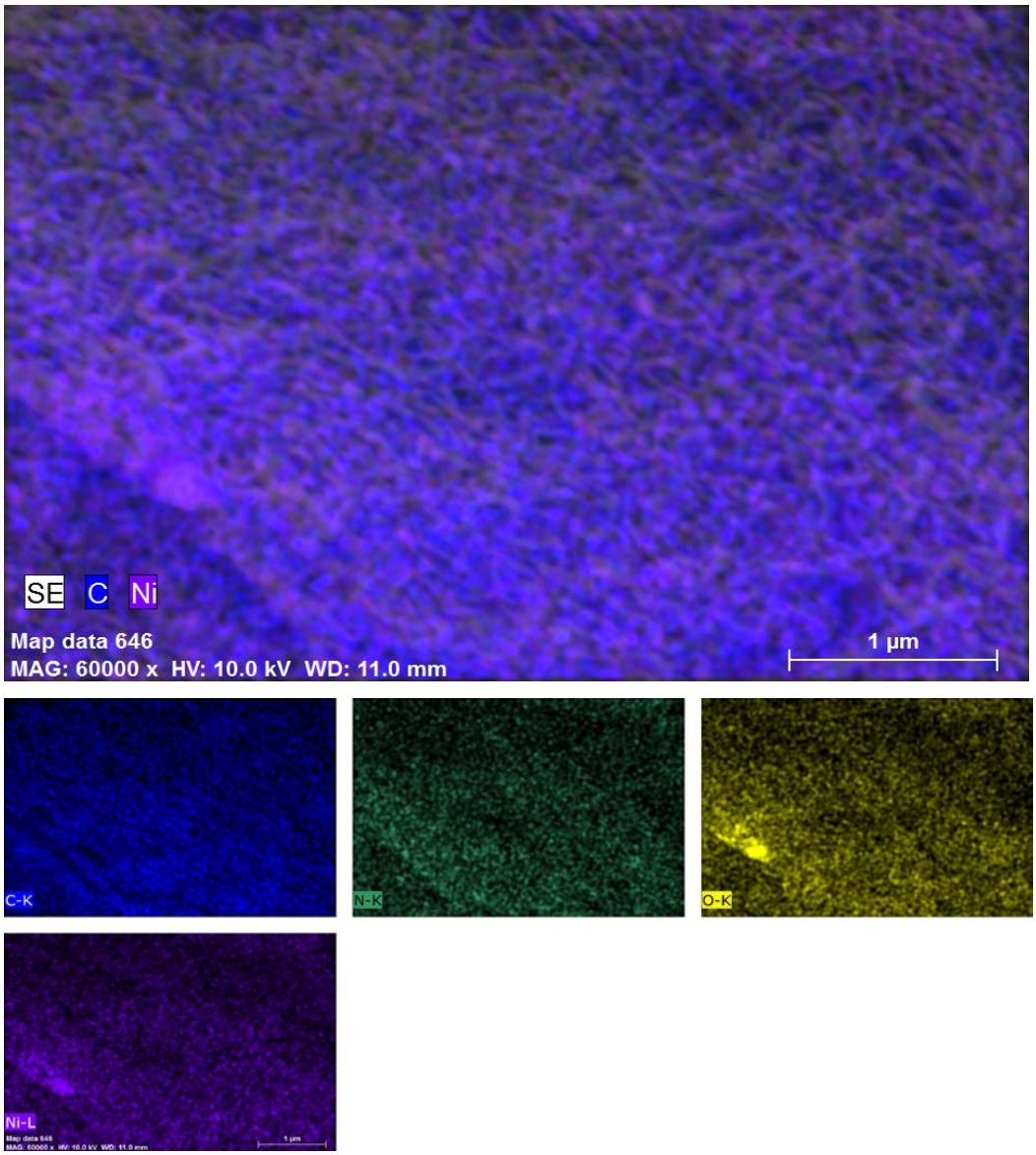

Figure 4.27. SEM images of Ni-SB2

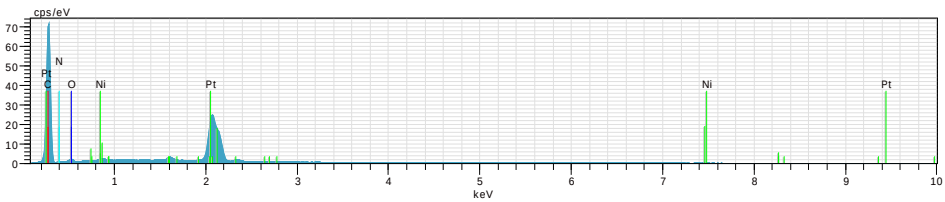

Figure 4.28. Point map of Ni-SB2 on MWCNT

Table 4.21. EDX point values for Ni-SB2

El AN	Series	Unn. C	norm. C	Atom. C	Error(1sigma)
C 6	K-series	50.51	58.32	91.59	5.42
Pt 78	M-series	32.10	37.07	3.58	1.24
O 8	K-series	1.71	1.98	2.33	0.27
N 7	K-series	1.39	1.60	2.16	0.26
Ni 28	L-series	0.90	1.04	0.33	0.15

Using the SEM EDX spectra, the percentage of metal adsorbed was calculated to be 1.65%. In Figure 4.10.2.2 the purple is representative of the nickel metal and the blue is representative of the carbon from the nanotubes, yellow and green represent impurities from oxygen and nitrogen, respectively, that were present in the precursor. From observing the images, it can be seen that the metal nanoparticles are distributed evenly with no visible metal clusters.

4.10.1.3. Deposition of Ni-SB3 on MWCNTs

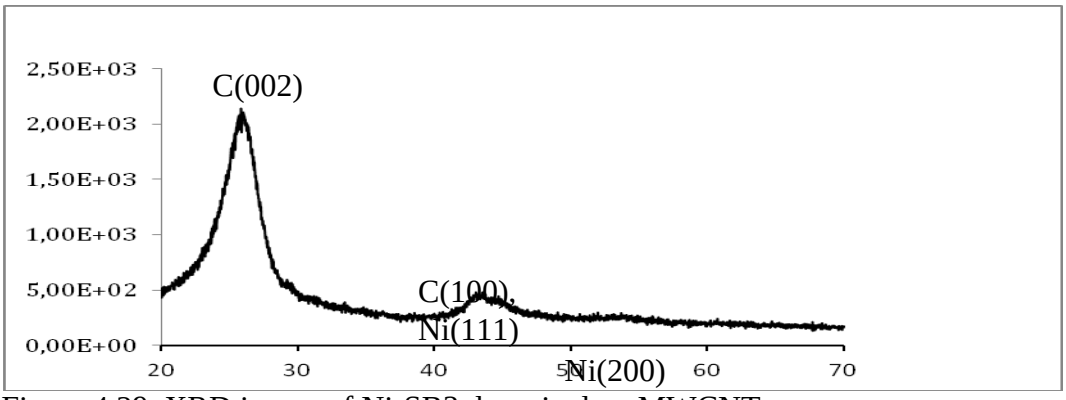

Figure 4.29. XRD image of Ni-SB3 deposited on MWCNTs

Table 4.22. XRD results for Ni-SB3

No.	2-theta(deg)	d (A)	Height(cps)	Int. I(cps deg)	FWHM(deg)	Size
3	26.13(2)	3.408(3)	918(28)	3981(19)	3.11(2)	27.4(2)
4	43.26(8)	2.090(4)	104(9)	470(10)	3.27(10)	27.3(8)

The XRD did not recognize the peak corresponding to Ni(200). This is postulated to be because the size of the nanoparticle metals was small. From the

SEM results shown below, it was determined that a small amount of deposition did occur.

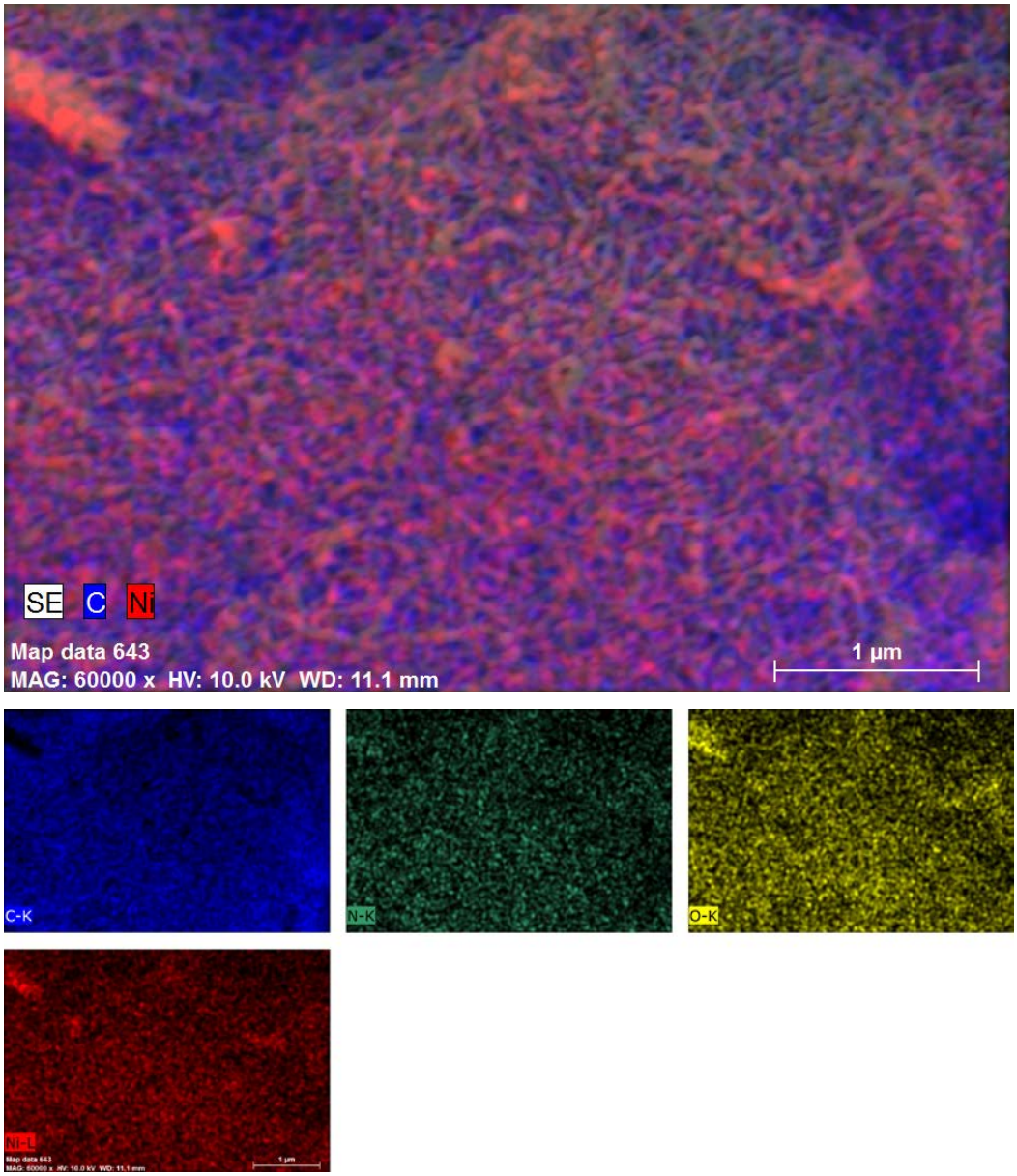

Figure 4.30. SEM images of Ni-SB3

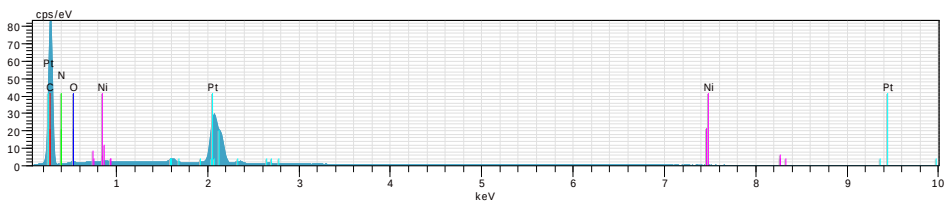

Figure 4.31. Point map of Ni-SB3 on MWCNT

Table 4.23. EDX point values for Ni-SB3

El AN	Series	Unn. C	norm. C	Atom. C	Error(1sigma)
C 6	K-series	56.94	57.79	90.88	6.08
Pt 78	M-series	36.73	37.28	3.61	1.42
N 7	K-series	2.14	2.17	2.92	0.36
O 8	K-series	1.95	1.98	2.33	0.30
Ni 28	L-series	0.78	0.79	0.25	0.14

Using the SEM EDX spectra, the percentage of metal adsorbed was calculated to be 1.26%. In Figure 4.10.1.3.2 the red color is representative of the nickel metal and the blue is representative of the carbon from the nanotubes, yellow and green represent impurities from oxygen and nitrogen, respectively, that were present in the precursor. From observing the images, it can be seen that the metal nanoparticles are distributed evenly with no visible metal clusters.

4.10.1.4. Deposition of Ni-SB4 on MWCNTs

Ni-SB4 was not successfully synthesized; therefore no Ni/MWCNT composite was analyzed.

4.10.1.5. Deposition of Ni-SB5 on MWCNTs

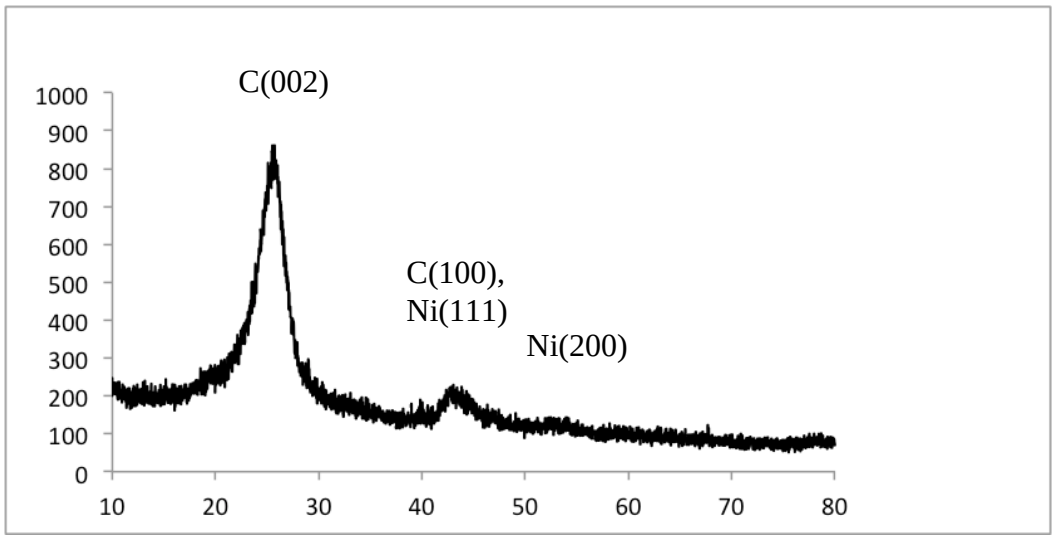

Figure 4.32. XRD image of Ni-SB5 deposited on MWCNTs

Table 4.24. XRD results for Ni-SB5

No.	2Theta(deg)	D (A)	Height(cps)	Int. I(cps deg)	FWHM(deg)	Size (A)
12	25.65(3)	3.470(4)	712(34)	3395(17)	3.12(3)	27.3(3)
13	43.17(12)	2.094(6)	69(11)	228(11)	3.06(11)	29.1(10)

The XRD did not recognize the peak corresponding to Ni(200). This is postulated to be because the size of the nanoparticle metals was small. From the SEM results shown below, it was determined that deposition did occur.

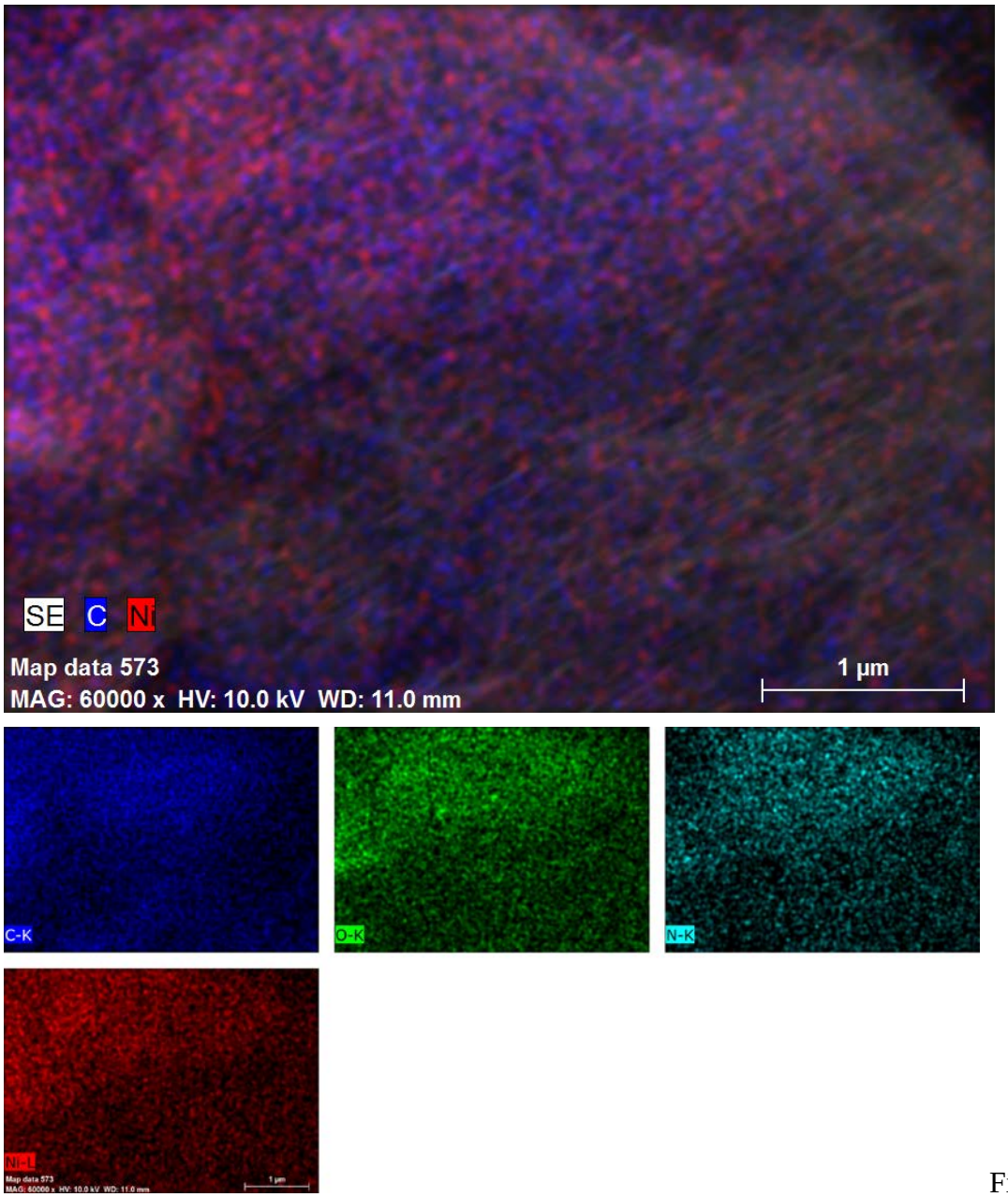

Fig
Figure 4.33. SEM images of Ni-SB5

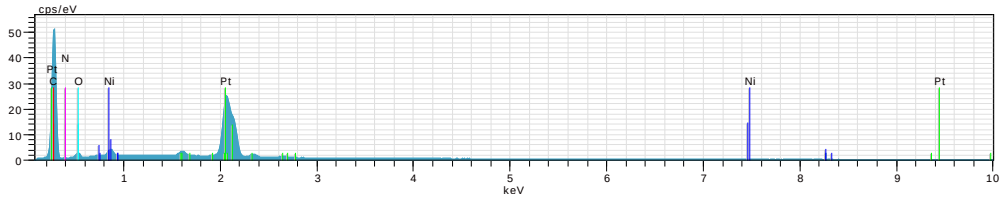

Figure 4.34. Point map of Ni-SB5 on MWCNT

Table 4.25. EDX point values for Ni-SB5

El AN	Series	Unn. C	norm. C	Atom. C	Error(1sigma)
Pt 78	M-series	41.96	42.67	4.65	1.62
C 6	K-series	48.55	49.37	87.39	5.28
Ni 28	L-series	3.03	3.08	1.12	0.41

Using the SEM EDX spectra, the percentage of metal adsorbed was calculated to be 5.37%. In Figure 4.10.1.5.2 the red color is representative of the nickel metal and the blue is representative of the carbon from the nanotubes, green and turquoise represent impurities from oxygen and nitrogen, respectively, which were present in the precursor. From observing the images, it can be seen that the metal nanoparticles are distributed evenly with no visible metal clusters.

4.10.1.6. Deposition of Ni-SB6 on MWCNTs

Ni-SB6 was not successfully synthesized; therefore no Ni/MWCNT composite was analyzed.

4.10.1.7. Deposition of Ni-SB7 on MWCNTs

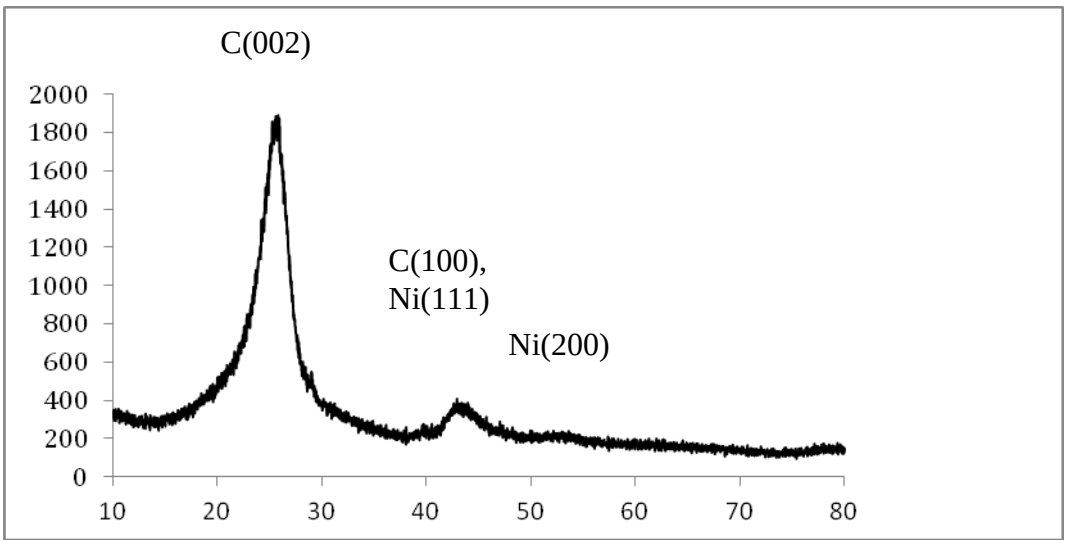

Figure 4.35. XRD image of Ni-SB7 deposited on MWCNTs

From the XRD, the size of the particles was determined according to the Scherrer equation. These values are given in the table below.

Table 4.26. XRD results for Ni-SB7

No.	2Theta(deg)	D (A)	Height(cps)	Int. I(cps deg)	FWHM(deg)	Size (A)
19	25.68(2)	3.466(3)	878(27)	4433(16)	3.14(3)	27.1(3)
20	43.58(9)	2.075(4)	81(8)	319(8)	2.91(11)	30.7(11)
21	**53.4(4)**	**1.714(10)**	**9(3)**	**42(6)**	**3.6(5)**	**26(3)**

Calculations were done based on the peak observed at 53.4 degrees, belonging to Ni (200). The mode size of the nanoparticle metals was calculated to be 2.6 nm.

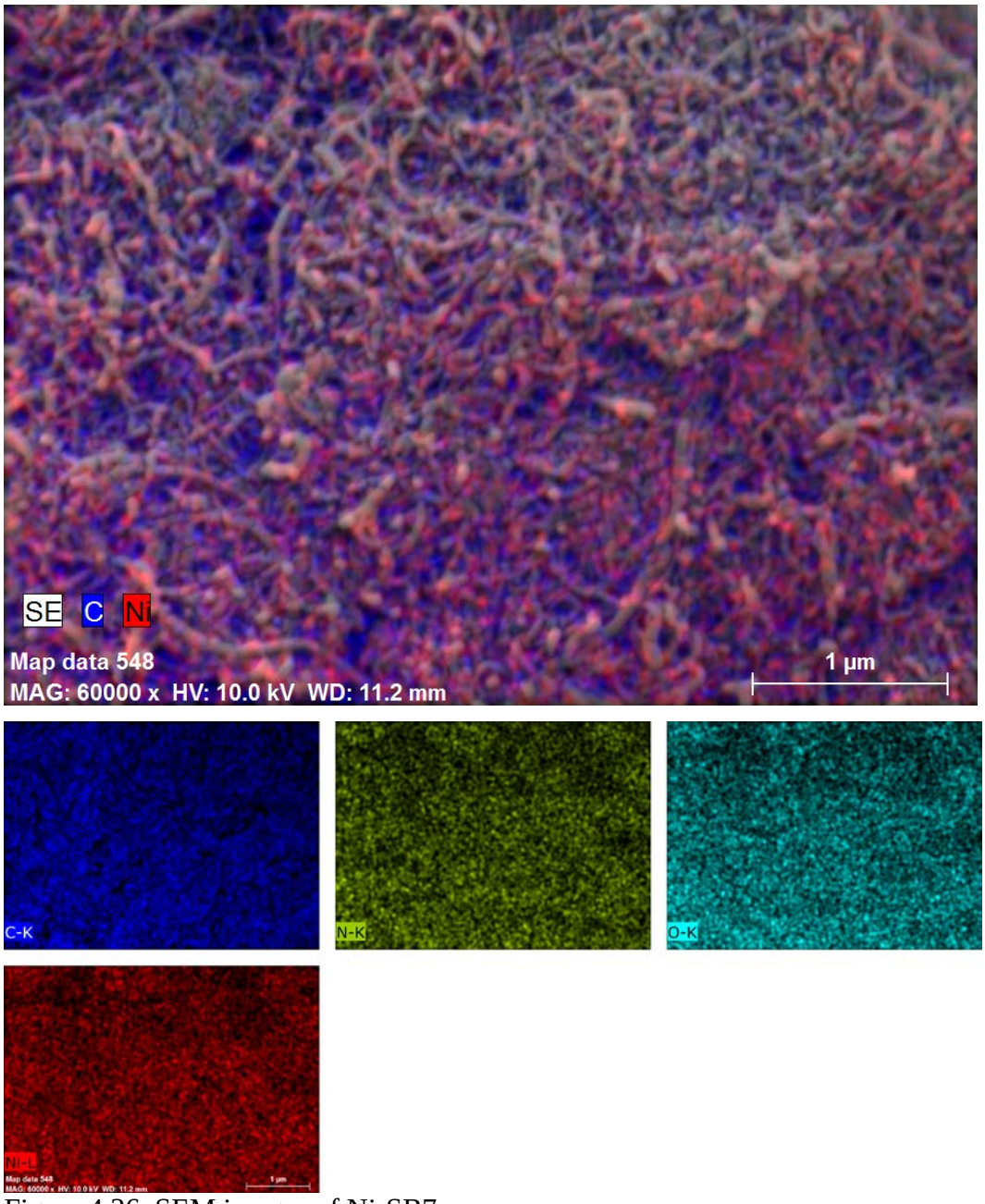

Figure 4.36. SEM images of Ni-SB7

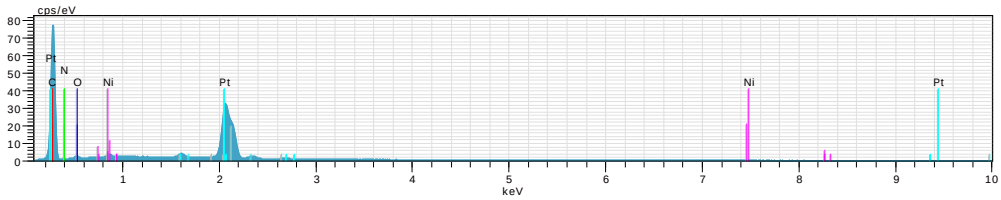

Figure 4.37. Point map of Ni-SB7 on MWCNT

Table 4.27. EDX point values for Ni-SB7

El AN	Series	Unn. C	norm. C	Atom. C	Error(1sigma)
Pt 78	M-series	36.57	40.55	4.16	1.62
C 6	K-series	48.49	53.77	89.56	5.20
N 7	K-series	1.99	2.21	3.15	0.33
O 8	K-series	1.93	2.14	2.67	0.29
Ni 28	L-series	1.21	1.34	0.46	0.19

Using the SEM EDX spectra, the percentage of metal adsorbed was calculated to be 2.25%. In Figure 4.10.1.6.2 the red color is representative of the nickel metal and the blue is representative of the carbon from the nanotubes, turquoise and green represent impurities from oxygen and nitrogen, respectively, that were present in the precursor. From observing the images, it can be seen that the metal nanoparticles are distributed evenly with no visible metal clusters

4.10.1.8. Deposition of Ni-ox1 on MWCNTs

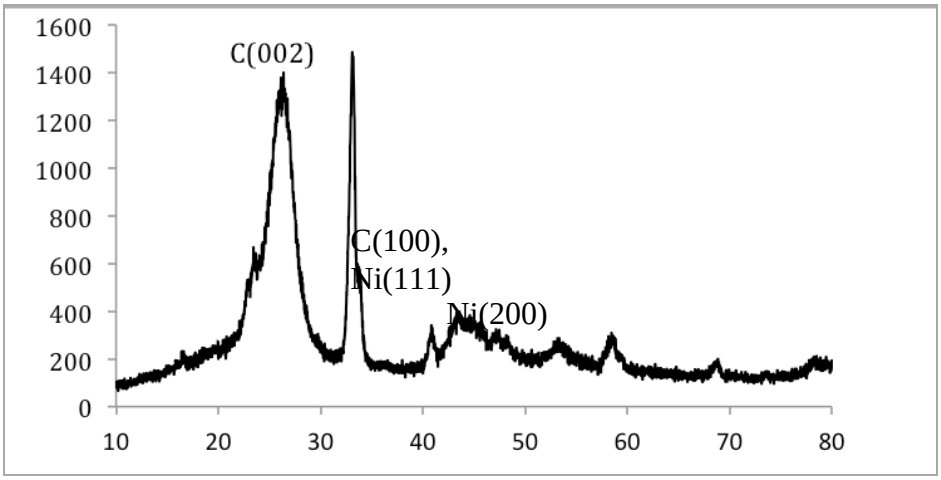

Figure 4.38. XRD image of Ni-ox1 deposited on MWCNTs

From the XRD, the size of the particles was determined according to the Scherrer equation. These values are given in the table below.

Table 4.28. XRD results for Ni-ox1

No.	2Theta(deg)	D (A)	Height(cps)	Int. I(cps deg)	FWHM(deg)	Size (A)
1	26.858(14)	3.3167(17)	578(22)	2121(18)	2.75(3)	31.0(3)
2	33.141(12)	2.7009(10)	695(24)	513(12)	0.646(16)	134(3)
3	33.79(3)	2.650(2)	170(12)	95(9)	0.47(4)	185(17)
4	43.12(5)	2.096(3)	62(7)	167(13)	2.18(17)	41(3)
5	**53.2(3)**	**1.719(8)**	**23(4)**	**103(11)**	**2.4(5)**	**39(8)**
6	58.31(6)	1.5812(15)	57(7)	90(4)	1.48(5)	64(2)
7	68.73(9)	1.3646(15)	30(5)	24(3)	0.74(7)	137(13)

Calculations were done based on the peak observed at 53.2 degrees, belonging to Ni (200). The mode size of the nanoparticle metals was calculated to be 3.9 nm.

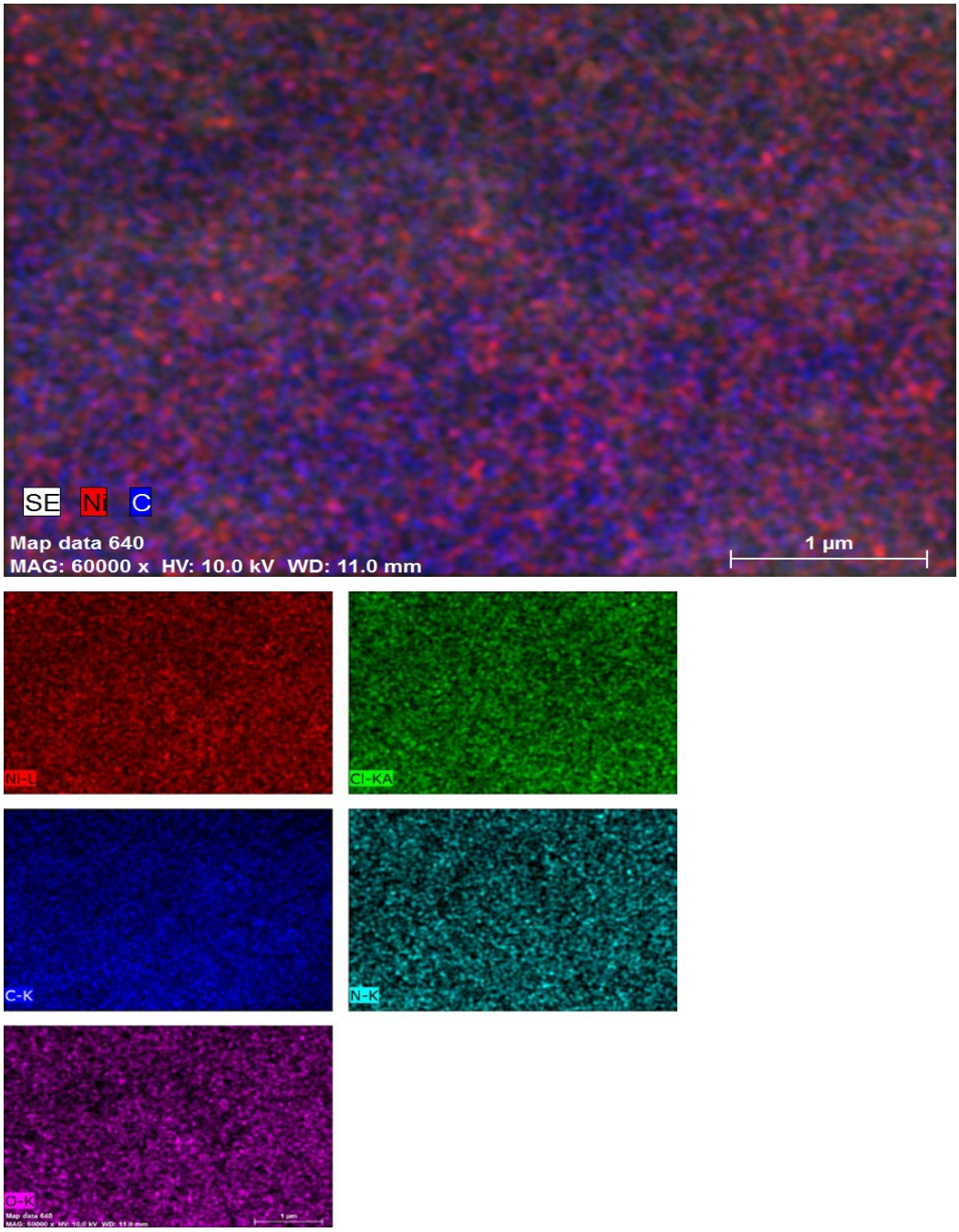

Figure 4.39. SEM images of Ni-ox1

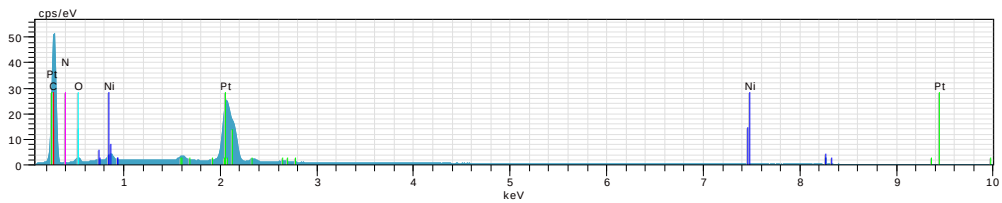

Figure 4.40. Point map of Ni-ox1 on MWCNT

Table 4.29. EDX point values for Ni-ox1

El AN	Series	Unn. C	norm. C	Atom. C	Error(1sigma)
C 6	K-series	49.97	53.67	90.74	5.51
Pt 78	M-series	38.36	41.21	4.29	1.48
N 7	K-series	1.59	1.71	2.48	0.33
Cl 17	K-series	1.17	1.26	0.72	0.07
O 8	K-series	1.03	1.11	1.41	0.21
Ni 28	L-series	0.97	1.05	0.36	0.18

Using the SEM EDX spectra, the percentage of metal adsorbed was calculated to be 1.79%. In Figure 4.10.1.8.2 the red color is representative of the nickel metal and the blue is representative of the carbon from the nanotubes, the green, turquoise and pink are representative of impurities. From observing the images, it can be seen that the metal nanoparticles are distributed evenly with no visible metal clusters.

4.10.1.9. Deposition of Ni-ox2 on MWCNTs

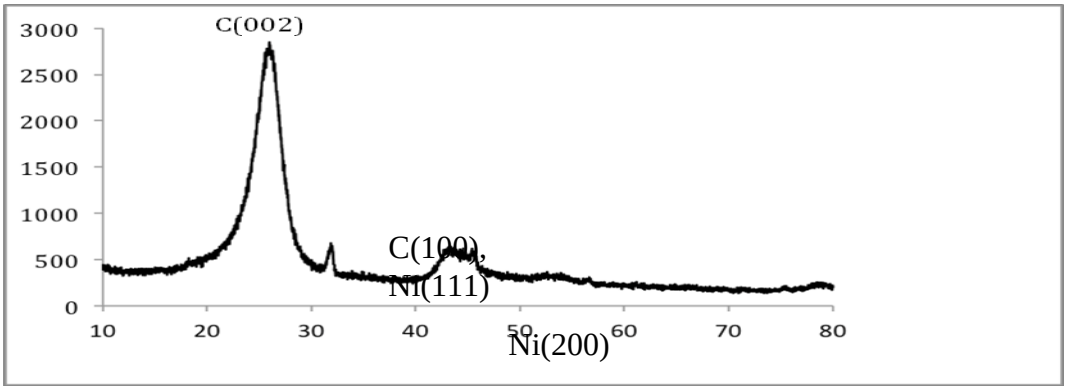

Figure 4.41. XRD image of Ni-ox2 deposited on MWCNTs

From the XRD, the size of the particles was determined according to the Scherrer equation. These values are given in the table below.

Table 4.30. XRD results for Ni-ox2

No.	2Theta(deg)	D (A)	Height(cps)	Int. I(cps deg)	FWHM(deg)	Size (A)
1	25.931(15)	3.4331(19)	1369(34)	6011(16)	3.014(16)	28.25(15)
2	31.91(2)	2.803(2)	148(11)	92(4)	0.55(2)	156(6)
3	44.17(6)	2.049(3)	176(12)	824(14)	3.63(6)	24.7(4)
4	**53.86(18)**	**1.701(5)**	**35(5)**	**211(12)**	**4.9(3)**	**19.1(13)**

Calculations were done based on the peak observed at 53.8 degrees, belonging to Ni (200). The mode size of the nanoparticle metals was calculated to be 1.9 nm.

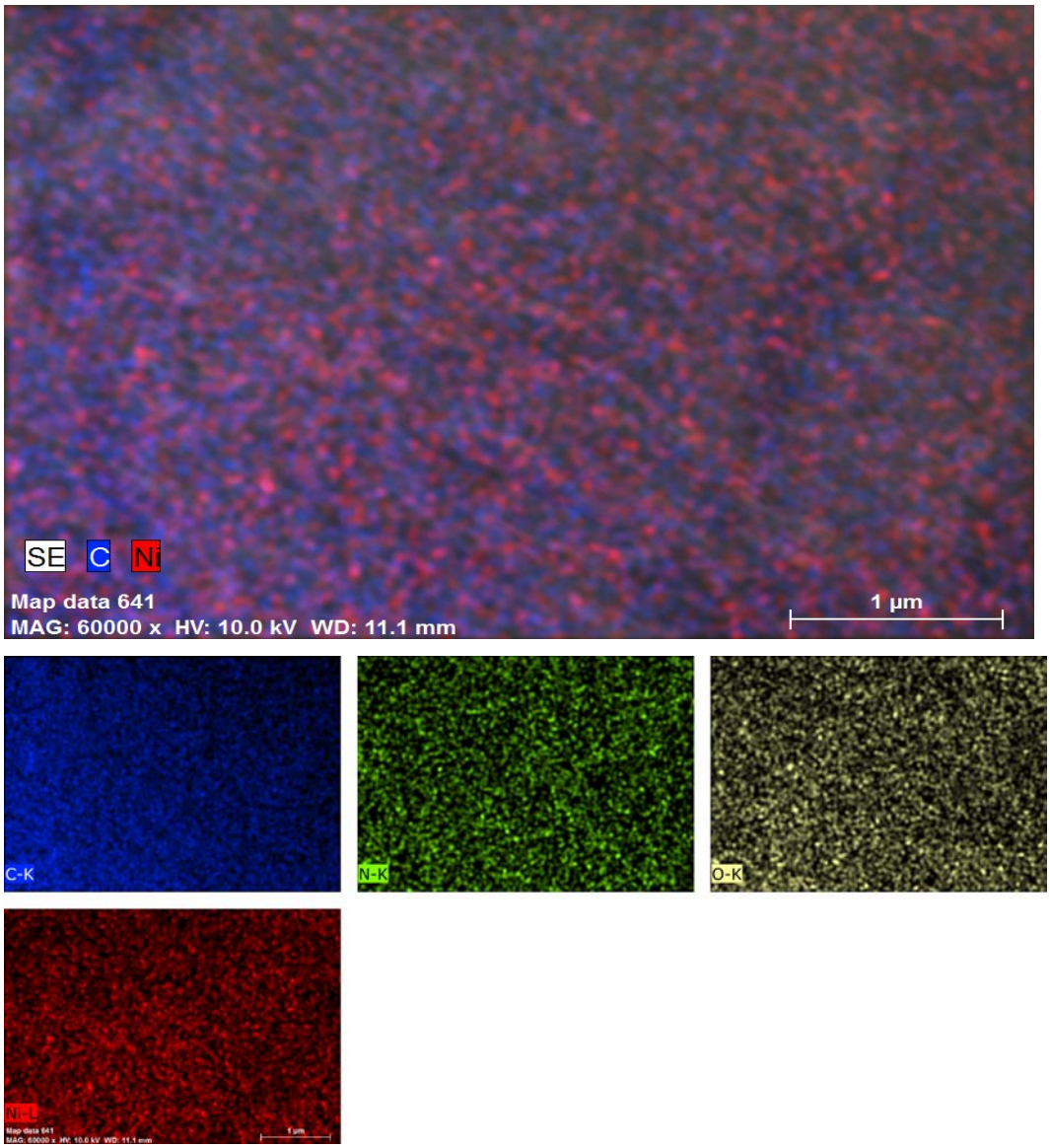

Figure 4.42. SEM images of Ni-ox2

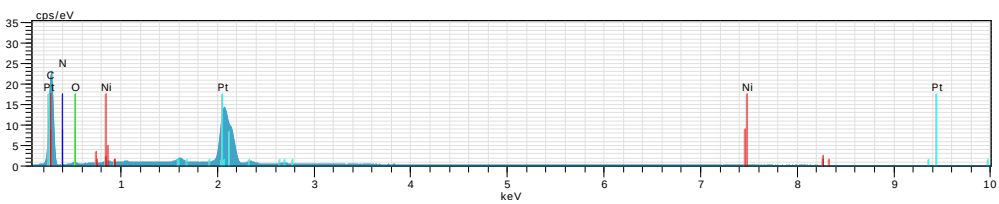

Figure 4.43. Point map of Ni-ox2 on MWCNT

Table 4.31. EDX point values for Ni-ox2

El AN	Series	Unn. C	norm. C	Atom. C	Error(1sigma)
Pt 78	M-series	41.84	48.83	5.67	1.61
C 6	K-series	41.05	47.91	90.41	4.64
O 8	K-series	1.11	1.30	1.84	0.23
N 7	K-series	0.92	1.07	1.73	0.24
Ni 28	L-series	0.77	1.90	0.35	0.16

Using the SEM EDX spectra, the percentage of metal adsorbed was calculated to be 3.71%. In Figure 4.10.1.8.2 the red color is representative of the nickel metal and the blue is representative of the carbon from the nanotubes, yellow and green represent impurities from oxygen and nitrogen, respectively, that were present in the precursor. From observing the images, it can be seen that the metal nanoparticles are distributed evenly with no visible metal clusters.

4.10.2. Palladium precursors

All nine palladium precursors were dissolved in $scCO_2$ and then bonded to MWCNTs. After an hour had passed for the completion of this, the precursors were reduced to their metallic forms in the presence of H_2 gas. Palladium is stable in its metallic form, so it was able to be adsorbed on the solid substrate in its metallic form; this was verified by XRD. The XRD measurements showed the 2θ angles to be between 10 and 80°. It also showed peaks around 40, Pd(111); 45, Pd(200); and 68, Pd(220). As before, the X-ray pattern of the MWCNT displays the presence of two peaks around 25° (3.5 Å) and 43° (2.0 Å). These are assigned to diffractions resulting from the interlayer spacing of the nanotube (002) and reflection of the carbon atoms (100). These values are in good agreement with that of the previously reported values. The peak near 43° led to an overlapping peak with Pd that was observed at 45°, making the interpretation of the data somewhat more complex. Nanoparticles ranging from 3.8-13.8nm were synthesized.

4.10.2.1. Deposition of Pd-SB1 on MWCNTs

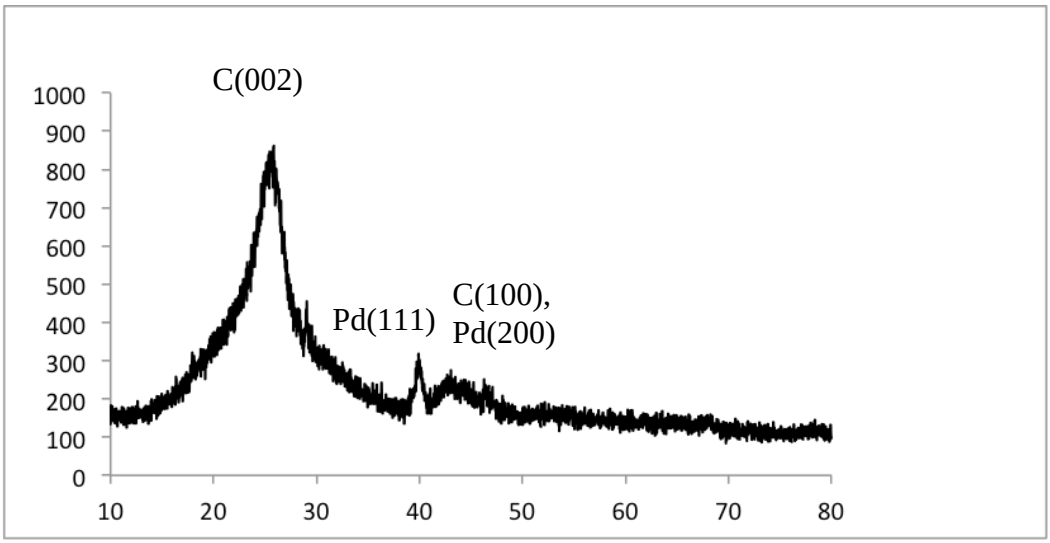

Figure 4.44. XRD image of Pd-SB1 deposited on MWCNTs

From the XRD, the size of the particles was determined according to the Scherrer equation. These values are given in the table below.

Table 4.32. XRD results for Pd-SB1

No.	2Theta(deg)	D (A)	Height(cps)	Int. I(cps deg)	FWHM(deg)	Size (A)
4	25.51(3)	3.489(5)	355(17)	2494(14)	3.67(6)	23.2(4)
5	**39.71(13)**	**2.268(7)**	**40(6)**	**181(12)**	**2.3(3)**	**38(5)**

Calculations were done based on the peak observed at 39.71 degrees, belonging to Pd(111). The mode size of the nanoparticle metals was calculated to be 3.8 nm.

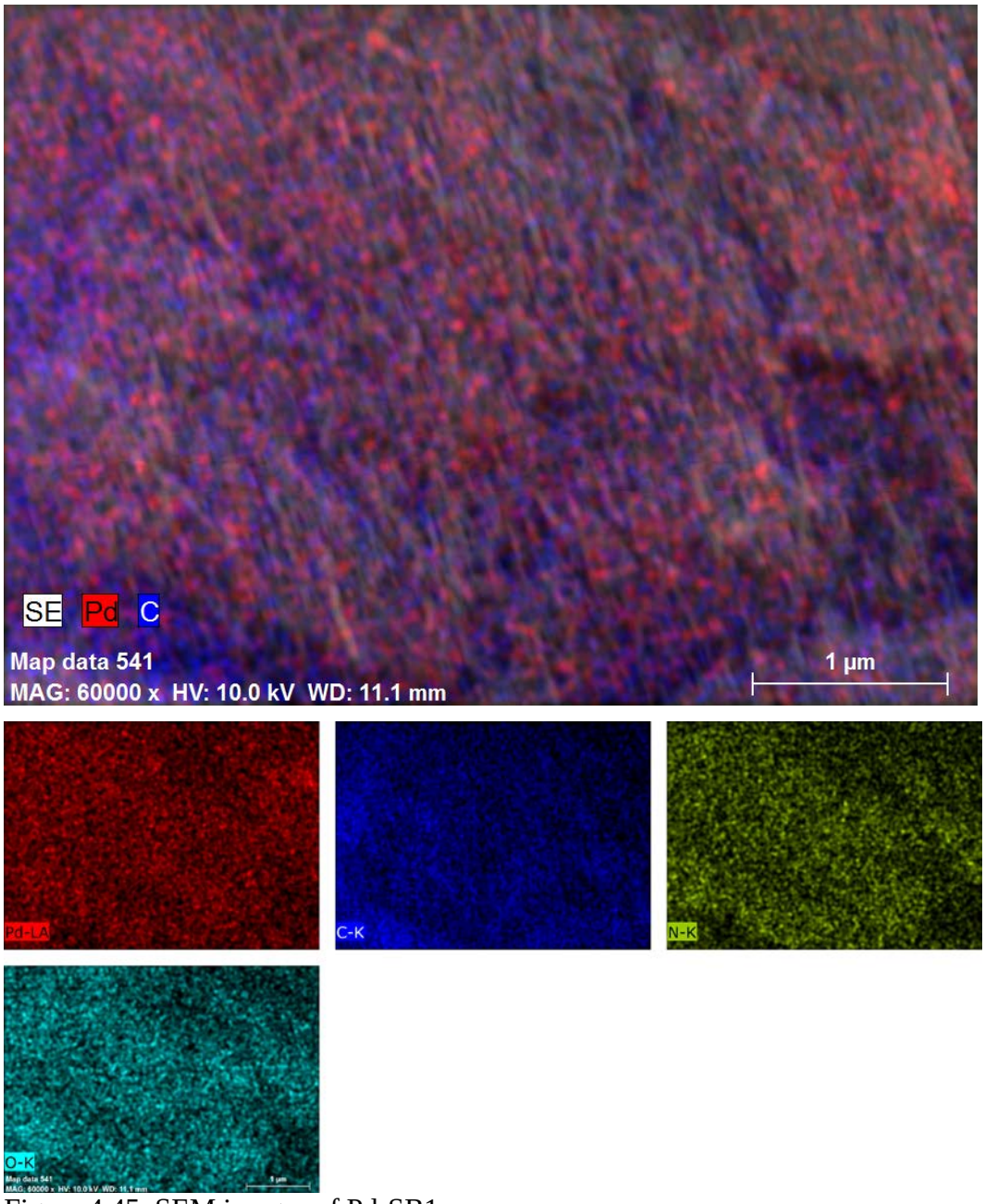

Figure 4.45. SEM images of Pd-SB1

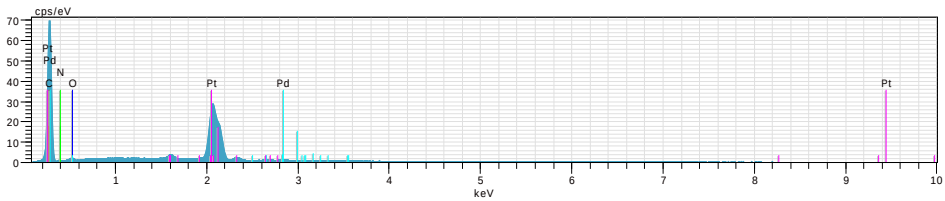

Figure 4.46. Point map of Pd-SB1 on MWCNT

Table 4.33. EDX point values for Pd-SB1

El AN	Series	Unn. C	norm. C	Atom. C	Error(1sigma)
Pt 78	M-series	40.16	45.46	5.05	1.55
C 6	K-series	44.47	50.35	90.84	4.82
Pd 46	L-series	1.45	1.64	0.33	0.08

Using the SEM EDX spectra, the percentage of metal adsorbed was calculated to be 3.01%. In Figure 4.10.1.2. the red is representative of the palladium metal and the blue is representative of the carbon from the nanotubes, turquoise and green represent impurities from oxygen and nitrogen, respectively, that were present in the precursor. From observing the images, it can be seen that the metal nanoparticles are distributed evenly with no visible metal clusters.

4.10.2.2. Deposition of Pd-SB2 on MWCNTs

From the XRD, the size of the particles was determined according to the Scherrer equation. These values are given in the table below.

Table 4.34. XRD results for Pd-SB2

No.	2Theta(deg)	D (A)	Height(cps)	Int. I(cps deg)	FWHM(deg)	Size (A)
14	25.52(3)	3.488(4)	478(20)	2015(11)	3.00(3)	28.3(3)
15	**40.01(2)**	**2.2518(11)**	**528(21)**	**757(8)**	**1.06(2)**	**83.1(16)**
16	46.53(4)	1.9503(14)	178(12)	589(9)	1.81(5)	50.0(15)
17	52.9(4)	1.729(11)	7(2)	17(5)	1.9(5)	49(13)
18	67.91(5)	1.3791(8)	90(9)	162(4)	1.20(5)	83(4)

Calculations were done based on the peak observed at 40.01 degrees, belonging to Pd(111). The mode size of the nanoparticle metals was calculated to be 8.31nm.

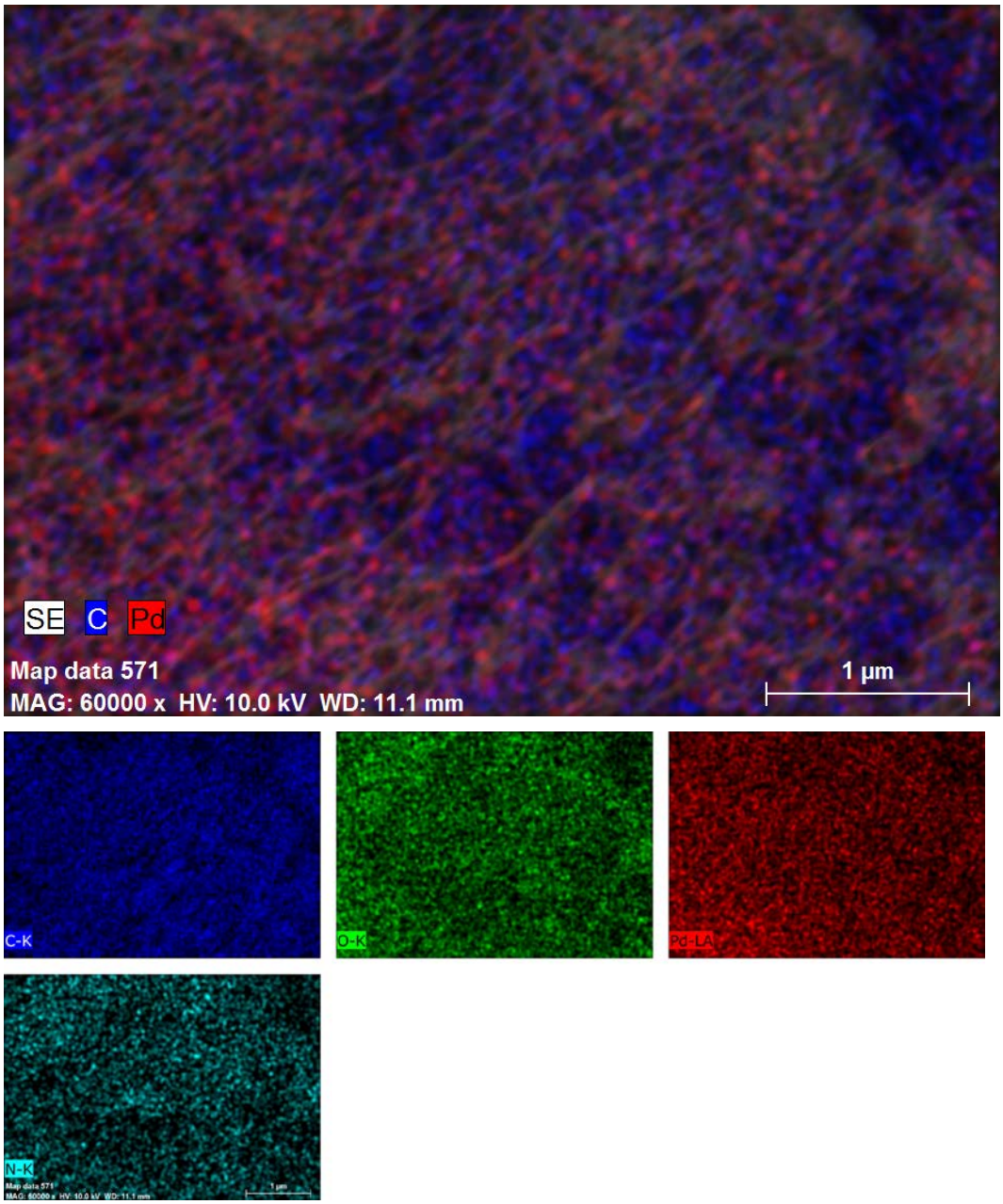

Figure 4.47. SEM images of Pd-SB2

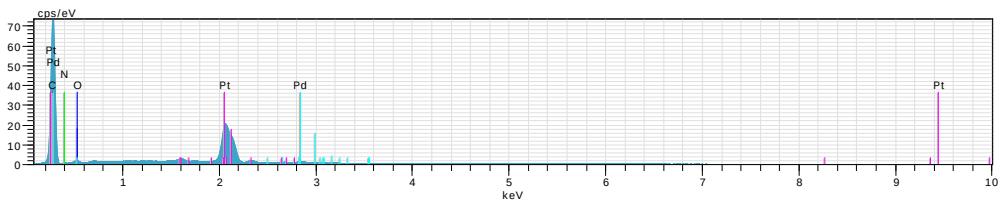

Figure 4.48. Point map of Pd-SB2 on MWCNT

Table 4.35. EDX point values for Pd-SB2

El AN	Series	Unn. C	norm. C	Atom. C	Error(1sigma)
C 6	K-series	49.72	56.56	91.67	5.37
Pt 78	M-series	33.12	37.68	3.76	1.28
Pd 46	L-series	2.32	2.64	0.48	0.11
N 7	K-series	1.48	1.68	2.34	0.29
O 8	K-series	1.26	1.43	1.74	0.22

Using the SEM EDX spectra, the percentage of metal adsorbed was calculated to be 4.24%. In Figure 4.10.2.2.2, the red color is representative of the palladium metal and the blue is representative of the carbon from the nanotubes, green and turquoise represent impurities from oxygen and nitrogen, respectively, that were present in the precursor. From observing the images, it can be seen that the metal nanoparticles are distributed evenly with no visible metal clusters.

4.10.2.3. Deposition of Pd-SB3 on MWCNTs

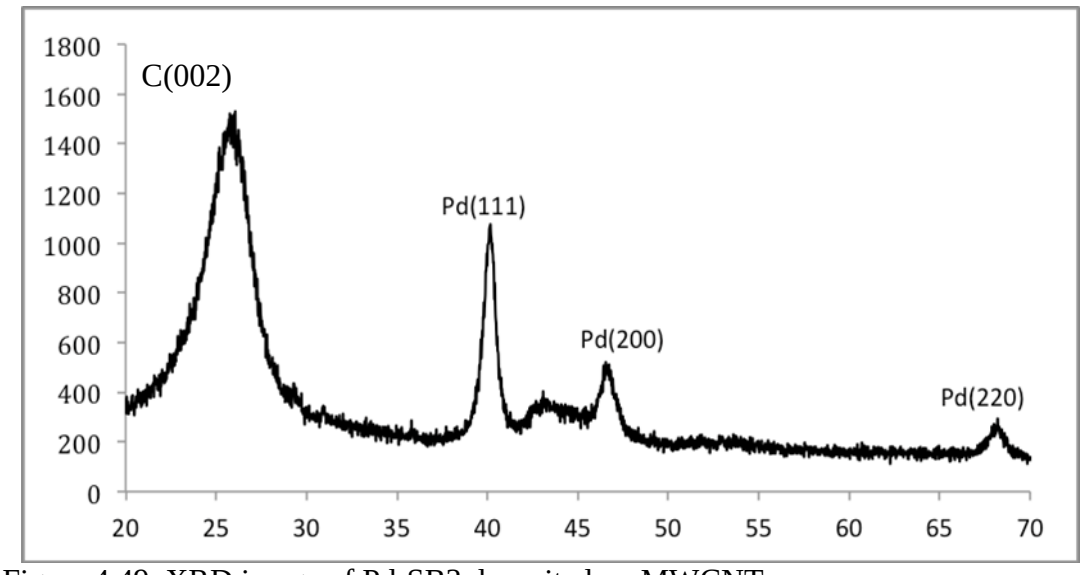

Figure 4.49. XRD image of Pd-SB3 deposited on MWCNTs

From the XRD, the size of the particles was determined according to the Scherrer equation. These values are given in the table below.

Table 4.36. XRD results for Pd-SB3

No.	2Theta(deg)	D (A)	Height(cps)	Int. I(cps deg)	FWHM(deg)	Size (A)
1	25.89(2)	3.438(3)	559(22)	1789(14)	2.69(2)	31.6(3)
2	**40.22(2)**	**2.2403(13)**	**412(19)**	**409(8)**	**0.80(2)**	**110(3)**
3	42.96(3)	2.1035(16)	51(7)	154(6)	2.83(14)	31.5(16)
4	46.57(3)	1.9486(12)	125(10)	133(4)	1.00(3)	90(3)
5	68.09(5)	1.3759(9)	56(7)	62(3)	1.02(4)	98(4)
6	25.89(2)	3.438(3)	559(22)	1789(14)	2.69(2)	31.6(3)

Calculations were done based on the peak observed at 40.22 degrees, belonging to Pd(111). The mode size of the nanoparticle metals was calculated to be 11.0 nm.

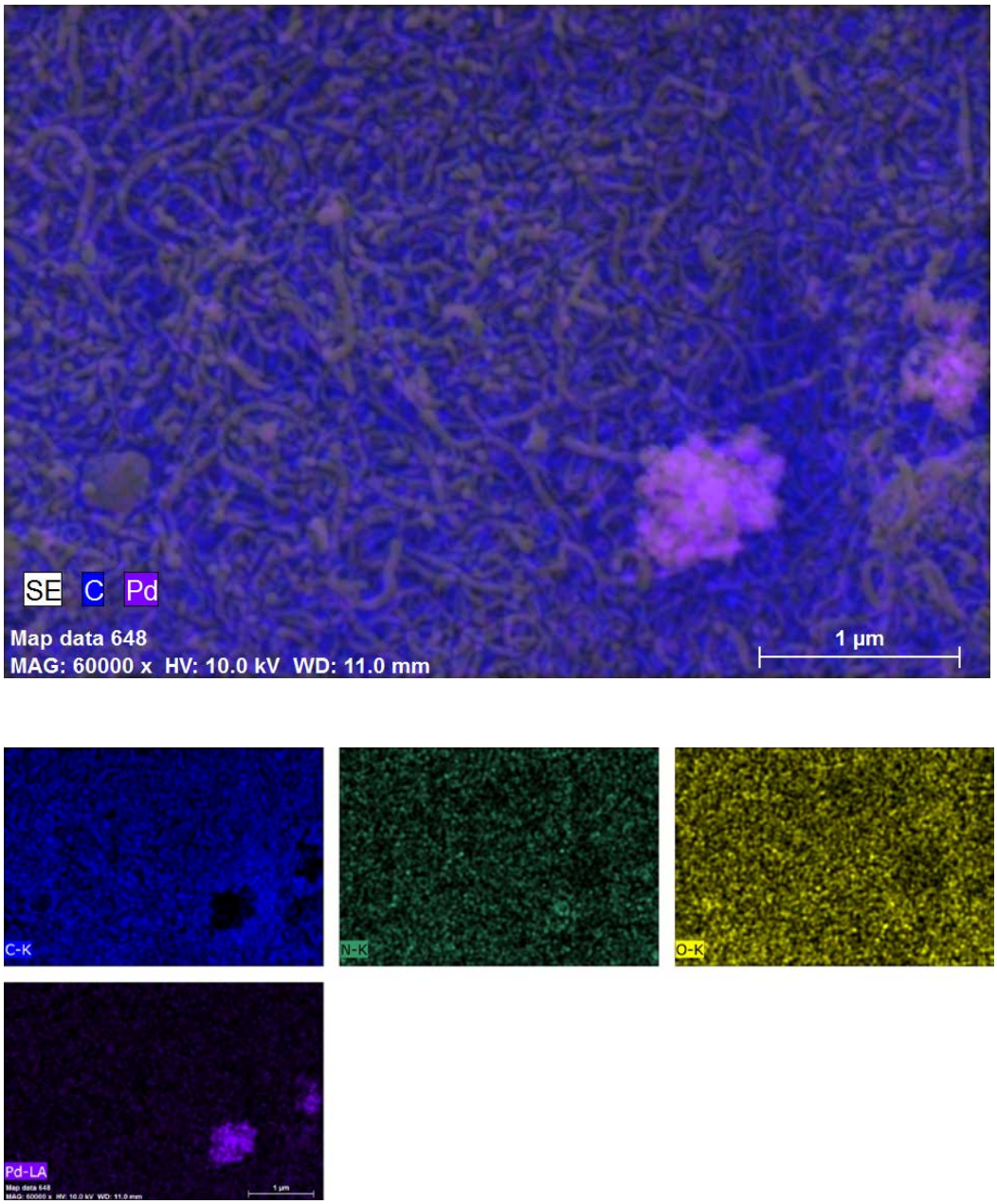

Figure 4.50. SEM images of Pd-SB3

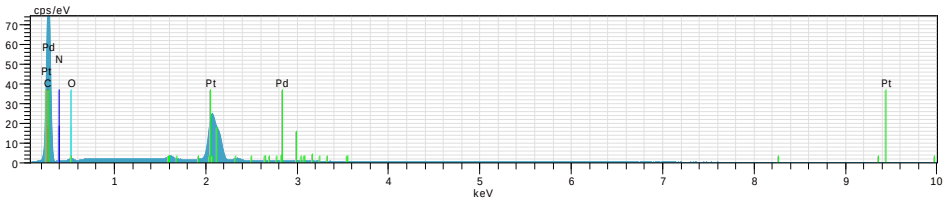

Figure 4.51. Point map of Pd-SB3 on MWCNT

Table 4.37. EDX point values for Pd-SB3

El AN	Series	Unn. C	norm. C	Atom. C	Error(1sigma)
C 6	K-series	55.09	55.20	91.68	5.95
Pt 78	M-series	40.96	41.05	4.20	1.58
N 7	K-series	2.20	2.21	3.14	0.38
Pd 46	L-series	0.89	0.89	0.17	0.06
O 8	K-series	0.65	0.65	0.81	0.14

Using the SEM EDX spectra, the percentage of metal adsorbed was calculated to be 1.51%. In Figure 4.10.2.3.2, the purple color is representative of the palladium metal and the blue is representative of the carbon from the nanotubes, the green and yellow represent impurities from nitrogen and oxygen which were present in the precursor. From observing the images, it can be seen that the metal nanoparticles are not distributed evenly and that significant metal clusters are visible.

4.10.2.4. Deposition of Pd-SB4 on MWCNTs

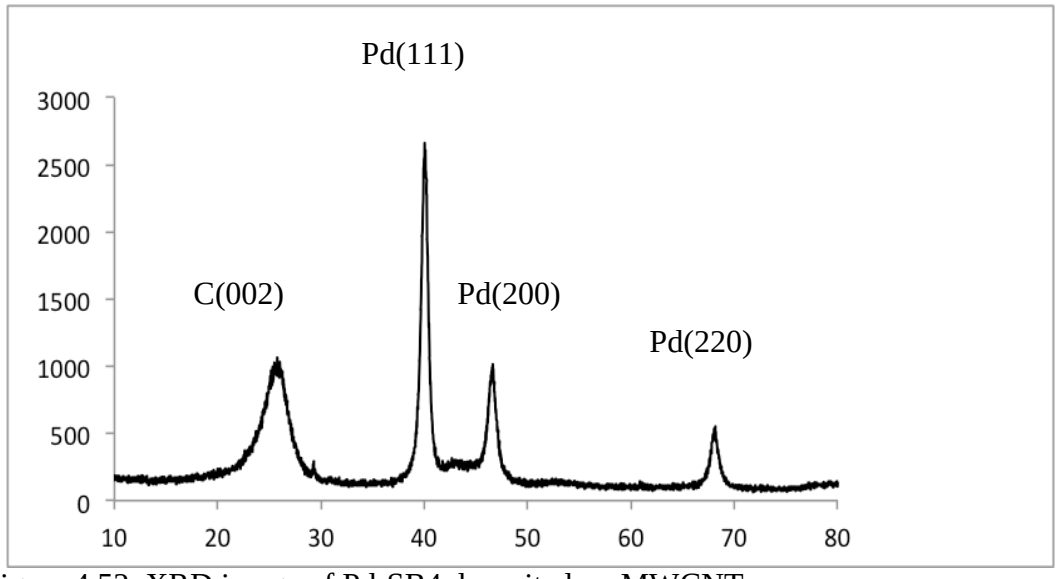

Figure 4.52. XRD image of Pd-SB4 deposited on MWCNTs

From the XRD, the size of the particles was determined according to the Scherrer equation. These values are given in the table below.

Table 4.38. XRD results for Pd-SB4

No.	2Theta(deg)	D (A)	Height(cps)	Int. I(cps deg)	FWHM(deg)	Size (A)
1	25.730(19)	3.460(3)	436(19)	1601(9)	2.939(18)	28.96(18)
2	29.28(3)	3.048(3)	48(6)	16.2(16)	0.27(3)	313(38)
3	**40.036(9)**	**2.2502(5)**	**1304(33)**	**1316(9)**	**0.801(8)**	**110.2(10)**
4	46.43(2)	1.9540(8)	397(18)	492(7)	0.96(2)	94(2)
5	52.9(4)	1.730(12)	10(3)	37(6)	3.6(4)	26(3)
6	67.97(2)	1.3781(4)	238(14)	335(3)	0.91(2)	110(3)

Calculations were done based on the peak observed at 40.04 degrees, belonging to Pd(111). The mode size of the nanoparticle metals was calculated to be 11.0 nm.

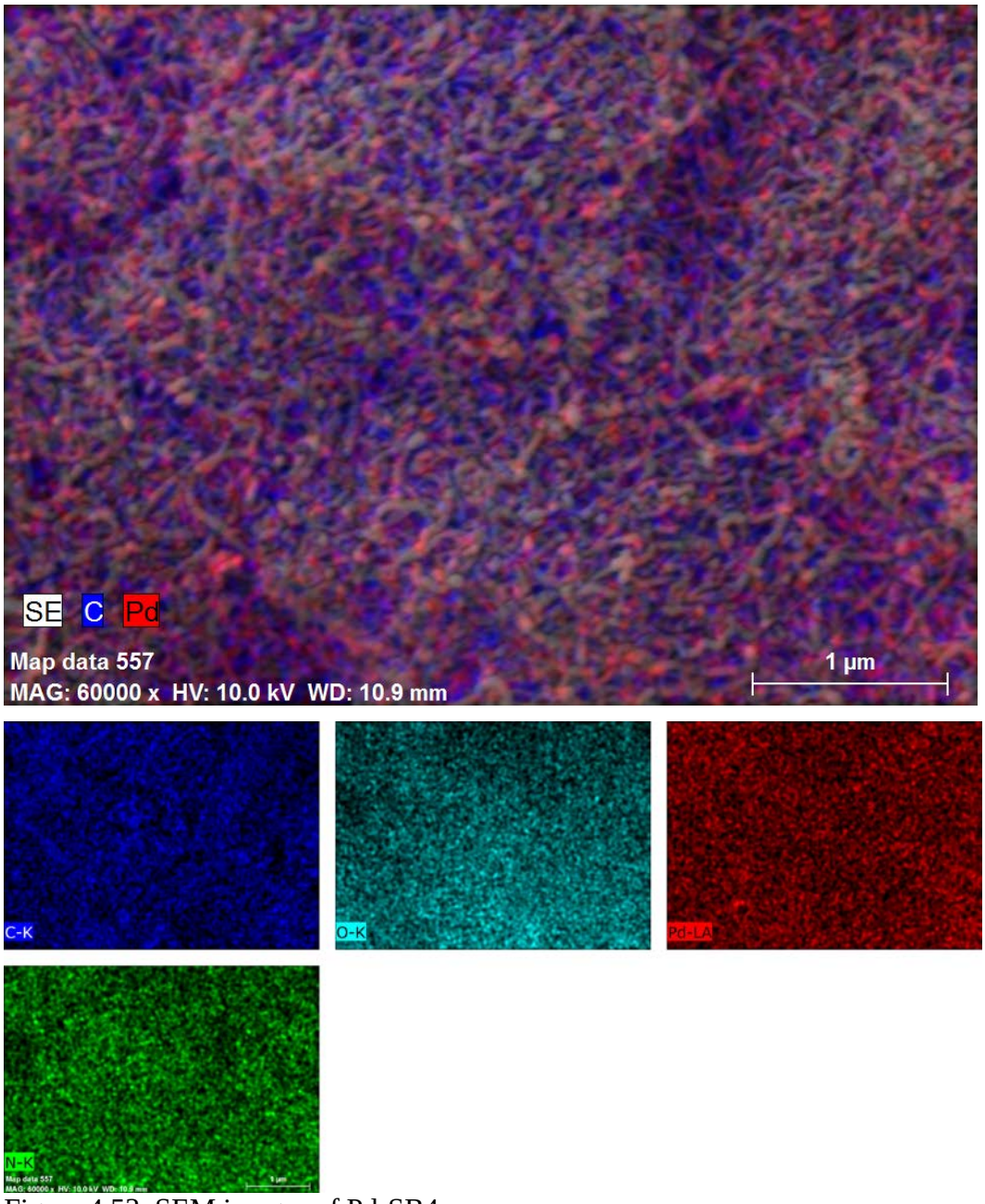

Figure 4.53. SEM images of Pd-SB4

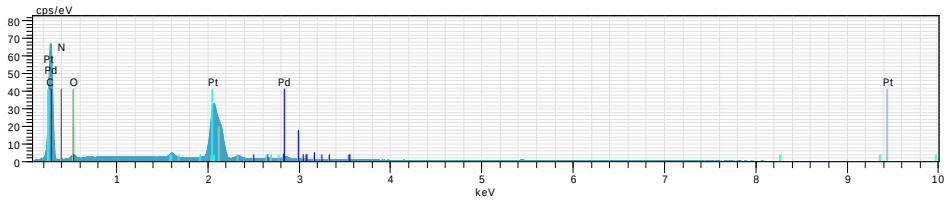

Figure 4.54. Point map of Pd-SB4 on MWCNT

Table 4.39. EDX point values for Pd-SB4

El AN	Series	Unn. C	norm. C	Atom. C	Error(1sigma)
Pt 78	M-series	42.36	47.71	5.78	1.63
C 6	K-series	38.49	43.36	85.36	4.19
Pd 46	L-series	3.38	3.81	0.85	0.14
O 8	K-series	2.68	3.02	4.46	0.38
N 7	K-series	1.87	2.10	3.55	0.32

Using the SEM EDX spectra, the percentage of metal adsorbed was calculated to be 7.29%. In Figure 4.10.2.4.2, the red color is representative of the palladium metal and the blue is representative of the carbon from the nanotubes, turquoise and green represent impurities from oxygen and nitrogen, respectively, that were present in the precursor. From observing the images, it can be seen that the metal nanoparticles are distributed evenly with no visible metal clusters.

4.10.2.5. Deposition of Pd-SB5 on MWCNTs

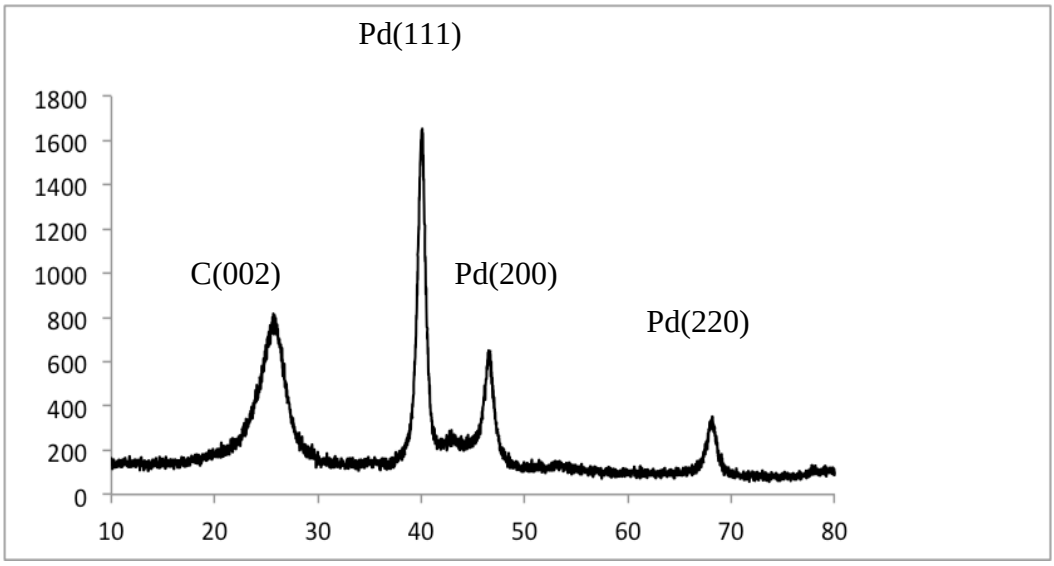

Figure 4.55. XRD image of Pd-SB5 deposited on MWCNTs

From the XRD, the size of the particles was determined according to the Scherrer equation. These values are given in the table below.

Table 4.40. XRD results for Pd-SB5

No.	2Theta(deg)	D (A)	Height(cps)	Int. I(cps deg)	FWHM(deg)	Size (A)
7	25.69(3)	3.465(4)	325(16)	1250(8)	2.82(3)	30.2(3)
8	**40.039(12)**	**2.2501(6)**	**775(25)**	**891(7)**	**0.929(10)**	**95.1(10)**
9	46.42(3)	1.9543(10)	235(14)	344(5)	1.10(3)	82(2)
10	53.59(18)	1.709(5)	13(3)	43(4)	2.1(3)	45(5)
11	68.07(3)	1.3762(6)	138(11)	237(3)	1.14(3)	87(2)

Calculations were done based on the peak observed at 40.04 degrees, belonging to Pd(111). The mode size of the nanoparticle metals was calculated to be 9.51 nm.

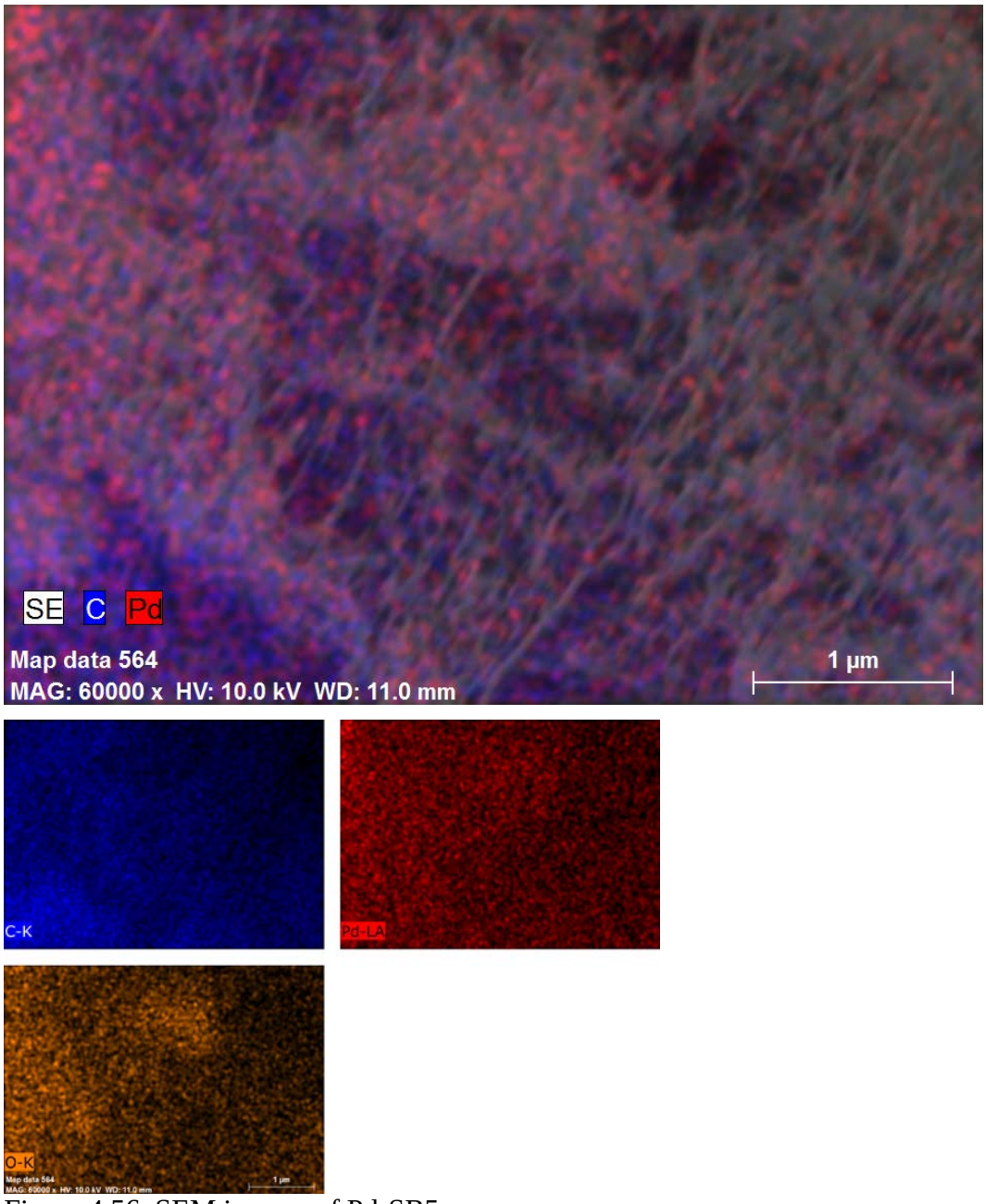

Figure 4.56. SEM images of Pd-SB5

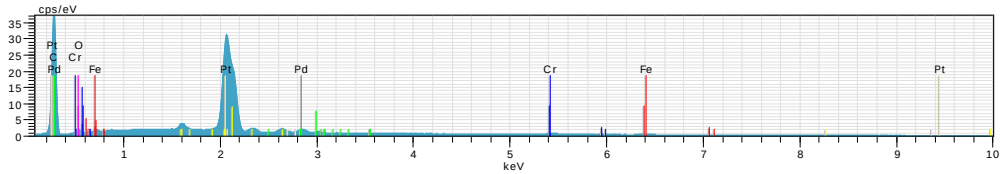

Figure 4.57. Point map of Pd-SB5 on MWCNT

Table 4.41. EDX point values for Pd-SB5

El AN	Series	Unn. C	norm. C	Atom. C	Error(1sigma)
Pt 78	M-series	50.40	55.07	8.16	1.94
C 6	K-series	32.57	35.60	85.63	3.62
Pd 46	L-series	2.92	3.19	0.87	0.13
O 8	K-series	1.48	1.62	2.93	0.25

Using the SEM EDX spectra, the percentage of metal adsorbed was calculated to be 7.10%. In Figure 4.10.2.5.2 the red color is representative of the palladium metal and the blue is representative of the carbon from the nanotubes, orange represent impurities from oxygen that were present in the precursor. From observing the images, it can be seen that the metal nanoparticles are distributed evenly with no visible metal clusters.

4.10.2.6. Deposition of Pd-SB6 on MWCNTs

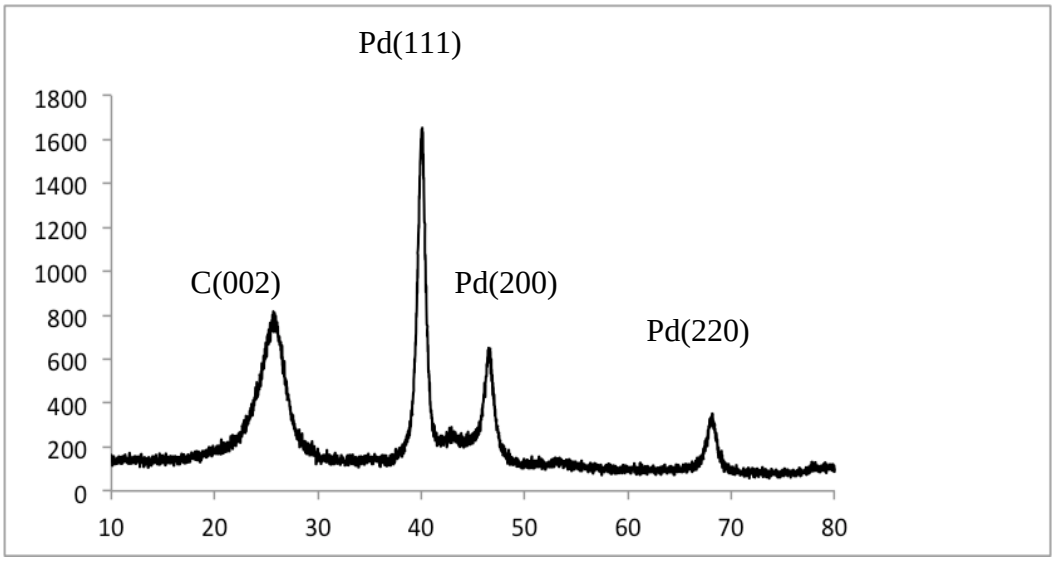

Figure 4.58. XRD image of Pd-SB6 deposited on MWCNTs

From the XRD, the size of the particles was determined according to the Scherrer equation. These values are given in the table below.

Table 4.42. XRD results for Pd-SB6

No.	2Theta(deg)	D (A)	Height(cps)	Int. I(cps deg)	FWHM(deg)	Size (A)
11	25.67(3)	3.468(4)	555(30)	2357(13)	3.03(3)	28.1(3)
12	**39.92(2)**	**2.2564(12)**	**673(33)**	**1079(11)**	**1.03(3)**	**86(2)**
13	46.54(4)	1.9498(18)	206(19)	735(12)	1.89(7)	47.9(17)
14	67.80(4)	1.3810(7)	94(13)	169(5)	1.29(6)	78(3)

Calculations were done based on the peak observed at 39.92 degrees, belonging to Pd(111). The mode size of the nanoparticle metals was calculated to be 8.6 nm.

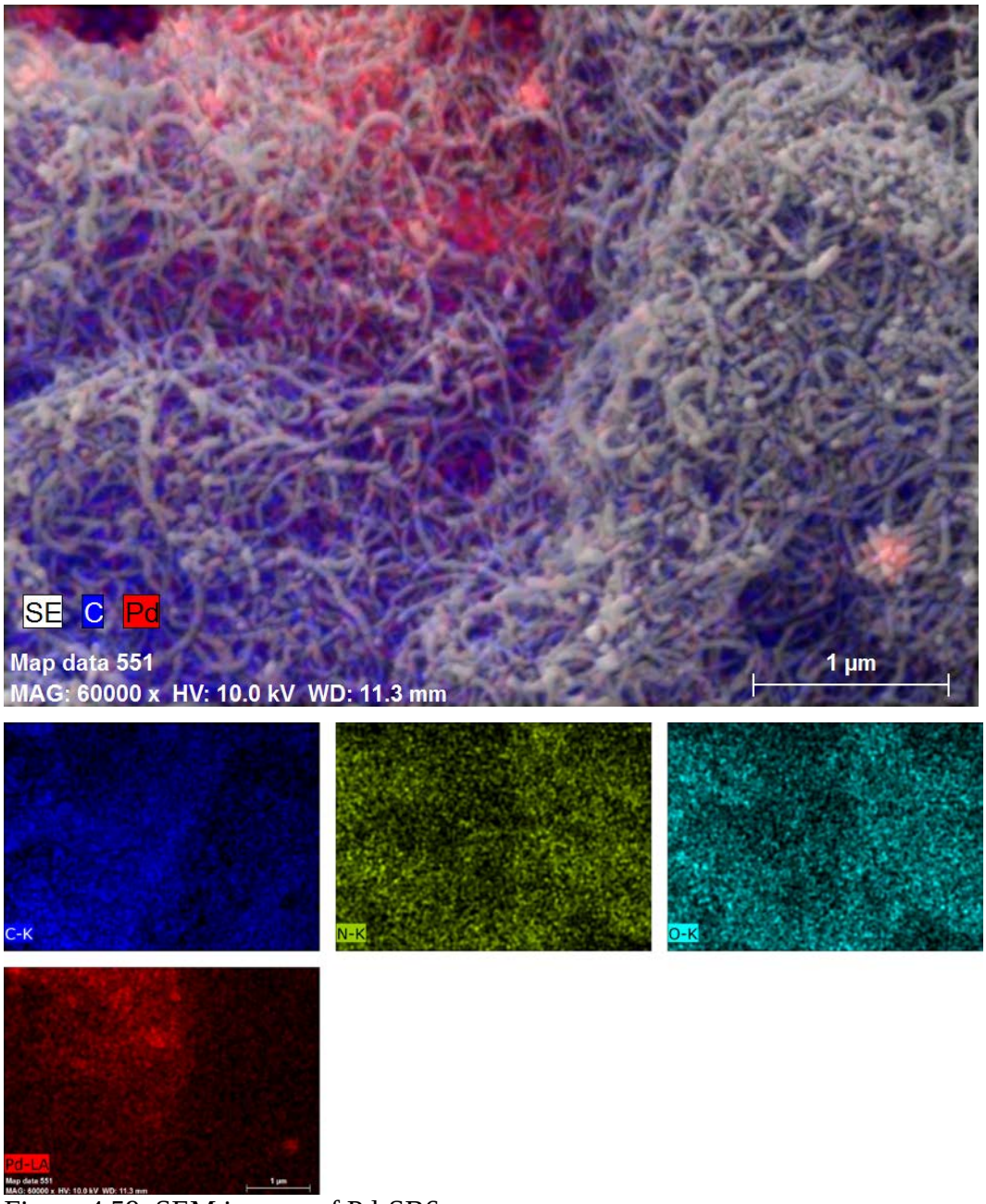

Figure 4.59. SEM images of Pd-SB6

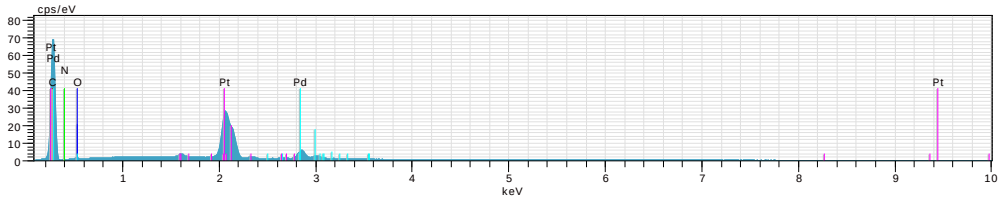

Figure 4.60. Point map of Pd-SB6 on MWCNT

Table 4.43. EDX point values for Pd-SB6

El AN	Series	Unn. C	norm. C	Atom. C	Error(1sigma)
Pt 78	M-series	43.10	43.12	5.63	1.66
C 6	K-series	41.97	41.99	89.00	3.27
Pd 46	L-series	13.68	13.69	3.27	0.49
N 7	K-series	0.88	0.88	1.59	0.19
O 8	K-series	0.32	0.32	0.51	0.09

Using the SEM EDX spectra, the percentage of metal adsorbed was calculated to be 24.07%. In Figure 4.10.2.6.2, the red color is representative of the palladium metal and the blue is representative of the carbon from the nanotubes, turquoise and green represent impurities from oxygen and nitrogen, respectively, that were present in the precursor. From observing the images, it can be seen that the metal nanoparticles are not distributed completely evenly. The palladium map shows that palladium is deposited throughout the nanotubes, however it is more heavily deposited in some areas than others. A few small metal clusters are also visible.

4.10.2.7. Deposition of Pd-SB7 on MWCNTs

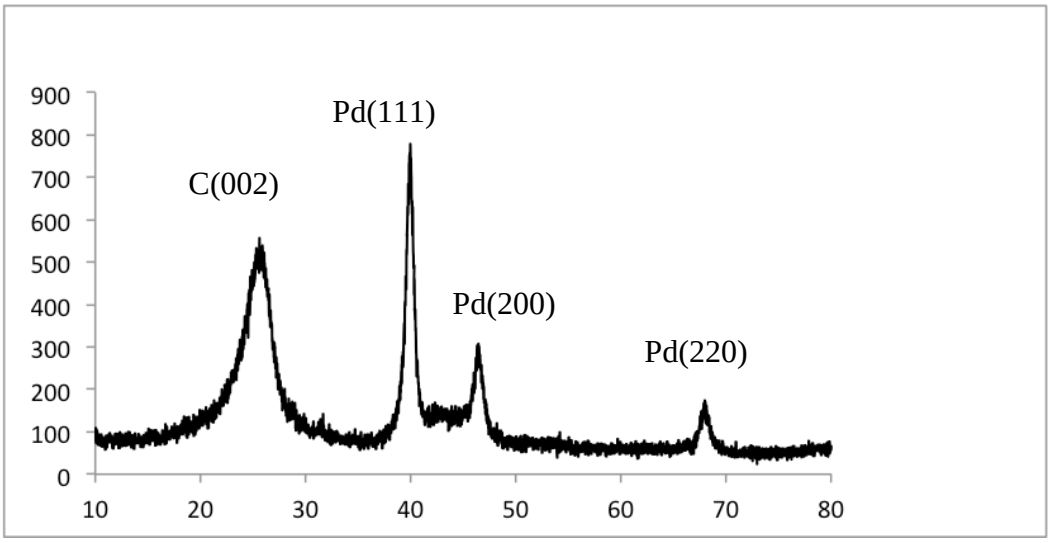

Figure 4.61. XRD image of Pd-SB7 deposited on MWCNTs

From the XRD, the size of the particles was determined according to the Scherrer equation. These values are given in the table below.

Table 4.44. XRD results for Pd-SB7

No.	2Theta(deg)	D (A)	Height(cps)	Int. I(cps deg)	FWHM(deg)	Size (A)
15	25.72(4)	3.460(5)	380(25)	1179(15)	2.91(3)	29.2(3)
16	**39.91(2)**	**2.2569(11)**	**713(34)**	**888(10)**	**0.89(2)**	**99(2)**
17	46.34(7)	1.958(3)	166(17)	235(12)	1.01(9)	89(8)
18	67.84(4)	1.3804(8)	95(13)	114(5)	1.12(4)	90(3)

Calculations were done based on the peak observed at 39.91 degrees, belonging to Pd(111). The mode size of the nanoparticle metals was calculated to be 9.9 nm.

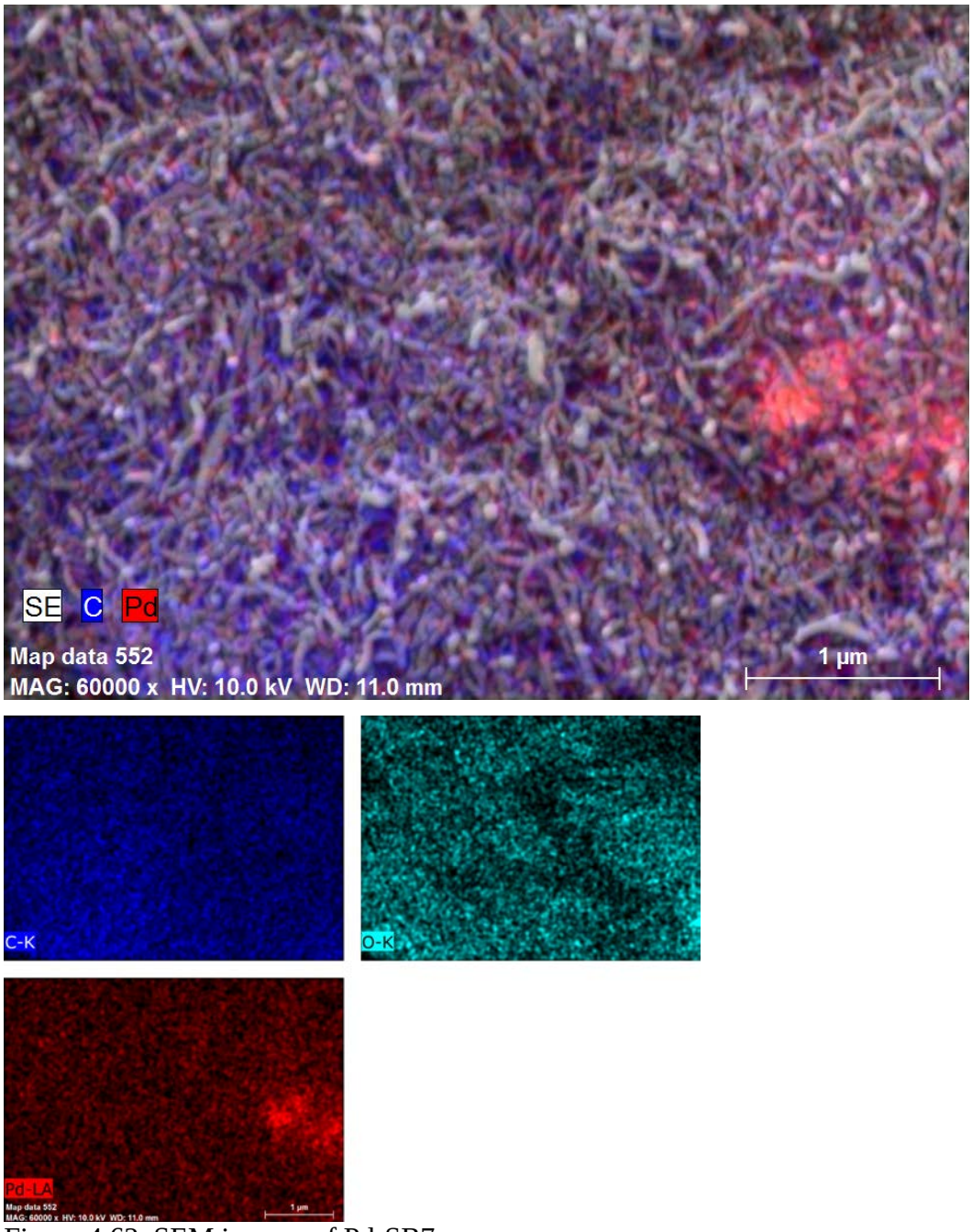

Figure 4.62. SEM images of Pd-SB7

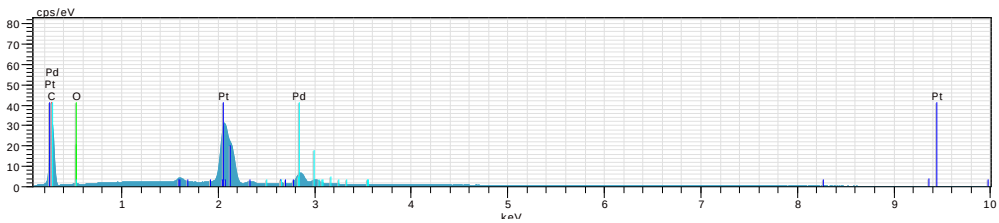

Figure 4.63. Point map of Pd-SB7 on MWCNT

Table 4.45. EDX point values for Pd-SB7

El AN	Series	Unn. C	norm. C	Atom. C	Error(1sigma)
Pt 78	M-series	53.79	56.27	11.36	2.06
C 6	K-series	23.49	24.58	80.58	2.66
Pd 46	L-series	17.86	18.69	6.92	0.63
O 8	K-series	0.44	0.46	1.14	0.11

Using the SEM EDX spectra, the percentage of metal adsorbed was calculated to be 42.74%. In Figure 4.10.2.7.2, the red color is representative of the palladium metal and the blue is representative of the carbon from the nanotubes, turquoise represents impurities from oxygen that were present in the precursor. From observing the images, it can be seen that the metal nanoparticles are not distributed evenly. The palladium map shows that palladium is deposited throughout the nanotubes, however it is more heavily deposited in some areas than others. No metal clusters are visible.

4.10.2.8 Deposition of Pd-ox1 on MWCNTs

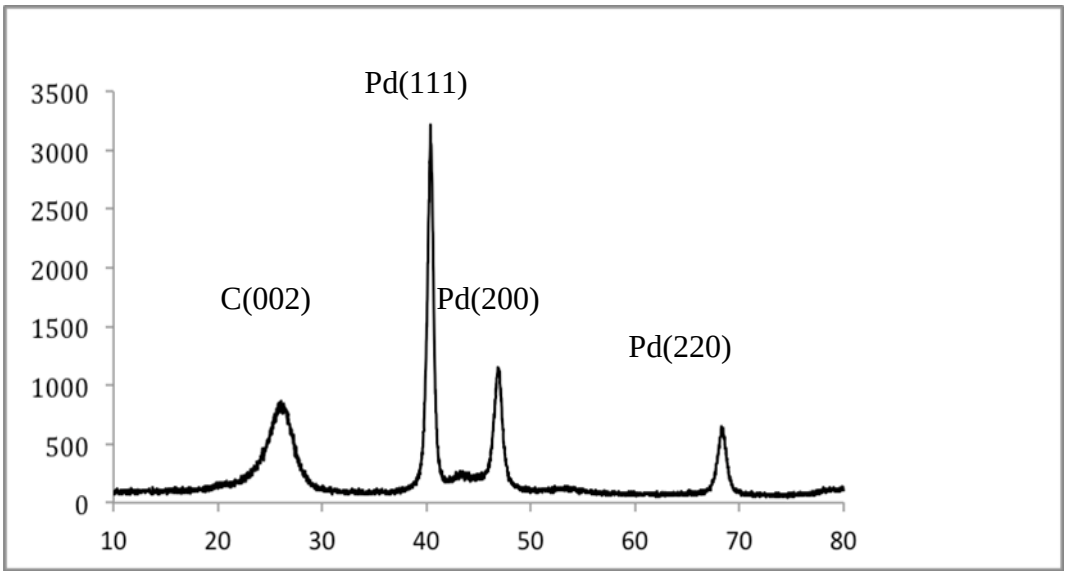

Figure 4.64. XRD image of Pd-ox1 deposited on MWCNTs

From the XRD, the size of the particles was determined according to the Scherrer equation. These values are given in the table below.

Table 4.46. XRD results for Pd-ox1

No.	2Theta(deg)	D (A)	Height(cps)	Int. I(cps deg)	FWHM(deg)	Size (A)
1	25.97(2)	3.429(3)	395(18)	1539(7)	2.89(2)	29.4(3)
2	40.393(5)	2.2311(3)	1682(37)	1522(6)	0.676(4)	130.8(8)
3	43.21(6)	2.092(3)	67(7)	329(10)	3.56(13)	25.1(9)
4	46.893(8)	1.9359(3)	559(22)	682(7)	0.910(9)	99.3(10)
5	68.271(15)	1.3727(3)	302(16)	385(3)	0.994(13)	100.8(13)

Calculations were done based on the peak observed at 40.4 degrees, belonging to Pd(111). The mode size of the nanoparticle metals was calculated to be 13.1 nm.

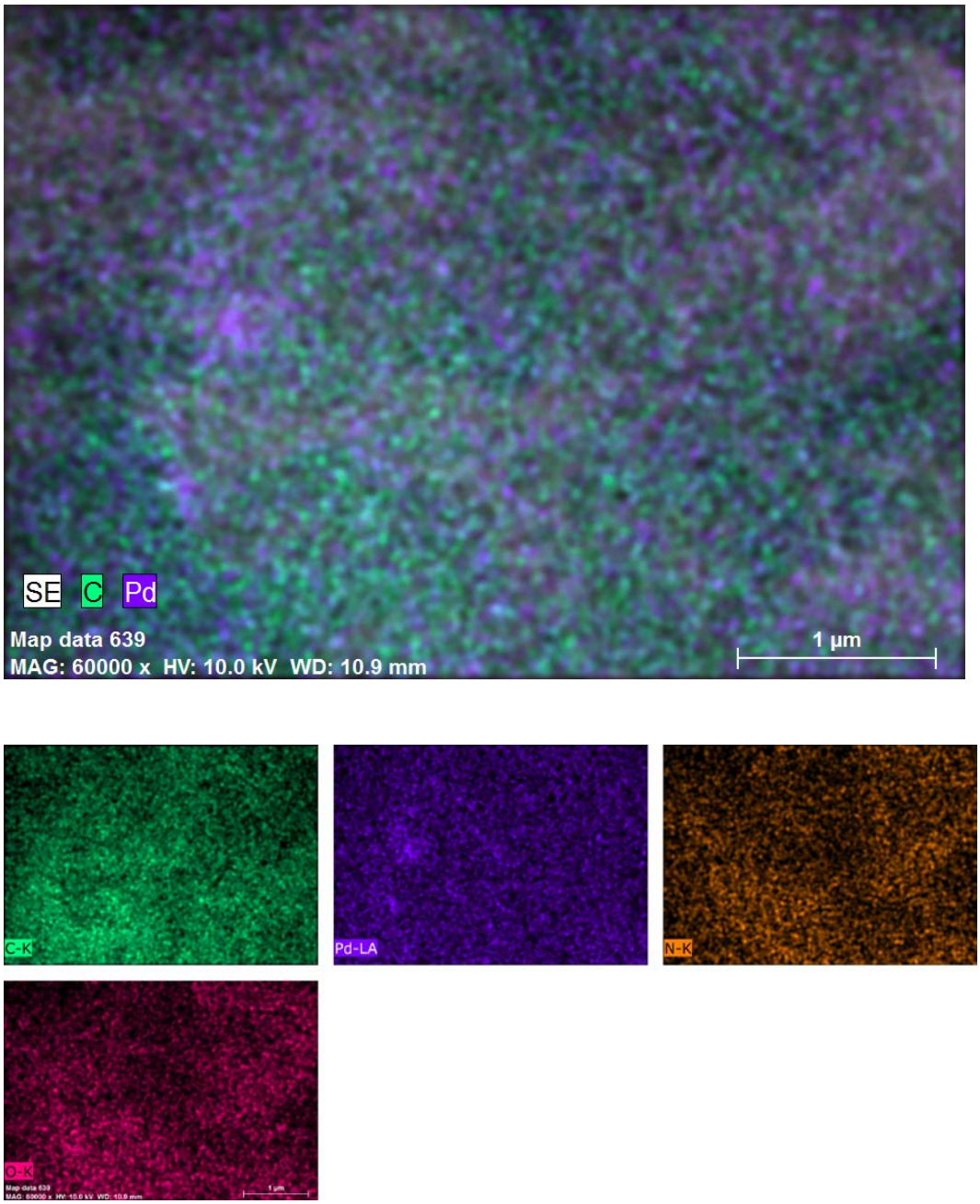

Figure 4.65. SEM images of Pd-ox1

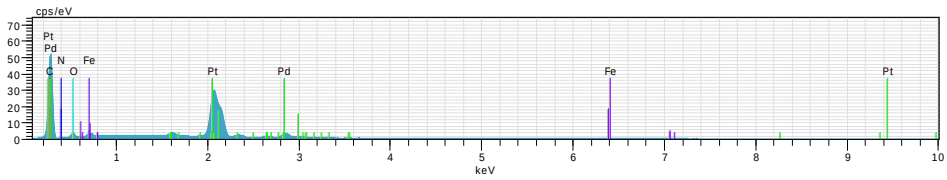

Figure 4.66. Point map of Pd-ox1 on MWCNT

Table 4.47. EDX point values for Pd-ox1

El AN	Series	Unn. C	norm. C	Atom. C	Error(1sigma)
Pt 78	M-series	44.68	50.52	7.25	1.72
C 6	K-series	31.30	35.39	82.51	3.47
Pd 46	L-series	5.86	6.63	1.74	0.23
O 8	K-series	2.16	2.44	4.27	0.33
N 7	K-series	1.01	1.14	2.28	0.21

Using the SEM EDX spectra, the percentage of metal adsorbed was calculated to be 14.40%. In Figure 4.10.2.8.2, the purple color is representative of the palladium metal and the green is representative of the carbon from the nanotubes, red and orange represent impurities from oxygen and nitrogen that were present in the precursor. From observing the images, it can be seen that the metal nanoparticles are evenly distributed. There are no visible metal clusters.

4.10.2.9 Deposition of Pd-ox2 on MWCNTs

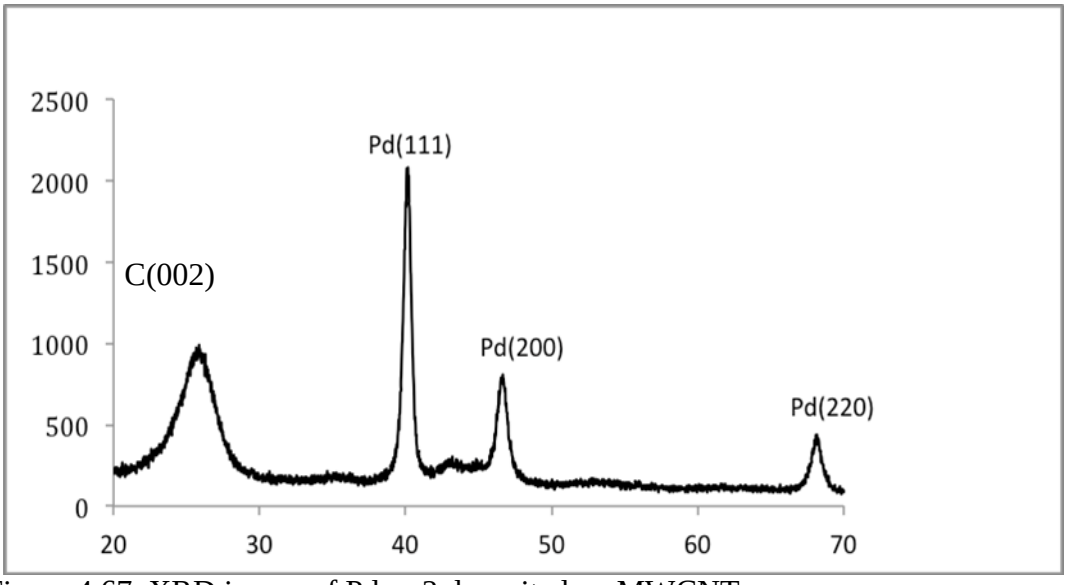

Figure 4.67. XRD image of Pd-ox2 deposited on MWCNTs

From the XRD, the size of the particles was determined according to the Scherrer equation. These values are given in the table below.

Table 4.48. XRD results for Pd-ox2

No.	2Theta(deg)	D (A)	Height(cps)	Int. I(cps deg)	FWHM(deg)	Size (A)
1	25.78(2)	3.453(3)	393(18)	1350(9)	2.88(2)	29.6(2)
2	**40.107(6)**	**2.2464(3)**	**1056(30)**	**867(5)**	**0.640(5)**	**138.1(12)**
3	42.96(8)	2.103(4)	52(7)	220(8)	3.30(15)	27.0(12)
4	46.605(12)	1.9472(5)	337(17)	367(6)	0.850(13)	106.3(16)
5	68.08(2)	1.3760(4)	169(12)	188(3)	0.916(17)	109(2)

Calculations were done based on the peak observed at 40.1 degrees, belonging to Pd(111). The mode size of the nanoparticle metals was calculated to be 13.8 nm.

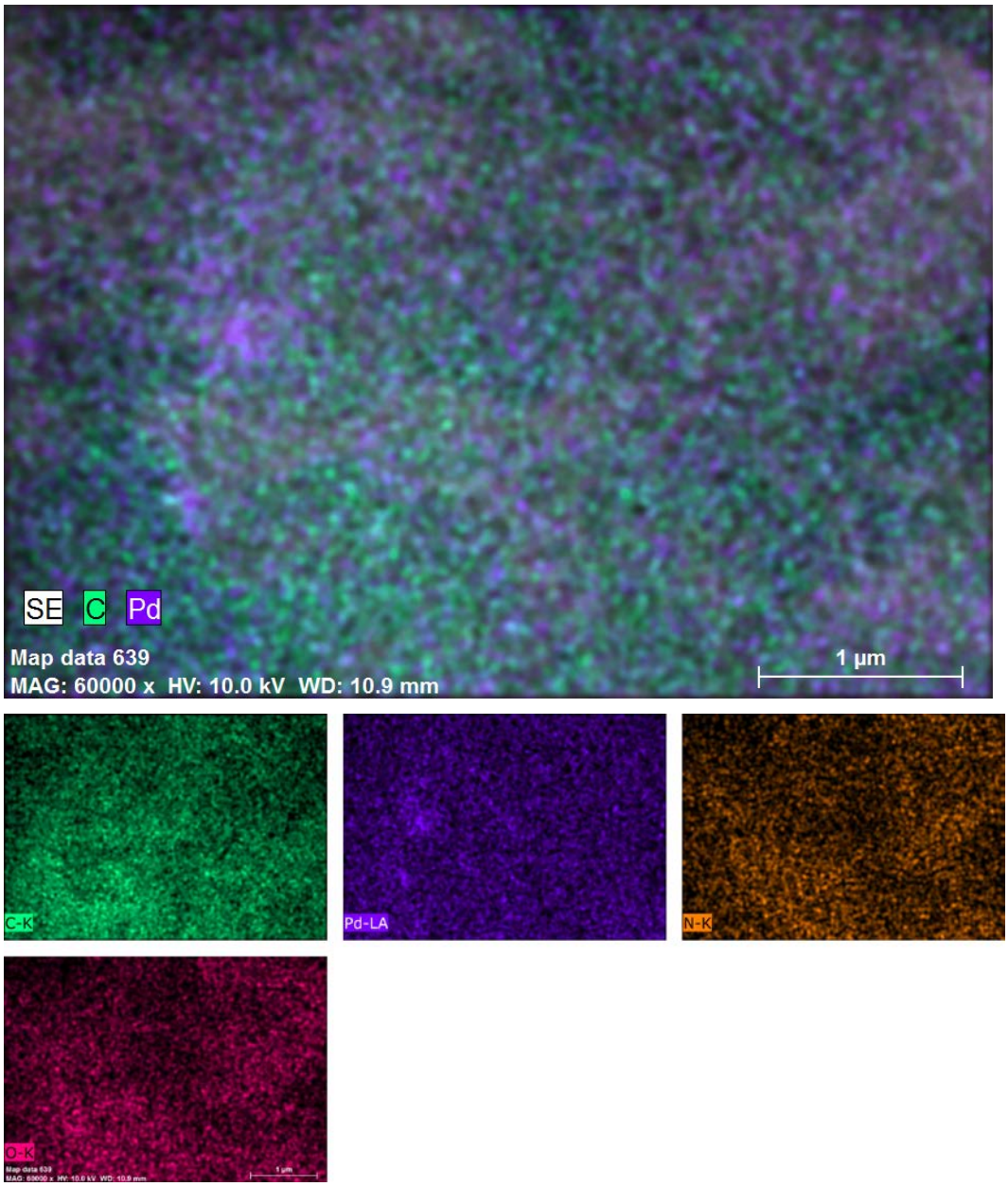

Figure 4.68. SEM images of Pd-ox2

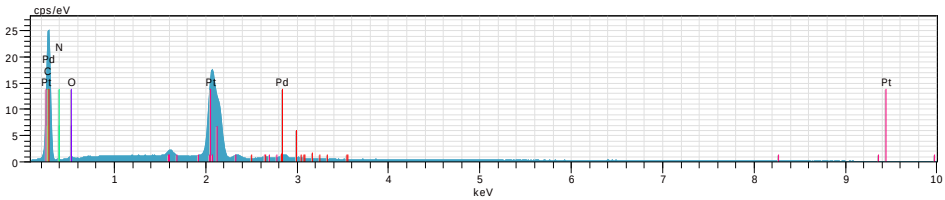

Figure 4.69. Point map of Pd-ox2 on MWCNT

Table 4.49. EDX point values for Pd-ox2

El AN	Series	Unn. C	norm. C	Atom. C	Error(1sigma)
Pt 78	M-series	54.17	57.33	8.39	2.08
C 6	K-series	34.58	36.59	86.94	3.97
Pd 46	L-series	4.04	4.28	1.15	0.17
N 7	K-series	1.16	1.22	2.49	0.27
O 8	K-series	0.55	0.58	1.03	0.14

Using the SEM EDX spectra, the percentage of metal adsorbed was calculated to be 10.03%. In Figure 4.10.2.9.2 the purple color is representative of the palladium metal and the green is representative of the carbon from the nanotubes, red and orange represent impurities from oxygen and nitrogen that were present in the precursor. From observing the images, it can be seen that the metal nanoparticles are evenly distributed. There are no visible metal clusters.

4.10.3. Tungsten precursors

The two tungsten precursors were dissolved in $scCO_2$ and then attached to MWCNTs. After an hour had passed for the completion of the reactions, the precursors were reduced to their metallic oxide forms in the presence of H_2 gas. Tungsten oxide was adsorbed on the solid substrate; this was verified by XRD. The XRD measurements taken at 2θ angles between 10 and 80°. It showed a peak belonging to tungsten around 25° (3.5 Å) and 53° (1.7 Å) corresponding to WO_3(002) and WO_3(220) respectively. As with the nickel and palladium, the X-ray pattern of the MWCNT displays the presence of two peaks around 25° (3.5 Å) and 43° (2.0 Å). These are assigned to diffractions resulting from the interlayer spacing of the nanotube (002) and reflection of the carbon atoms (100). These values are in good agreement with that of the previously reported values. The peak corresponding to tungsten at 25° and that of the nanotube at 25° overlapped. This made interpretation using that peak difficult. There for the peak at 53° was used for interpretation. Previous studies have reported tungsten nanoparticles as small as

10nm (Dillon et al, 2008), the average size of tungsten nanoparticles reported in this study ranges from 0.9- 3.0nm.

4.10.3.1. Deposition of W-SB1 on MWCNTs

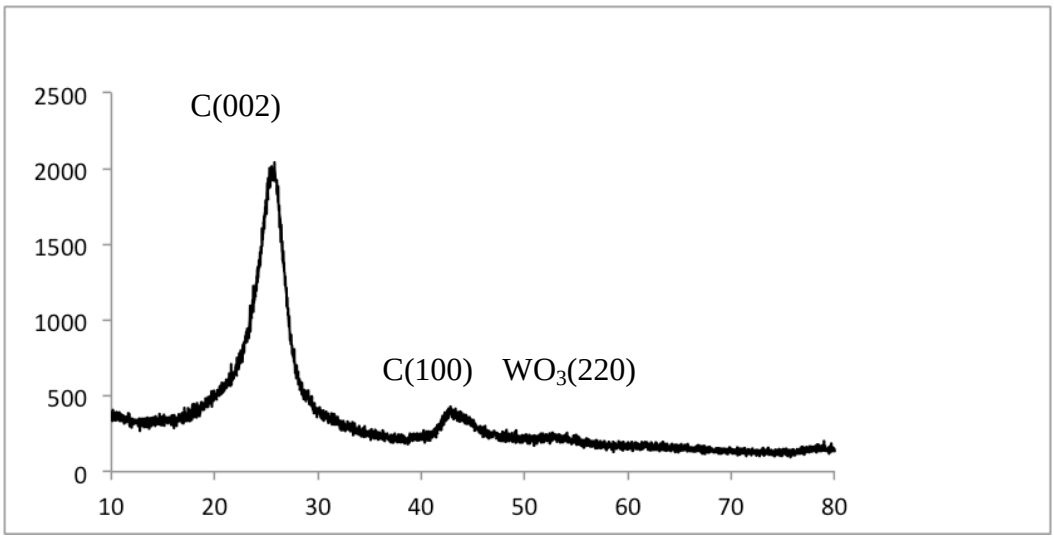

Figure 4.70. XRD image of W-SB1 deposited on MWCNTs

From the XRD, the size of the particles was determined according to the Scherrer equation. These values are given in the table below.

Table 4.50. XRD results for W-SB1

No.	2Theta(deg)	D (A)	Height(cps)	Int. I(cps deg)	FWHM(deg)	Size (A)
6	25.67(2)	3.467(3)	953(28)	4693(16)	3.13(3)	27.2(2)
7	43.43(9)	2.082(4)	92(9)	356(9)	2.89(10)	30.8(11)
8	**52.9(4)**	**1.730(13)**	**13(3)**	**56(7)**	**3.1(5)**	**30(5)**

Calculations were done based on the peak observed at 52.9 degrees, belonging to WO_3(220). The mode size of the nanoparticle metals was calculated to be 3.0 nm.

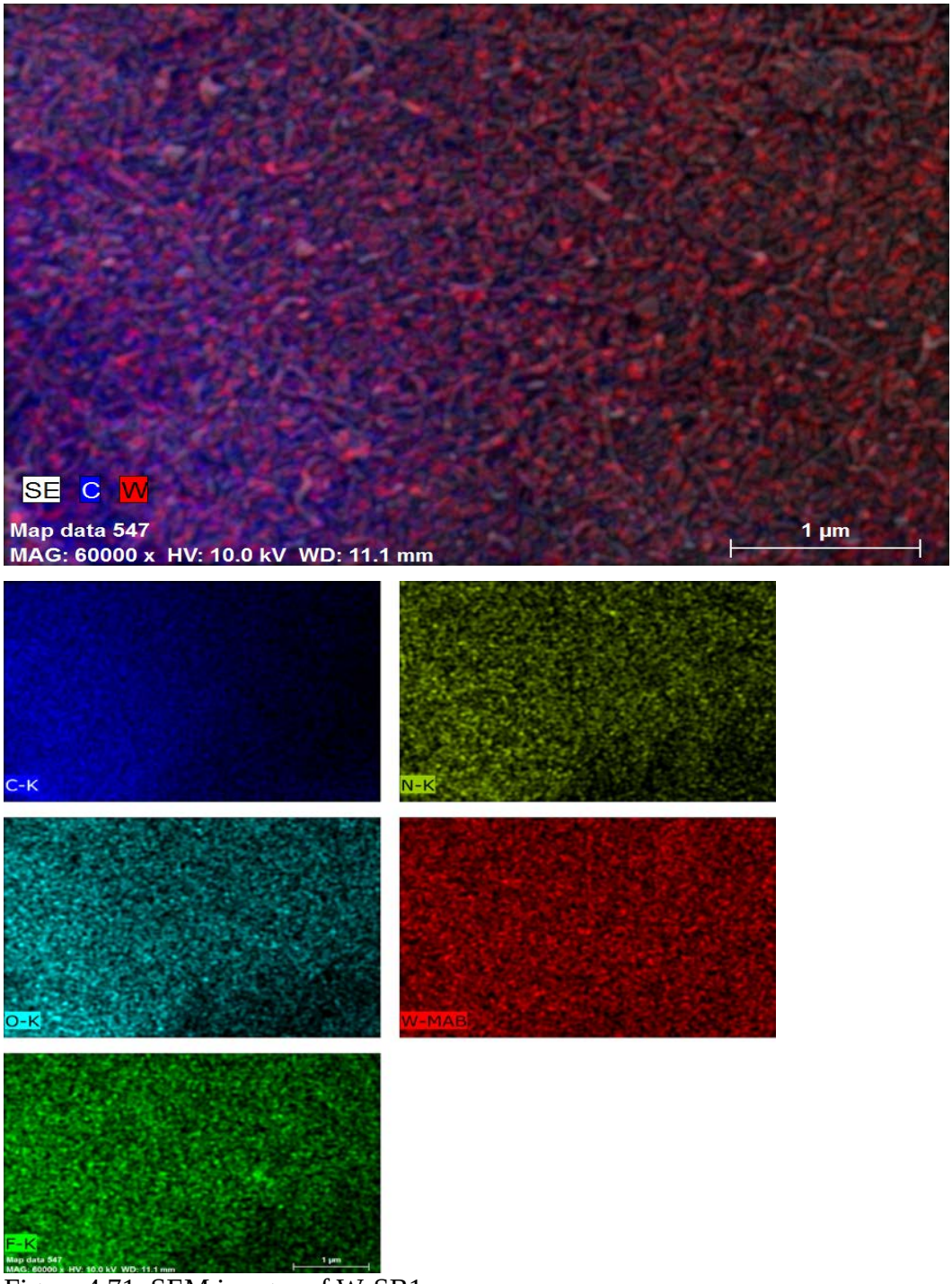

Figure 4.71. SEM images of W-SB1

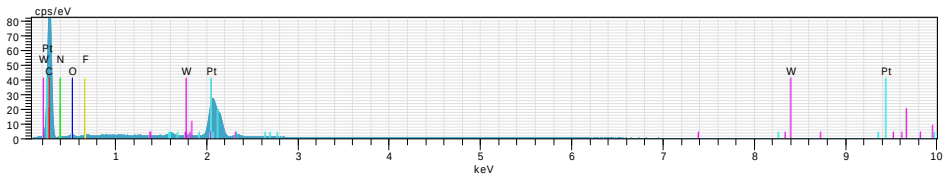

Figure 4.72. Point map of W-SB1 on MWCNT

Table 4.51. EDX point values for W-SB1

El AN	Series	Unn. C	norm. C	Atom. C	Error(1sigma)
C 6	K-series	58.43	59.53	90.37	6.22
Pt 78	M-series	33.92	34.57	3.23	1.31
N 7	K-series	2.17	2.22	2.88	0.36
O 8	K-series	2.04	2.08	2.37	0.31
F 9	K-series	1.13	1.15	1.10	0.18
W 74	L-series	0.45	0.45	0.05	0.05

Using the SEM EDX spectra, the percentage of metal adsorbed was calculated to be 1.03%. In Figure 4.10.3.1.2 the red color is representative of the tungsten metal and the blue is representative of the carbon from the nanotubes, turquoise represents oxygen, which is present due to impurities as well as because the tungsten was deposited in an oxide form. Yellow and green represent impurities from nitrogen and fluorine, respectively, that were present in the precursor. From observing the images, it can be seen that the metal nanoparticles are distributed completely evenly. The tungsten map shows that tungsten is deposited throughout the nanotubes with no visible metal clusters.

4.10.3.2. Deposition of W-ox1 on MWCNTs

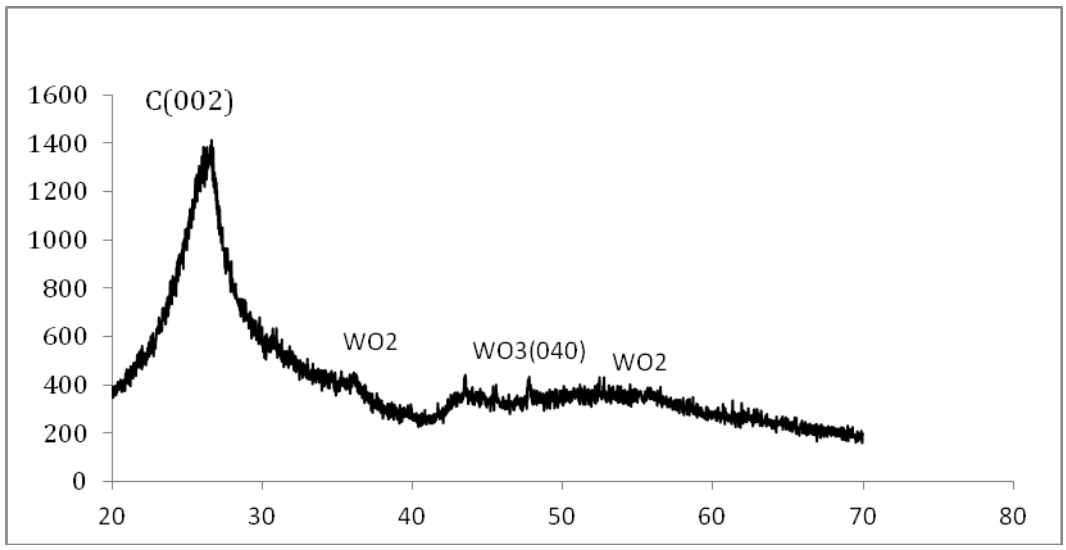

Figure 4.73. XRD image of W-ox1 deposited on MWCNTs

From the XRD, the size of the particles was determined according to the Scherrer equation. These values are given in the table below.

Table 4.52. XRD results for W-ox1

No.	2Theta(deg)	D (A)	Height(cps)	Int. I(cps deg)	FWHM(deg)	Size (A)
6	26.44(4)	3.368(5)	524(21)	3250(28)	3.93(5)	21.7(3)
7	**55.5(3)**	**1.655(9)**	**53(7)**	**590(24)**	**9.5(3)**	**9.8(3)**

Calculations were done based on the peak observed at 55.5 degrees, belonging to WO_2(220). The mode size of the nanoparticle metals was calculated to be 0.9 nm.

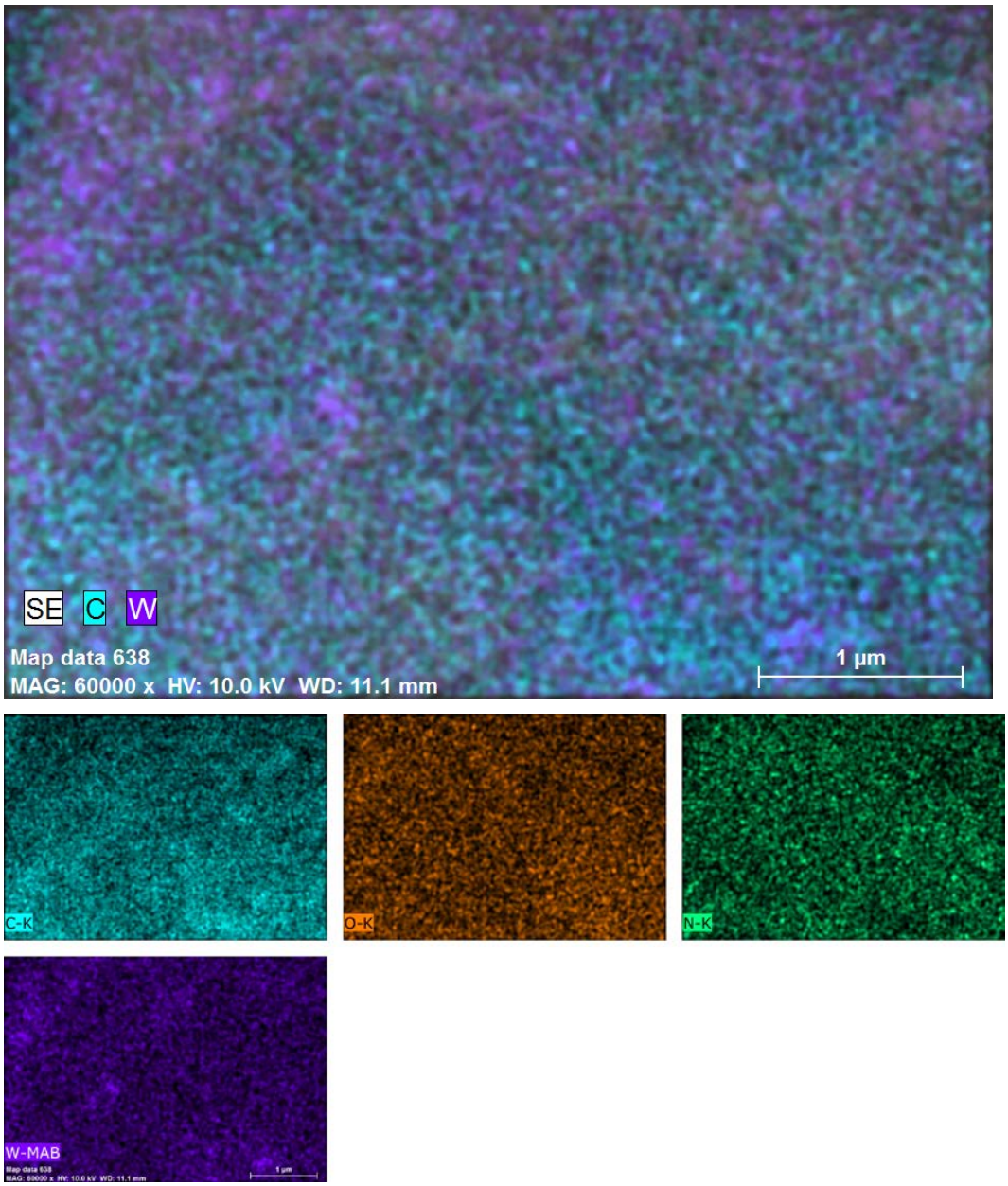

Figure 4.74. SEM images of W-ox1

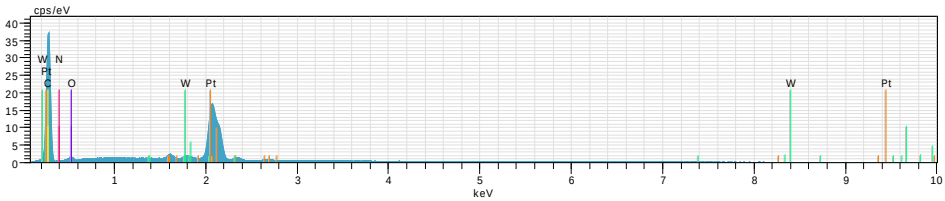

Figure 4.75. Point map of W-ox1 on MWCNT

Table 4.53. EDX point values for W-ox1

El AN	Series	Unn. C	norm. C	Atom. C	Error(1sigma)
C 6	K-series	45.97	53.39	90.53	5.06
Pt 78	M-series	35.86	41.65	4.35	1.39
O 8	K-series	1.77	2.06	2.62	0.30
N 7	K-series	1.40	1.62	2.36	0.29
W 74	M-series	1.10	1.28	0.14	0.07

Using the SEM EDX spectra, the percentage of metal adsorbed was calculated to be 2.19%. In Figure 4.10.3.2.2 the purple color is representative of the tungsten metal and the turquoise is representative of the carbon from the nanotubes, orange is representative of oxygen, which is present due to impurities as well as because the tungsten was deposited in an oxide form. Green represents impurities from nitrogen, which was present in the precursor. From observing the images, it can be seen that the metal nanoparticles are distributed completely evenly. The tungsten map shows that tungsten is deposited throughout the nanotubes with no visible metal clusters.

5. CONCLUSIONS

The chemical reduction of nanoparticle metals in super critical carbon dioxide onto multi-walled carbon nanotubes is a method used in the synthesis of nanoparticle metal catalysts. Currently there are three ligands most commonly used to synthesize metal precursors: β-diketonate, 1,1,1-trifluoroacetylacetonate and 1,1,1,5,5,5-hexafluoroacetylacetonate. This study presents the synthesis and successful use of eighteen novel fluorous precursors with ligands derived from Schiff bases and oximes.

One factor that can limit the usefulness of a precursor in the deposition of its metal particles is the precursor's solubility in supercritical carbon dioxide (Erkey, 2009). Some have also proposed that a precursor's being soluble is not only important, but that there may be a range of optimal solubility. It is postulated that if the precursor is too soluble, it can hinder the precursor from bonding to the substrate and may also allow for a bonded precursor to unbind from the substrate and return to the solution. On the other hand, if the precursor is not soluble enough then an even distribution of small particles is not observed. It has been shown that complexes with fluorine groups can be up to 100 times more soluble in scCO2 that their analogous complexes without fluorine. For this reason all the precursors synthesized for this study were made with fluorine groups. Some of the precursors were synthesized with only a few fluorine atoms while others had many, in order to test a wide range of solubility.

The synthesized ligands were either Schiff base or oxime derivatives, both of which are considered good chelating agents. The ligands were characterized by various methods including FT-IR and ^{1}H NMR. The complexes were synthesized from these ligands with nickel, palladium and tungsten metal centers. The complexes were characterized by FT-IR and ^{1}H NMR. The results from these analyses were in agreement with other reported data for similar compounds, which confirmed that the desired compounds were synthesized. Two attempted nickel complexes were unable to be synthesized.

The solubility of the complexes were tested qualitatively in $scCO_2$, all the complexes were found to be soluble.

The synthesized precursors were used to deposit nanoparticle metals on MWCNTs in $scCO_2$, which is an environmentally friendly process. The M/MWCNT composites were analyzed using XRD and SEM-EDX. These results showed that fluorous Schiff base and oxime derivatives were used successfully for deposition. The percent uptake of the metal was similar for the reported ligands as in previous research. The size of the nanoparticles was somewhat large for palladium and smaller than previously reported for nickel and tungsten. For most precursors an even distribution of the metal over the surface of the substrate was observed and with the exception of three Pd complexes, none of the composites had observable metal clusters.

The metal nanoparticles showed a homogenous distribution on the MWCNTs, with adsorbed nanoparticles ranging in sizes from 0.9-13.8nm (Ni:1.9-4.0nm, Pd:3.8-13.8 , W: 0.9-3.0nm). The percentage of metal was between 1.03 and 42.74%. The synthesized nanocatalysts proved to be thermally stable, soluble in common organic solvents and stable in an open environment.

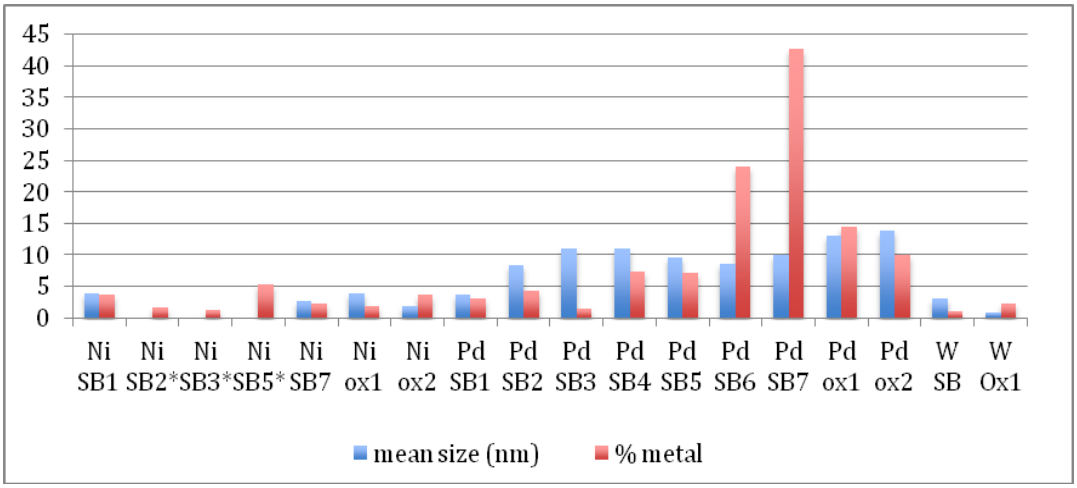

Figure 5.1. Relationship of % metal deposited and size of nanoparticles (*mean particle size was not able to be determined by XRD)

The relationship between the metal to support material ratio and the size of the nanoparticles is also a topic of research (Erkey, 2009). Figure 5.1 shows the relationship for the precursors used in this study. It can be seen that a clear correlation cannot be determined. More studies would need to be conducted to determine whether a correlation can be established.

All of the precursors that were successfully synthesized were also successfully deposited on MWCNTs. In this study, only nickel, palladium and tungsten metals were studied. However, there are many metals that react easily with oximes and Schiff bases and it is thought that further research could be done on the use of these ligands with different metal centers for deposition.

The precursors developed in this thesis were successfully used in the creation of nanocatalysts via the supercritical deposition of metal nanoparticles on MWCNTs. Although the precursor has been shown to have a large impact on the overall success of these deposition procedures, few studies have been done on the topic of novel and varied precursors. This research will add significantly to that number, and for that reason is an important study for the future of nanocatalysts synthesized via a supercritical deposition method.

This study included the synthesis of Schiff base and oxime ligands; however, in the future, this study is hoped to be expanded by researching the usefulness of polymer Schiff bases and salen molecules as ligands for precursors. Also, more research on a wider variety of tungsten precursors is hoped to be conducted.

In conclusion, 8 novel ligands (and one ligand that has been previously synthesized but that has not been used as a ligand for a precursor in deposition processes) were synthesized, 18 novel precursors were synthesized and successfully used in deposition. It was shown that similar results can be achieved for palladium and significantly smaller nanoparticle metals were synthesized for nickel and tungsten than have been previously reported, as far as the author is aware.

SOURCES

ABEYWICKRAMA, C., and BAKER, A.D.,2004. “Efficient Synthesis of 1,4,5,12-Tetraazatriphenylene and Derivatives”, American Chemical Society, 69, 7741-7744

ALEXANDROVA, A. "Atomic Scale Design: Chemistry." Atomic Scale Design Network, n.d. Web. 15 Dec. 2013

ALLHOFF, F., LIN, P., MOORE, D., 2010. “What is nanotechnology and why does it matter?: from science to ethics”, John Wiley and Sons, 3–5

ALONSO, F., RIENTE, P., YUS. M., 2009. “Transfer hydrogenation of olefins catalyzed by nickel nanoparticles”, Tetrahedron doi:10.1016/j.tet.2009.10.057

ANASTAS, P.T., 2010. Handbook of Green Chemistry: Volume 4 supercritical solvents

BELGHOUL, B., WELTERLICH, I., MAIER, A., TOUTIANOUSH, A., RABINDRANATH, A.R., TIEKE, B., 2007. “Supramolecular sequential assembly of polymer thin films based on dimeric, dendrimeric, and polymeric schiff-base ligands and metal ions”, Langmuir 23, 5062.

BHADURI GA , SILLER L,Nickel nanoparticles catalyze reversible hydration of carbon dioxide for Carbon Capture and Storage via Mineralization,CATALYSIS SCIENCE AND TECHNONLOGY, 3(5), 1234-1239, APR 2013

BLACKBURN, J. M., LONG, D.P., CABANAS, A., WATKINS, J.J., 2001. “Deposition of conformal copper and nickel films from supercritical carbon dioxide”, Science. 294, 141.

BOZBAG, S.E., ERKEY, C., 2011. “Supercritical Fluids in fuel cell research and development” J. of Supercritical Fluids, 62, 1-31

BOZBAG, S.E., ZHANG, L.C., AINDOW, M., ERKEY, C., 2012. “Carbon aerogel supported nickel nanoparticles and nanorods using supercritical deposition”, J. of Supercritical Fluids 66, 265

BROWN, S.M. HOWDLE, 2002. “Clean preparation of nanoparticulate metals in porous supports: a supercritical route”, J. Mater. Chem. 12, 1898.

CERVENY, L., 1989. “Palladium catalysts in hydrogenation reactions”, Chemical Engineering Communications, 83, 31-63

CHAKRABORTY, H., PAUL, N., RAHMAN, M.L., 1994. “Catalytic activities of Schiff base aquocomplexes of copper (II) towards hydrolysis of amino acid esters” Trans Met Chem (Lond) 19 , 524-526

CHATURVEDI, S., PRAGNESH, N.D., & SHAH, N.K., 2010. “Applications of nano-catalyst in new era”, Journal of Saudi Chemical Society, 1319-6103

COOMBS, R.R., RINGER, M.K., BLACQUIERE, J.M., SMITH, J.C. NEILSEN, J.S., UH, Y., GILBERT, J.B., LEGER, L.J., ZHANG, H., IRVING, A.M., WHEATON, S.L., VOGELS, C.M., WESTCOTT, S.A., 2005. “Palladium(II) Schiff base complexes derived from sulfanilamides and aminobenzothiazoles”, Transition Metal Chemistry, 30, 411-418

DAOUSHB W. M., LIMA B. K., MOA C. B., NAMA D. H., HONGA S. H., 2009. “Electrical and mechanical properties of carbon nanotube reinforced copper nanocomposites fabricated by electronless deposition process”, Materials Science and Engineering: A, 513–514, 247–253

DASH B., MAHAPATRA, P.K., PANDA, D., PATNAIK, L.M., 1984, “Fungicidal activities of Schiff bases derived from p-hydroxybenzaldehydes and their derivatives”, J Indian Chem Soc. 61, 1061-1064

DEMOPOULOS, G.P., 1986. “Solvent Extraction in precious metals refining”, JOM, 38, 13-17

DILLON, A.C., MAHAN, A.H., DESHPANDE, R., PARILLA, P.A., JONES, K.M., LEE, S-H., 2008. “Metal oxide nano-particles for improved electrochromic and lithium-ion battery technologies”, Thin Solid Films, 516, 794-797

EL-ANSARY, A.L., ABDEL-KADER, N.S., 2012. “Synthesis, Characterization of La(III), Nd(III), and Er(III) Complexes with Schiff Bases Derived from Benzopyran-4-One and Their Fluorescence Study”, International Journal of Inorganic Chemistry, 2012, 901415.

ERKEY, C., 2009. “Preparation of metallic supported nanoparticles and films using supercritical fluid deposition”, J. Supercrit. Fluids. 47, 517

FENG, Z.Q., YANG, X.L., YE, Y.F., 2013. “Pd(II) and Zn(II) based complexes with Schiff base ligands: Synthesis, characterization, luminescence, and antibacterial and catalytic activities”, The Scientific World Journal, 2013, Article ID 956840

GAOWEN, Y., XIAPING, X., HUAN, T., CHENXUE, Z., 1995. “Synthesis and anti tumor activity of Schiff base coordination compounds”, Chem. Abstr., 123:101089.

GHARAH, N., CHAKRABORTY, S., MUKHERJEE, A.K., BHATTACHARYYA, R., 2009. “oxoperoxomolydenum(VI)- and tungsten(VI) complexes with 1-(2’-hydroxyphenyl) ethanone oxime: synthesis, structure and catalytic uses in the oxidation of olefins, alcohols, sulfides and amines using H2O2 as a terminal oxidant”, Inorganica Chimica Acta, 362, 1089-1100

GILANI, S.R., MAHMOOD, Z., 2003. “Synthesis and Characterization of Cu(II) Complexes with Schiff Base of Salicylidene-4-Tri-Flouro-Methyl Aniline and its Hydrogen Analouge” Jour, Chem, Soc. Pak. 5, 34-36

GRUMUS, F., GURKAH, P., GUNDUZ, N., ABBASOGLU, U., 1994. “In vitro antibacterial activities of Schiff bases and Ni(II) complexes”, Chem Abstr, 121, 153127

HEGAZY, W.H., GAAFAR, A.E.D.M., 2012. “Synthesis and characterization and antibacterial activities of new Pd(II) and Pt(IV) complexes of some nonsymmetrical tetradentate Schiff Bases”, American Chem. Sci. Journal, 2, 86-99

HUNECK, S., SCHREIBER, K., GRIMMECKE, H.D., 1985. “Schiff bases and derived secondary amines as plant growth inhibitors, Chem Abstr, 102, 1871.

IBRAHIM, W. N. W., SHAMSUDDIN, M., 2012, “Symmetrical Palladium (II) N,N,O,O-Schiff Base Complex: Efficient catalyst for heck and Suzuki reactions”, Crystal Structure Theory and Applications, 1, 25-29.

IREZ, G. AND BEKAROGLU, O. 1983. The Synthesis and Complex Formation of Some New Substituted Amino and Diaminoglyoximes. Synth. React. Inorg. Met.-Org. Chem., 13, 781-797.

KANAN, S.M., EL-KADRI, O.M., ABU-YOUSEF, I.A., KANAN, M.C., 2009. "Semiconducting metal oxide based sensors for selective pollutant detection", Sensors, 9, 8158-8196

KAUL, B., 1986. "Metal complex dyes and their use for dyeing plastic compositions", Chem. Abstr., 104, 150788

KHALIL, M.M.H., ISMAIL, E.H., MOHAMED, G.G., ZAYED, E.M., BADR, A., 2012. "Synthesis and characterization of a novel Schiff base metal complexes and their application in determination of iron in different types of natural water", Open Journal of Inorganic Chem, 2, 13-21

KIM, J.N., RYU, E. K., 1992. "Regeneration of carbonyl compounds from their nitrogeneous derivatives: chemical transformation of the dicarbonyl compounds", Bull. Korean Chem. Soc. 13, 184-187

KUMAR, S., DHAR, D. N., AND SAXENA, P. N., 2009. "Applications of metal complexes of Schiff bases-a review," Journal of Scientific and Industrial Research, 68, 181–187

LIN, CHI-KAI, 2001. "Novel synthesis and characterization of precious-metal nanocatalysts for clean energy applications", N. IL. Uni. 128

LIN, Y.H., CUI, X.L., YEN, C., WAI, C.M., 2005. "Platinum/carbon nanotube nanocomposite synthesized in supercritical fluid as elecrocatalysts for low-temperature fuel cells", J. Phys. Chem. B. 109, 14410

MARTINEZ, L., GANCHEFF, J.S., HAHN, F.E., BURROW, R.A., GONZALEZ, R., KREMER, C., CHIOZZONE, R., 2013. "Nickel(II) complexes with methyl(2-pyridyl)ketone oxime: synthesis, crystal structure and DFT calculations", Spectrochimica Acta Part A: Molecular and bimolecular spectroscopy, 105, 439-445

MARWAN, K.R., 1970. "Process of treating leather and fibrous material with polyisocyanate derivatives" US3493426 A

MATHIS, R.D., TAYLORS, DIX, J.S., 1974. “Polymer of 1-olefins protected against ultraviolet light”, US3786021

MENG, F., ZHAO, Q., LI, M., XIN, Y., 2002. *Yingying Huaxue*, 19, 1183-1185

MENNICKE, W., WESTPHAL, 1986. “Mixtures of 1:2 chromium complex dyes, Chem Abstr, 104, 111359.

MORLEY, S.K., MARR, P.C., WEBB, P.B., BERRY, A.R., ALLISON, F.J., MOLDOVAN, G., BROWN, P.D., HOWDLE, S.M., 2002. Clean preparation of nanoparticulate metals in porous supports: a supercritical route, J. Mater. Chem. 12, 1898

NEJO, A.A., 2009. “Metal (II) Schiff base complexes and the insulin-mimetic studies on the oxovanadium (IV) complexes”, University of Zululand, 188 pages; 206001421.

NISHINAGA, A., YAMADA, T., FUJISAWA, H., ISHIZAKI, K., 1988. “Catalysis by cobalt Schiff complexes in the oxygenation of alkenes on the mechanism of ketonization” J. Mol. Catal., 48, 249-264.

PANZIO, G. VE BALDROCCO, F., 1930, Ricerche Sulle Diossime, Gazzetto Chemica Italiana, 60, 415-429

PARK P. W., LEDFORD J. S., 1998. “The influence of surface structure on the catalytic activity of alumina supported copper oxide catalysts. Oxidation of carbon monoxide and methane”, Applied Catalysis B: Environmental, 15, 221–231

PENG, Q., SPAGNOLA, J.C., PARSONS, G.N., 2008. “Self-catalyzed hydrogenolysis of nickelocene: functional metal coating of three-dimensional nanosystems at low temperature”, J. Electrochem. Soc. 155, D580.

PHATAK, P., JOLLY, V.S, SHARMA, K.P., 2000. “Synthesis and anticancer activity of Schiff bases of indole-2-carboxadehydes”, Orient J. Chem. 16, 493-494.

RATHER S., ZACHARIA R., HWANG S. W., NAIK M., NAHM K. S., (2007). “Hydrogen uptake of palladium-embedded MWCNTs produced by impregnation and condensed phase reduction method”, Chemical Physics Letters, 441, 261–267

"Recognizing the Best in Innovation: Breakthrough Catalyst". R&D Magazine, September 2005, p. 20

REIBOLD, M., PAUFLER, P., LEVIN, A.A., KOCHMANN, W., PÄTZKE, N., MEYER, D.C., 2006. "Materials: Carbon nanotubes in an ancient Damascus sabre", Nature 444 (7117), 286.

REID, R.C., PRAUSNITZ, J.M., POLING, B.E. 1987. “The properties of gases and liquids, 4th edition”, McGraw-Hill: New York, NY

SCHROCK, R. R., HOVEYDA, A. H., 2003. “Molybdenum and Tungsten Imido Aklylidene complexes as efficient olefin-metathesis catalysts”, Chem. Int. Ed 42, 4592-4633

SMART, N.G., CARLESON, T., KAST, T., CLIFFORD, A.A., BURFORD, M.D., WAI, C.M., 1997. “Solubility of chelating agents and metal-containing compounds in supercritical fluid carbon dioxide”, Talanta 44, 137

SMOKEFOOT, Wikipedia, Catalysis, Web. 19 July 2009, 15 Dec 2013

SOGA, S., SHARMA, S.V., SHIOTSU, Y., SHIMIZU, M., TAHARA, H., YAMAGUCHI, K., IKUINA, Y., MURAKATA, C., TAMAOKI, T., KUREBAYASHI J., SHULTE, T.W., NECKERS, L.M., AKINAGA, S., 2001. “Stereospecific antitumor activity of radicicol oxime derivatives”, Cancer Chemother Parmacol, 48, 435-445

SPIVEY, J. J., 2002. Catalysis. Royal Soc. Of Chem. 239

STRÖCK, M, 2006. “A 3D model of a en:C60 molecule, also called a ‘Buckyball’”

SUNEEL, S.D., Industrial Production Engineering, n.d. Web. 15 Dec 2013

TRENDAFILOVA, N., BAUER, G., GEORGIEVA, I., DODOFF, N., 1999. “Synthesis and vibrational study of platinum(II) and palladium(II) complexes of glyoxilic acid oxime”, Spectrocimica Acta Part A, 55, 2849-2859

UH, Y, ZHANG, H., VOGELS, C.M., DECKEN, A. WESTCOTT, S. A., 2004. “Palladium (II) Schiff base complexes derived from allylanime and vinylaniline”, Bull. Korean chem. Soc. 25, 7

WERMUTH, C.G., SCHWARTH 2, J., 1977, “Improvements in or to o-Aminoalkyl Oximes Ing. Pat.N. 14743.

WIESER, E., 2010. “A multi-walled armchair carbon nanotube, rendered in POVRay”

Xi, Z., Liu, W., Cao, G., Du, W., Huang, J., Cai, K., Guo, H., 1986. “Catalytic oxidation of naphthol by metalloporphyrins” Cuihau Xuebao, 7, 357-363

YE, X.R., LIN, Y., WAI, C.M., 2003. “Decorating catalytic palladium nanoparticles on carbon nanotubes in supercritical cabon dioxide”, Chem. Commun. 5, 64

ZHANG, Y., ERKEY, C., 2006. “Preparation of supported metallic nanoparticles using supercritical fluids: a review”, J. of Supercritical Fluids, 38, 252-26

ZHAO, Y.D., PAND, D.W., ZONG, Z., CHENG, J.K., LUO, Z.F., FENG, C.J., SHEN, H.Y., ZHUNG, X.C., 1988. “Electrochemical studies of antitumor drugs, fundamental electrochemical characteristics of an iron(III) Schiff base complex and its interaction with DNA”, Huaxe Xuebao, 56:178-183

ZHENG, Q.R., GU, A.Z., LU, X.S., LIN, W.S., 2005. “Adsorption equilibrium of supercritical hydrogen on multi-walled carbon nanotubes”, Journal of Supercritical Fluids 34, 71

ZHOU, X., JIN, ZHAO, J., SANTOS, A.M, KÜHN, F.E., 2004. “Molybdenum(VI) cis-dioxo complexes with chiral Schiff base ligands: synthesis, characterization, and catalytic applications”, Z. Naturforsch. 59b, 1223-1228

CURRICULUM VITAE

The author was born in 1984 in Las Vegas, Nevada. She graduated from Spencer High School in Spencer, IA in 2002. In 2006, she graduated with a Bachelors of Science in Chemistry from Iowa State University. In 2010, she was admitted into the Ph.D. program at Çukurova University in Adana, Turkey.

APPENDIX

Appendix 1

FT-IR spectrum of SB1

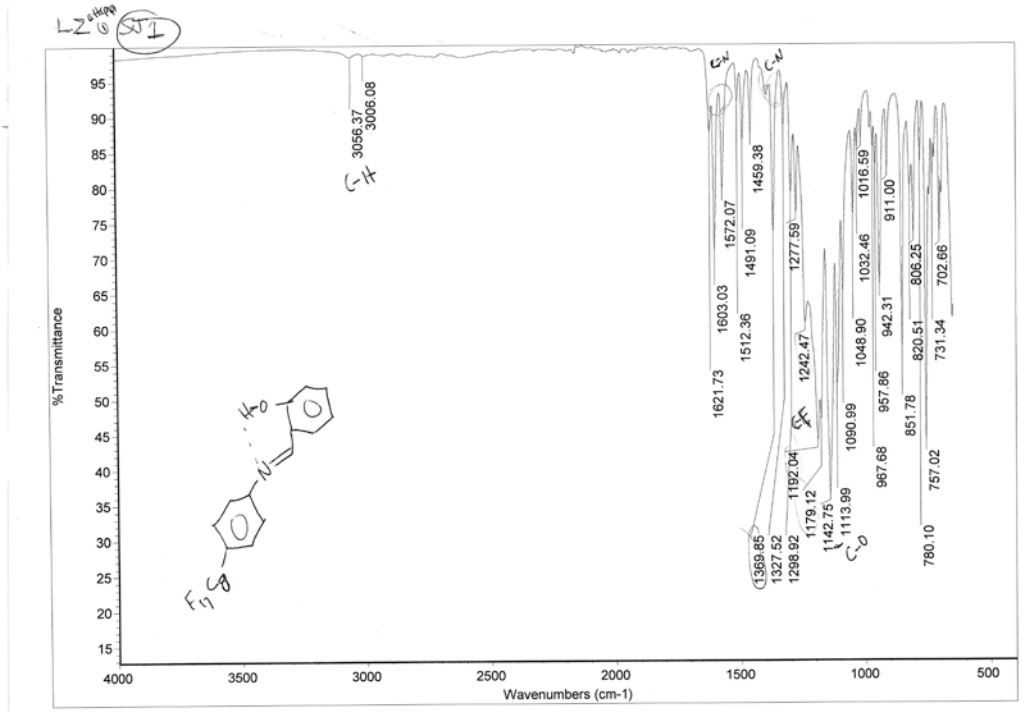

Appendix 2

^{1}H NMR spectrum of SB1

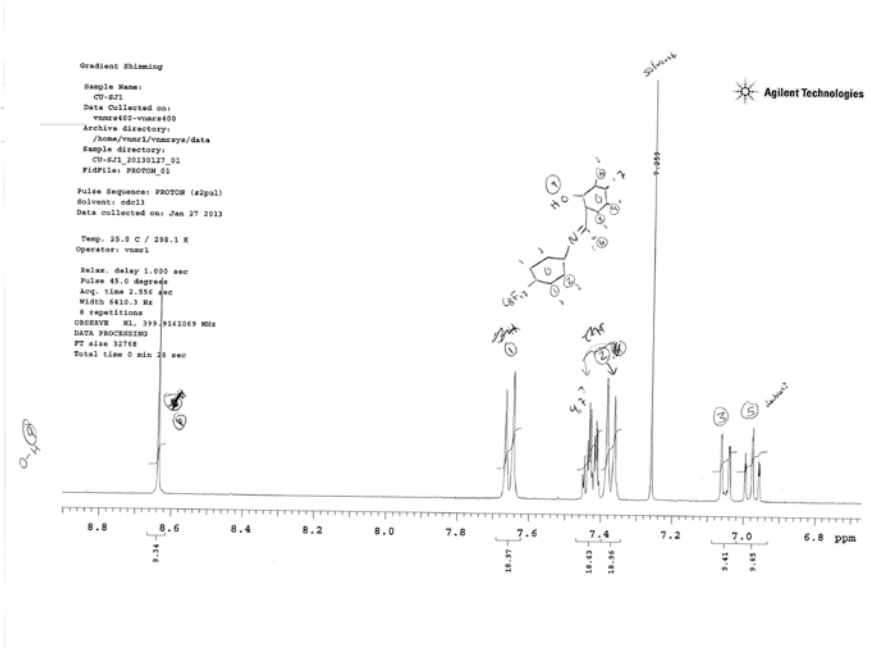

Appendix 3

^{19}F NMR spectrum of SB1

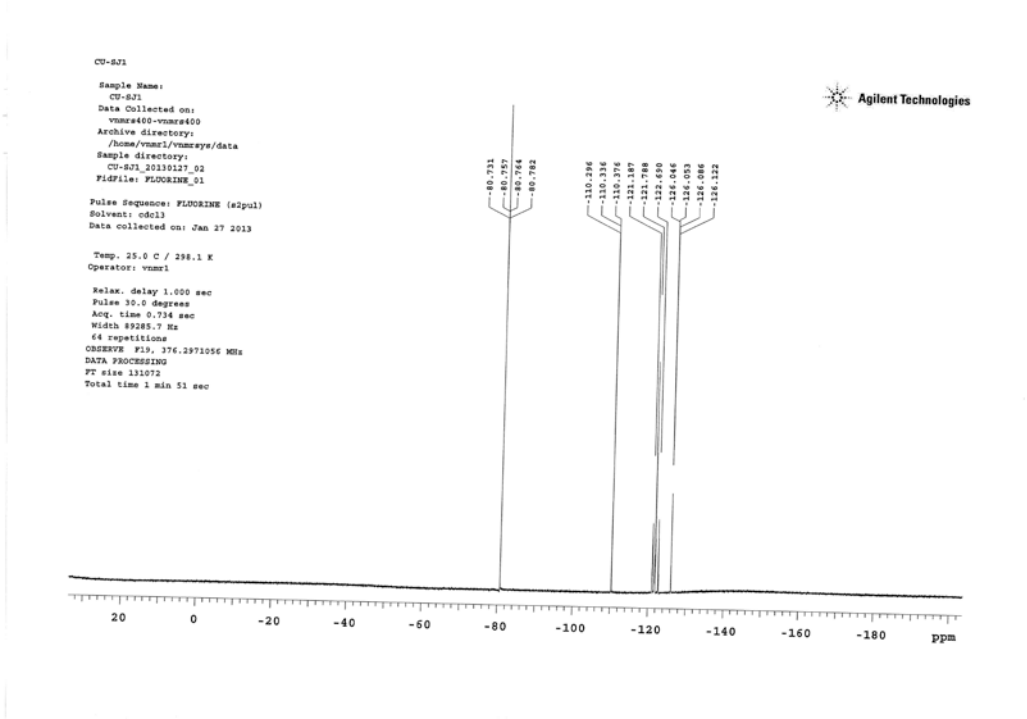

Appendix 4

FT-IR data of SB2

Appendix 5

^{1}H NMR spectrum of SB2

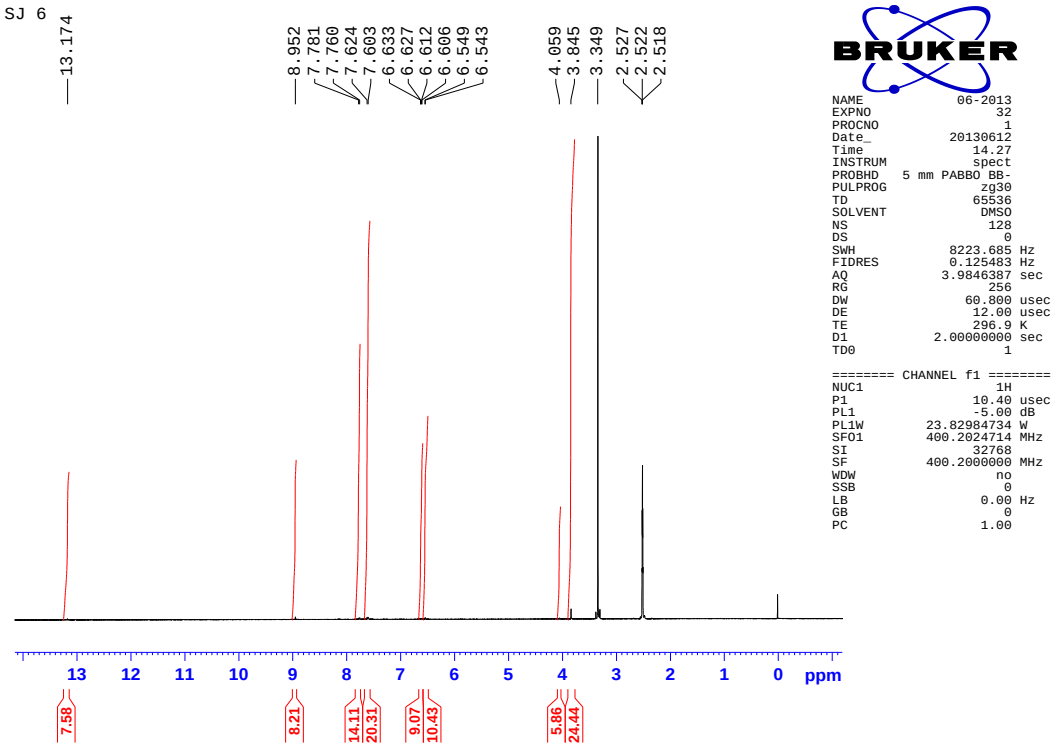

Appendix 6

FT-IR spectrum of

SB3

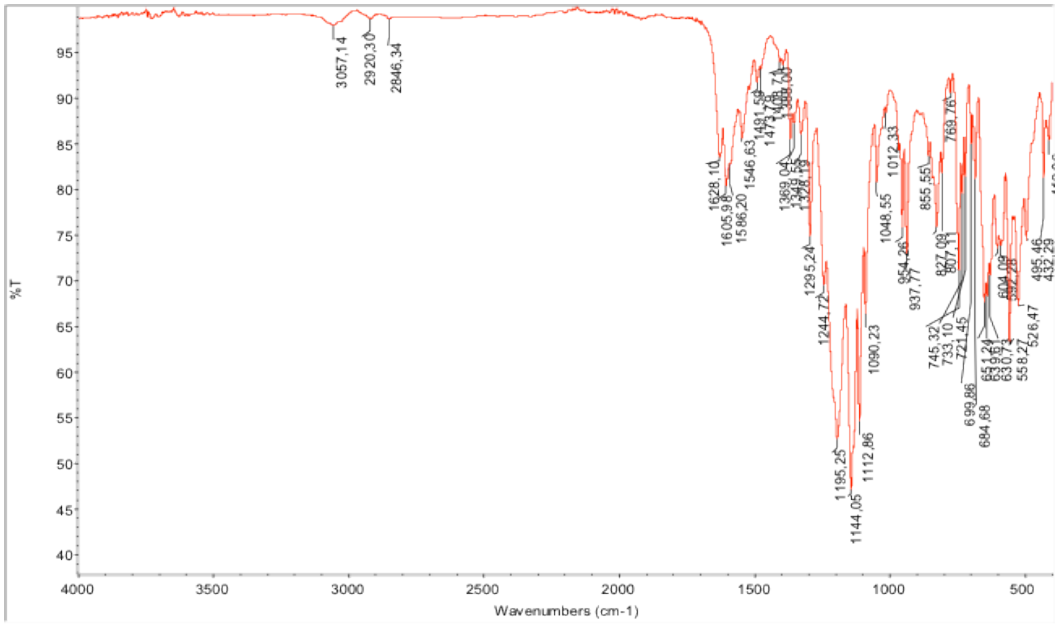

Appendix 7

^{1}H NMR spectrum of SB3

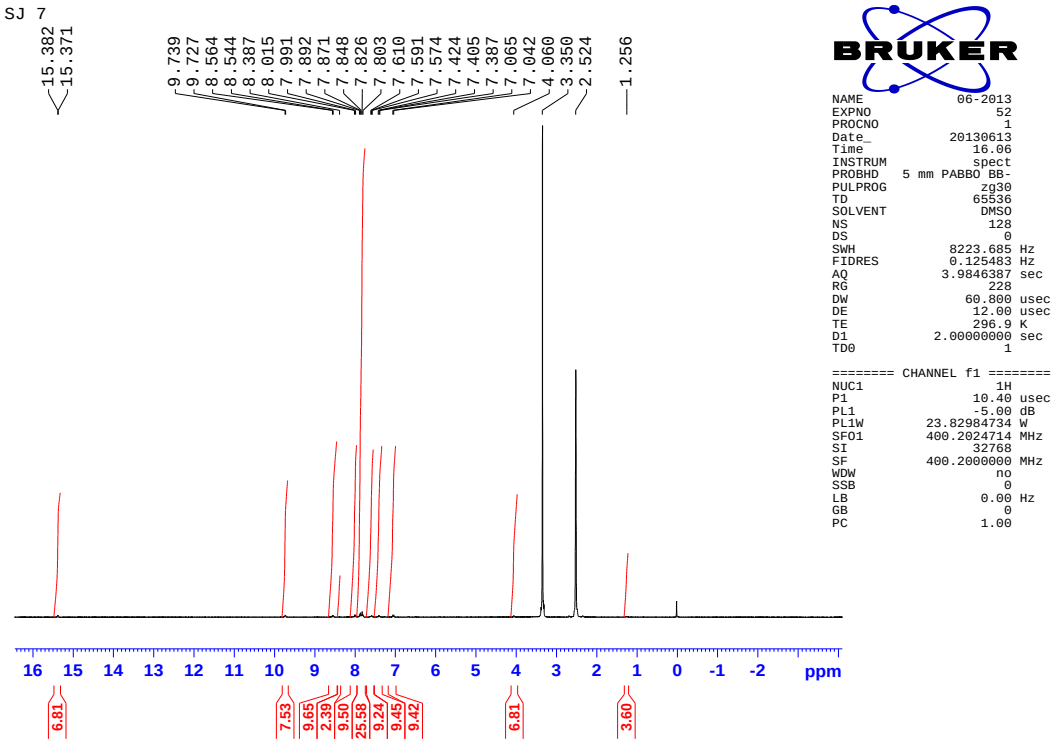

Appendix 8

FT-IR spectrum for SB4

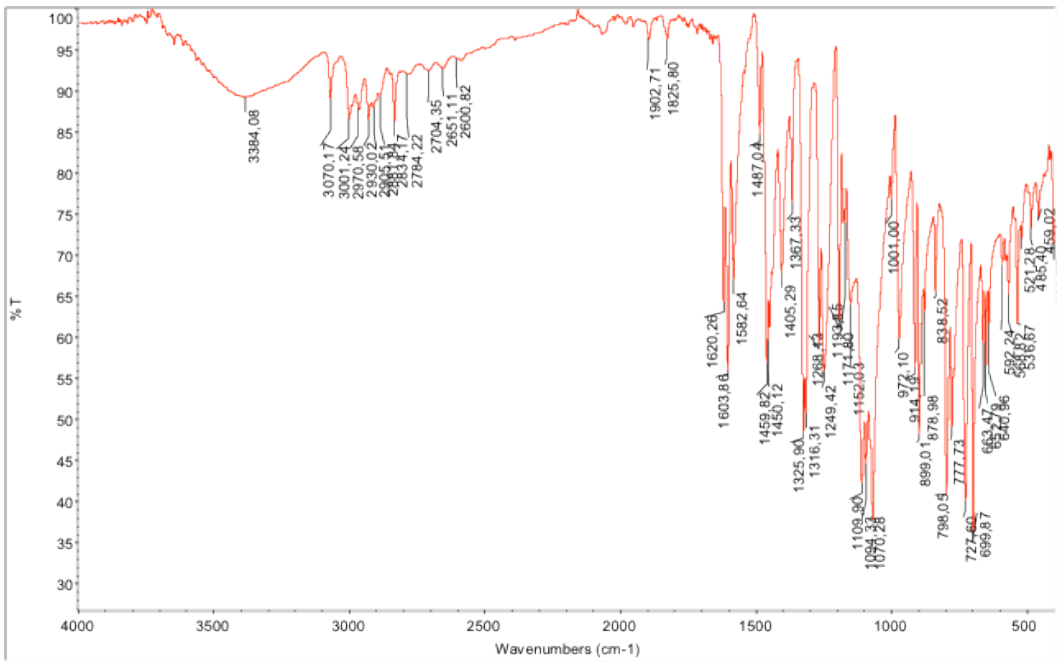

Appendix 9

^{1}H NMR spectrum of SB4

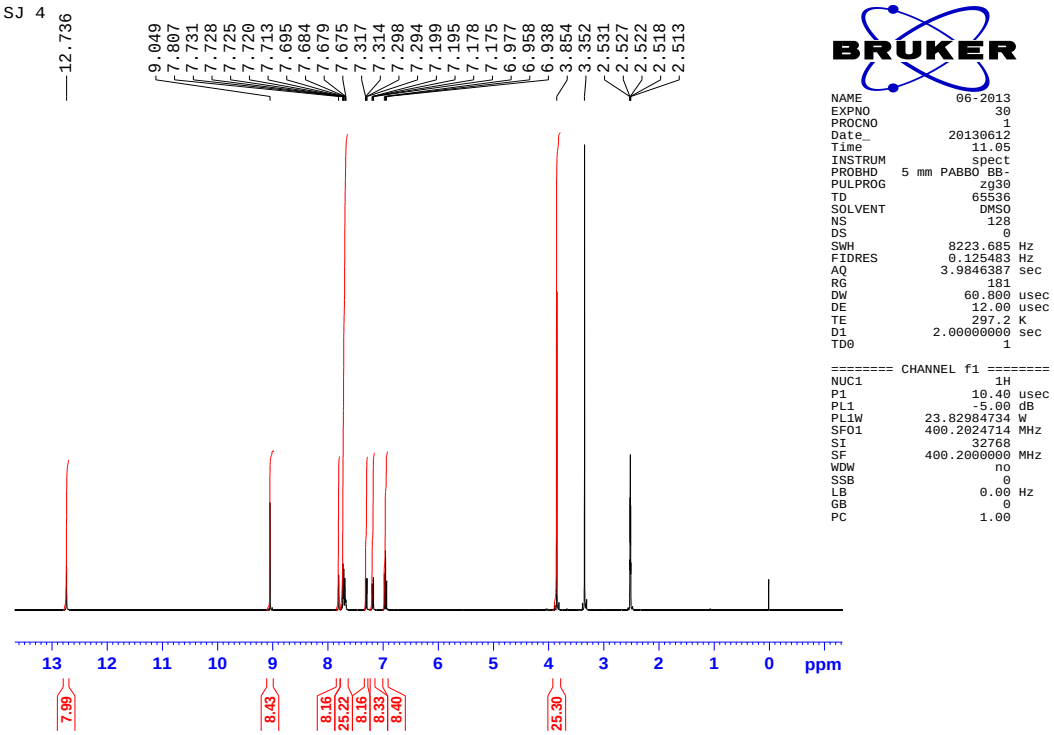

Appendix 10

FT-IR spectrum of SB5

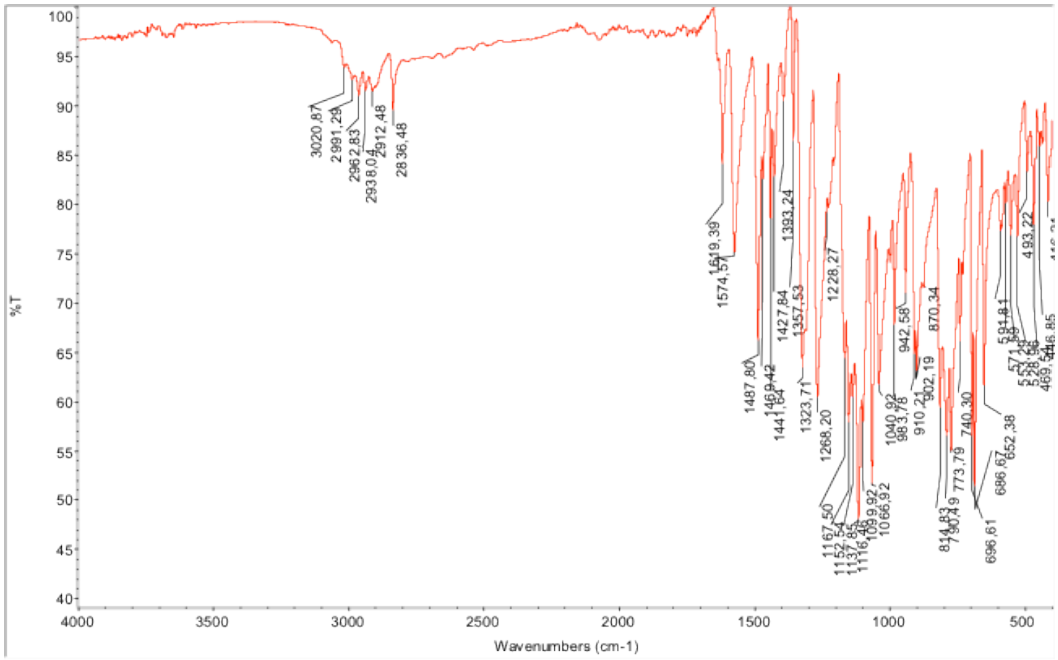

Appendix 11

^{1}H NMR spectrum of SB5

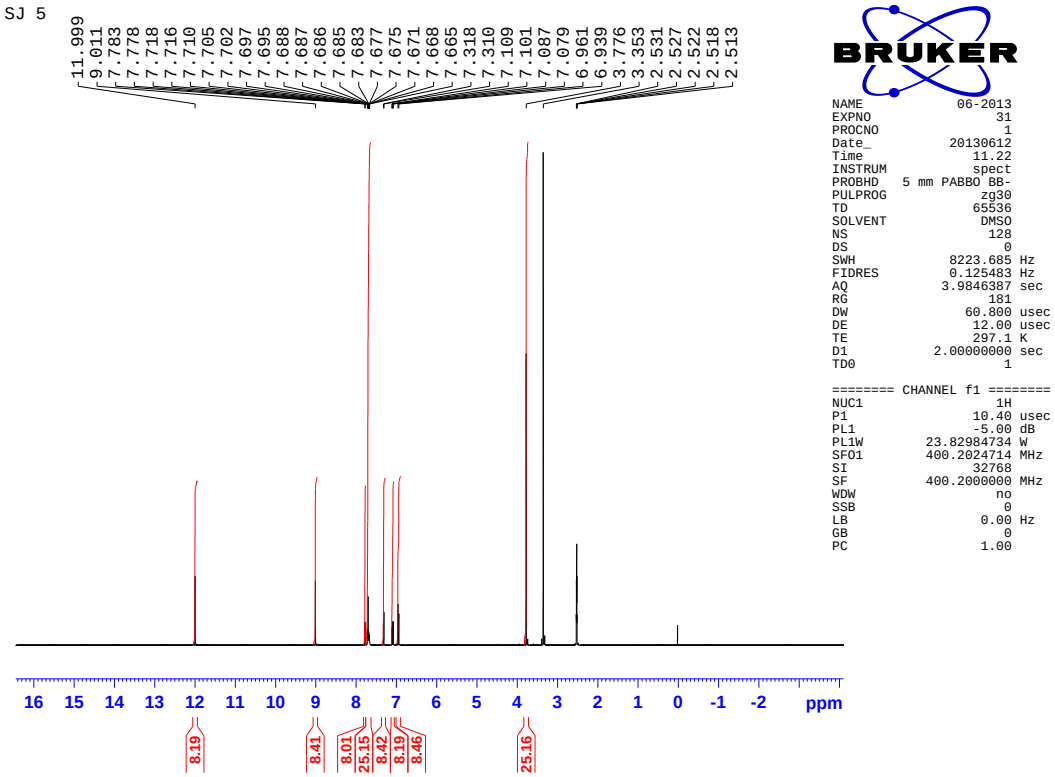

Appendix 12

FT-IR spectrum of SB6

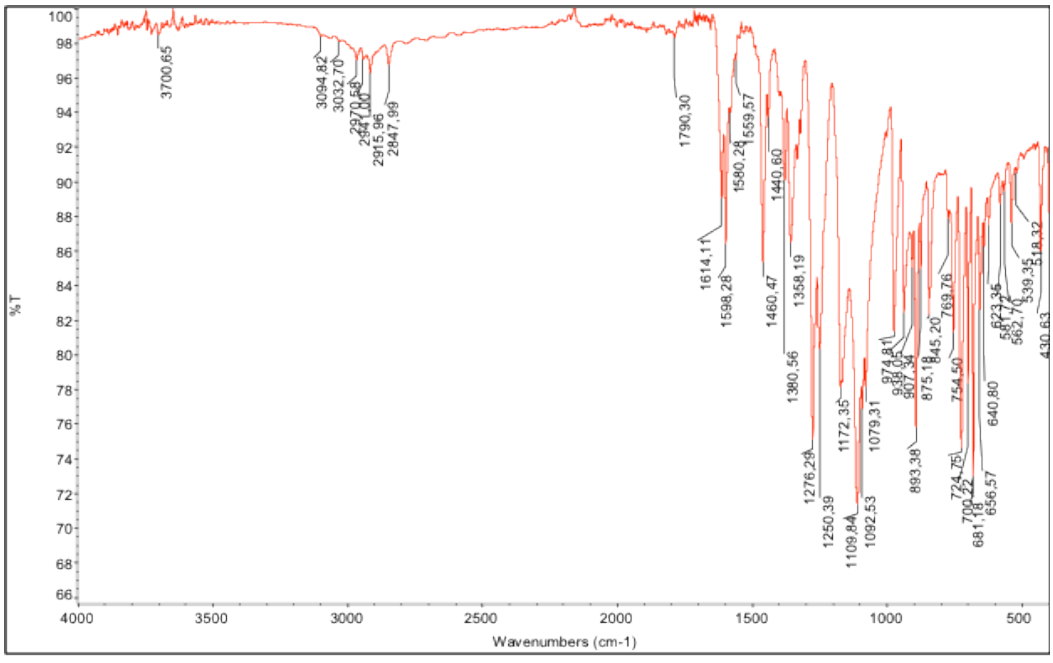

Appendix 13

^{1}H NMR spectrum of SB6

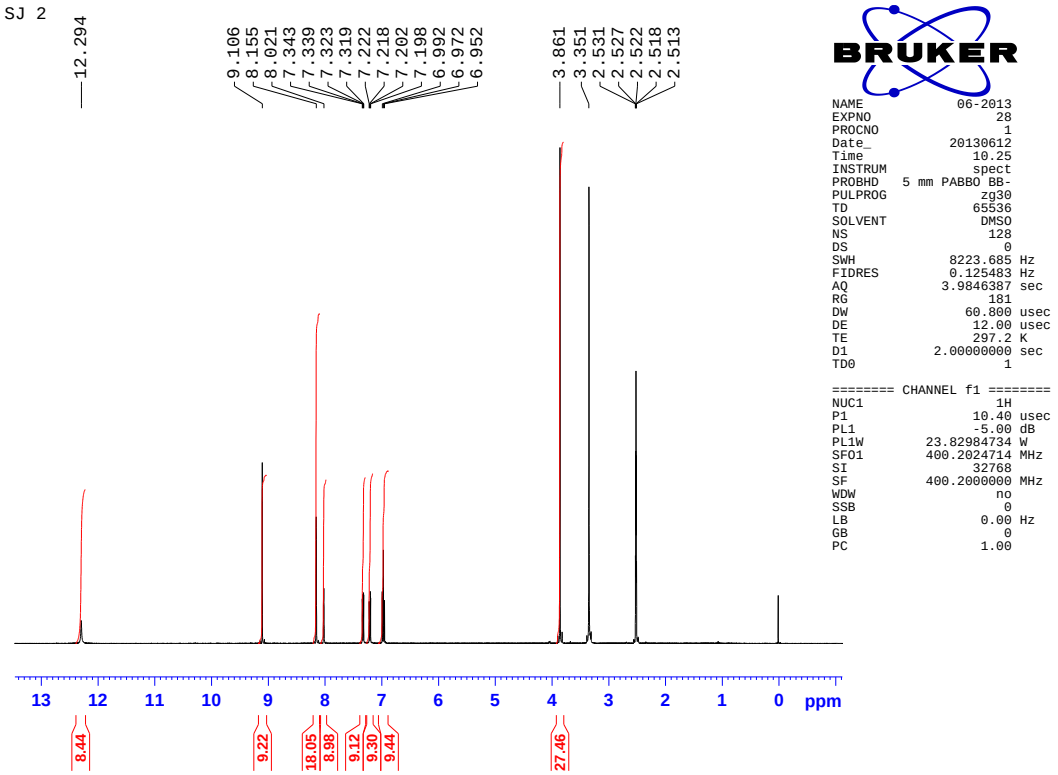

Appendix 14

FT-IR spectrum of SB7

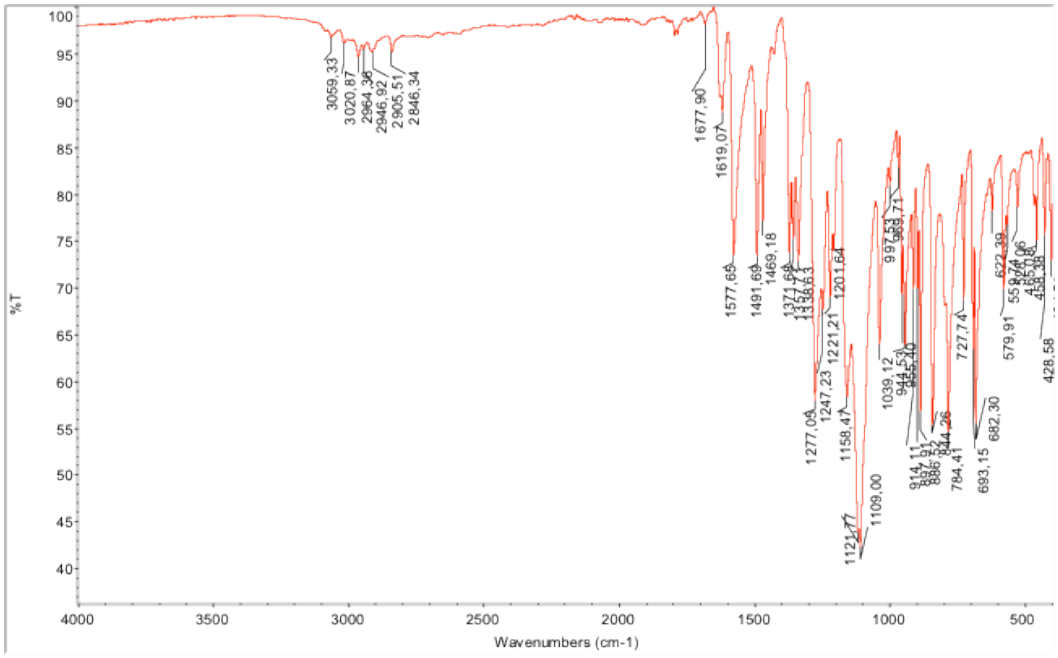

Appendix 15

^{1}H NMR spectrum of SB7

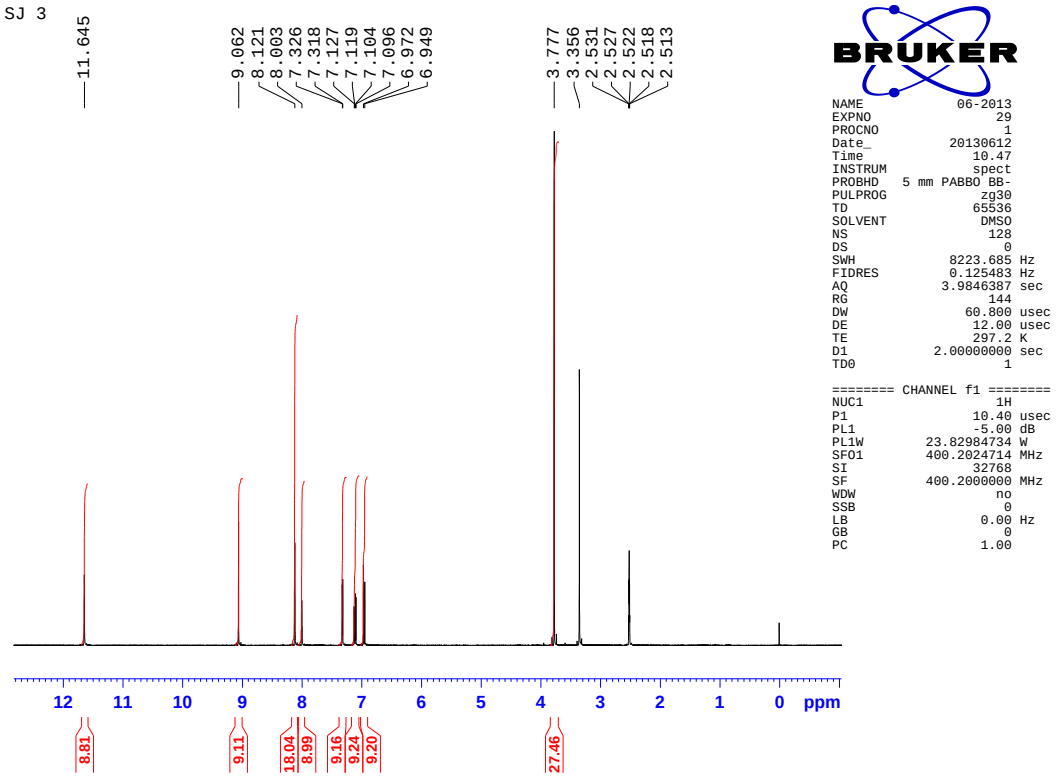

Appendix 16

FT-IR spectrum of ox1

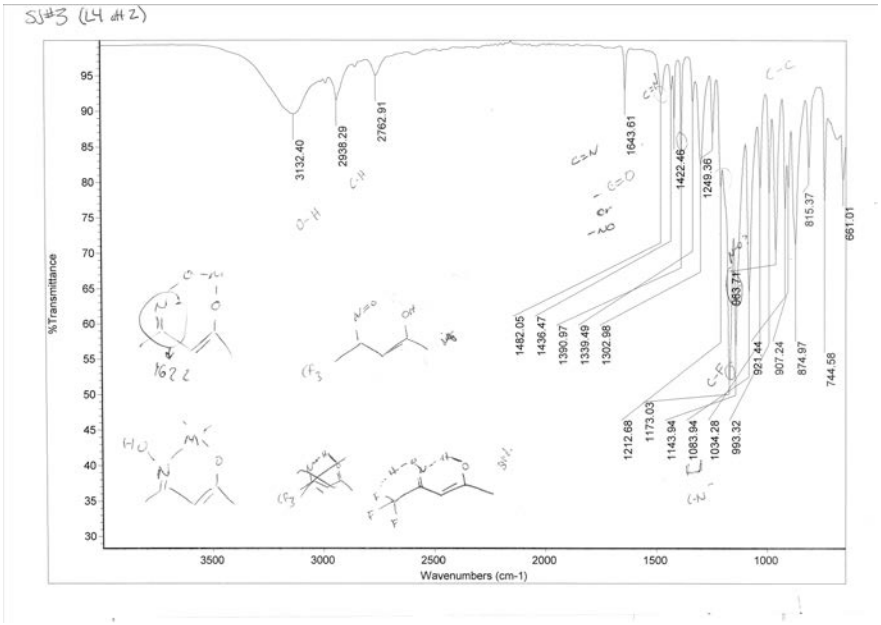

Appendix 17

^{1}H NMR spectrum for ox1

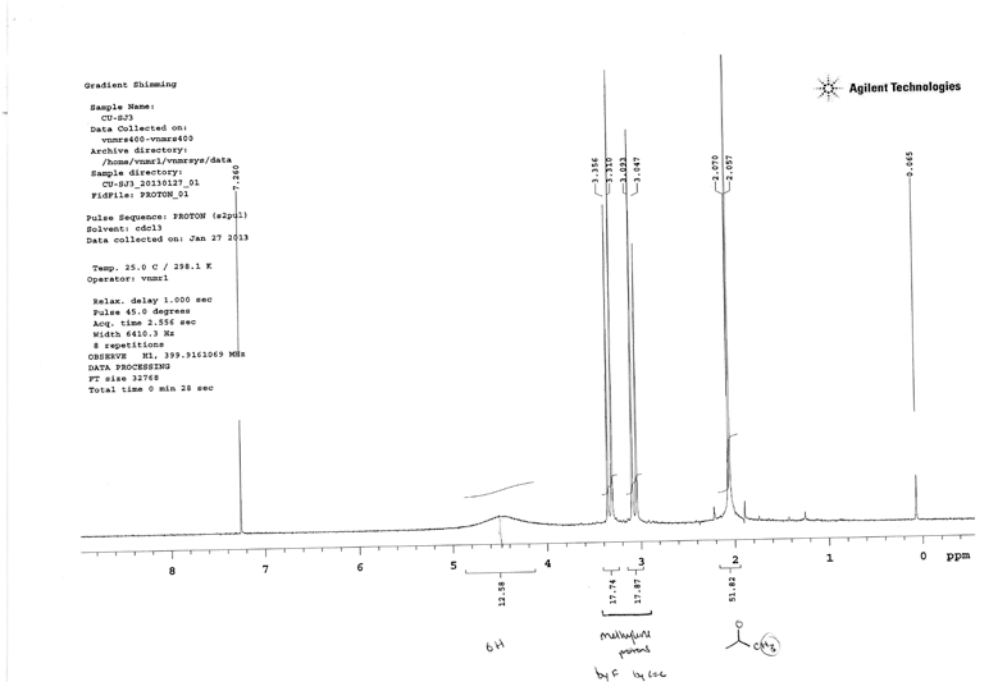

Appendix 18

^{13}C NMR spectrum for ox1

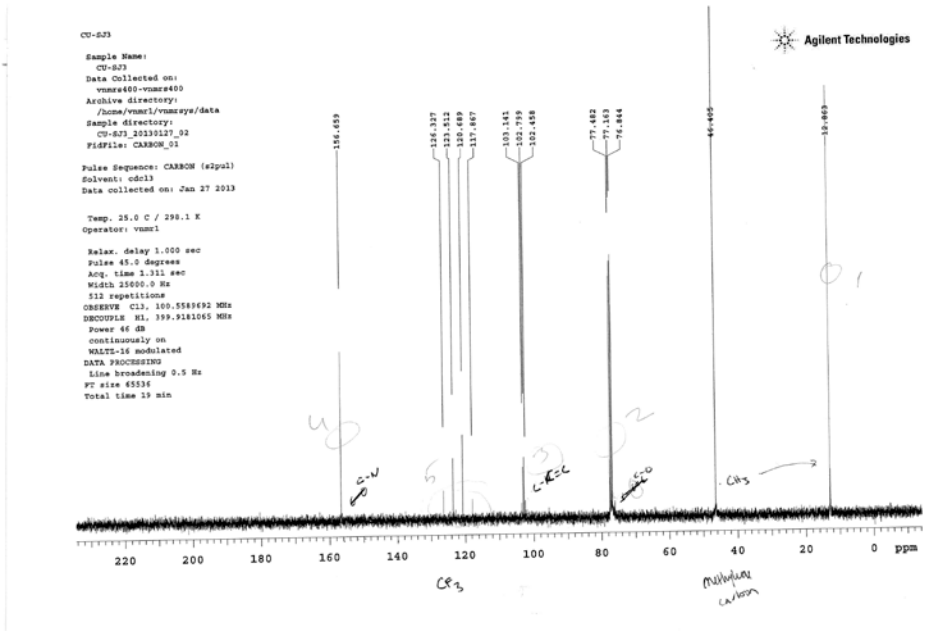

Appendix 19

FT-IR spectrum of

ox2

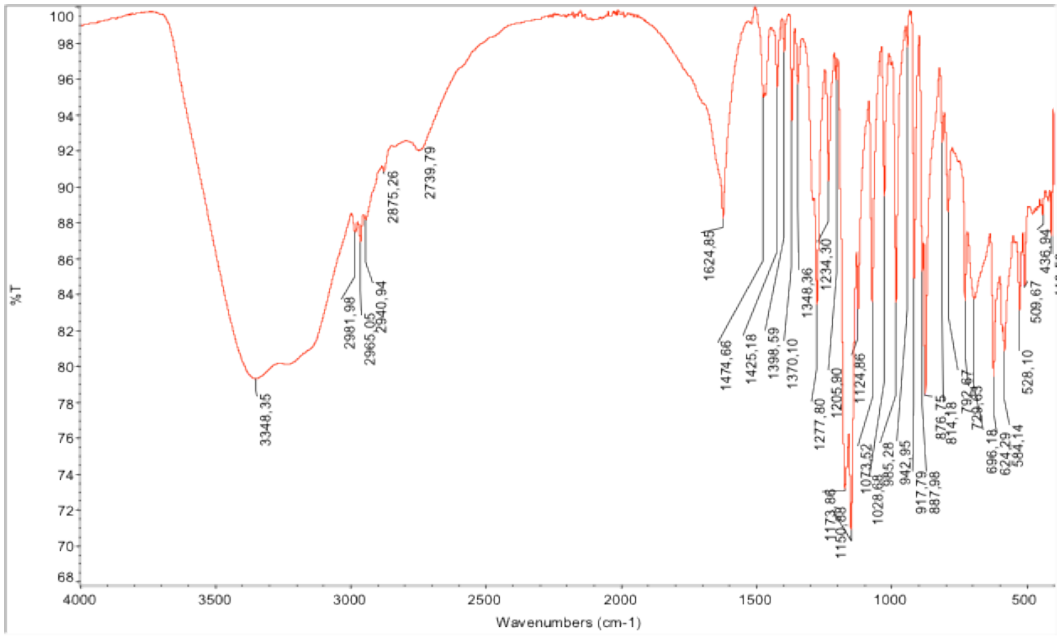

Appendix 20

^{1}H NMR spectrum of ox2

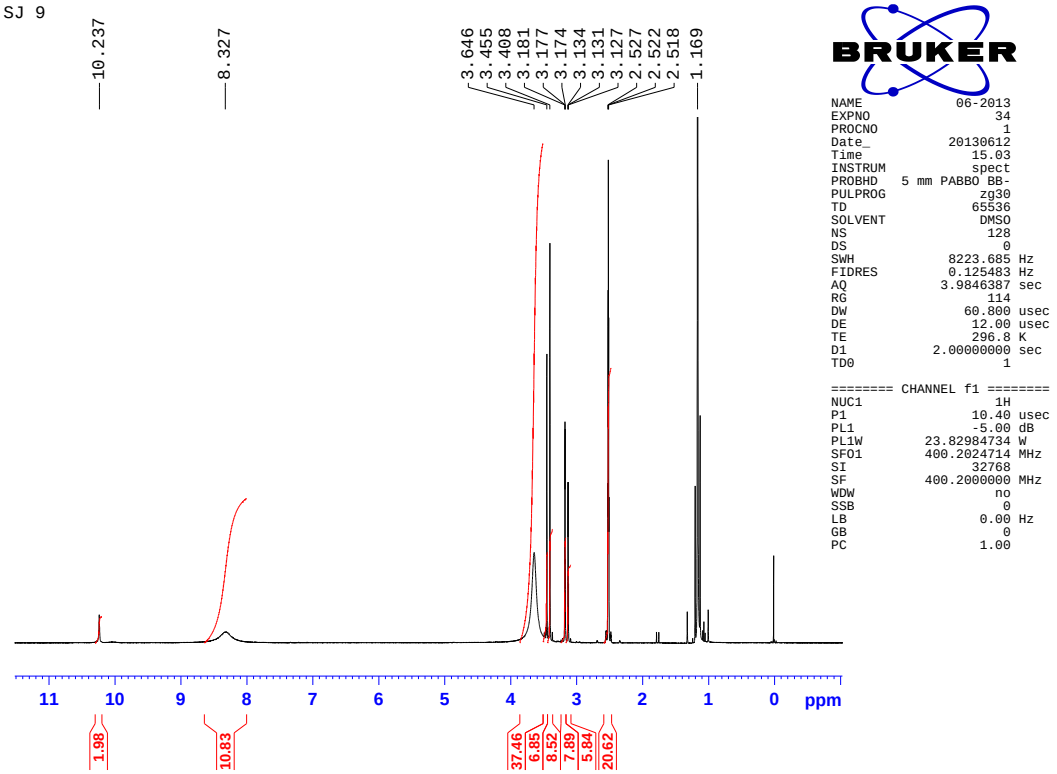

Appendix 21

FT-IR spectrum of Ni-SB1

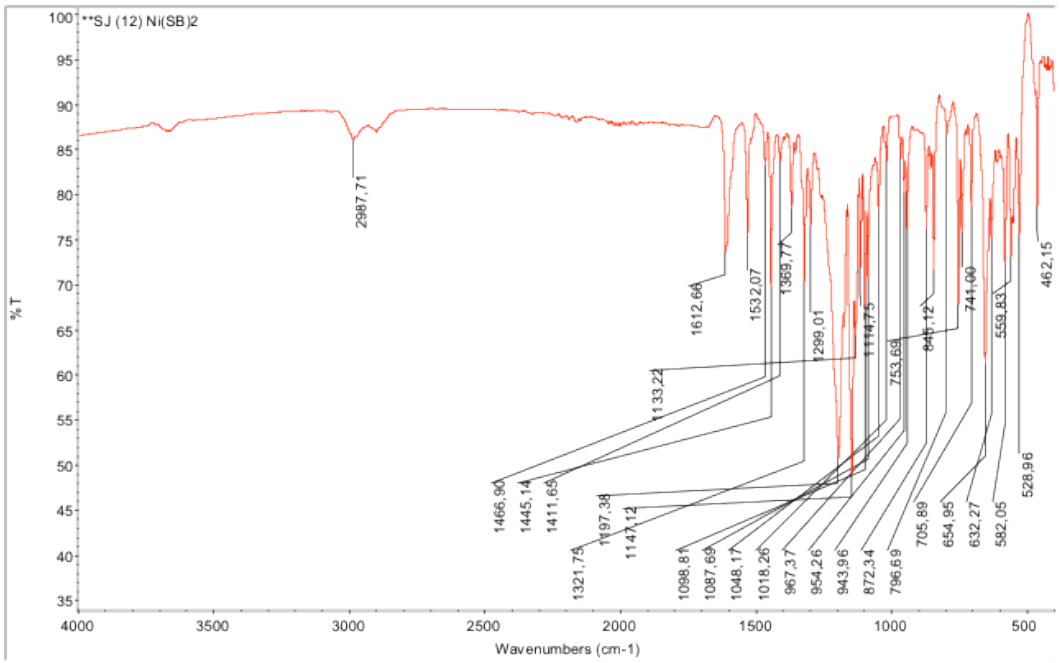

Appendix 22

^{1}H NMR spectrum for Ni-SB1

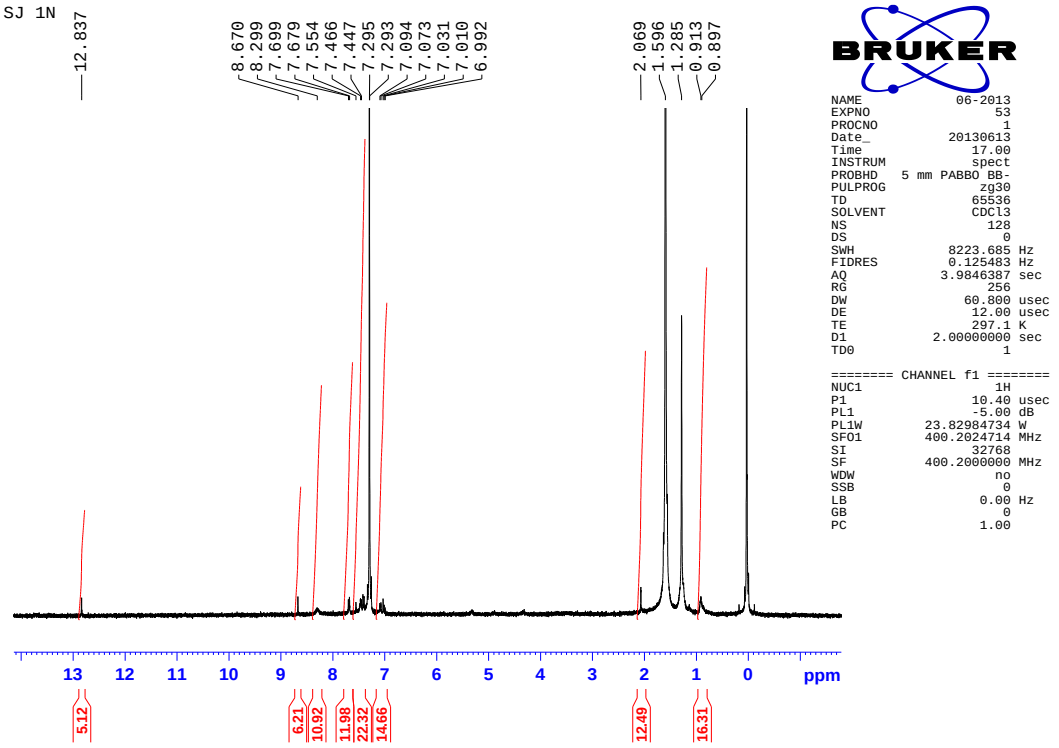

BRUKER

NAME	06-2013
EXPNO	53
PROCNO	1
Date_	20130613
Time	17.00
INSTRUM	spect
PROBHD	5 mm PABBO BB-
PULPROG	zg30
TD	65536
SOLVENT	CDCl3
NS	128
DS	0
SWH	8223.685 Hz
FIDRES	0.125483 Hz
AQ	3.9846387 sec
RG	256
DW	60.800 usec
DE	12.00 usec
TE	297.1 K
D1	2.00000000 sec
TD0	1
======== CHANNEL f1 ========	
NUC1	1H
P1	10.40 usec
PL1	-5.00 dB
PL1W	23.82984734 W
SFO1	400.2024714 MHz
SI	32768
SF	400.2000000 MHz
WDW	no
SSB	0
LB	0.00 Hz
GB	0
PC	1.00

Appendix 23

FT-IR spectrum of Ni-SB2

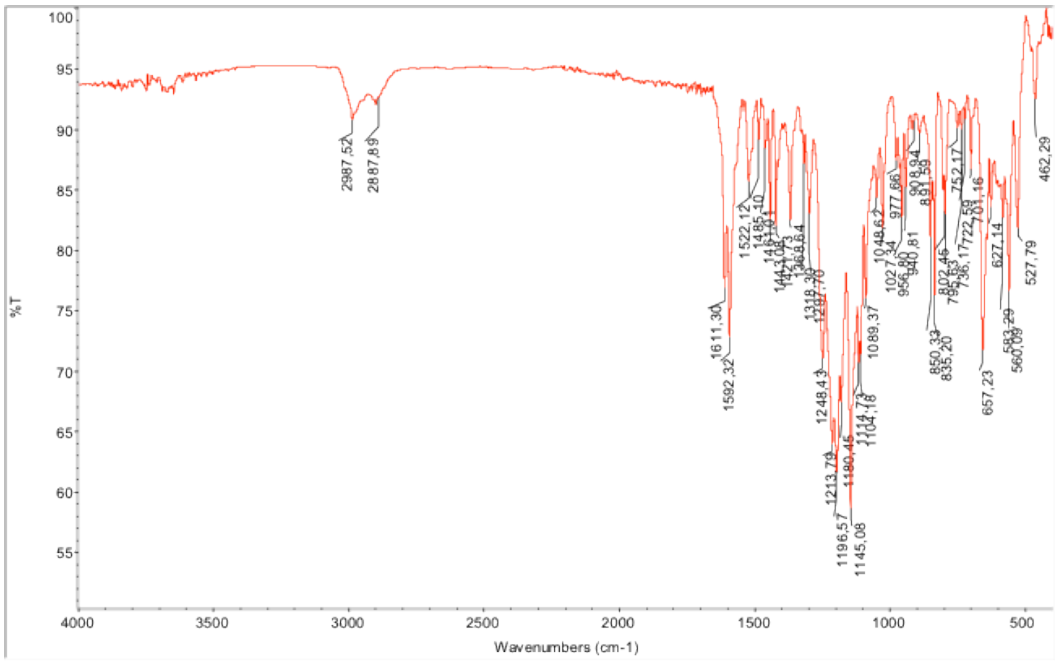

Appendix 24

^{1}H NMR spectrum of Ni-SB2

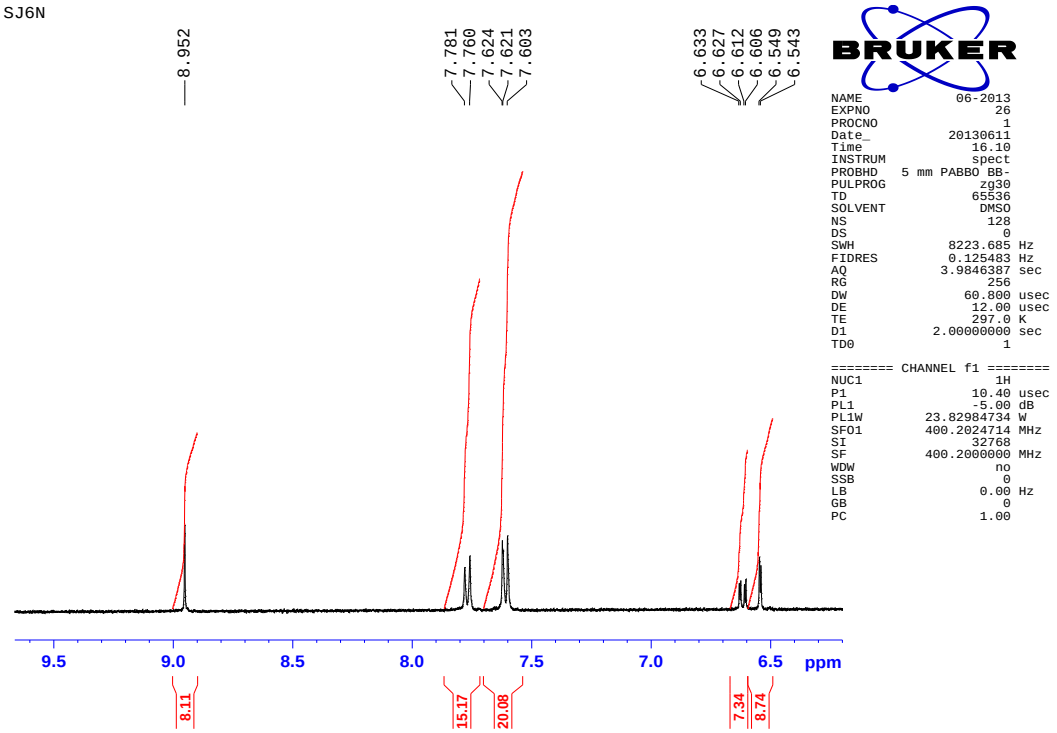

Appendix 25

FT-IR Spectrum of Ni-SB3

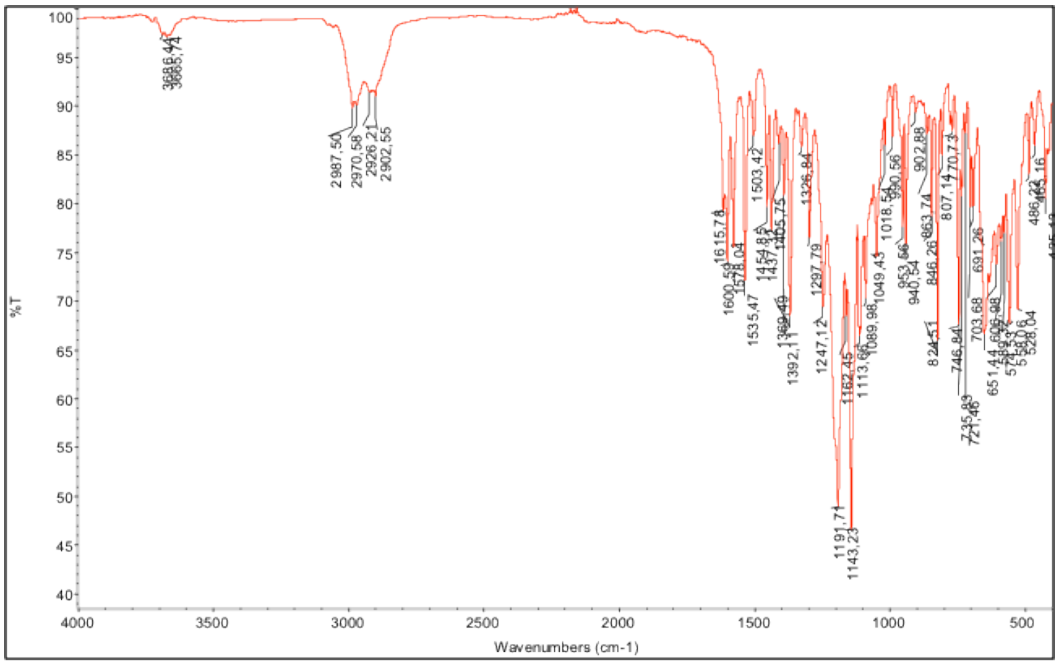

Appendix 26

^{1}H NMR spectrum of Ni-SB3

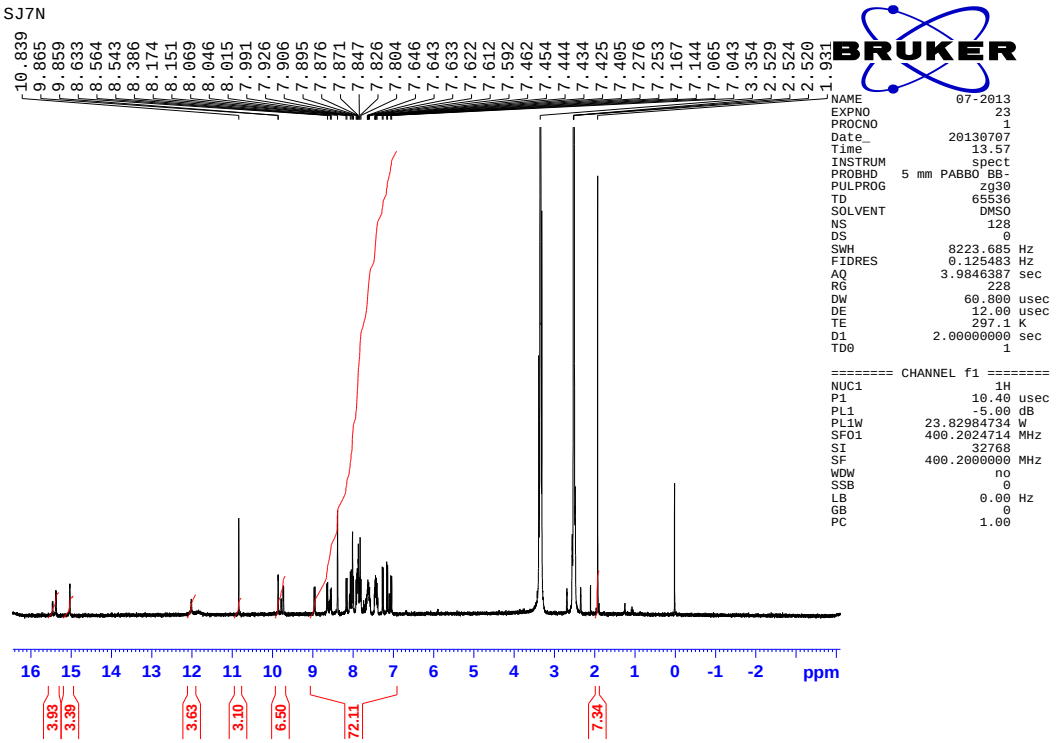

Appendix 27

FT-IR spectrum of Ni-SB4

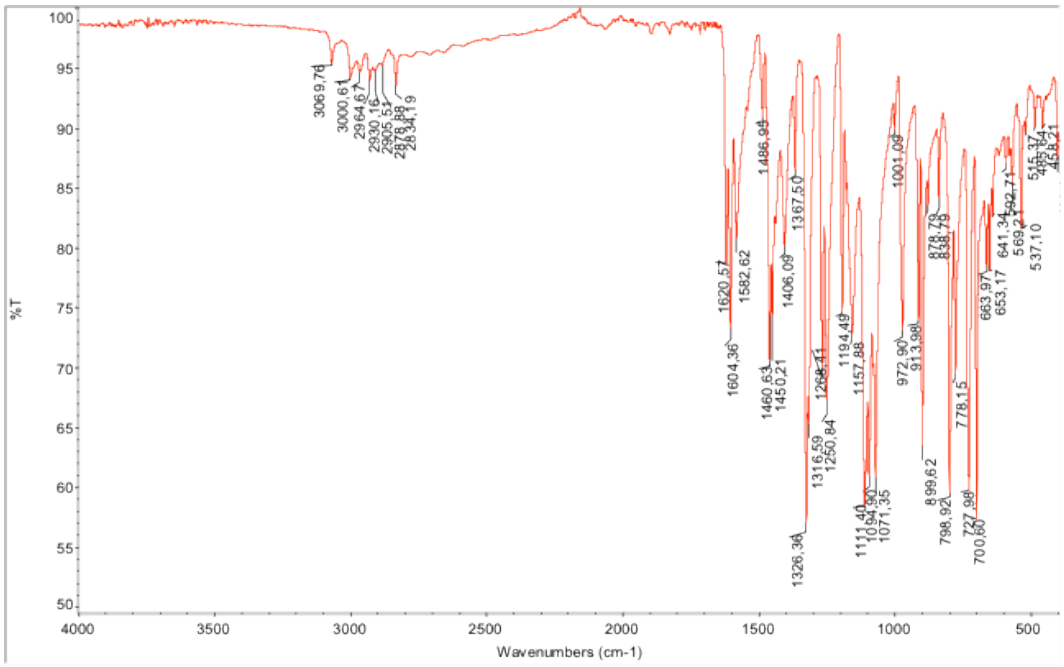

Appendix 28

FT-IR spectrum of Ni-SB5

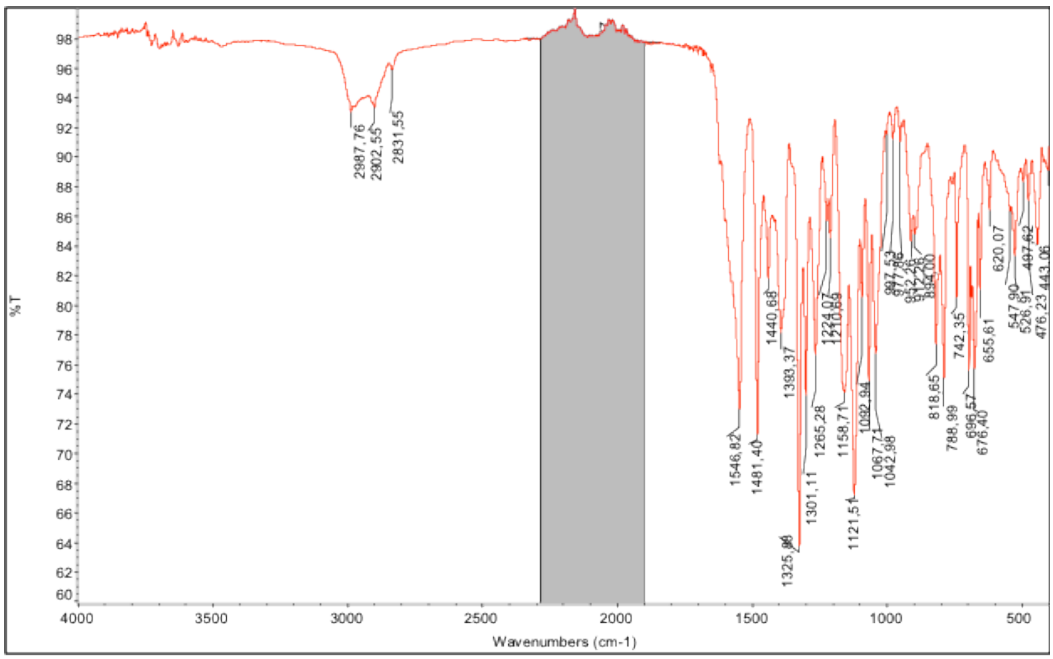

Appendix 29

^{1}H NMR spectrum of Ni-SB5

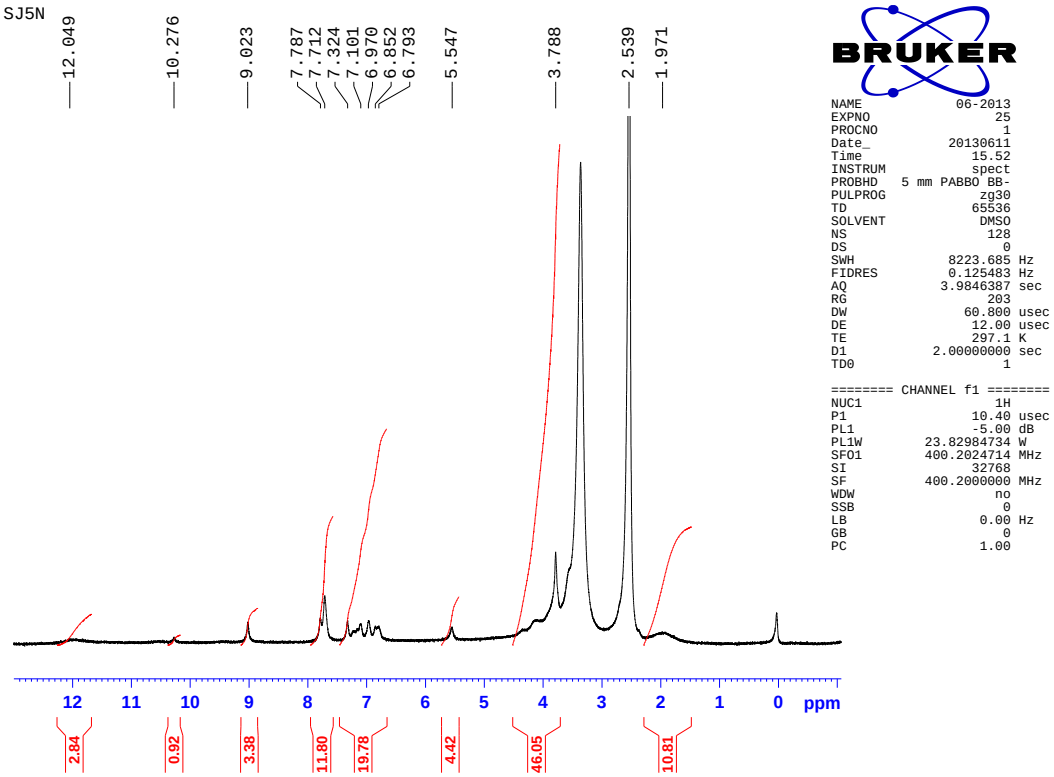

Appendix 30

FT-IR spectrum of Ni-SB6

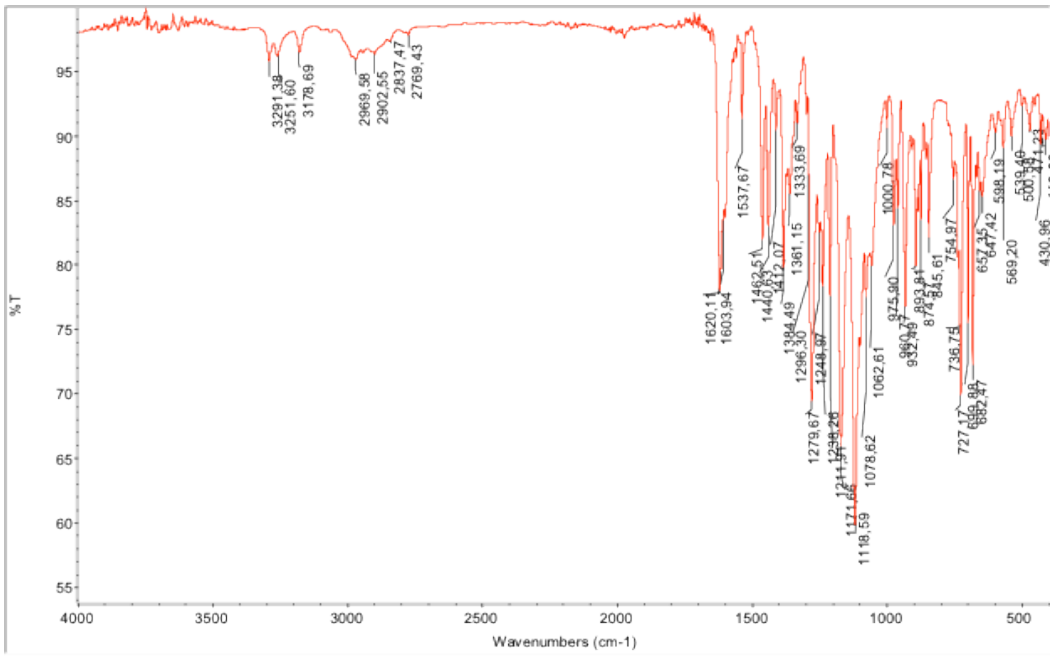

Appendix 31

FT-IR spectrum of Ni-SB7

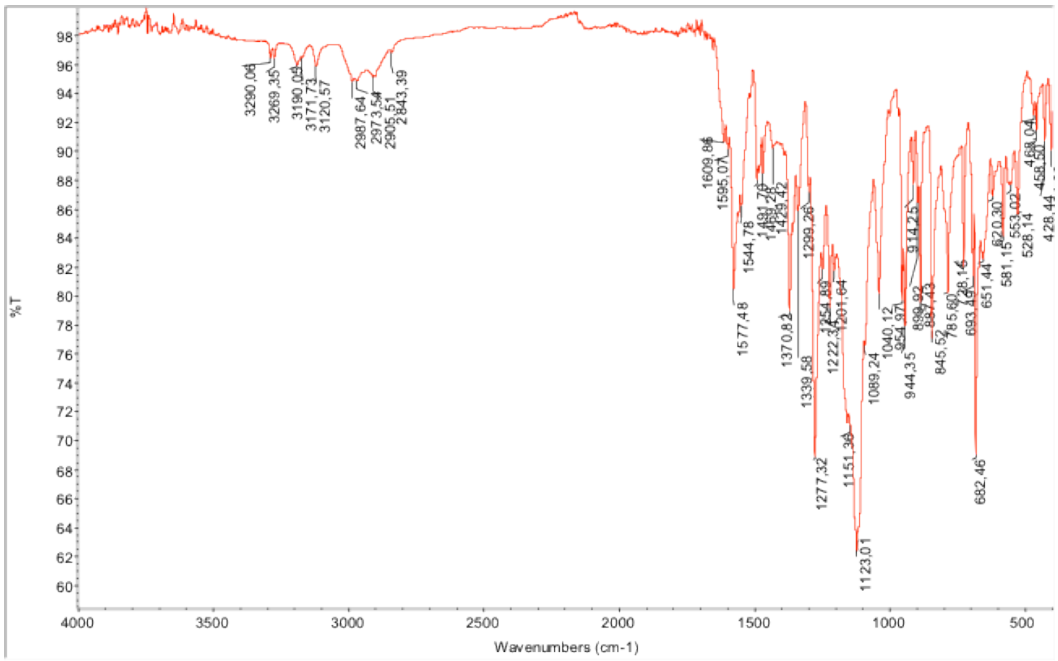

Appendix 32

^{1}H NMR spectrum of Ni-SB7

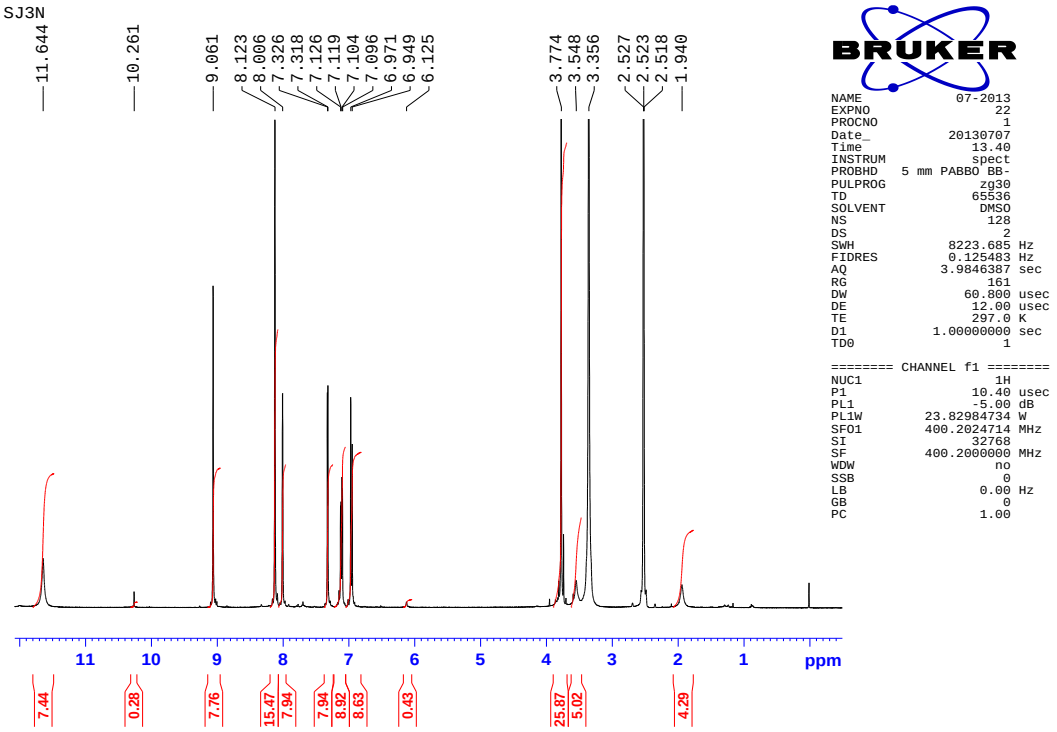

Appendix 33

FT-IR spectrum of Ni-ox2

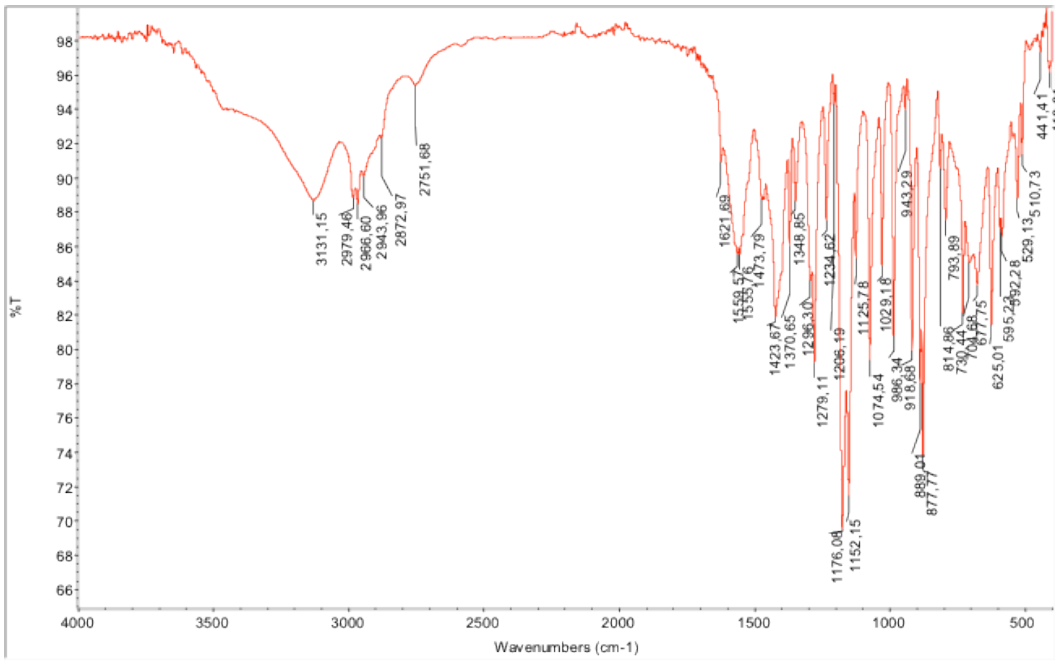

Appendix 34

^{1}H NMR spectrum of Ni-ox2

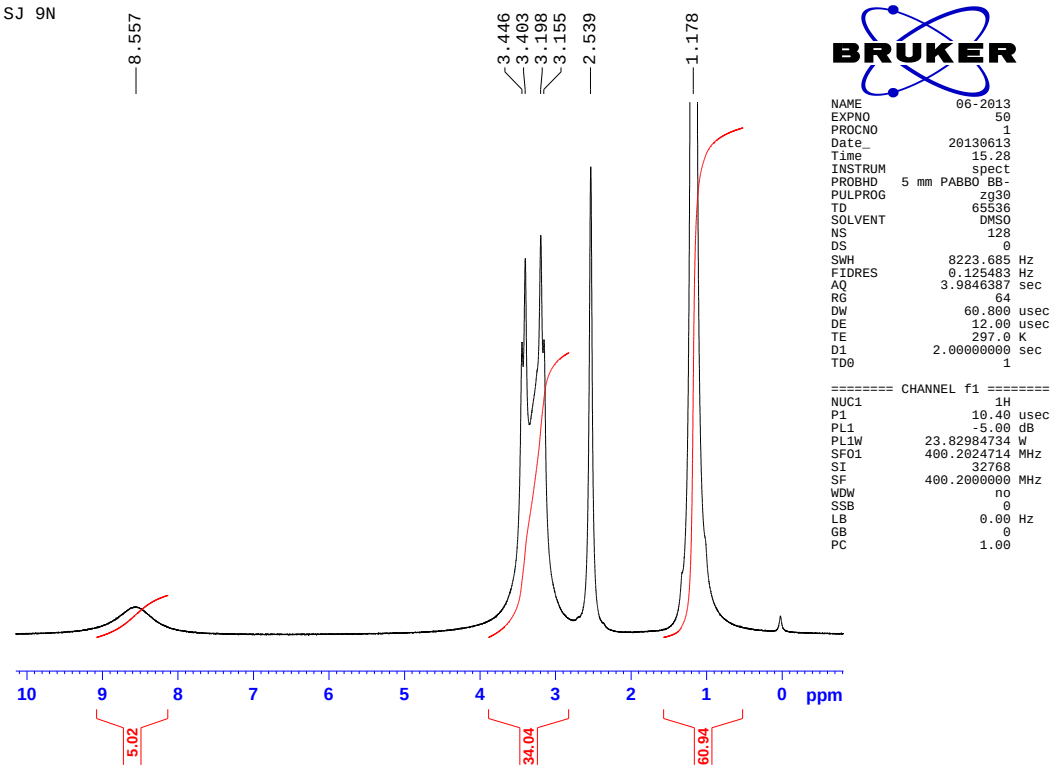

Appendix 35

FT-IR spectrum of Pd-SB1

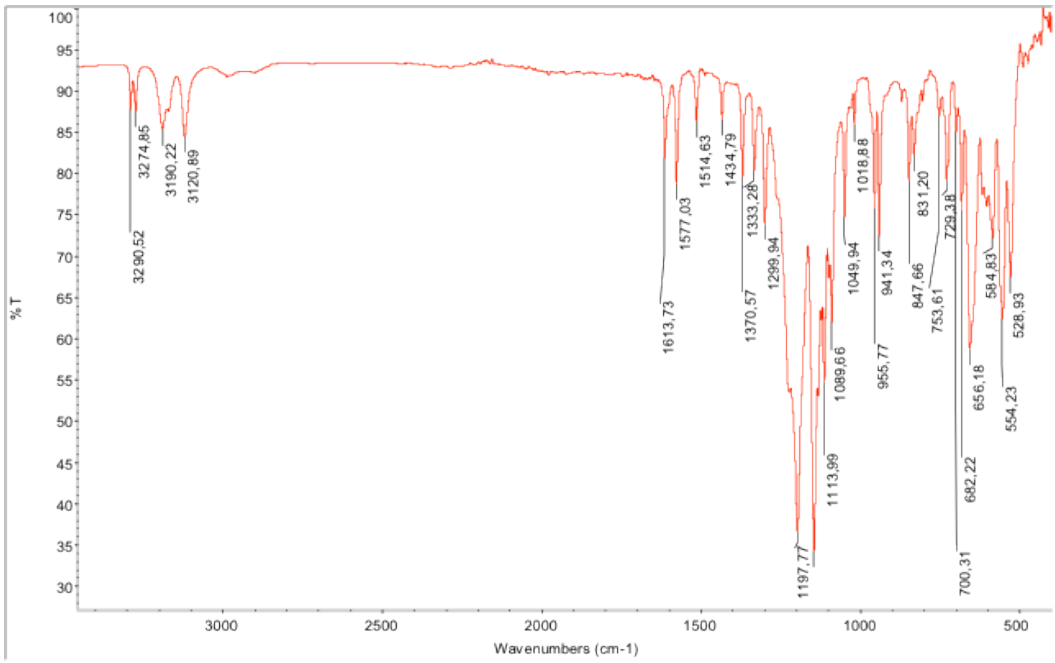

Appendix 36

^{1}H NMR of Pd-SB1

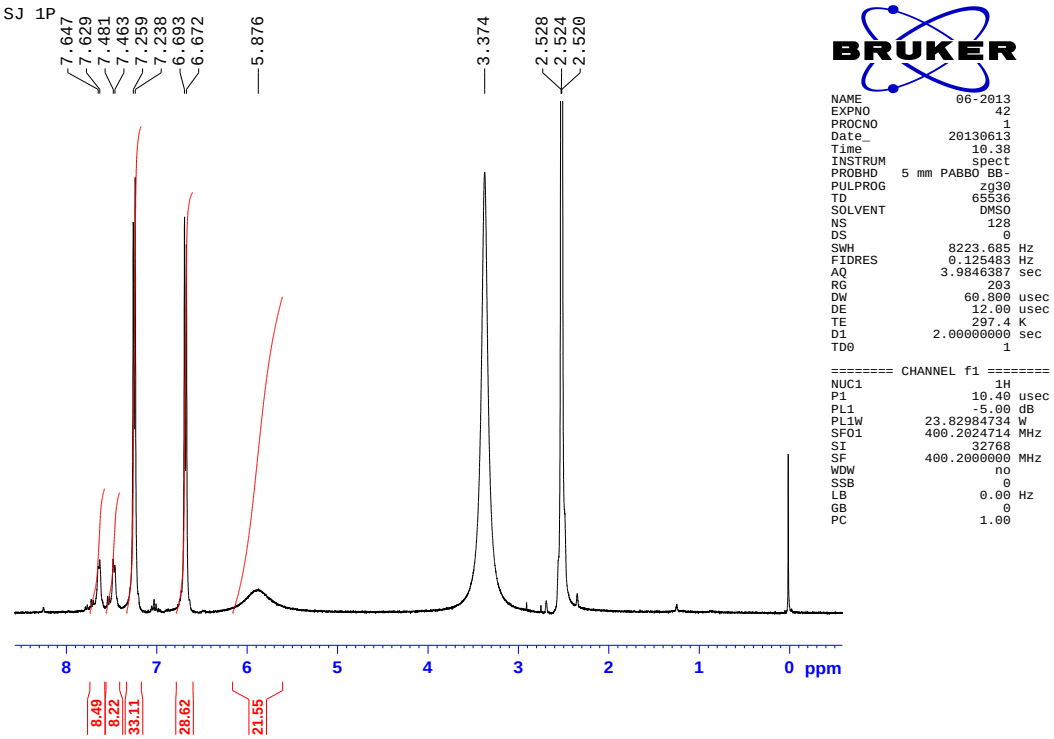

BRUKER

```
NAME                  06-2013
EXPNO                      42
PROCNO                      1
Date_               20130613
Time                   10.38
INSTRUM                spect
PROBHD   5 mm PABBO BB-
PULPROG                zg30
TD                    65536
SOLVENT                DMSO
NS                       128
DS                         0
SWH                 8223.685 Hz
FIDRES              0.125483 Hz
AQ                  3.9846387 sec
RG                       203
DW                    60.800 usec
DE                    12.00 usec
TE                    297.4 K
D1                 2.00000000 sec
TD0                        1

======== CHANNEL f1 ========
NUC1                      1H
P1                    10.40 usec
PL1                   -5.00 dB
PL1W             23.82984734 W
SFO1             400.2024714 MHz
SI                      32768
SF               400.2000000 MHz
WDW                       no
SSB                        0
LB                    0.00 Hz
GB                         0
PC                     1.00
```

Appendix 37

FT-IR of Pd-SB2

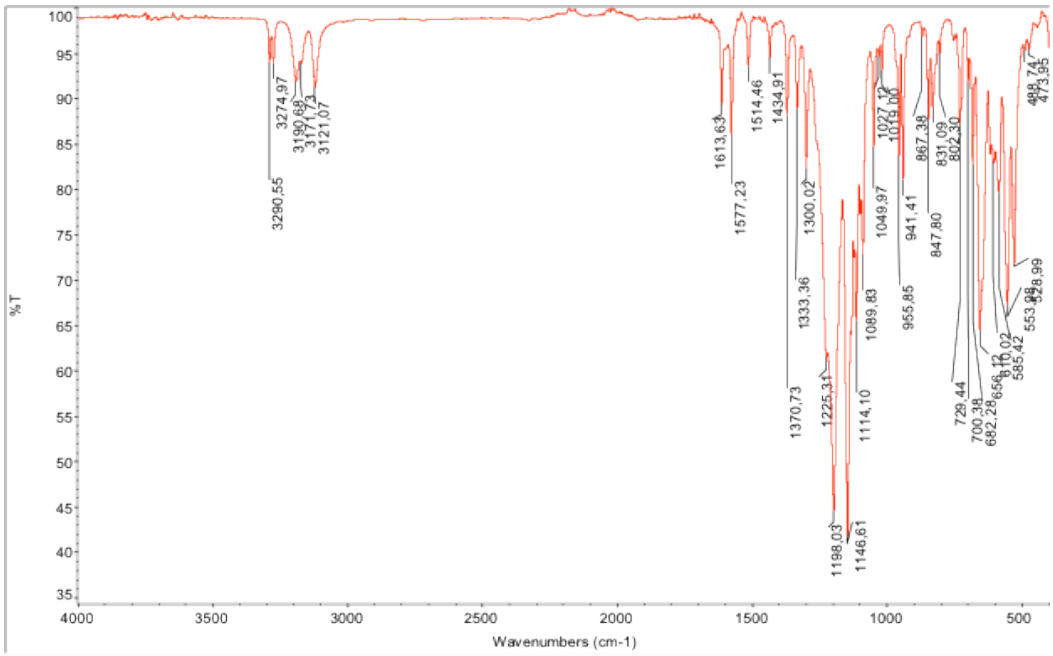

Appendix 38

^{1}H NMR spectrum of Pd-SB2

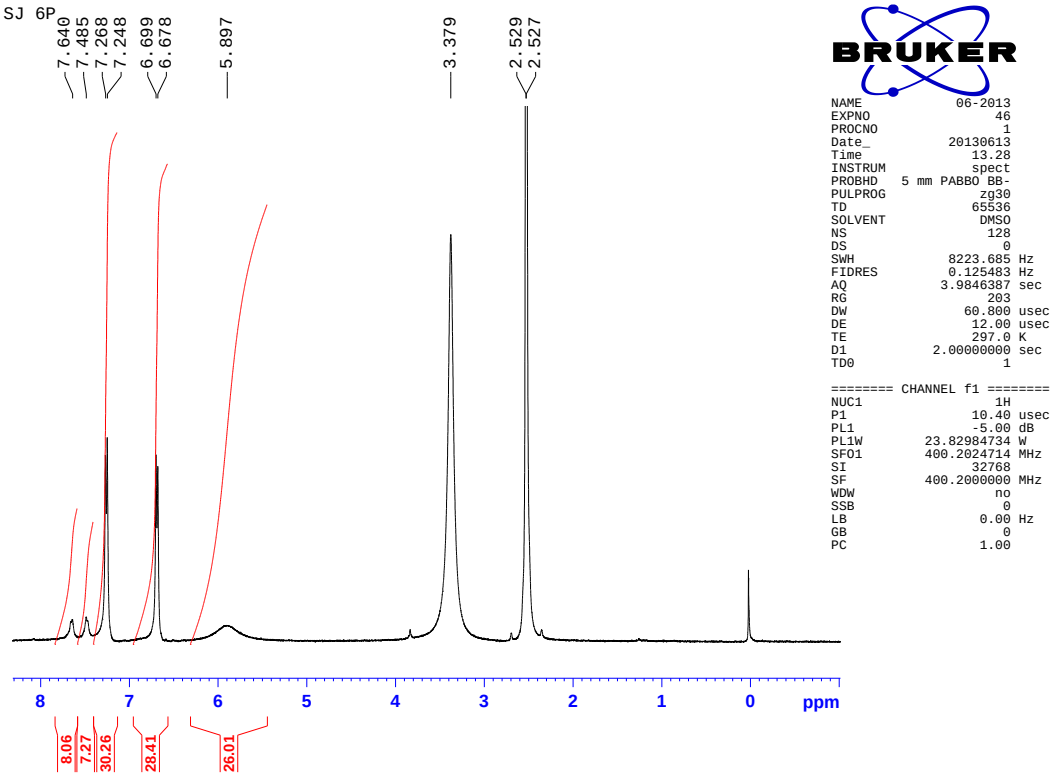

BRUKER

```
NAME                 06-2013
EXPNO                     46
PROCNO                     1
Date_               20130613
Time                   13.28
INSTRUM                spect
PROBHD   5 mm PABBO BB-
PULPROG                zg30
TD                    65536
SOLVENT                DMSO
NS                      128
DS                        0
SWH                8223.685 Hz
FIDRES            0.125483 Hz
AQ                3.9846387 sec
RG                      203
DW                   60.800 usec
DE                   12.00 usec
TE                   297.0 K
D1              2.00000000 sec
TD0                       1

======== CHANNEL f1 ========
NUC1                      1H
P1                   10.40 usec
PL1                  -5.00 dB
PL1W            23.82984734 W
SFO1            400.2024714 MHz
SI                     32768
SF              400.2000000 MHz
WDW                       no
SSB                       0
LB                     0.00 Hz
GB                        0
PC                     1.00
```

Appendix 39

FT-IR Spectrum of Pd-SB3

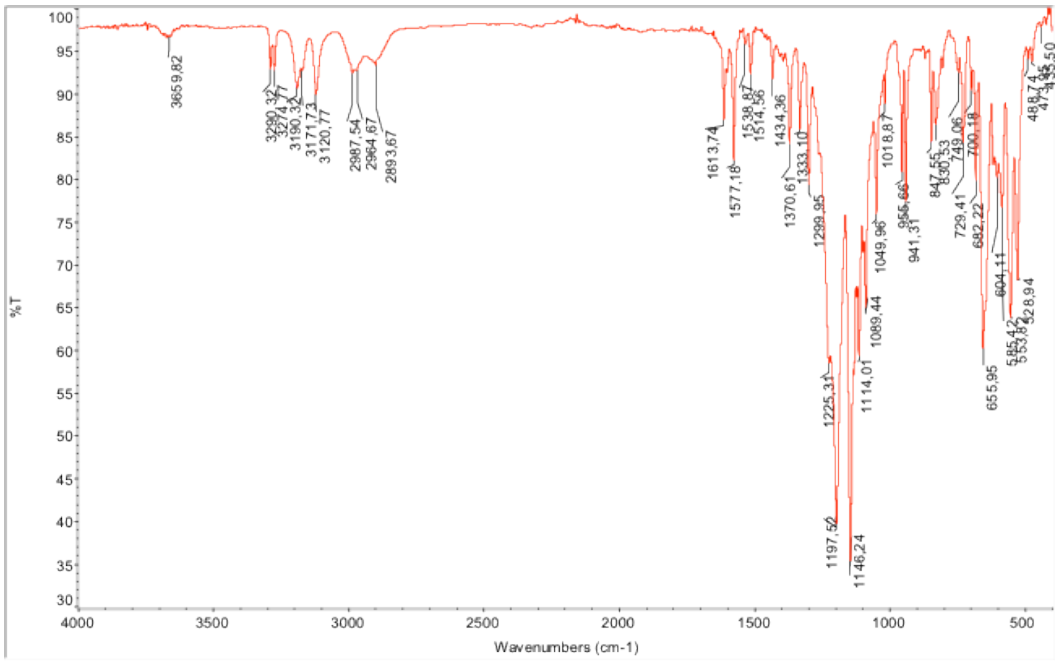

Appendix 40

^{1}H NMR spectrum of Pd-SB3

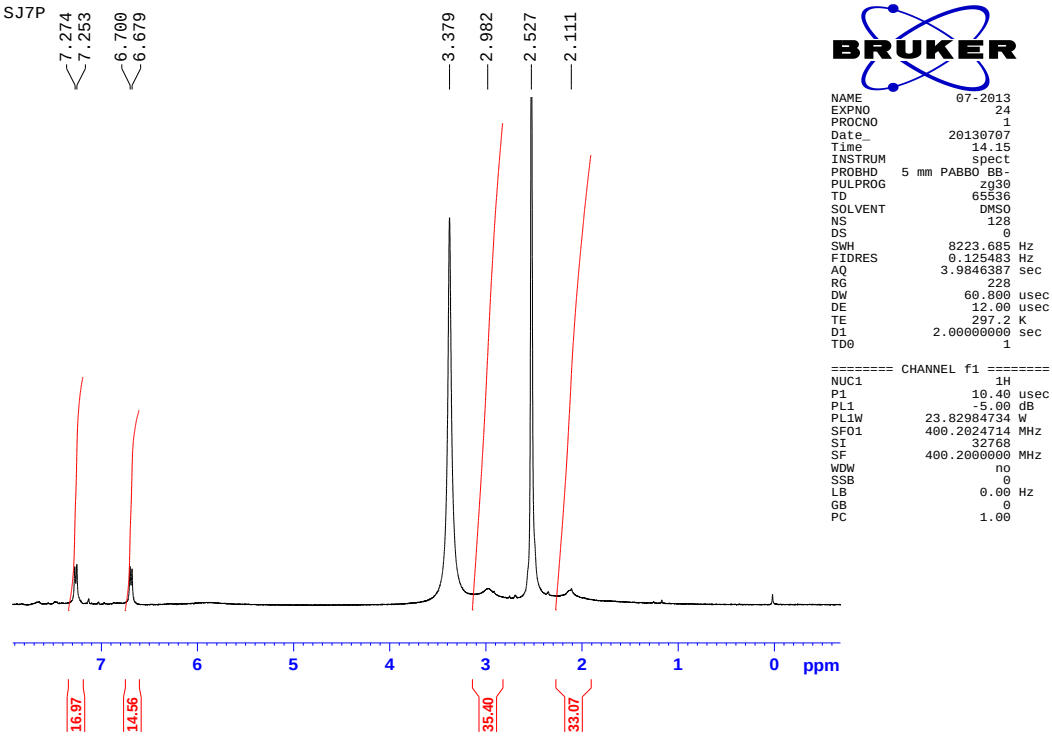

Appendix 41

FT-IR spectrum of Pd-SB4

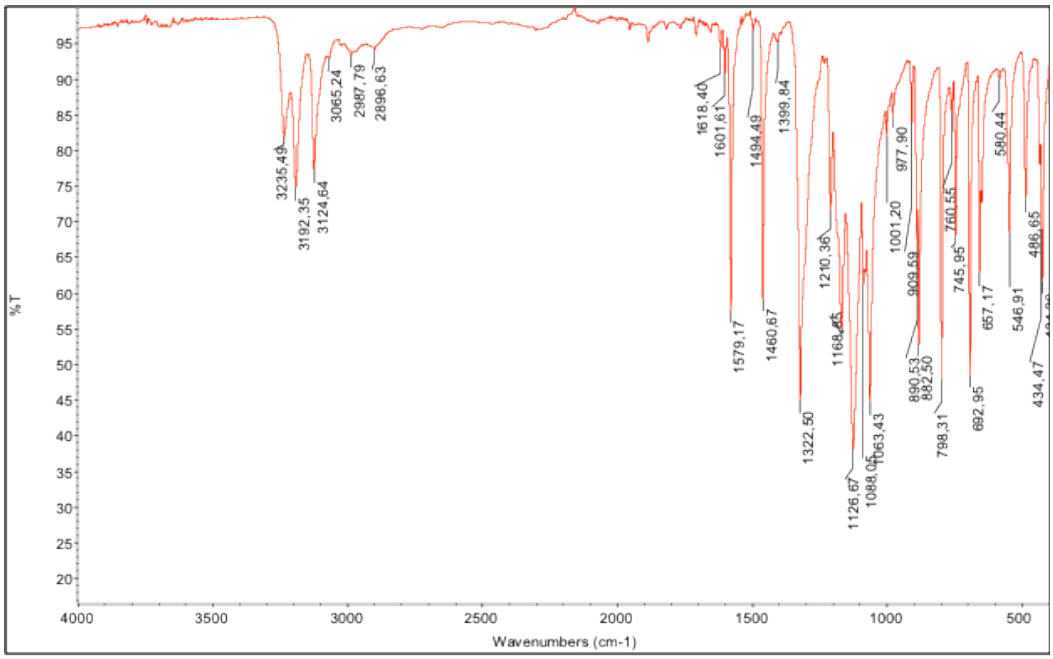

Appendix 42

^{1}H NMR spectrum of Pd-SB4

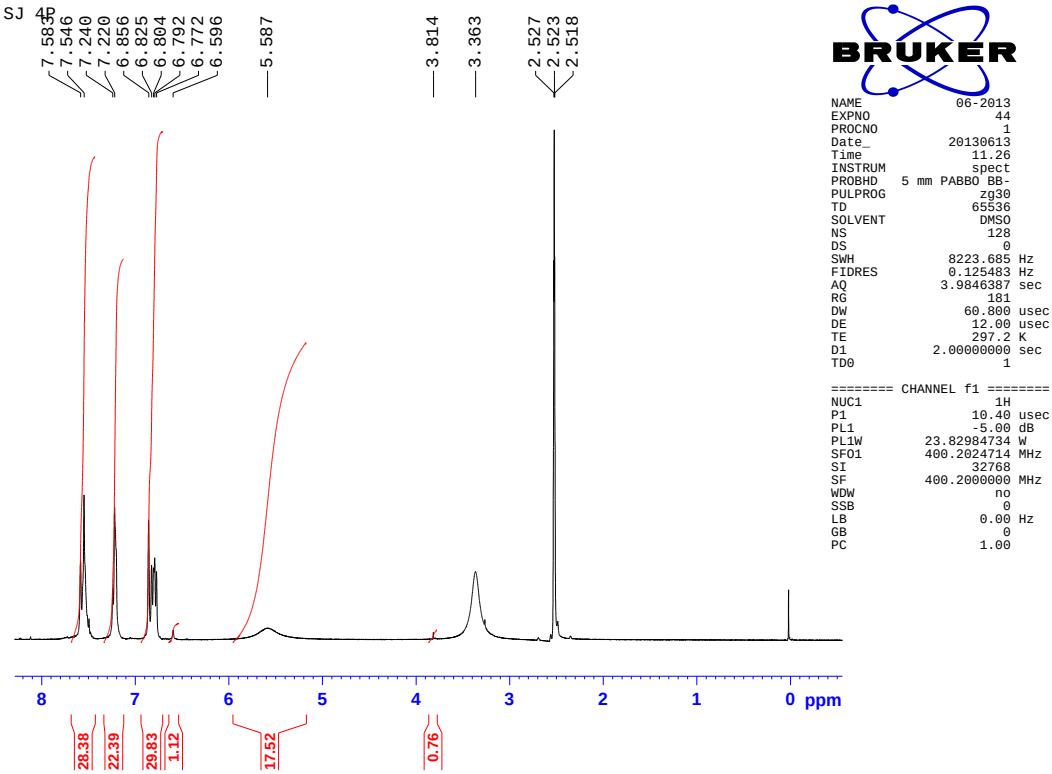

BRUKER

NAME	06-2013
EXPNO	44
PROCNO	1
Date_	20130613
Time	11.26
INSTRUM	spect
PROBHD	5 mm PABBO BB-
PULPROG	zg30
TD	65536
SOLVENT	DMSO
NS	128
DS	0
SWH	8223.685 Hz
FIDRES	0.125483 Hz
AQ	3.9846387 sec
RG	181
DW	60.800 usec
DE	12.00 usec
TE	297.2 K
D1	2.00000000 sec
TD0	1
======== CHANNEL f1 ========	
NUC1	1H
P1	10.40 usec
PL1	-5.00 dB
PL1W	23.82984734 W
SFO1	400.2024714 MHz
SI	32768
SF	400.2000000 MHz
WDW	no
SSB	0
LB	0.00 Hz
GB	0
PC	1.00

Appendix 43

FT-IR spectrum of Pd-SB5

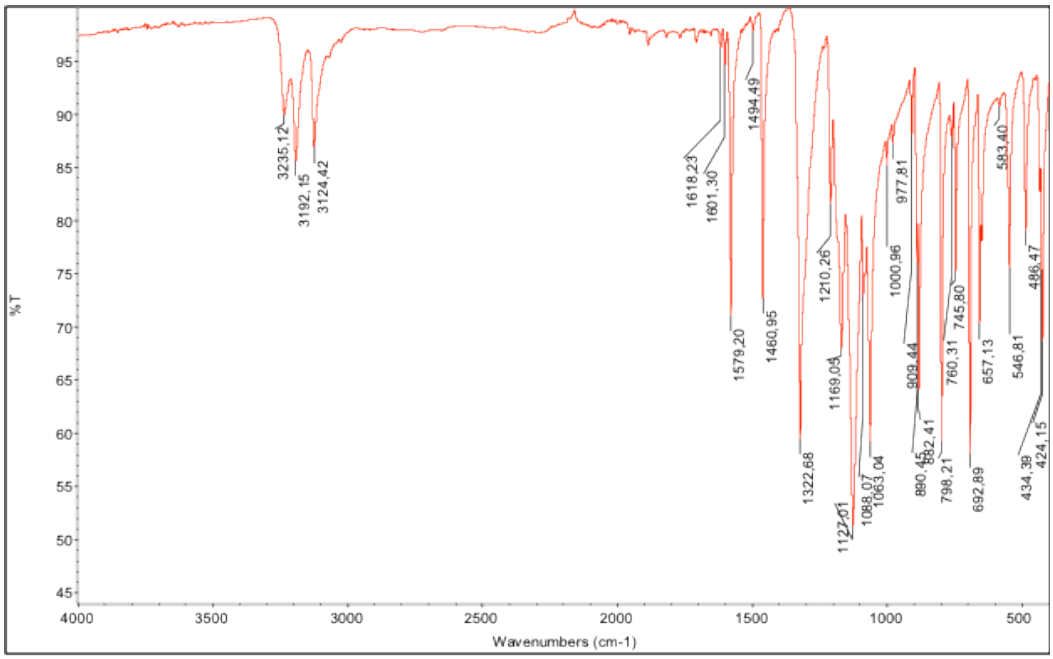

Appendix 44

^{1}H NMR spectrum of Pd-SB5

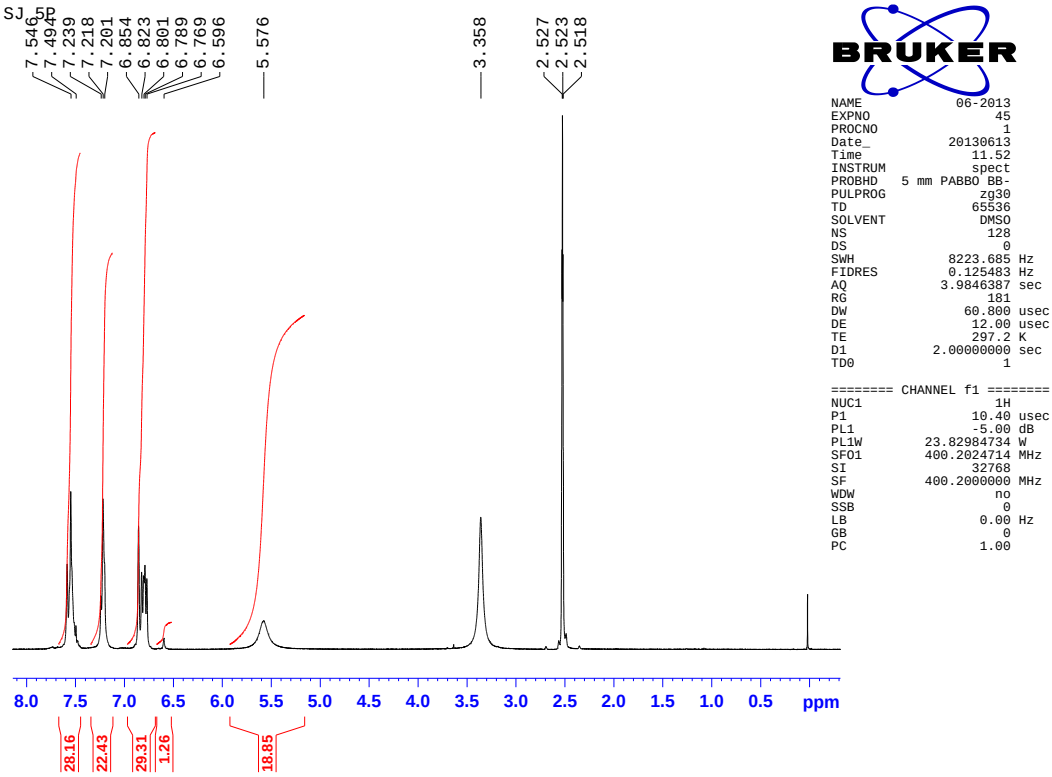


```
NAME                 06-2013
EXPNO                     45
PROCNO                     1
Date_               20130613
Time                   11.52
INSTRUM                spect
PROBHD   5 mm PABBO BB-
PULPROG                zg30
TD                    65536
SOLVENT                DMSO
NS                      128
DS                        0
SWH                8223.685 Hz
FIDRES            0.125483 Hz
AQ                3.9846387 sec
RG                      181
DW                   60.800 usec
DE                   12.00 usec
TE                   297.2 K
D1              2.00000000 sec
TD0                       1

======== CHANNEL f1 ========
NUC1                    1H
P1                   10.40 usec
PL1                  -5.00 dB
PL1W            23.82984734 W
SFO1            400.2024714 MHz
SI                    32768
SF              400.2000000 MHz
WDW                     no
SSB                      0
LB                    0.00 Hz
GB                       0
PC                    1.00
```

Appendix 45

FT-IR spectrum of Pd-SB6

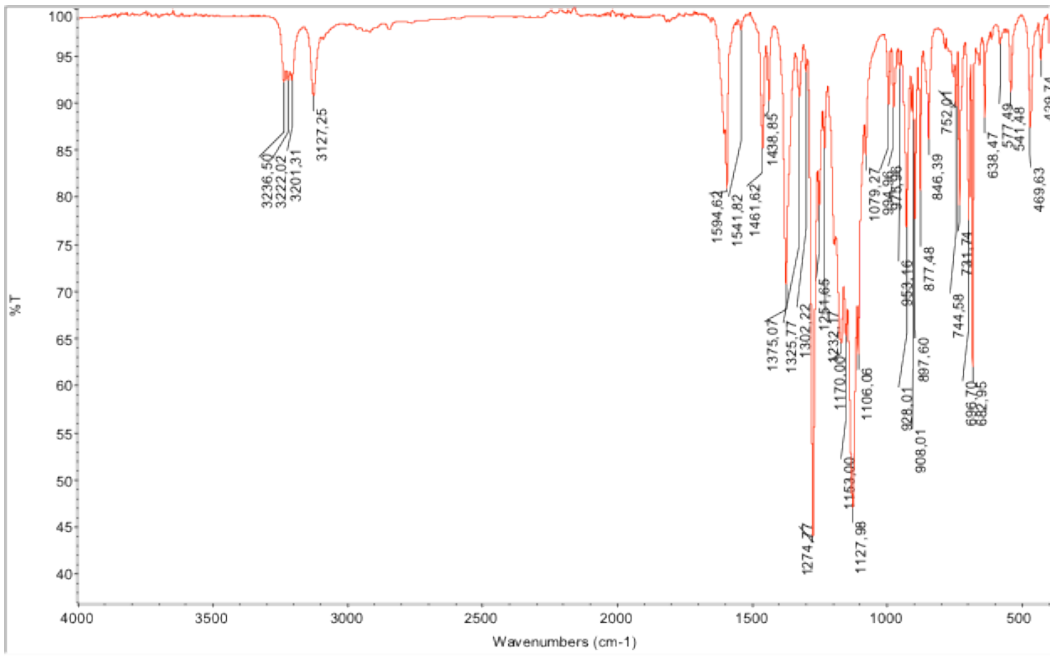

Appendix 46

^{1}H NMR spectrum of Pd-SB6

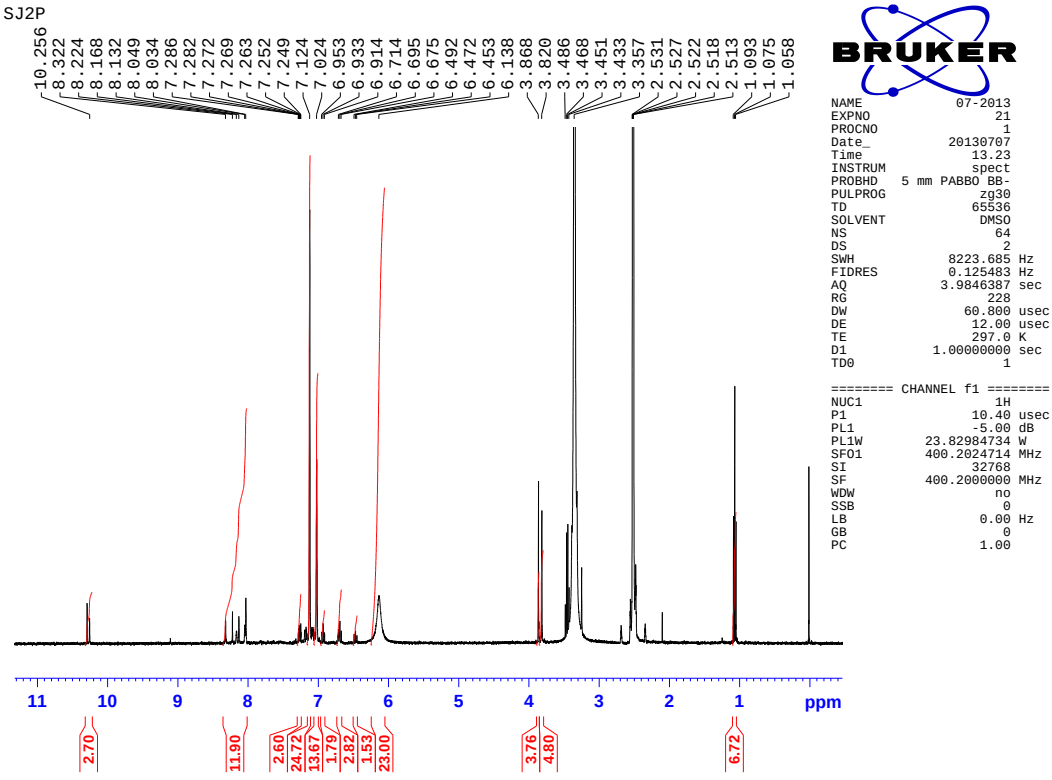

Appendix 47

FT-IR spectrum of Pd-SB7

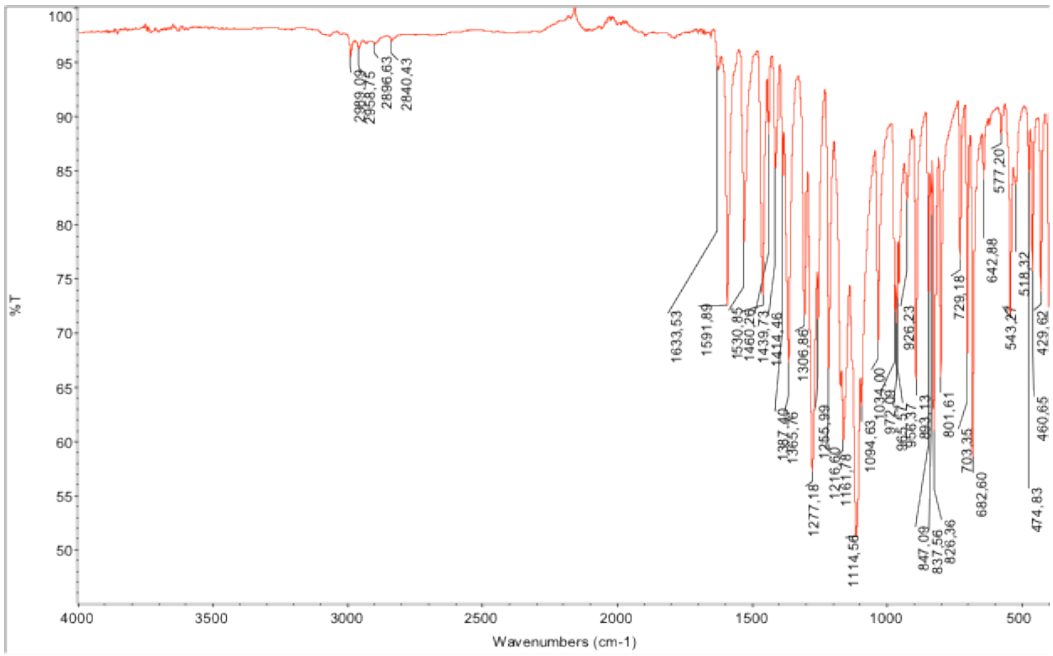

Appendix 48

^{1}H NMR spectrum of Pd-SB7

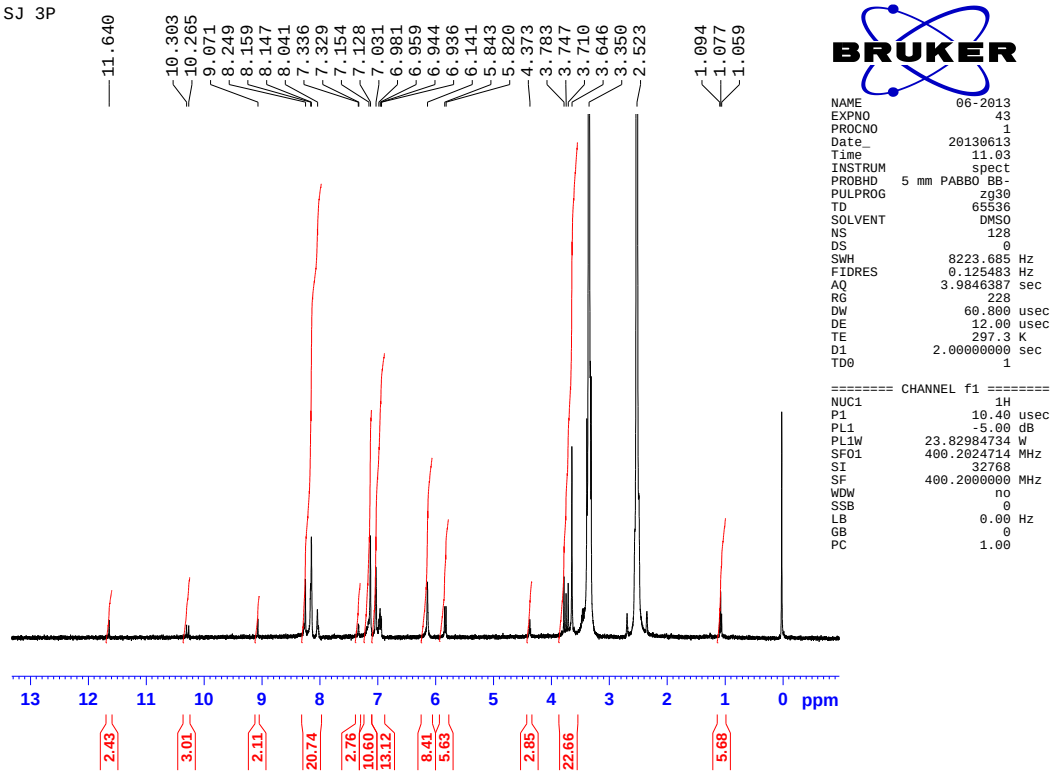

Appendix 49

FT-IR spectrum of Pd-ox1

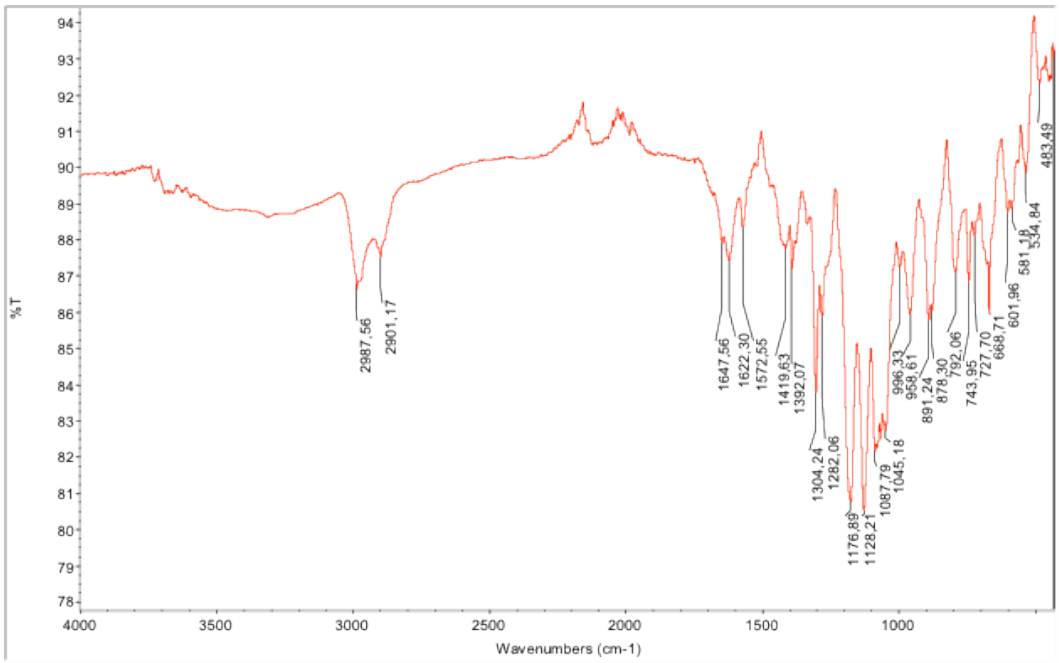

Appendix 50

FT-IR spectrum of Pd-ox2

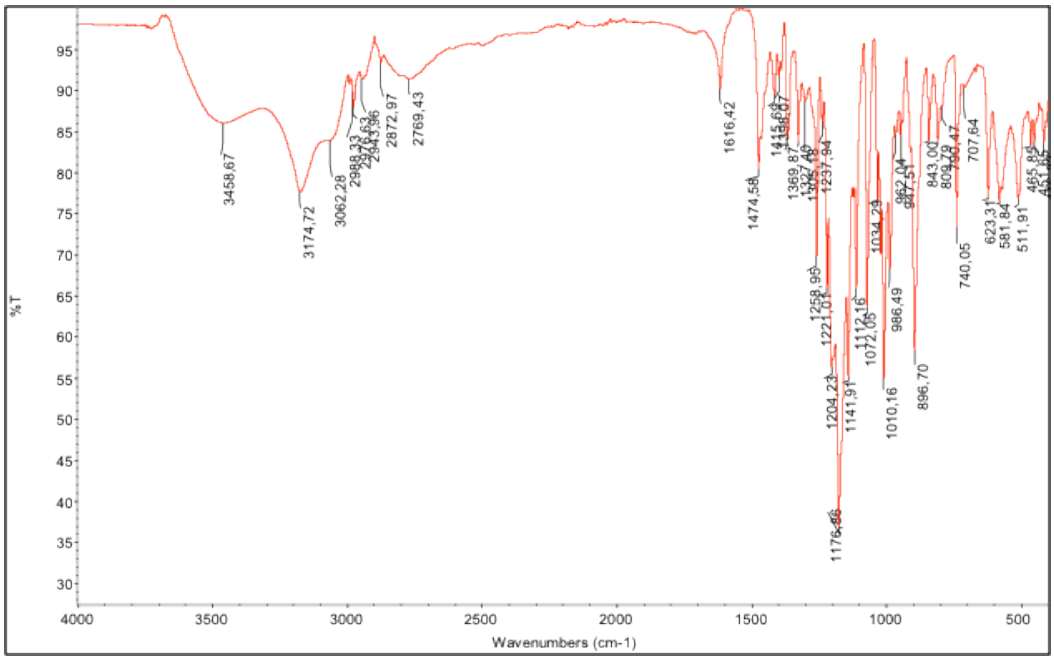

Appendix 51

NMR spectrum of Pd-ox2

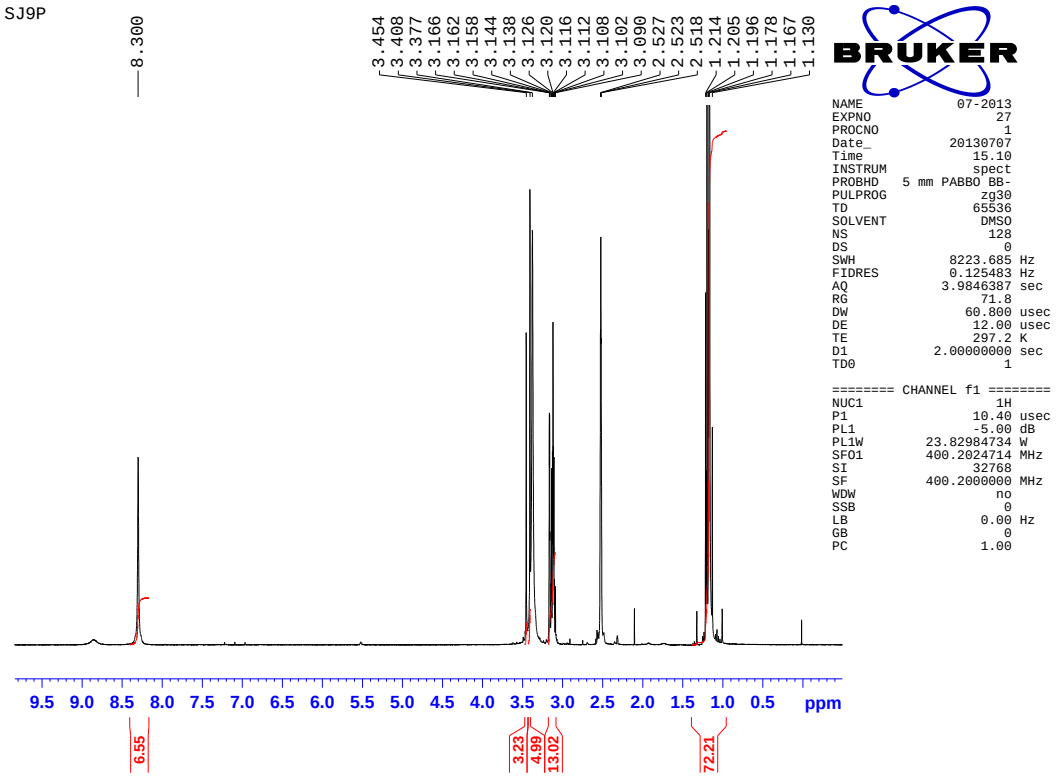

Appendix 52

FT-IR spectrum of W-SB1

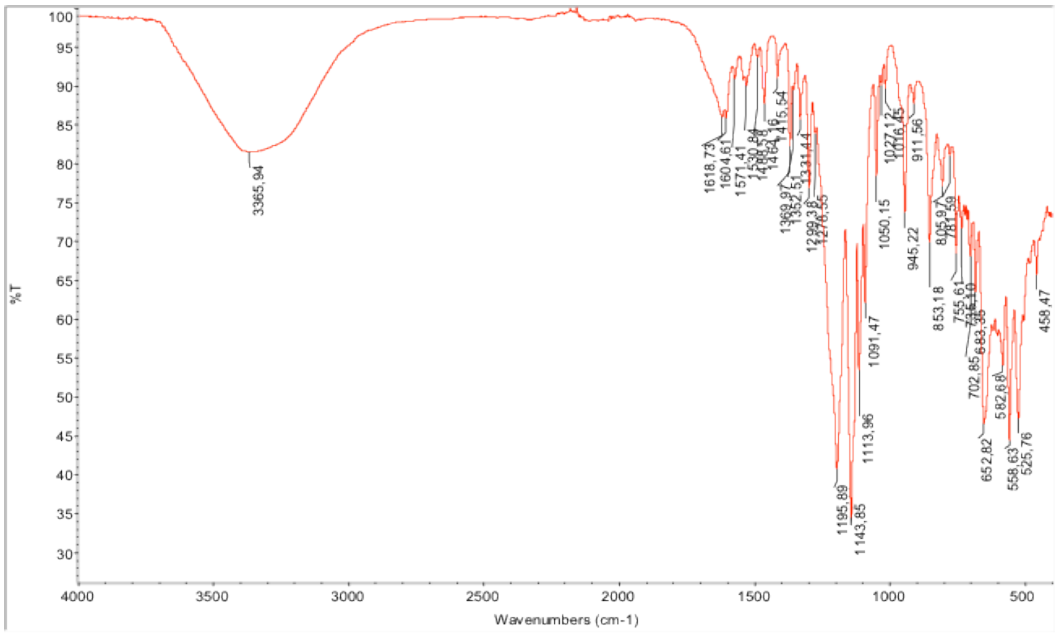

Appendix 53

^{1}H NMR spectrum of W-SB1

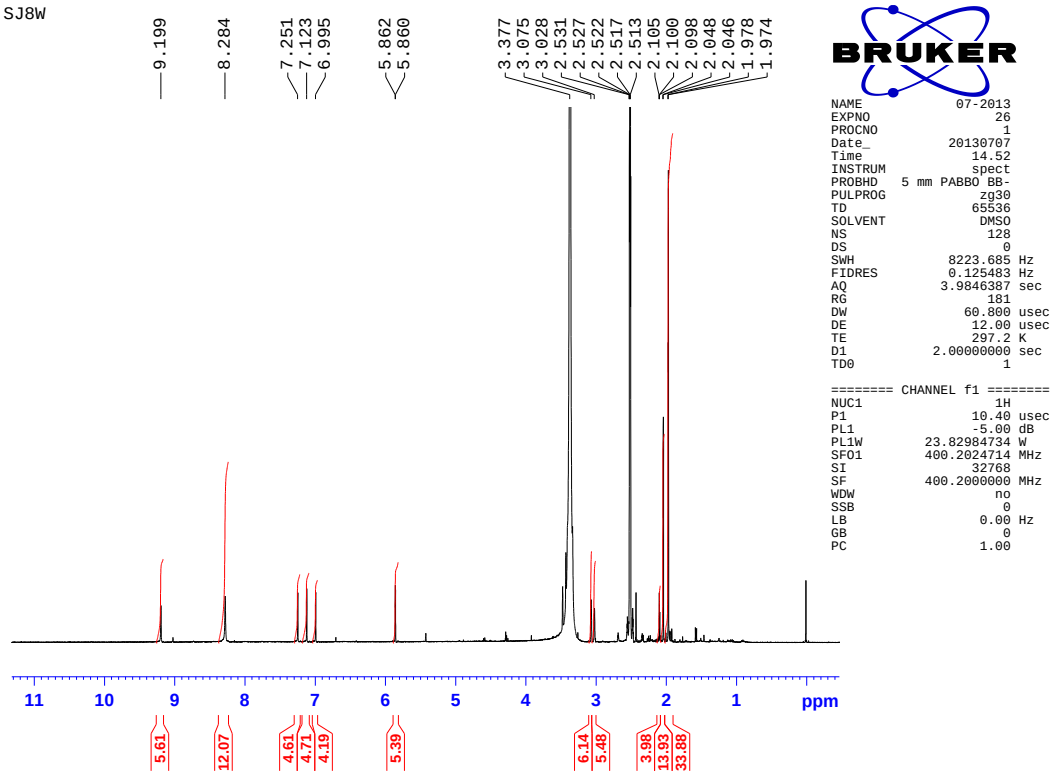

Appendix 54

FT-IR spectrum of W-ox1